Title
CHEMISORPTION AND REACTIVITY STUDIES OF SMALL MOLECULES ON RHODIUM SURFACES

Author
Castner, David G.

Publication Date
1979-09-01

LBL-9471 c.2

Lawrence Berkeley Laboratory

UNIVERSITY OF CALIFORNIA

Materials & Molecular Research Division

CHEMISORPTION AND REACTIVITY STUDIES OF SMALL MOLECULES ON RHODIUM SURFACES

David G. Castner
(Ph. D. thesis)

September 1979

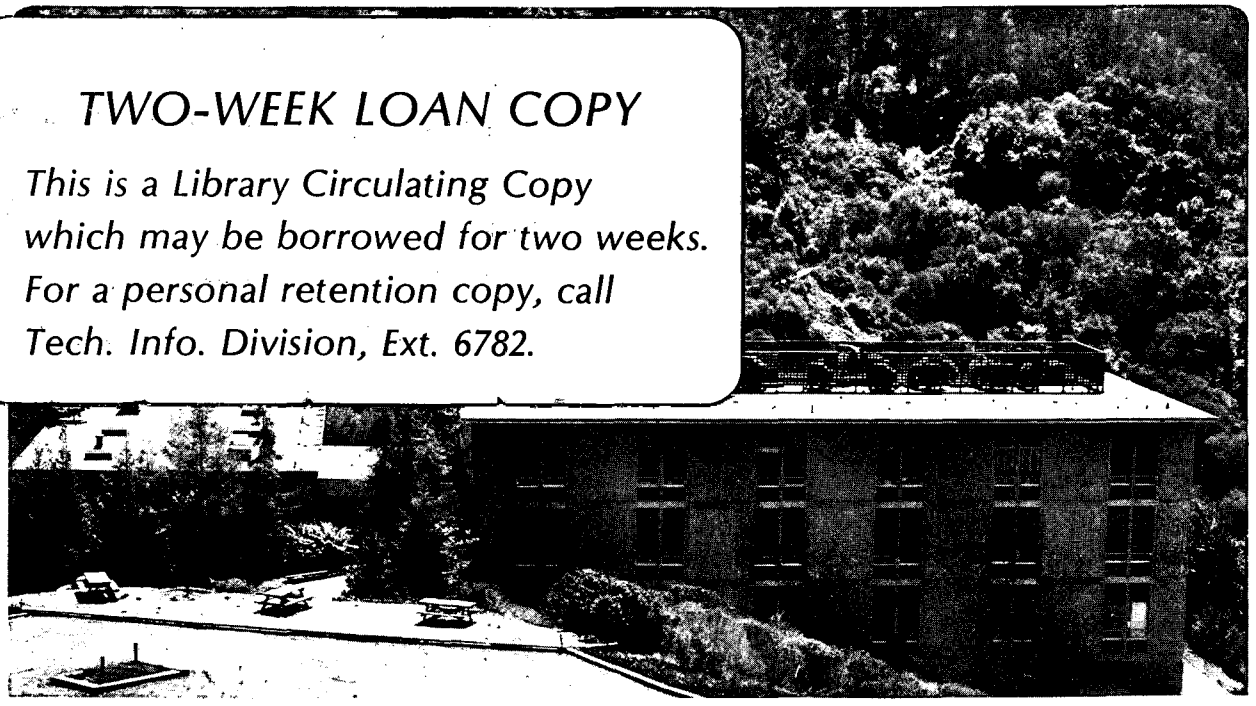

Prepared for the U.S. Department of Energy under Contract W-7405-ENG-48

DISCLAIMER

CHEMISORPTION AND REACTIVITY STUDIES OF SMALL MOLECULES ON RHODIUM SURFACES

David G. Castner

Materials and Molecular Research Division, Lawrence Berkeley Laboratory
and Department of Chemistry, University of California
Berkeley, California 94720

ABSTRACT

The chemisorption of H_2, O_2, CO, CO_2, NO, C_2H_2, C_2H_4 and C has been studied on the clean Rh(111), (100), (755) and (331) surfaces. Low-energy electron diffraction (LEED), Auger electron spectroscopy (AES) and thermal desorption mass spectroscopy (TDS) were used to determine the size and orientation of the unit cells, desorption temperatures and decomposition characteristics for each adsorbate. All of the molecules studied readily chemisorbed on all surfaces and several ordered surface structures were observed. Carbon dioxide appears to dissociate to CO upon adsorption on the rhodium surfaces as indicated by the similar ordering and desorption characteristics of CO_2 and CO. NO adsorption was dissociative at low exposures and associative at high exposures. C_2H_4 and C_2H_2 were associatively adsorbed at -60°C. Upon warming the adsorbed hydrocarbons to room temperature they underwent molecular rearrangement. The chemisorption results indicate that the same adsorbed species was produced from this rearrangement. Decomposition of C_2H_4 produced a sequence of ordered carbon surface structures on the (111) face as a result of a bulk-surface carbon equilibrium. The LEED patterns

seen on the stepped Rh(755) surface were due to the formation of surface structures on the (111) terraces, while on the stepped Rh(331) surface the step periodicity played an important role in the determination of the unit cells of the observed structures. When heated in O_2 or C_2H_4 the (331) surface was more stable than the (755) surface which readily formed (111) and (100) facets. In the CO and CO_2 TDS spectra a peak due to dissociated CO was observed on both stepped surfaces. Four different oxygen species were detected during the oxidation of the Rh(111) surface. Initially chemisorbed oxygen atoms were produced from the low temperature dissociative adsorption of oxygen and underwent an activated ordering process to form three domains of a (2×1) structure. The chemisorbed oxygen was readily removed by exposure to hydrogen above 50°C. Heating the Rh(111) crystal in the presence of oxygen resulted in oxygen diffusing into the near surface region. Prolonged high temperature annealing produced an unreactive surface oxide. The epitaxial growth of Rh_2O_3 (0001) on Rh(111) occurred during high temperature annealing in 1 torr of O_2. This epitaxial oxide did not adsorb detectable amounts of either hydrogen or CO at 25°C and could be decomposed by heating the crystal to 500°C in vacuum. Reacting a $3H_2$:1CO gas mixture at 300°C and 6 atm over clean polycrystalline Rh foil or single crystalline Rh(111) produced primarily methane at an initial rate of 0.15 molec·site^{-1}·sec. Preoxidation of the Rh catalysts resulted in changes in catalyst activity and selectivity, with oxygenated products only formed over the preoxidized catalysts. The major effect of gas phase additives was to increase the percentage of C_3 hydrocarbons in the product distribution.

TABLE OF CONTENTS

I. INTRODUCTION

Rhodium is one of the more versatile metal industrial catalysts, being used both in homogeneous and heterogeneous catalytic reactions. A number of rhodium-catalyzed homogeneous reactions have been introduced in recent years.[1] In the hydroformylation and carbonylation reactions rhodium complexes have replaced the traditional cobalt complexes because these reactions will proceed at significantly lower pressures over the rhodium catalysts. Examples of homegenous reactions which rhodium complexes catalyze are the synthesis of n-butyraldehyde from CO, hydrogen and propylene[2,3] (hydroformylation), acetic acid from CO and methanol[4,5] (carbonylation) and ethylene glycol from CO and hydrogen.[6,7] An important heterogeneous use of rhodium catalysts is in the three-way automotive catalytic converters. Rhodium catalysts have been shown to be very effective in reducing nitrogen oxides to nitrogen in the presence of oxygen.[8,9] Combining a supported 0.002 wt % Rh catalyst with either a supported Pt or Pd catalyst produces a three-way catalyst capable of eliminating NO, CO and HC from typical model feeds of automotive exhausts.[8] Rhodium is also a Fischer-Tropsch (FT) catalyst, producing various hydrocarbons by hydrogenating CO. At low reaction pressures (1-6 atm) CO hydrogenation over supported Rh/Al_2O_3[10] and unsupported clean Rh[11,12] catalysts primarily produces methane while above 20 atm CO hydrogenation over supported Rh/SiO_2 catalysts[13,14] yields a product distribution containing more than 40% C_2 chemicals such as acetic acid, acetaldehyde and ethanol. The large amount of oxygenated hydrocarbons produced by rhodium catalysts is in contrast to other

FT catalysts such as Ni which is primarily a methanation catalyst,[10] Fe and Co which produce large amounts of higher molecular weight hydrocarbons[10] and Ru which produces high molecular weight paraffinic waxes.[15] Some of the other reactions which are catalyzed by rhodium are hydrogenation of olefins[16] and benzene,[17] deuterium exchange with hydrocarbons[18] and NH_3,[19] ketone reduction[17] and oxidation of hydrogen,[17,20] NH_3[21] and CO.[11] The above examples show rhodium catalysts do indeed have a rich chemistry, readily breaking N-O, N-H, C-O, C-C, C-H and H-H bonds and inserting CO molecules into hydrocarbons.

The chemisorption and catalytic properties of small molecules on rhodium surfaces have only been investigated in recent years with surface sensitive techniques. These investigations have primarily been low-energy electron diffraction (LEED) studies on low index crystal faces. The earliest studies were LEED investigations of oxygen and CO adsorption on the Rh(100), (110) and (210) surfaces.[22-24] Several ordered surface structures were observed in these experiments, but since Auger electron spectroscopy (AES) was not used to monitor the surface composition there is some doubt as whether these structures were due to the adsorbates or to surface impurities. Recent experiments have found that impurities such as boron will diffuse to the surface and form ordered surface structures. A brief LEED and AES investigation of oxygen, CO and CO_2 adsorption on Rh(111) has been reported.[25] Only one surface structure was observed for each adsorbate and very little explanation of these structures were given. In the last two years

several investigations of small molecule chemisorption on rhodium single crystal surfaces have been reported. A systematic survey of the chemisorption properties of H_2, O_2, CO, CO_2, NO, C_2H_4, C_2H_2 and carbon have been investigated by LEED and thermal desorption mass spectroscopy (TDS) on the low index (111) and (100)[26] and stepped (755) and (331)[27] rhodium surfaces. Further LEED, AES and TDS investigations have been carried out for hydrogen,[28] oxygen[29,30] and CO[31] adsorption on the Rh(111) surface. LEED, AES, TDS and surface potential studies have been reported for oxygen, CO and NO adsorption on the Rh(110) surface.[32,33] In the above LEED studies only the size and shape of the adsorbate unit cells were reported. To determine such quantities as the binding site or molecular structure of an adsorbate by LEED requires an analysis of the diffraction beam intensity vs beam voltage (I-V) curves. Presently no I-V analysis have been reported for adsorbates on rhodium surfaces. AES and TDS used in conjunction with the LEED results in the above investigations did indicate possible arrangments of the adsorbate on the surface.

Recently high resolution energy loss spectroscopy (ELS) has been used in conjunction with LEED and TDS to make definitive assignments of the adsorbates species produced by adsorption of O_2, CO, CO_2, C_2H_2 and C_2H_4 on Rh(111).[34-36] High resolution ELS is a powerful technique for probing the interaction of adsorbates with metal single crystal surfaces because the observed inelastic losses in the ELS spectrum correspond to the various vibrational modes of an adsorbate. The number of observed modes and the energy at which they appear can be used to determine the

molecular structure and binding site of the adsorbate. The ELS investigations have shown on Rh(111) that CO_2 is dissociatively adsorbed and that adsorbed C_2H_2 and C_2H_4 undergo molecular rearrangement.

Several LEED I-V analysis have been carried out on the clean rhodium (111),[37] (100)[38,39] and (110)[40] surfaces. In addition Debye surface temperatures have been determined for the rhodium (111)[41,42] and (100)[41] surfaces. These investigations have shown that the Rh surfaces do not reconstruct and have topmost interlayer spacings within 5% of the bulk interlayer spacing.

This author is only aware of two investigations of catalytic reactions over Rh single crystal surfaces, the reaction of H_2 with adsorbed oxygen to produce H_2O[20] and the hydrogenation of CO to produce hydrocarbons.[12] Both of these reactions were carried out on the (111) crystal face. Investigations of catalytic reactions over polycrystalline Rh foils and wires are more prevalent. CO oxidation and hydrogenation over polycrystalline Rh foils have been investigated.[11,12] CO oxidation,[43,44] NO reduction[45] and NH_3 oxidation[46] are some the catalytic investigations reported over polycrystalline Rh wires. Even more catalytic studies have been carried out over supported Rh catalysts. Some of these studies include NO reduction,[8,9,47-49] CO hydrogenation,[10,13,14] pentane hydrogenolysis[49] and ethylene and acetylene hydrogenation.[50] Several catalytic homogeneous reactions involving Rh complexes were mentioned earlier.

FT synthesis has been in existence for over fifty years,[51,52] but the mechanism of this synthesis is still undetermined. Several mechamisms have been proposed, including the carbide theory,[53-55] hydrogenation of undissociated CO[56,57] and CO insertion.[58] The proposed mechanisms and experimental data over the last fifty years have been described in detail in several articles.[15,53-65] Because of the wide range of FT catalysts which produce an even wider range of products it is likely that the several mechanisms are operative in the FT synthesis. Selection of the catalyst and reaction conditions (temperature, pressure, H_2:CO ratio) would determine which mechanism and product distribution would be favored.

The results presented in this thesis can be divided into two parts, the chemisorption and the CO hydrogenation investigations on rhodium surfaces. In the chemisorption investigations a systematic survey of the chemisorption properties of several small molecules (H_2, O_2, CO, CO_2, NO, C_2H_2 and C_2H_4) on four different Rh single crystal surfaces was undertaken. These studies were carried out to probe the interaction of these molecules with the Rh surfaces, to find the interesting areas of rhodium surface chemistry, to determine the chemisorption structure sensitivity of these molecules on Rh surfaces and in general document the chemisorption properties of Rh surfaces. These experiments were carried out under ultra-high vacuum (UHV) conditions using LEED to detect the formation of ordered surface structures, AES to monitor the surface composition and TDS to yield information about binding energies and decomposition, desorption and dissolution characteristics of the adsorbates.

The results of these experiments will yield some insight into the catalytic properties of rhodium.

The CO hydrogenation reaction was studied over polycrystalline Rh foil and single crystalline Rh(111) catalysts at a total pressure of 6 atm. An UHV chamber equipped with a high pressure isolation cell[66] was used in these experiments so the catalysts could be characterized both before and after the reaction by LEED, AES and TDS. The reaction conditions (H_2:CO ratio, reaction temperature and surface pretreatment) were systematically varied to determine the optimum conditions for production of oxygenated hydrocarbons by the rhodium catalysts at 6 atm. Correlations were made between catalyst activity, selectivity, lifetime, surface composition and structure. A detailed mechanistic and kinetic study of the FT synthesis on rhodium catalysts was not carried out here but instead the major emphasis was placed on determining the conditions necessary for oxygenated product formation.

The experimental details and apparatus employed in the chemisorption and CO hydrogenation studies will be described in detail in Chapter II. The three surface characterization techniques (LEED, AES and TDS) used in these studies will also be described in Chapter II. The main emphasis in the technique discussions will be on the information these techniques yield and how this information is obtained from the experimental data. In Chapter III the results of the chemisorption and CO hydrogenation studies will be presented and discussed. Chapter III is divided into five parts: the characterization of the clean rhodium (111), (100), (755) and (331) surfaces; the chemisorption properties of small molecules on the rhodium (111) and (100)surfaces; the

chemisorption properties of small molecules on the stepped rhodium (755) and (331) surfaces; the oxidation of the Rh(111) surface; and the CO hydrogenation reaction (FT synthesis) over clean and oxidized rhodium polycrystalline foil and single crystalline (111) surfaces. In Chapter V the major conclusions of the chemisorption and reactivity studies will be summarized.

II. EXPERIMENTAL

A. Surface Characterization by LEED

Low-energy electron diffraction (LEED) is a surface sensitive technique ideally suited for probing the ordering of adsorbate overlayers on metal single crystal surfaces. The low-energy monoenergetic electrons (10 to 500 eV) used in LEED have de Broglie wavelengths of 4 to 0.5 Å making them suitable for diffraction from single crystals such as rhodium (nearest neighbor distance of 2.69 Å). The surface sensitivity of LEED results from the strong interaction of these low-energy electrons with the metal causing the electrons to undergo multiple scattering in the upper 3 or 4 atomic layers of the crystal. This behavior is schematically depicted in Fig. II-1 and contrasted with the weak interacting kinematical x-rays which penetrate well into the bulk of a sample. The escape depth of electrons depends on electron energy as shown by the "universal curve" in Fig. II-2. The escape depth of the low-energy electrons used in LEED is less than 10 Å or less than 3 or 4 atomic layers.

LEED is capable of providing the same information about the structure of surfaces that x-ray crystallography provides for bulk crystal structures. In LEED the position of the diffraction beams determine the two dimensional periodicity of the surface mesh and the I-V profiles of these diffracted beams determine the location of the atoms in this mesh. The complication which exists in LEED analysis is mutliple scattering, which makes determination of the atomic locations difficult. Therefore

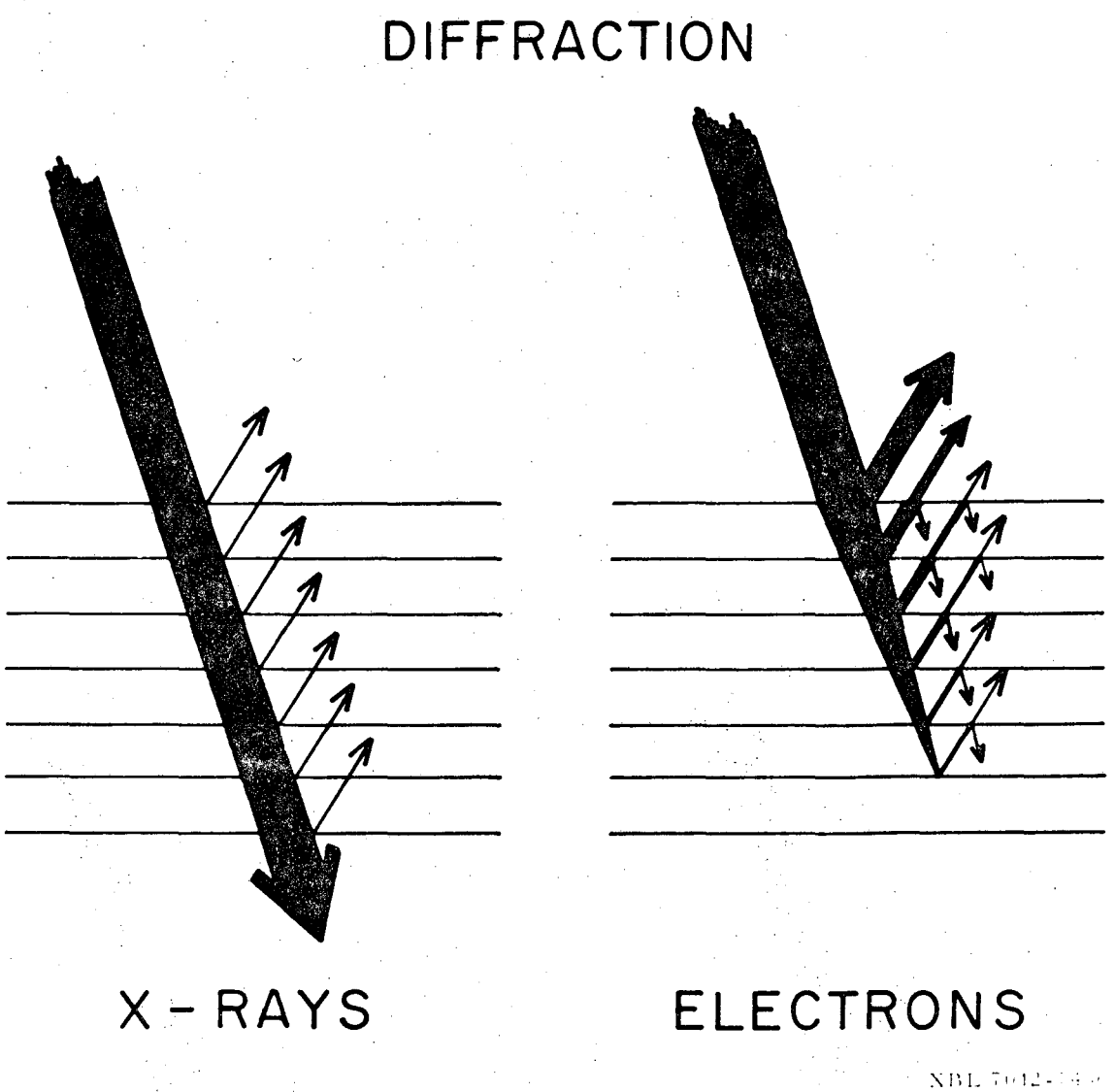

Figure II-1. Scattering characteristics of x-rays and low-energy electrons.

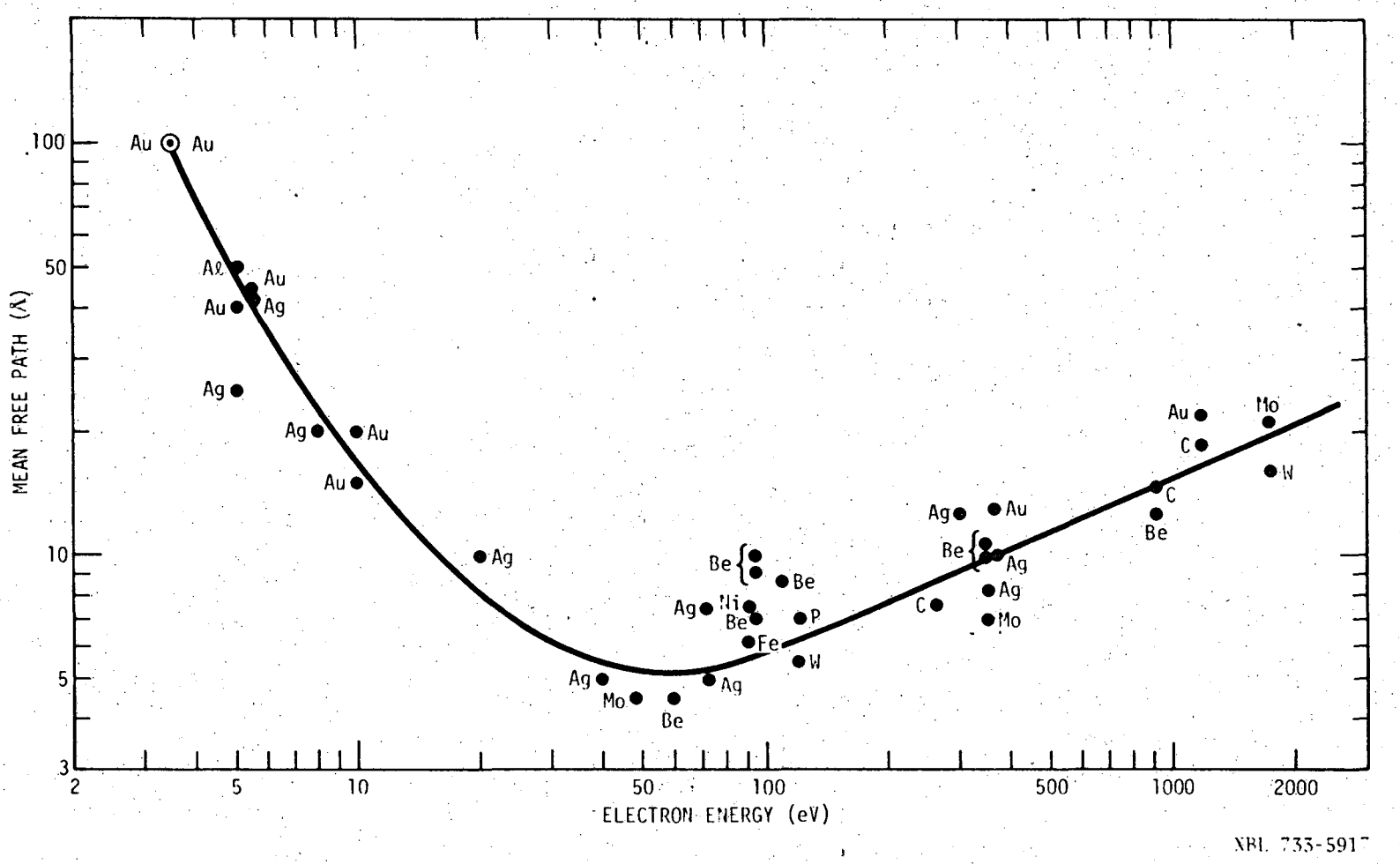

Figure II-2. Universal curve for the escape depth of electrons in metals.

most LEED investigations report only on the size, shape and rotational orientation of the surface mesh. To properly analyze the I-V profiles of the diffraction beams requires extensive computer calculations. Several recent reviews have discussed these I-V calculations.[67-72] In this thesis only the readily attainable geometrical information of the two dimensional surface mesh and kinematical information of the I-V profiles will be reported. Results obtained from other surface sensitive techniques such as AES, TDS and high resolution ELS will be used to provide information about the location and structure of adsorbates in the surface mesh. In the literature the surface unit meshs determined by LEED are often referred to as surface unit cells even though unit cell usually refers to a three dimensional structure. Both terms will be used interchangeably here.

1) Kinematical LEED Theory

In this section diffraction theory will be developed to predict the energies at which the kinematical or Bragg peaks occurs in the diffraction beam I-V profiles. Other quantities such as multiple scattering structure factors, scattering amplitudes and width of the diffracted beam will not be discussed here but have been discussed in detail elsewhere.[68,71,73,75]

An electron with wavevector $\underset{\sim}{k}_o$ incident on a crystal will generate a scattered electron with wavevector $\underset{\sim}{k}$. The wavevector $\underset{\sim}{k}$ is defined by the equation

$$|\underset{\sim}{k}| = \frac{2\pi}{\lambda} = \frac{2\pi}{h} (2m(E + V_o))^{1/2}, \qquad (1)$$

where λ is the wavelength of electron, h is Plank's constant, m is the mass of the electron, E is the energy of the electron in vacuum and V_o is the inner potential of the solid. The scattering process is shown in Fig. II-3a. Also shown in Fig. II-3a is a lattice vector $\underline{c}$ of the crystal and the scattering vector $\underline{S}$, the vector difference between $\underline{k}$ $\underline{k}_o$.

$$\underline{S} = \underline{k} - \underline{k}_o. \tag{2}$$

The wavevector $\underline{k}$ can be divided into the vectors $\underline{k}_{\parallel}$ and $\underline{k}_{\perp}$ which are the wavevector components parallel and perpendicular to the surface (Fig. II-3b). The dot product of $\underline{S}$ and $\underline{c}$ is defined by the Laue conditions to be

$$\underline{S} \cdot \underline{c} = 2\pi\ell, \tag{3}$$

where ℓ is an integer. For $\underline{c}$ normal to the surface and for backscattering Eq. (3) becomes

$$S_{\perp} c = 2\pi\ell. \tag{4}$$

From Eq. (2) and Fig. II-3 $S_{\perp}$ can be written as

$$S_{\perp} = |\underline{k}_{\perp}| + |\underline{k}_{o\perp}| = (k^2 - k_{\parallel}^2)^{1/2} + (k_o^2 - k_{o\parallel}^2)^{1/2}. \tag{5}$$

Diffraction conditions require that $\underline{k}_{o\parallel}$ can only differ from $\underline{k}_{\parallel}$ by a surface reciprocal lattice vector $\underline{G}$.

$$\underline{k}_{o\parallel} + \underline{G} = \underline{k}_{\parallel}. \tag{6}$$

Substitution of Eq. (6) into Eq. (5) yields

$$S_{\perp} = (k^2 - (k_{o\parallel} + G)^2)^{1/2} + (k_o^2 - k_{o\parallel}^2)^{1/2}. \tag{7}$$

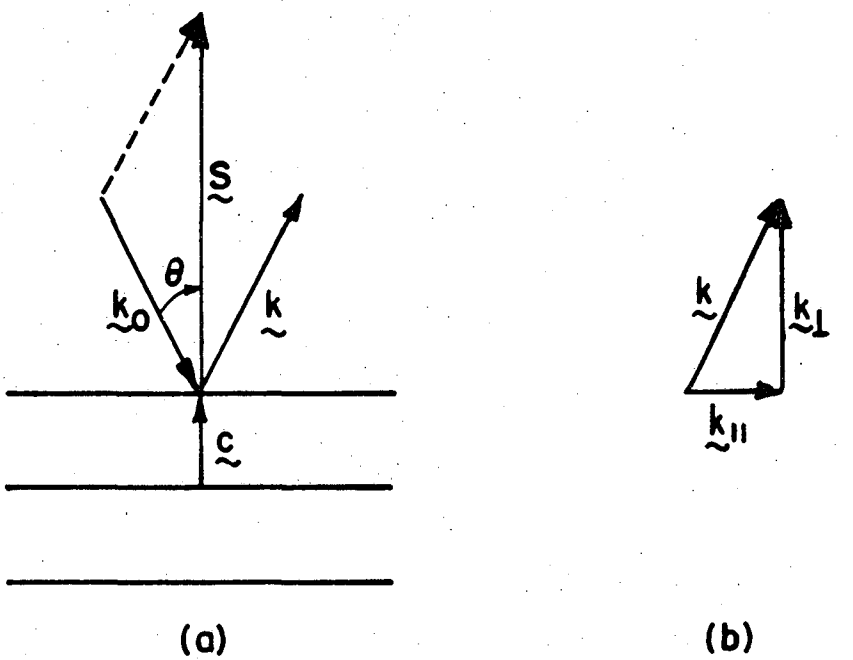

Figure II-3.

(a) Diagram of the specular electron scattering process at a surface.

(b) Diagram of the vector relationships between the electron wavevectors $\underset{\sim}{k}$, $\underset{\sim}{k}_{\perp}$ and $\underset{\sim}{k}_{\parallel}$.

Using Eq. (1) the energy dependence of $S_\perp$ can be determined, but the inner potential only affects the perpendicular component of the wave-vector so

$$k^2 = k_o^{\ 2} = \frac{8\pi^2 m}{h^2} (E + V_o) \tag{8}$$

and

$$|k_{o\|}| = \left(\frac{8\pi^2 m}{h^2} E\right)^{1/2} \sin\theta. \tag{9}$$

For the (0,0) or specular beam $\mathcal{G} = 0$. Therefore combining Eqs. (4), (7) - (9) and inserting numerical values for m and h yield

$$E = \frac{150.4}{4c^2\cos^2\theta} \ell^2 - \frac{V_o}{\cos^2\theta} \tag{10}$$

where E and V_o are expressed in eV and c is expressed in Å. If the inner layer spacing c and inner potential V_o are known for a crystal then the Eq. (10) predicts the occurrence of Bragg peaks at energies E in the I-V profile of (0,0) diffraction beam. Alternately the values of c and V_o may calculated from the experimental I-V profiles by plotting E vs ℓ^2. This plot would yield a straight line with a slope of $150.4/4c^2\cos^2\theta$ and an intercept of $V_o/\cos^2\theta$.

2) Temperature Dependence of LEED Beam Intensities

In the previous section the energies at which Bragg peaks occur in the I-V profiles was determined. In this section the temperature dependence of the intensities of these Bragg peaks will be developed. Maximum intensity is only achieved from a perfect crystalline lattice

at absolute zero where all of the atoms are in their equilibrium positions. For real crystals thermal energy causes the atoms to vibrate about their equilibrium positions. Therefore the electrons are scattered from a lattice of vibrating atoms and only the electrons scattered from atoms in their equilibrium positions will contribute to the intensity of the Bragg peaks. The electrons scattered from atoms displaced from their equilibrium positions will contribute to diffuse background intensity. The vibration of the atoms do not change the width of the diffraction beams only their intensity. Increasing the crystal temperature increases the amount of time the atoms spend away from their equilibrium position thus the intensity of the Bragg peaks will fall off as the crystal temperature is raised.

The expression for the diffracted intensity must be considered in order to generate an analytical expression for the temperature dependence. The intensity, I, is simply the square of the structure factor, F. For an ideal lattice F has the form[75]

$$F_o = \sum_j f_j \, e^{-i \, \underset{\sim}{S} \cdot \underset{\sim}{r}_n}, \tag{11}$$

where f_j is the atomic scattering factor of atom j at the lattice position $\underset{\sim}{r}_n$. For an real lattice with thermal vibrations $\underset{\sim}{r}_n$ must be replaced by $\underset{\sim}{r}_n + \underset{\sim}{u}_n$ where $\underset{\sim}{u}_n$ represents the atomic displacement from the equilibrium position. Because the vibrational motion of the atoms is rapid compared to the time scale of the LEED intensity measurements a thermal average must be taken. Therefore the intensity from a real lattice has the form

$$I = F_o^2 \sum_{n,m} \langle e^{-i \underset{\sim}{S}\cdot(\underset{\sim}{u}_n + \underset{\sim}{u}_m)} \rangle . \tag{12}$$

Assuming the vibrational amplitudes are small and harmonic yield

$$I = F_o^2 \, e^{-2M} \tag{13}$$

where 2M is the Debye Waller factor.

$$M = \frac{1}{2} \langle (\underset{\sim}{S}\cdot\underset{\sim}{u})^2 \rangle . \tag{14}$$

For the scattering vector $\underset{\sim}{S}$ shown in Fig. II-3a $|\underset{\sim}{S}| = \frac{4\pi}{\lambda}\cos\theta$. Therefore

$$M = \left(\frac{8\pi^2\cos^2\theta}{\lambda^2}\right) \langle u_\perp^2 \rangle , \tag{15}$$

where $u_\perp$ is the component of $\underset{\sim}{u}$ perpendicular to the surface. Inserting Eq. (15) into Eq. (13) yields

$$I = F_o^2 \exp[-16\pi^2\lambda^{-2}\cos^2\theta) \langle u_\perp^2 \rangle]. \tag{16}$$

Equation (16) shows the relationship between the intensity and mean-square displacement, $\langle u_\perp^2 \rangle$ with F_o^2 being the intensity from an ideal lattice. An increase in $\langle u_\perp^2 \rangle$ will cause the intensity to fall off exponentially.

For a classical harmonic oscillator the average potential energy $\langle u \rangle$ is 3/2 $k_B T$. Thus

$$\langle u \rangle = \frac{1}{2} K \langle u_\perp^2 \rangle = \frac{1}{2} M \omega^2 \langle u_\perp^2 \rangle = \frac{3}{2} k_B T, \tag{17}$$

where K is the force constant, M is the mass of the atom, ω is the frequency of the oscillator and k_B is Boltzmann's constant. The relationship

$K = M\omega^2$ was used in Eq. (17). Using the high temperature limit of the Debye model ($T > \theta_D$) and equating ω with the Debye cutoff frequency[75]

$$\omega_D = 2\pi k_B h^{-1} \theta_D, \tag{18}$$

where θ_D is the Debye temperature Eq. (17) can be rewritten for N harmonic oscillators as

$$\langle u^2 \rangle = \frac{3N h^2}{4\pi^2 M k_B \theta_D^2} T. \tag{19}$$

Substituting Eq. (19) into Eq. (16) yields

$$I = F_o^2 \exp\left(-\frac{12N h^2 \cos^2\theta}{M k_B \lambda^2 \theta_D^2} T\right). \tag{20}$$

Thus the intensity of the diffracted beam decreases exponentially with increasing temperature. In order to readily determine θ_D from the experimentally observed intensities it is useful to take the logarithm of both sides of Eq. (20). Taking the logarithms, using the de Broglie relationship and inserting the proper numerical constants yield

$$\ell n\ I = \frac{0.153\ E}{M \theta_D^2} T + C, \tag{21}$$

where E is the electron energy including the inner potential, M is the mass of the scattering atom in kg/mole, θ_D and T are both in K and $C = \ell n\ F_o^2$, a constant. Therefore plotting ℓn I vs T will generate a straight line with a slope of $(0.153\ E)/(M\ \theta_D^2)$.

The penetration depth of electrons depends on their energy as shown in Fig. II-2. Since the bulk θ_D differs from the surface θ_D the value of θ_D that is obtained experimentally will depend on the energy at

which it is determined. At high electron energies the experimental value of θ_D should approach the bulk value of θ_D. At the lower electron energies where most of the scattering is from the surface layer the experimental value of θ_D should approach the surface value of θ_D.

3) The LEED Experiment

A typical LEED apparatus is shown in Fig. II-4. A monoenergetic beam of electrons (10 eV to 500 eV) is directed at the surface of a single crystal which backscatters a portion of the incoming electrons. A set of four herispherical grids is used to remove the inelastically backscattered electrons while the elastically backscattered electrons are post-accelerated onto a phosphorous screen for viewing of the diffraction pattern. The crystal and first grid are grounded in order to maintain a field free region between the LEED optics and the single crystal sample. Grid B is a closely spaced double layer grid maintained at the potential of the electron gun filament so that only the electrons elastically scattered from the target could penetrate the grid system. Grid C is grounded to shield grid B from the $\sim$ 5 kV positive potential of the phosphorous screen. The crystal and the detection system are enclosed in an UHV chamber in order to attain and maintain a clean surface. As seen in Fig. II-4 there is a window present in the UHV chamber directly opposite the phosphorous screen which allows the diffraction pattern to be viewed and photographed from outside the UHV chamber. A polaroid camera was used for photographing the diffraction pattern.

A well ordered crystal surface will yield a diffraction pattern consisting of bright, well defined spots with very low background

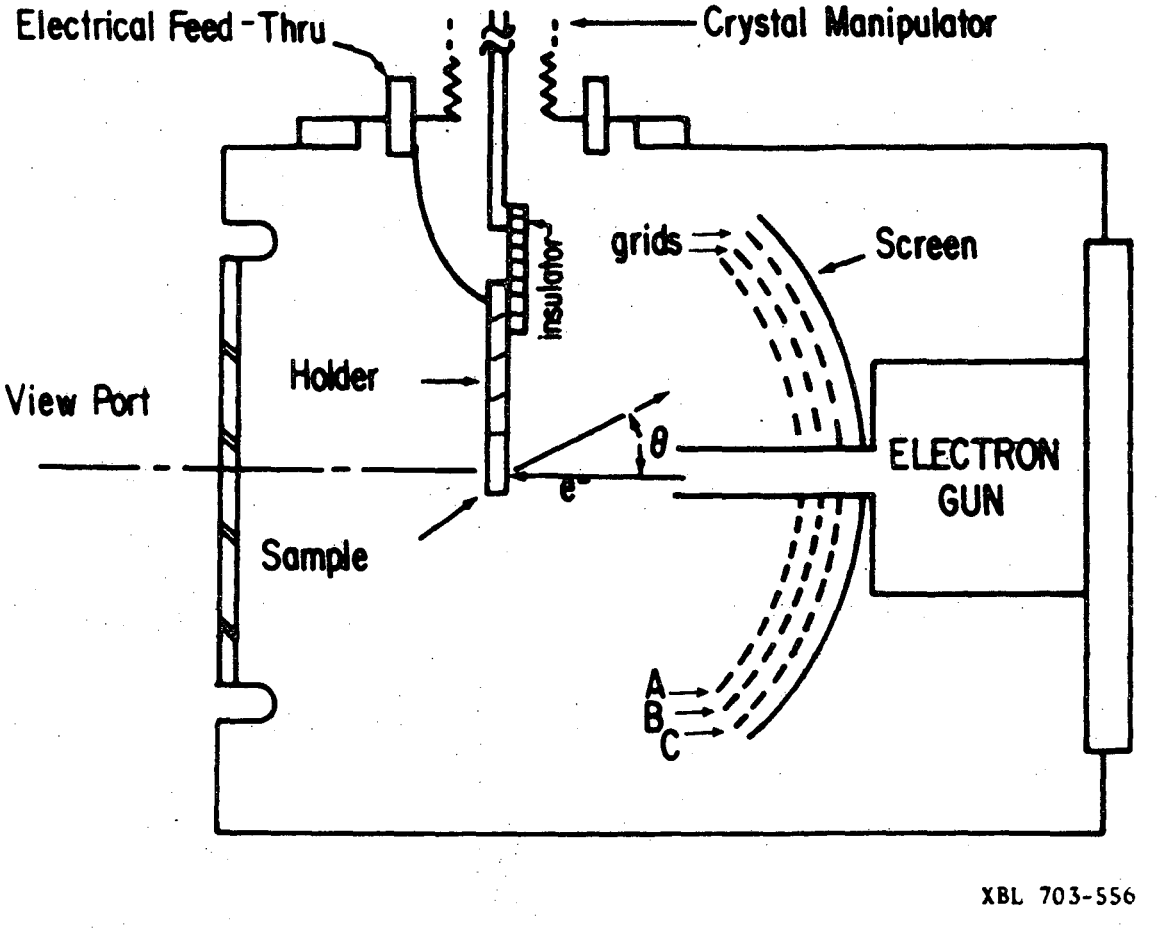

Figure II-4. Schematic diagram of a typical LEED apparatus.

intensity. The sharpness and overall intensity of the spots depend on the degree of order on the surface. Although the surface may be irregular on a microscopic and submicroscopic scale (e.g., consisting of atomic terraces and ledges) the presence of sharp diffraction features indicates that the surface is ordered on an atomic scale, that is most of the surface atoms are located in a two-dimensional lattice structure. The size of these ordered domains determines the quality of the diffraction pattern. Because of the experimental limitations on the coherence width of the electron beam, the quality of the diffraction pattern does not improve when the ordered domains become larger than 200 Å in diameter. However, if the ordered domains are significantly smaller than 200 Å the diffractions spots become broader and less intense.

4) Conversion of the Diffraction Pattern to a Surface Structure

LEED diffraction patterns represent the reciprocal lattice of the surface and the diffraction pattern must be converted to real space in order to obtain the surface structure. This section will show how this conversion is carried out. First the relationship between the reciprocal and real lattices of the substrate will be shown, then determination of adsorbate surface structures from the LEED patterns will be discussed.

The diffraction pattern or reciprocal lattice has translational periodicity which is given by the vector $\vec{T}^*$ which has the form

$$\vec{T}^* = h\vec{a}^* + k\vec{b}^* \qquad (22)$$

where h and k are integers and $\vec{a}^*$ and $\vec{b}^*$ are the vectors of the

primitive surface reciprocal mesh. The translational periodicity of the surface in real space is given by the vector $\vec{T}$ which has the form

$$\vec{T} = n\vec{a} + m\vec{b} \tag{23}$$

where n and m are integers and $\vec{a}$ and $\vec{b}$ are the vectors of the primitive surface mesh. The reciprocal unit cell vectors $\vec{a}^*$ and $\vec{b}^*$ are related to the real space unit cell vectors $\vec{a}$ and $\vec{b}$ by the following equations:

$$\vec{a}^* = \frac{\vec{b} \times \vec{c}}{\vec{a} \cdot \vec{b} \times \vec{c}} \tag{24a}$$

$$\vec{b}^* = \frac{\vec{z} \times \vec{a}}{\vec{a} \cdot \vec{b} \times \vec{c}} \tag{24b}$$

where $\vec{c}$ is the surface normal. The relationship between the reciprocal and real space vectors is illustrated for a two-dimensional hexagonal lattice in Fig. II-5.

Adsorbing a gas on a surface usually results in a change in the diffraction pattern, corresponding to the appearance of a new surface mesh. This is illustrated in Fig. II-6 which shows a diffraction pattern of a clean Rh(111) surface and the diffraction pattern formed after the adsorption of acetylene. Figure II-7 shows the unit mesh responsible for the diffraction patterns in Fig. II-6 superimposed on a model of the Rh(111) surface. No information concerning the location of the acetylene molecule within this unit mesh is indicated since this information can only be obtained from analysis of the diffraction spot intensities.

In order to make the transition from the diffraction pattern in Fig. II-6 to the surface structure in Fig. II-7 the adsorbate surface reciprocal mesh is referenced to the substrate reciprocal mesh. This is

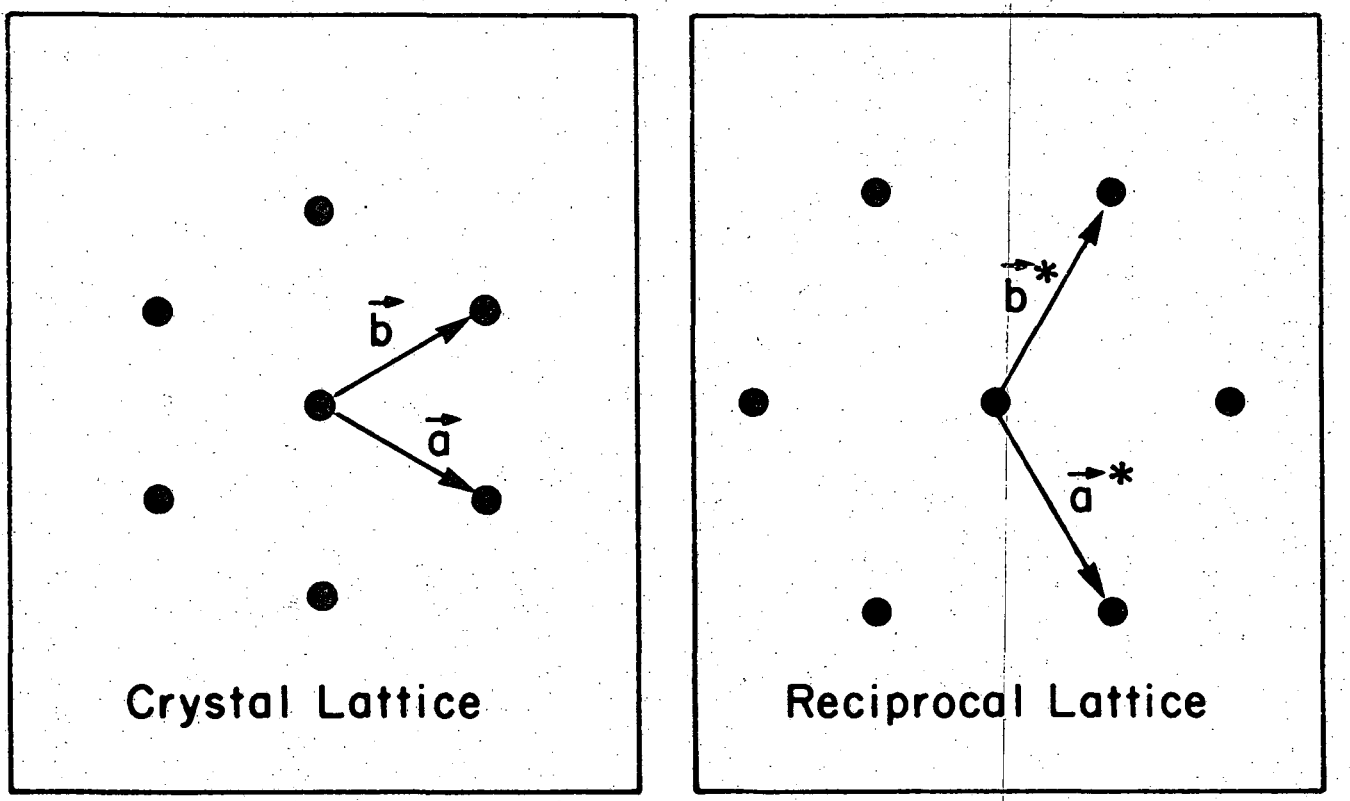

XBL 787-9590

Figure II-5. Real space vectors $\vec{a}$ and $\vec{b}$ and reciprocal space vectors $\vec{a}^*$ and $\vec{b}^*$ of a two-dimensional hexagonal lattice.

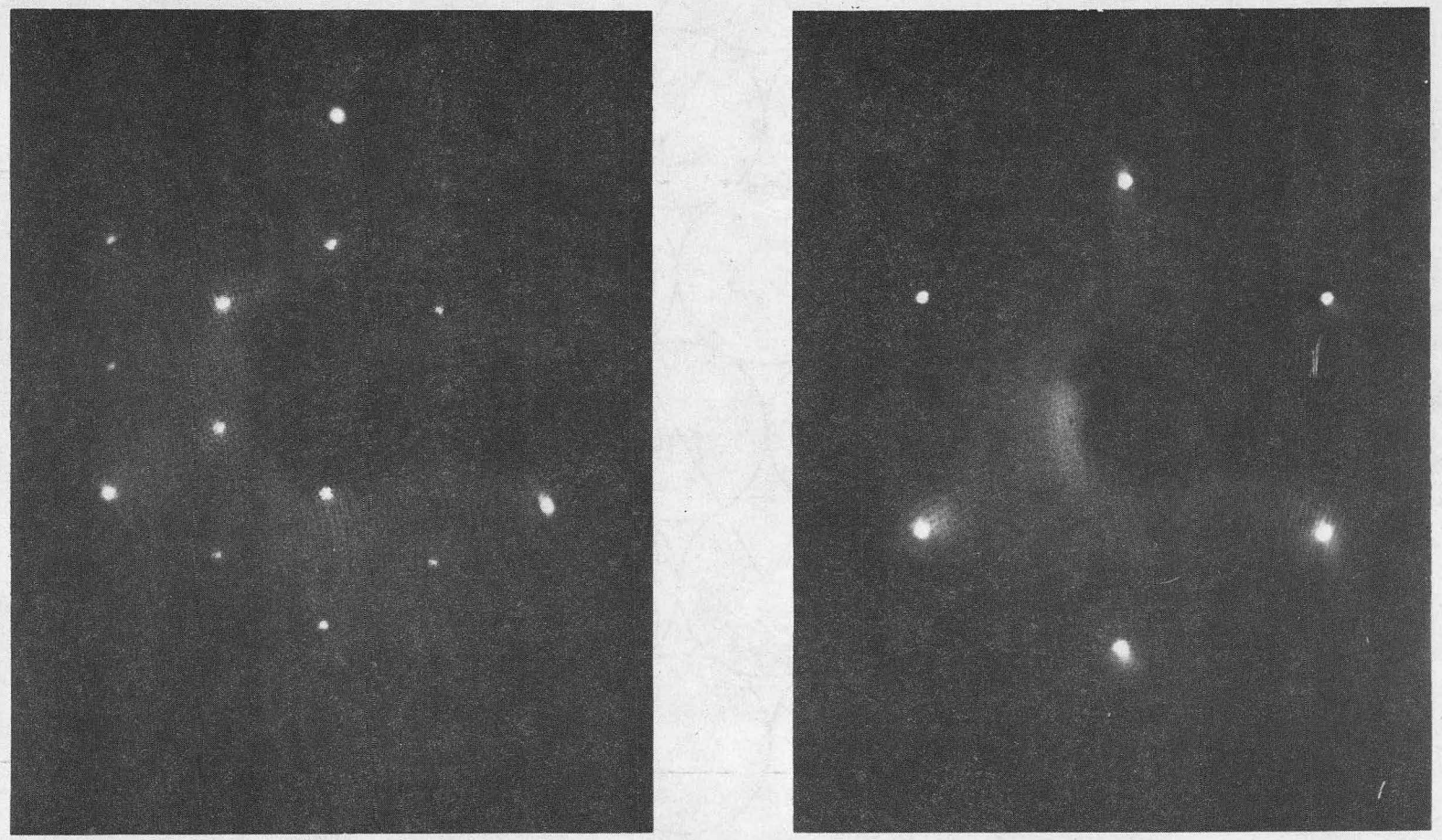

XBB 750-8226

Figure II-6. LEED patterns of a clean Rh(111) surface and the same surface after exposure to C_2H_2. In both diffraction patterns the incident electron beam energy is 68 eV.

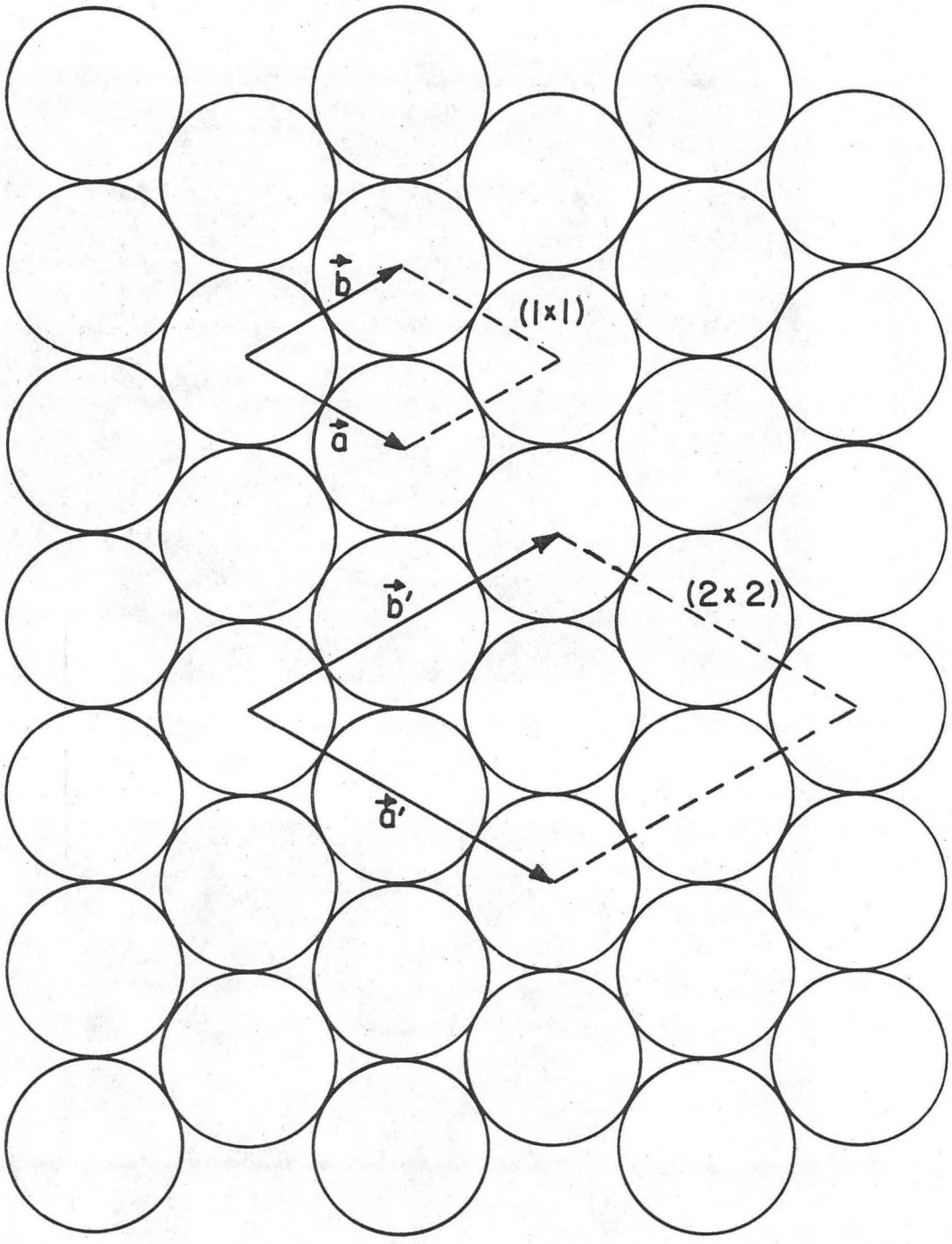

XBL7510-7551

Figure II-7. Real space unit cells of Rh(111)-(1×1) and Rh(111)-(2×2)-C_2H_2.

done by visual inspection of the diffraction pattern where the differences in spot intensities are neglected and only the positions of the diffraction beams are considered.

For the general case the relationship of adsorbate reciprocal mesh to the substrate reciprocal mesh is given by the equations

$$\vec{a}^{*\prime} = m^*_{11}\,\vec{a}^* + m^*_{12}\,\vec{b}^* \tag{25a}$$

$$\vec{b}^{*\prime} = m^*_{21}\,\vec{a}^* + m^*_{22}\,\vec{b}^* \tag{25b}$$

where $\vec{a}^{*\prime}$ and $\vec{b}^{*\prime}$ are the vectors of the primitive adsorbate reciprocal mesh and the coefficients m^*_{11}, m^*_{12}, m^*_{21} and m^*_{22} define the matrix

$$M^* = \begin{pmatrix} m^*_{11} & m^*_{12} \\ m^*_{21} & m^*_{22} \end{pmatrix}.$$

In real space the adsorbate mesh is related to the substrate mesh by the equations

$$\vec{a}' = m_{11}\vec{a} + m_{12}\vec{b} \tag{26a}$$

$$\vec{b}' = m_{21}\vec{a} + m_{22}\vec{b} \tag{26b}$$

where $\vec{a}'$ and $\vec{b}'$ are the vectors of the primitive adsorbate mesh and the coefficients m_{11}, m_{12}, m_{21} and m_{22} define the matrix

$$M = \begin{pmatrix} m_{11} & m_{12} \\ m_{21} & m_{22} \end{pmatrix}.$$

The coefficients of the two matrices M and M* are related by the following equations:

$$m_{11} = \frac{m_{22}^*}{m_{11}^* m_{22}^* - m_{21}^* m_{12}^*} \tag{27a}$$

$$m_{12} = \frac{-m_{21}^*}{m_{11}^* m_{22}^* - m_{21}^* m_{12}^*} \tag{27b}$$

$$m_{21} = \frac{-m_{12}^*}{m_{11}^* m_{22}^* - m_{21}^* m_{12}^*} \tag{27c}$$

$$m_{22} = \frac{m_{11}^*}{m_{11}^* m_{22}^* - m_{21}^* m_{12}^*} \tag{27d}$$

so that if either M or M* is known the other may be readily calculated. In LEED experiments M* is determined by visual inspection of the diffraction pattern and then transformed to give M which defines the surface structure in real space.

For the case of acetylene adsorption on Rh(111) visual inspection of the LEED patterns in Fig. II-6 yields $M^* = \begin{pmatrix} 1/2 & 0 \\ 0 & 1/2 \end{pmatrix}$. From employing equations (27a) through (27d) the matrix M is determined to be $\begin{pmatrix} 2 & 0 \\ 0 & 2 \end{pmatrix}$, so $\vec{a}' = 2\vec{a}$ and $\vec{b}' = 2\vec{b}$ as depicted in Fig. II-7.

In addition to the matrix method of denoting surface structures another system, originally proposed by Wood[76], is also used. While the matrix notation can be applied to any system, Wood's notation can only be used when the angle between the adsorbate vectors $\vec{a}'$ and $\vec{b}'$ is the same as the angle between the substrate vectors $\vec{a}$ and $\vec{b}$. If this condition is met, then the surface structure is labeled using the general form (nxm) R$\Phi°$ or c(nxm) R$\Phi°$, depending on whether the unit mesh is primitive or centered. In Wood's notation the adsorbate unit mesh is related to substrate unit mesh by the scale factors n and m where

$$|\vec{a}'| = n \; |\vec{a}'| \tag{28a}$$

$$|\vec{b}'| = m \; |\vec{b}'|. \tag{28b}$$

$R\Phi°$ indicates a rotation of the adsorbate unit mesh by $\Phi°$ from the substrate unit mesh. For $\Phi = 0$ the $R\Phi°$ label is omitted, so the surface structure in Fig. II-7 is labeled as a (2×2). The label for the total system refers to the type of substrate, the surface structure formed by the adsorbate and the adsorbate. The rhodium-acetylene system shown in Fig. II-7 would be labeled as Rh(111) - $\begin{pmatrix} 2 & 0 \\ 0 & 2 \end{pmatrix}$ - C_2H_2 in matrix notation and as Rh(111) - (2×2) - C_2H_2 in Wood's notation. Wood's notation is more commonly used and the matrix notation is usually only applied to systems where the angle between the adsorbate vectors differs from the angle between substrate vectors.

An example of an adsorbate which has a centered unit mesh is shown in Figs. II-8 and II-9. In Fig. II-8 diffraction patterns from a clean Rh(100) surface and a Rh(100) surface after exposure to oxygen are shown. By visual inspection it can be seen that $M^* = \begin{pmatrix} 1/2 & -1/2 \\ 1/2 & -1/2 \end{pmatrix}$, so using equations (27a) through (27d) yields $M = \begin{pmatrix} 1 & 1 \\ -1 & 1 \end{pmatrix}$. M defines the primitive unit mesh of the adsorbate, which is drawn in with solid lines in Fig. II-9. This unit mesh is labeled as $(\sqrt{2} \times \sqrt{2})$ R45° in Wood's notation. Since the centered unit mesh drawn in with dotted lines in Fig. II-9 also describes the adsorbate mesh, another way of labeling this strucutre would be c(2×2). The total system is labeled as Rh(100) - $\begin{pmatrix} 1 & 1 \\ -1 & 1 \end{pmatrix}$ - 0, Rh(100) - $(\sqrt{2} \times \sqrt{2})$ R45° - 0 or Rh(100) -c(2×2) -0. Of these three labels only the first two refer to the primitive unit mesh of the oxygen surface structure.

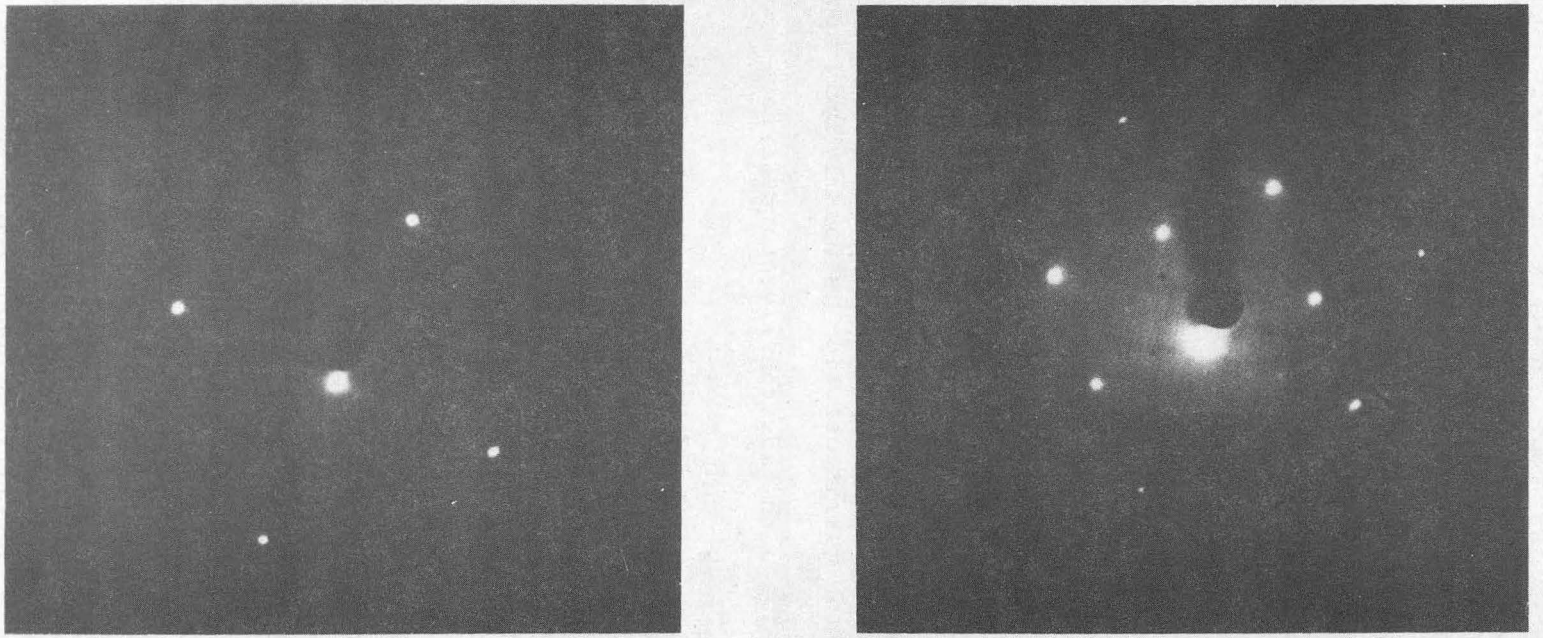

XBB 7810-13148

a b

Figure II-8. LEED patterns of (a) clean Rh(100) at 74 eV and (b) oxygen covered Rh(100 at 85 eV.

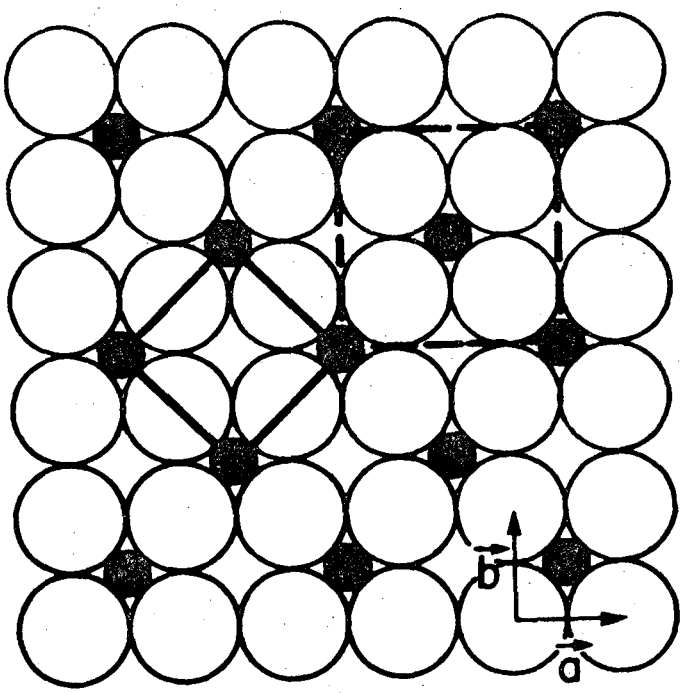

XBL 787-9589

Figure II-9. Real space units cells of the ($\sqrt{2} \times \sqrt{2}$) R45°-0 (solid lines) and c(2 × 2)-0 (dashed lines) on the Rh(100) surface.

5) LEED from Stepped Surfaces

The four rhodium single crystal faces used in this investigation were the (111), (100), (755) and (331). The low Miller index (111) and (100) surfaces have the lowest surface free energy and therefore are the most stable, have the highest rotational symmetry and are the most densely packed. These surfaces are flat and have primitive unit meshes which contain only one Rh atom. The (755) and (331) are high Miller index surfaces which are made of microfacets of the low Miller index crystal faces. The atomic structure of these surfaces consists of periodic arrays of low index terraces and steps and a nomenclature more descriptive of the actual surface configuration has been developed for these surfaces.[77] Using this nomenclature a Rh(755) surface would be designated as a Rh(S) - [6(111) × (100)] surface which indicates it is a stepped surface consisting of six atom wide (111) terraces separated by one atom high (100) steps.

Assigning the [6(111) × (100)] label to the (755) surface assumes that this surface is stable in a monoatomic step height configuration. Other surface configurations such as the two step height [12(111)×2(100)] surface also have a (755) macroscopic surface. LEED is sensitive to atomic structure of surfaces and therefore can be employed to determine which configuration properly describes the surface. This is in contrast to other techniques such as back reflection Laue x-ray diffraction where only the macroscopic orientation of a crystal's surface can be determined. In LEED patterns of stepped surfaces the step periodicity is superimposed on the terrace periodicity resulting in the splitting of

the terrace diffraction spots into doublets or triplets at certain beam voltages. The direction of the splitting is perpendicular to the step edge and the magnitude of the splitting is inversely proportional to the terrace width, so the terrance width can be obtained by measuring the splitting observed in the LEED pattern. The step height can be determined by using Eq. 10 as

$$E_{oo}\ (\text{singlet max}) = \frac{150.4}{4d^2\cos^2\theta}\, s^2 - \frac{V_o}{\cos^2\theta}, \qquad (29)$$

where E_{oo} are the voltages where a singlet intensity maximum of the (0,0) beam is observed, d is the step height, s is an integer, θ is the angle between incident electron beam and the surface normal and V_o is the inner potential. Therefore from the LEED pattern both the step height and terrace width can be determined and then combined with the angle between the terrace and step planes to determine the macroscopic surface plane. This calculated macroscopic surface can then be compared with back reflection Laue x-ray diffraction results for the same surface.

The values determined by LEED for the terrace width and step height are only average values because a given macroscopic surface may have a distribution of terrace widths and step heights. These distributions must be fairly broad to have a significant effect on the LEED pattern and these effects have been discussed in detail elsewhere.[78-80]

The stability of stepped surfaces is an important consideration in LEED studies because these surfaces have higher surface free energies than the low index faces. Most of the clean stepped surfaces are stable in a single step height configuration, but when gases are adsorbed on

these surfaces their stability can noticeably change. Some stepped surfaces reconstruct, forming multiple height steps and large terraces. Other high Miller index surfaces form large low index facets while some retain the single step height configuration. Because of LEED's sensitivity to the atomic structure of surfaces it is well suited for determining the stability or reconstruction of stepped surfaces.

B. Surface Characterization by AES

Auger electron spectroscopy (AES) was used to monitor the surface composition of the rhodium crystals during the chemisorption and reactivity investigations. AES is surface sensitive for the same reason LEED is, the small escape depth of low-energy electrons from a solid. The Auger electrons are inelastic and each element has a characteristic spectrum which can be used as a "fingerprint" to identify the presence of an element on the surface. The identification of an element is relatively straightforward since Auger electrons are generally not markedly affected by the chemical environment of the element. The Auger process and experimental aspects of AES have been discussed in detail elsewhere[81-85] and will be only be discussed briefly here.

The initial step in the Auger process is to eject an inner shell electron from an atom by allowing high energy electrons or x-rays to strike the sample. If a monoenergetic source such as the Kα line of Al is used for this excitation the kinetic energy of the ejected electrons can be analyzed to determine their binding energies. This process is called x-ray photoelectron spectroscopy (XPS). For the experiments described in Chapter III 2 keV electrons from a modified cathode ray

tube electron gun with a W ribbon filament were used to eject the inner shell electrons. This was not a monoenergetic source therefore no XPS experiments were carried out.

Once an atom has been ionized it has two modes of relaxation available to it, Auger electron emission and x-ray fluorescence. These are illustrated in Fig. II-10. In the Auger process an outer shell electron relaxes to the inner shell vacancy and then transfers the energy released in this transition to another outer shell electron which is then ejected from the sample. This ejected electron is the Auger electron and has a energy of

$$E_{ABC} = E_A - E_B - E_C\,(Z-\Delta) - \phi_a, \tag{30}$$

where A, B, C refer to the various electron shells of an atom (K, L, M, N ...), Z is the atomic number of the atom, Δ is the change in charge due to the initial ionization and ϕ_a is the effective work function of the analyzer. The Δ term is included in Eq. (30) because the Auger electron is emitted from an ionized atom and not a neutral atom. Experimental values of Δ are generally between 1/2 and 3/4.[81] In the second mode of relaxation, x-ray fluorescence, an outer shell electron relaxes to the inner shell vacancy, but instead transferring its excess energy to another electron the excess energy is emitted as a photon.

The energy of the Auger electron only depends on the energy levels of the atom involved in the Auger transition. Therefore changes in the chemical environment which shift the energy levels of an atom will result in a shift in energy of the Auger transition. For Auger transitions involving the tightly bound inner shell electrons these

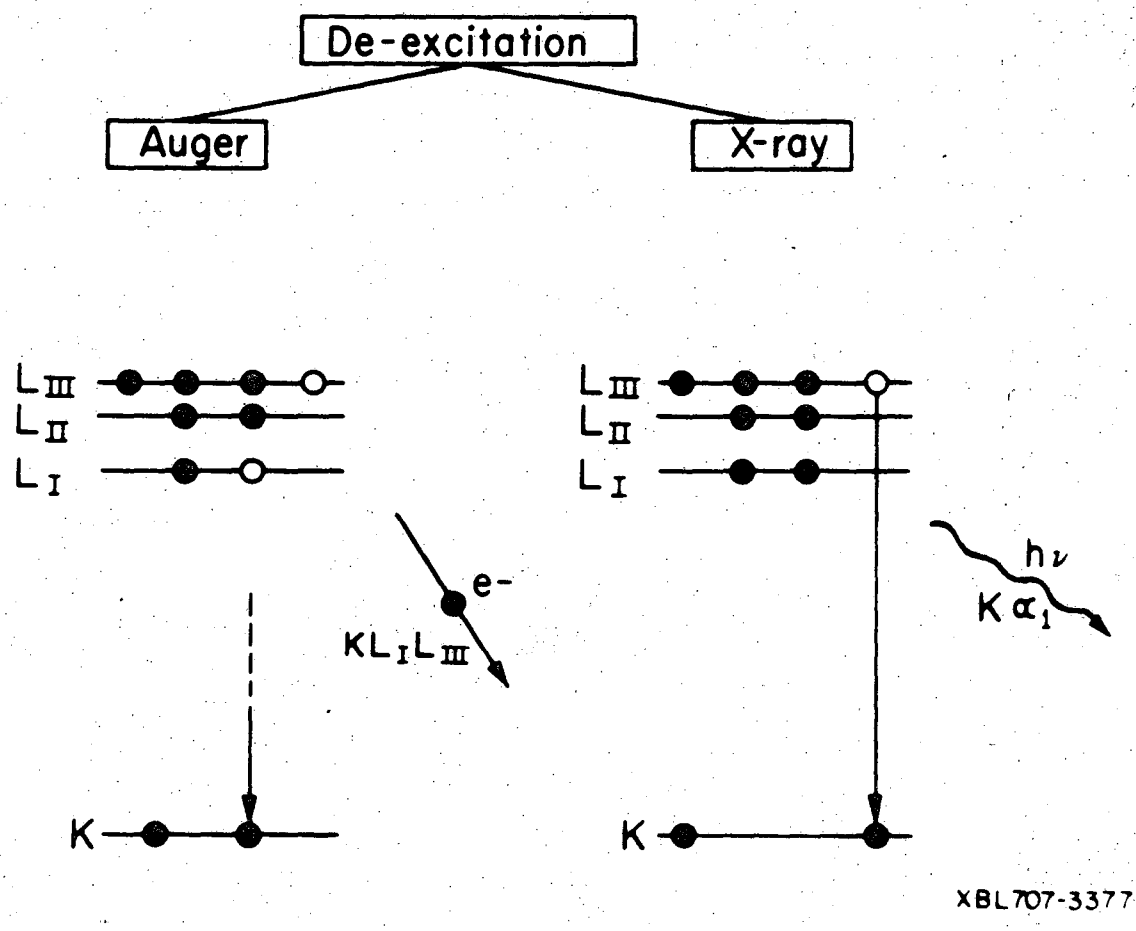

Figure II-10. Energy level diagrams representations of the (a) Auger and (b) x-ray fluorescence de-excitation processes.

chemical shifts are usually too small (<0.5 eV) to be detected with the commonly used analyzers (2 to 10 eV resolution). These transitions are ideally suited for fingerprinting an element since they are insensitive to the environment. Low-energy Auger transitions (<100 eV) involve the valence band electrons which can be noticeably affected by changes in the chemical environment. For example oxidizing a metal can result in a chemical shift of 3 eV or more in these low-energy transitions.[29] The lineshape of the Auger transition can also be useful in identifying the chemical nature of an element. For example the lineshape of the carbon KLL transition from graphite and Ni carbide are markedly different.[86] There are also lineshape differences between the oxygen KLL transition from chemisorbed oxygen and metal oxides.[87,88] Therefore AES can be used to both identify the presence of an element on the surface and gain some information about the chemical environment of that element.

The degree of surface sensitivity that an Auger electron has depends its energy (see Fig. II-2). The incident energy of 2 keV used in these experiments allows the electrons to penetrate ~ 20 Å into sample. By impinging the electrons onto the surface at a glancing angle of 20° the distance the electrons penetrate normal to the surface can be reduced to ~ 8 Å. Although Auger electrons can be created at depths of 20 or more Å from the surface whether they have sufficient energy to escape from crystal and be detected by the analyzer is determined by the energy of the Auger transitions. Most of the detected intensity for Auger transitions between 20 and 150 eV originates from the upper two

layers while for Auger transitions above 1000 eV a significant portion of the detected intensity originates from below the upper two layers. Therefore different Auger transitions will provide information about different regions of the crystal. This fact can be used to determine alloy compositions in the surface and near surface regions[82] and to determine the growth mechanism of epitaxial layers.[89]

Two types of analyzers are commonly employed in AES experiments, the cylindrical minor analyzer (CMA) and retarding field analyzer (RFA). For the experiments reported here the LEED optics where used as a RFA. In these experiments a glancing incident 2 keV electron beam ~ 1 mm in diameter was used to excite the Auger transitions. The crystal was rotated 15 to 20° from its rest position perpendicular to the LEED gun to obtain the glancing angles of 15 to 20°. The RFA was then used to collected the angle integrated AES spectrum. In order to operate the LEED optics as a RFA the crystal and grids A and C were grounded, a DC voltage ramp was applied to grid B and a 300 volt positive potential was applied to the screen (see Fig. II-4). The ramp voltage on grid B acted as a high pass cutoff filter, allowing only electrons with energies greater than the ramp voltage to pass through the analyzer. Because Auger transitions have weak intensities compared to the large background intensity from secondary electron emission it is advantageous to differentiate the AES spectrum. The slope of the secondary electron emission is fairly constant, especially above 100 eV, and will be removed by the differentiation, enhancing the signal to noise ratio in the Auger spectrum. In these experiments the differentiation was done electronically

by placing a small AC modulation voltage (2 to 5 eV, peak-to-peak) on the DC ramp voltage. The second harmonic of the modulation voltage was detected at screen by a phase sensitive lock-in amplifier. The second harmonic has been shown to be a good approximation to the first derivative.[82] All AES spectra reported here were taken in this manner and a 5 eV modulation voltage was used to record all Auger transitions except the low-energy rhodium NVV transition where 2 eV was used. Ideally the modulation voltage should be kept as low as possible because it determines the resolution of the RFA, but the signal intensity falls off as the modulation voltage is decreased. 5 eV was found to be a good compromise for these experiments.

C. Adsorbate Characterization by TDS

TDS experiments can determine five important parameters about a desorption process: (1) its order n, (2) the activation energy of desorption E_d, (3) the pre-exponential factor of the desorption expression ν_n, (4) the number of binding states of an adsorbate and (5) the decomposition characteristics of an adsorbate. Although performing the desorption experiment itself is straight-forward, carrying out the data analysis can be rather involved. The spectra obtained from TDS are simply traces of pressure vs crystal temperature, using a quadrupole mass spectrometer to monitor the pressure so the contributions from various species (mass numbers) can be determined. Several parameters such as n, E_d, ν_n, the heating rate β, the pumping speed of the system, the surface coverage θ, nonuniform heating of the crystal, the effect of increasing temperature on the adsorbate and surface reactions involving the adsorbate can influence the shape and behavior of the desorption

spectra. Several methods of accounting for the effects of these parameters and extracting the desorption rate parameters from the experimental desorption traces have been extensively described elsewhere.[90-96] These analyses are fairly involved, the validity of some of the assumptions made is questionable and in some cases require parameter values to be varied over a wider range than is experimentally possible. Because of these reasons quantitative interpretation of the desorption spectra was not undertaken here. However desorption parameters such as the number of binding states, decomposition characteristics and the order of desorption can be obtained fairly readily from the shape and behavior of the desorption traces and these will be discussed. For first order desorption processes an estimate of E_d will also be determined.

The information obtained in TDS experiments can be applied to catalysis since the final step of every heterogeneous catalytic reaction is the desorption of the reaction products. TDS also can supply information on the chemisorption properties of a molecule. The order of the desorption process can indicate whether a molecule is associatively of dissociatively adsorbed. Monitoring a wide range of mass numbers during the desorption experiment will indicate whether an adsorbate would rather decompose or dissolve into the crystal than desorb and if an adsorbate decomposes what species are formed. TDS can also be used to follow surface reactions of adsorbates.

To analyze the TDS spectra the Polanyi-Wigner model was used to describe the desorption of a species in a given binding state from the surface of a crystal (Eq. (31)).

$$-\frac{d\theta}{dt} = \nu_n \theta^n \exp(-E_d/RT). \tag{31}$$

In the TDS experiments reported here the pumping speed was much larger than the desorption rate and the cyrstal was heated linearly. For these conditions and assuming uniform crystal heating and E_d is independent of t or T it has been shown that[90]

$$E_d/RT_p^2 = \frac{\nu_1}{\beta} \exp(-E_d/RT_p) \text{ for } n = 1, \tag{32}$$

$$E_d/RT_p^2 = \frac{\theta_o \nu_2}{\beta} \exp(-E_d/RT_p) \text{ for } n = 2, \tag{33}$$

where T_p is the temperature at which the maximum desorption rate occurs and θ_o is the surface coverage of the binding state when the desorption trace is begun.

Equations (32) and (33) show that in a first order desorption process T_p is independent of θ_o while in a second order desorption process T_p decreases as θ_o increases. Therefore by following the temperature of a desorption peak as the surface coverage is increased it should be possible to determine whether a desorption process is first or second order. In most TDS experiments gas exposures instead of surface coverages are used because they are more easily obtained. T_p has a similar dependence on exposure since

$$\theta = S \varepsilon, \tag{34}$$

where S is the sticking coefficient and ε is the gas exposure, usually measured in Langmuirs where $1L = 10^{-6}$ torr sec. Difficulties can arise if E_d is a function of surface coverage. If E_d decreased as θ increased then in the first order desorption process T_p would decrease as θ is increased giving the appearance of a second order desorption process.

This difficulty general arises for adsorbates which form compression structures. A good example is the adsorption of CO on transition metal surfaces resulting in a widely spaced overlayer at low θ which compresses to closely pack overlayer and high θ.[97] As the adsorbed CO compresses repulsive forces can develop between CO molecules resulting in a decrease in E_d, hence the dependence of E_d on θ. Therefore just because T_p decreases with increasing exposure does not make it a second order desorption process.

A value of E_d for the first order process in Eq. (32) can be calculated providing T_p, ν_1 and β are known. T_p and β are readily available from the experimental data and conditions. Determining ν_1 is more involved. It can be determined by varying β while keeping θ_o constant and observing the change in T_p, but this is not feasible because for the crystals used in the experiments β can not be varied over a wide enough range to accurately calculate ν_1. Therefore in all determinations of E_d of first order desorption processes ν_1 was assumed to be 10^{13} sec^{-1}. For the determination of E_d by Eq. (33) in T_p, ν_2, β and θ_o must be known. Because of the difficulties mentioned above in calculating ν and the difficulty in determining θ_o accurately E_d was not calculated for second order desorption processes.

D. Crystal Preparation

Two types of crystals were used in the investigations reported here, single crystals and polycrystalline foil. The single crystal

samples were cut ~ 1 mm in thickness by spark errosion from a single crystal Rh rod 6 mm in diameter. The single crystals were cut from two different Marz grade Rh rods, obtained from Materials Research Corporation. Back reflection Laue x-ray diffraction was used to orientate the Rh rods to the desired crystal face before spark errosion. After the wafer had been sliced from the rod it was mounted in Koldmount and reoriented to the desired crystal face. The crystal was then ground to this orientation with silicon carbide paper (240 and 320 grit) mounted on a facing wheel. The crystal face was then mechanically polished in the following sequence: four successively finer grades of energy paper (1/0 to 4/0), then 1 micron diamond paste on a rotating wheel and finally a slurry of 0.05 micron Al_2O_3 in H_2O in a syntron. For the chemisorption experiments only one side of the crystal was polished while for the catalysis experiments both sides of the crystal were polished. The final accuracy of the polished surfaces was ± 1/2° for the (111) and (100) surfaces and ±1° for the stepped (755) and (331) surfaces. An extensive discussion of the use of back reflection Laue x-ray diffraction for orienting single crystal samples for use in LEED experiments has been given elsewhere and will not be repeated here.[98] The polycrystalline foil was high purity Rh from Alfa Products which had been rolled to a thickness of 0.125 mm.

After initially mounting the rhodium crystals (one at a time) in the UHV chamber the presence of phosphorus, sulfur, boron and carbon impurities could be detected by AES. Most of the carbon could be removed by annealing the crystal at 1000°C in vacuum. The remaining carbon could be removed by heating the crystal in oxygen (1×10^{-7} to 1×10^{-6} torr O_2, 800°C) or by argon ion bombardment (500 to 2000 eV, 5×10^{-5} torr Ar, 25°C) and annealing at 800°C. The initial 1000°C anneal increased the amount of phosphorous, sulfur and boron on the surface. Also after this anneal silicon could be detected on the surface. Argon ion bombardment (500 to 2000 eV, 5×10^{-5} torr Ar, 25°C) and annealing at 800°C removed the silicon, phosphorous and sulfur. Boron which is a major bulk impurity (17 ppm) segregated to the surface upon annealing and many cycles of argon ion bombardment (500 eV, 5×10^{-5} torr Ar, 25°C) and annealing at 800°C were required to remove it from the near surface region. The segregation of boron to the surface was enhanced by heating the crystal in O_2 and resulted in the formation of a boron oxide, particularly on the polycrystalline foils. The boron AES transition from the oxide was shifted downward in energy by several eV from elemental boron AES transitiion. The same shift in the boron signal was also seen when boron nitride was formed by heating the crystal in a nitrogen containing gas. Using the cleaning methods described here resulted in lowering the amount of all impurities but boron below the detectable limits of AES. Boron was never completely removed and a small amount (< 5% of a monolayer) was always detected by AES. LEED patterns from the single crystal samples after this cleaning all had sharp intense integral diffraction spots, low background intensities and no diffraction features from any impurity structures. These were the "clean"

rhodium surfaces on which the experiments in Chapter III were performed.

During the cleaning procedure several LEED patterns from ordered surface structures were observed. Boron formed (6×6) and $(2\sqrt{3}\times 2\sqrt{3})$ R30° surface structures on Rh(111) and a (3×3) surface structure on Rh(100). Sulfur formed (2×2) and C(2×2) surface structures on Rh(100) and a $(\sqrt{3}\times\sqrt{3})$ R30° surface structure on Rh(111). Carbon formed a (12×12) coincidence lattice structure on Rh(111). Complex LEED patterns were observed when both boron and sulfur were present on the stepped rhodium surfaces, but these patterns were not indexed.

E. Experimental Apparatus

1) Chemisorption Experiments

The apparatus used in the chemisorption experiments is shown in Fig. II-11. It is comprised of a cylindrical stainless steel main chamber pumped by two Varian VacSorb cryopumps, a water cooled titanium sublimation pump (TSP) and a 140 ℓ/sec Varian VacIon pump. The vacsorb pumps were employed to pumpdown the system below 1 micron at which time they were valved off and the VacIon pump and TSP were used to complete the system pumpdown to UHV conditions. After a 48 hour bakeout at 225°C and thoroughly degassing all filaments in the system a base pressure of 5×10^{-10} torr was obtained.

The system was equipped with a 2 keV glancing incidence electron gun for exciting Auger electrons, a precision manipulator which allowed the crystal to rotated about the z axis and translated in the x, y and z directions, a 0-3 keV Varian ion sputter gun for cleaning the crystal,

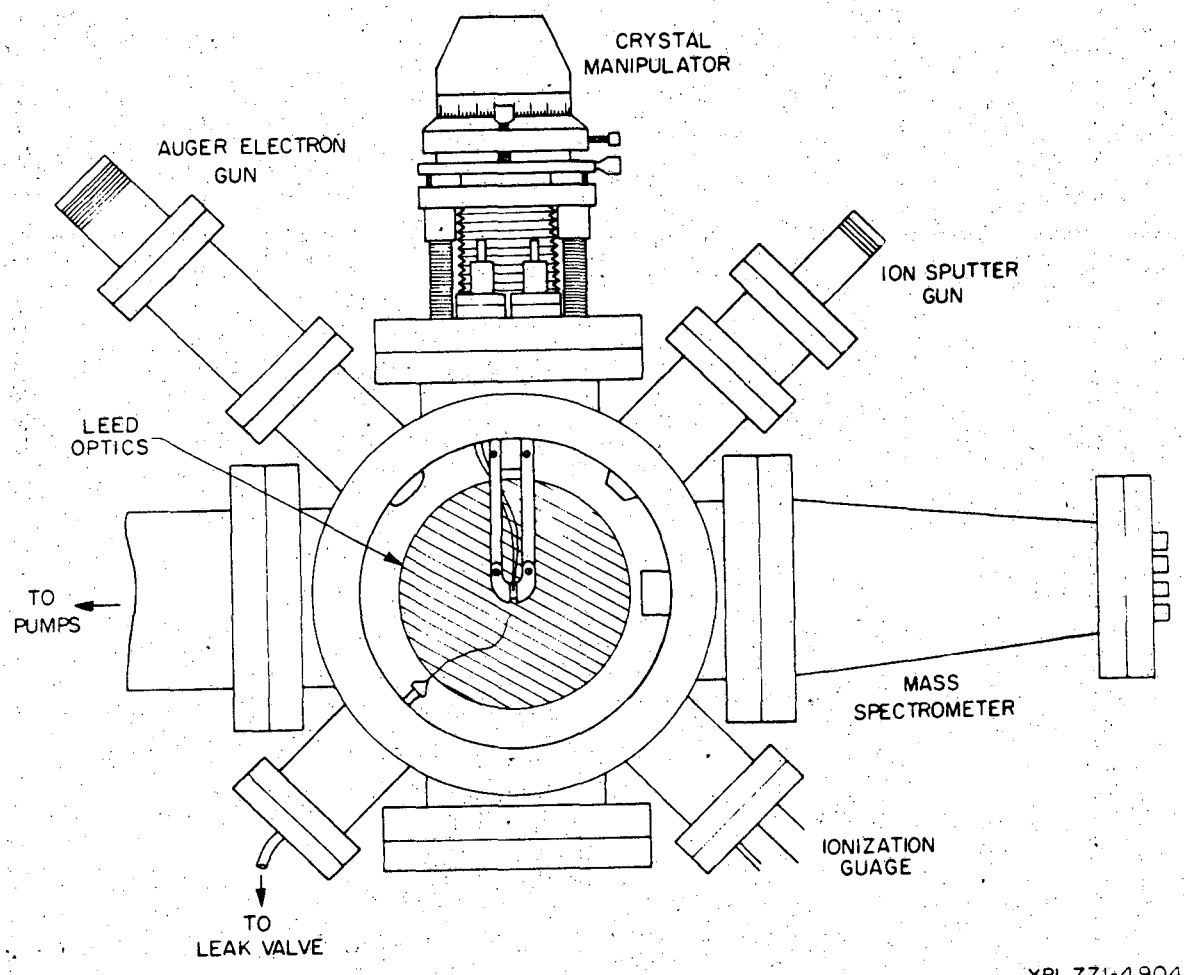

Figure II-11. Schematic diagram of the apparatus used in the chemisorption experiments.

a UTI model 100C quadrupole mass spectrometer used for residual gas analysis (RGA) and for the TDS experiments, a nude ionization guage for pressure measurement, a Varian variable leak valve for admitting gases into the chamber and a 4 grid LEED optics used both as a LEED analyzer and a AES retarding field analyzer. The crystals were connected to 0.635 cm square Cu bar supports by 0.018 cm thick Ta foil, with the rhodium crystals spot welded to the Ta foil. The crystals were mounted such that the Ta foil masked off the back side of the crystal. The crystals were heated resistively by a high current AC power supply and the crystal temperature was monitored with a chromel-alumel thermocouple spot welded to the back side of the crystals. Outside the UHV chamber Cu rods (1.6 cm in diameter and 30 cm in length) were attached to the heating feedthroughs in addiition to heating leads from the high current AC power supply. These Cu rods were immersed in LN_2 to cool the crystal by conduction. The cooling had two major benefits, the crystal cooled faster after flashing it to high temperatures and the LEED patterns were generally sharper at the lower temperatures. For all the experiments except the oxidation (III-D) and hydrocarbon adsorption (III-B-5) experiments on the Rh(111) surface the lowest adsorption temperature attained was 0°C. The Cu braid connecting the heating feedthroughs to the Cu bar supports was found to be the factor limiting the cooling to 0°C and by employing larger Cu braid adsorption temperatures of -63°C could be attained. This extended range of adsorption temperatures was used for the experiments in III-D and III-B-5.

The chemisorption properties of H_2, O_2, CO, CO_2, NO, C_2H_4 and C_2H_2 were studied at gas pressures between 1×10^{-8} and 1×10^{-5} torr and crystal temperatures between 0 and 1000°C. As mentioned above the temperature range was extended in the oxidation and hydrocarbon experiments. Also the pressure range in the oxidation studies was increased to 1 torr. When gases were admitted to the chamber at pressures of 1×10^{-5} torr or below the VacIon pump was throttled down by the gate valve between the pump and main chamber. Continually pumping the chamber during gas exposures kept the pressure of the residual background gases low during the adsorptions. For pressures above 1×10^{-5} torr the VacIon pump was completely valved off resulting in the pressure of the background gases being higher during these exposures. Several ordered structures were observed both with increasing exposure and after the gas was pumped away. As discussed in II-C the TDS experiments were carried out by linearly ramping the crystal temperature. The temperature ramp was controlled by a variac and the crystal heating rates generally used were 40°/sec for the oxygen, hydrogen and hydrocarbon experiments and 25°/sec for the CO, CO_2 and NO experiments.

All gases used in the chemisorption experiments were high purity (> 99.5%) and only C_2H_2 required further purification. The C_2H_2 was purified by passing it through a molecular sieve trap at -78°C (dry ice-acetone) to remove a small acetone impurity. The conditions (O_2 partial pressure, crystal temperature, time) for formation of the various oxygen species described in III-D did not always generate reproducible amounts of the various oxygen species. This was particularly true for the

formation of the strongly bound oxygen and epitaxial oxide. For these cases additional variables such as the pressure of the residual background gases, the presence of impurities in the surface and/or near surface region and the previous oxygen and heat treatments of the sample were found to be important. The conditions given in III-D are for oxygen exposures on a clean surface (as determined by AES) in a well baked UHV system with all filaments and the crystal holder thoroughly degased to keep the pressures of the residual background gases at a minimum. The pressures were measured by a nude ionization gauge and were not corrected for the sensitivity differences of the ionization gauge to the various gases.

2) Catalysis Experiments

A schematic drawing of the apparatus used for the CO hydrogenation experiments is shown in Fig. II-12. It has been described in detail elsewhere.[66] This chamber is equipped with a high pressure isolation cell and is pumped by water cooled TSP and a LN_2 trapped 6 inch diffusion pump. After bakeout a base pressure of 1×10^{-9} torr could be attained.

With the cell open the system operated just as the system described in II-E-1 and the samples characterized by LEED, AES and TDS. A rotary feedthrough only allowing rotation about the z axis was used as the crystal manipulator. The rhodium crystals were spotted welded to 0.05 cm Pt wires which were in turn mounted in 0.317 cm Cu rods. The crystal was heated resistively by a high current AC power supply and the crystal temperature was monitored by a Pt-10% Rh/Pt thermocouple.

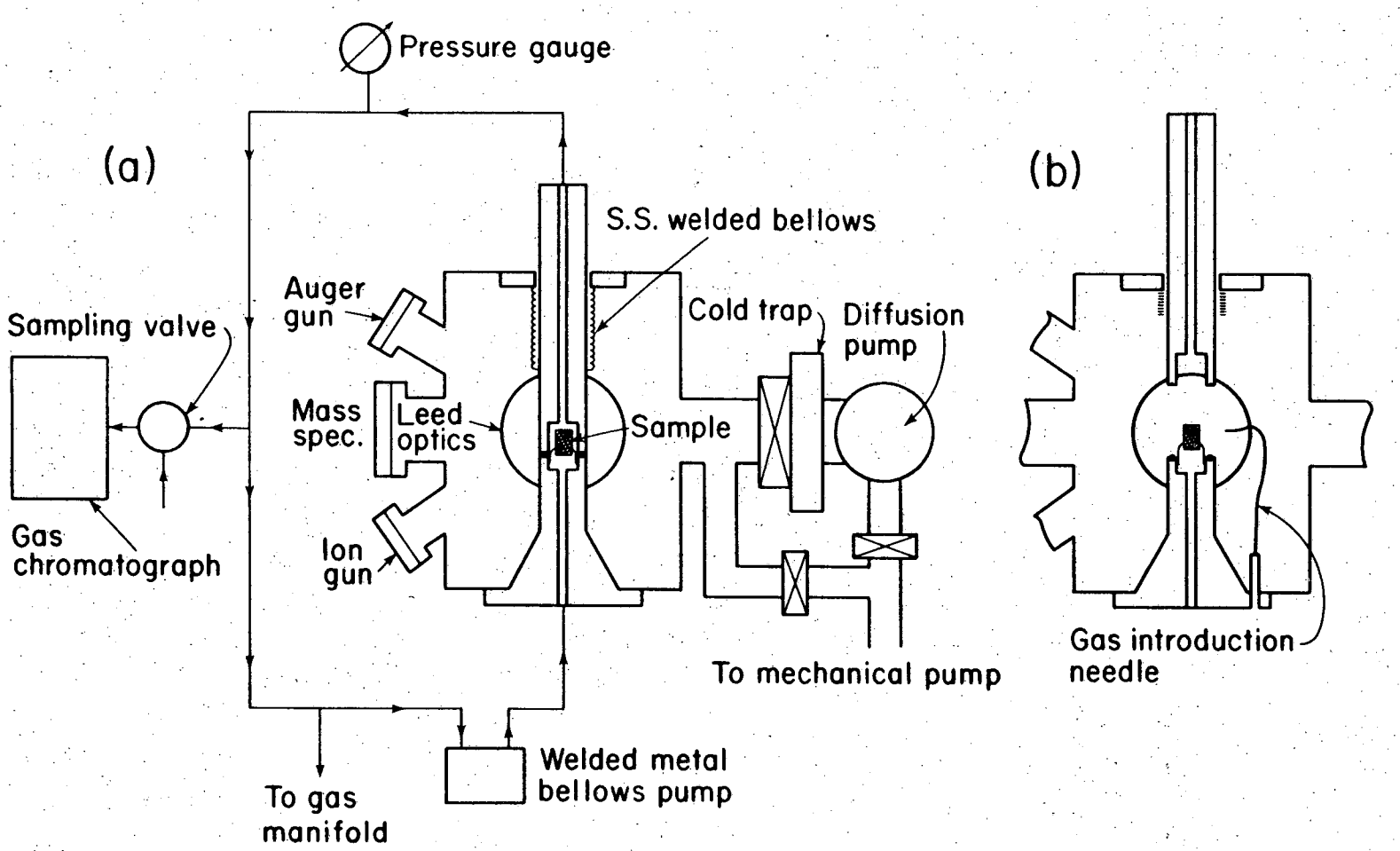

Figure II-12. Schematic diagram of the apparatus used in high pressure catalysis experiments.

A temperature regulator was employed to operate the heating supply and the crystal temperature could be kept within ± 2° of the desired temperature during a reaction.

With the cell closed the system could be operated either as a pretreatment chamber or a batch reactor. The crystal manipulator could also be removed at this time allowing easy and fast exchange of samples or repair of the mounting wires and the thermocouple without having to bakeout afterwards. Oxygen pretreatments of the Rh crystals were carried out by admitting 1 atm of O_2 into the cell loop and then heating the crystal for 30 min at 600°C. After this pretreatment the O_2 was pumped away with sorption pumps and the cell opened so the crystals could be characterized with LEED and AES. The oxides formed under these conditions were amorphous and generally had O_{515}/Rh_{302} peak-to-peak ratios of 0.6. Some variance from the value of 0.6 was observed for the reasons discussed in II-E-1. In particular ratios greater than 0.6 were generally obtained when a crystal having a monolayer or more of carbon on the surfaces was oxidized.

After the crystal had been prepared and characterized the cell was closed and the system was operated as a batch reactor. The desired H_2:CO ratio and total reaction pressure was attained by expanding first H_2 then CO into the cell loop (total cell volume = 159.5 cm^3). Both gases were research grade, but required further purification. The CO was passed through a dry ice-ethanol bath to remove trace amounts of Ni carbonyl and the H_2 was passed over Ag foil which acted as a Cl and S getter. The gases were then circulated in the cell loop for several

minutes by a piston displacement circulation pump to insure adequate mixing of the gases. During the admitting and mixing of gases the crystal was kept at room temperature. The reaction was begun by raising the crystal to the desired reaction temperature and the buildup of products as a function of time was monitored by a Perkin-Elmer (model 3920) gas chromatograph. This gas chromatograph was equipped with a Chromosorb 102 column, flame ionization detector (FID), and 0.1 mℓ sampling valve. The peaks obtained from the chromatograph were integrated with a Spectra-Physics Minigrator (model 23000-111). The peak areas were calibrated by circulating a Matheson standard (100 ppm CH_4 in N_2) at 6 atm in the cell loop. Corrections were made for the differences in the FID to the various products[99] and for fact the a FID detects the number of carbon atoms (weight %) and not the number of molecules (molecule %). An FID only detects hydrocarbons which is a mixed blessing. The reactants, H_2 and CO, are not detected so they don't interfere with product detection but possible reaction products H_2O and CO_2 are not detected either. In a batch reactor the reaction rate is the slope of the product concentration vs time plot. Therefore in order to determine the initial reaction rates a linear least squares fit was made to the initial region of the product curve.

After a reaction the crystal is cooled, the gases pumped away by the sorption pumps and then the cell is opened and the surface characterized by LEED and AES. Pumpdown from 6 atm to UHV takes ~5 minutes. Generally the surface was only characterized before and after a experiment (total reaction time 2 to 3 hrs), but some experiments were stopped

at various stages of the reaction in order to analyze the surface structure and composition. This apparatus is ideally suited for making correlations of surface structure and composition with catalyst activities, selectivities and lifetimes.

III. RESULTS AND DISCUSSION

A. Characterization of the Clean Rhodium (111), (100), (755) and (331) Surfaces

1) The Clean Rhodium (111) and (100) Surfaces

The LEED patterns of the clean Rh(111) and (100) surfaces shown in Fig. III-1 exhibit the (1×1) symmetry characteristic of the unreconstructed clean surfaces. These LEED patterns have sharp intense spots and low background intensity. The AES spectrum of these surfaces is shown in Fig. III-2. The I-V curves for the (0,0) diffraction beams from these two surfaces are shown in Fig. III-3. The diffraction beam intensities were measured with a spot photometer. To select the Bragg peaks and determine the inner potential, V_o, and topmost interlayer spacing, c, Eq. (10) was employed. First the energies which the Bragg peaks are expected to occur are determined using the bulk interlayer spacing and V_o = 10 eV, typical valves for most metals. These calculated energies are then matched to the experimental energies as shown in Tables III-1 and III-2. Bragg peaks are generally the major peaks in a I-V profile and this fact can be used as a guide in separating the Bragg peaks from the multiple scattering peaks. For the Rh(111) surface the separation is straight forward because the I-V profile is nearly kinematical. The I-V profile from the Rh(100) surface has several large multiple scattering peaks below 125 eV making the Bragg peak assignment more difficult in this region. Either the 77 or 91 eV peaks could be taken as the $\ell = 3$ Bragg peak. On the bsis of the θ_D calculations the 77 eV peak was taken

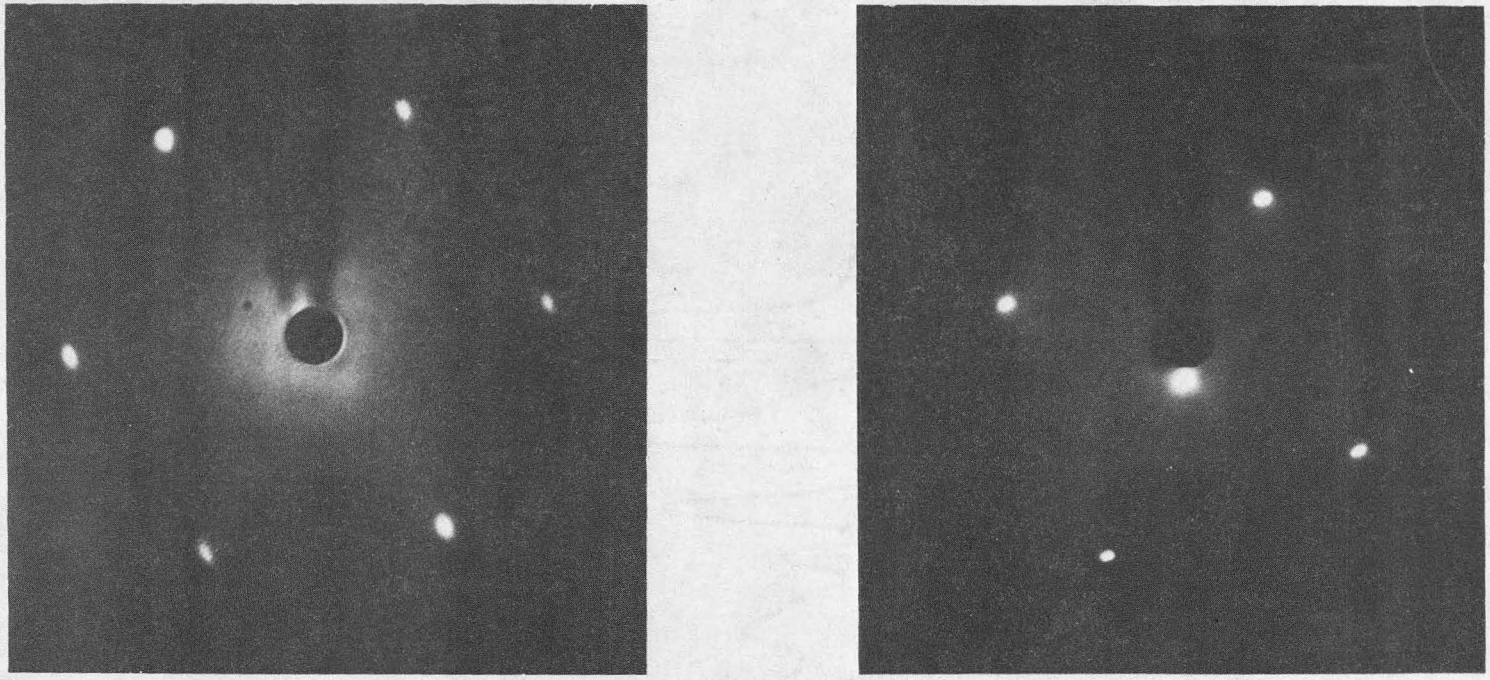

XBB 771-17

Figure III-1. LEED patterns from the clean rhodium(111) and (100) surfaces.

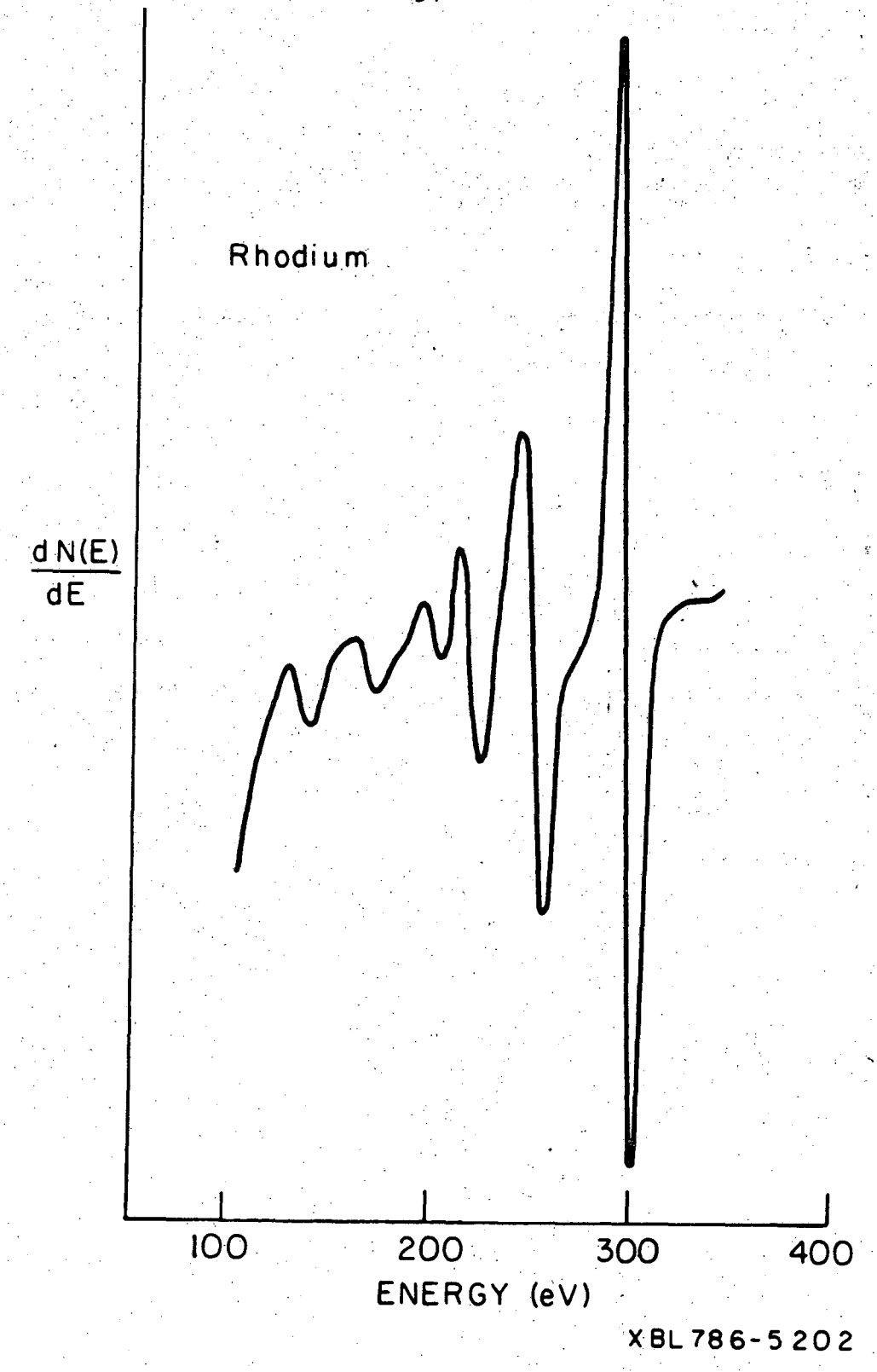

Figure III-2. AES spectrum from a clean rhodium surface.

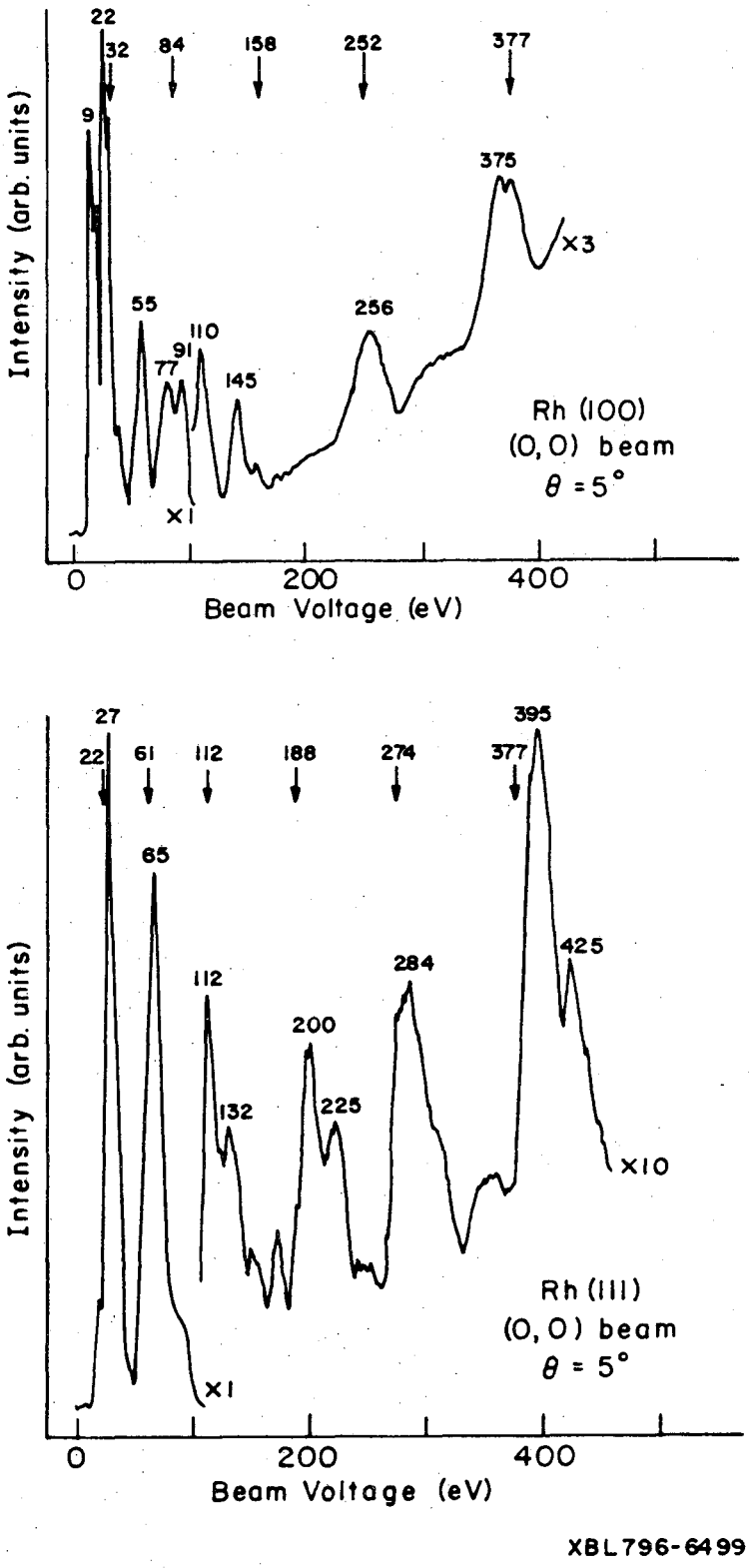

Figure III-3. I-V curves for the Rh(111) and (100) specular diffraction beams.

Table III-1. Selection of the Bragg peaks for Rh(111).

ℓ	ℓ^2	E_{calc} (eV)[†]	E_{expt} (eV)
1	1	---	---
2	4	22	27
3	9	61	65
4	16	112	112
5	25	188	200
6	36	274	284
7	49	377	395

[†]Values of V_o = 10 eV and c = 2.19 Å were used to determine E_{calc} from Eq. (10).

Table III-2. Selection of the Bragg peaks for Rh(100).

ℓ	ℓ^2	E_{calc} (eV)[‡]	E_{expt} (eV)
1	1	---	---
2	4	32	22
3	9	84	77
4	16	158	145
5	25	252	256
6	36	368	375

[‡]Values of V_o = 10 eV and c = 1.90 Å were used to determine E_{calc} from Eq. (10).

as the Bragg peak. This will be discussed below in further detail. After the Bragg assignments have been made experimental values for c and V_o are calculated from the slope and intercept of the straight line drawn through the E_{expt} vs ℓ^2 data points. The results obtained from the data in Tables III-1 and III-2 are summarized in Table III-3. The slight contraction of the surface layer is smaller than the experimental error therefore within the accuracy of these calculations the rhodium (111) and (100) surfaces are unrelaxed. Multiple scattering calculations have shown that Δc is between -3% and 0% and V_o ranges between 10.7 and 11.5 eV on the rhodium(111), (100) and (110) surfaces.[37-40] Thus the kinematical and multiple scattering calculations are in very good agreement.

A determination of θ_D was made for each of the Bragg peaks listed in Tables III-1 and III-2. An intensity vs temperature profile at $\theta = 5°$ for the specular $\ell = 7$ Bragg peak from the Rh(111) surface is shown in Fig. III-4. The other Bragg peaks had similar profiles. These profiles were obtained by monitoring the intensity of a given Bragg peak with a spot photometer as the crystal cooled from 800 to 50°C. The crystal was then rotated back to $\theta = 0°$ and the background intensity was measured in the same manner. The intensities were monitored during cooling instead of heating to avoid distortions from the heating currents. The values of I_{oo} (Bragg peak intensity), I_{bkgd} (background intensity), $I_{oo}^* = I_{oo} - I_{bkgd}$, and $\ell n\ I_{oo}^*$ for the curves in Fig. III-4 have been tabulated in Table III-4. The plot of $\ell n\ I_{oo}^*$ vs temperature of these values shown in Fig. III-5 yields a straight line with a slope of -5.14×10^{-3}.

Table III-3. Calculation of the topmost interlayer spacing and inner potential for Rh(111) and Rh(100).

Crystal face	Slope	c_{expt} (Å)	c_{bulk} (Å)	$\frac{\Delta c}{c_{bulk}} = \left(\frac{c_{expt} - c_{bulk}}{c_{bulk}} \times 100\right)$	Intercept	V_o (eV)
Rh(111)	8.23	2.15	2.19	- 2%	-10	10
Rh(100)	10.9	1.86	1.90	- 2%	-11	11

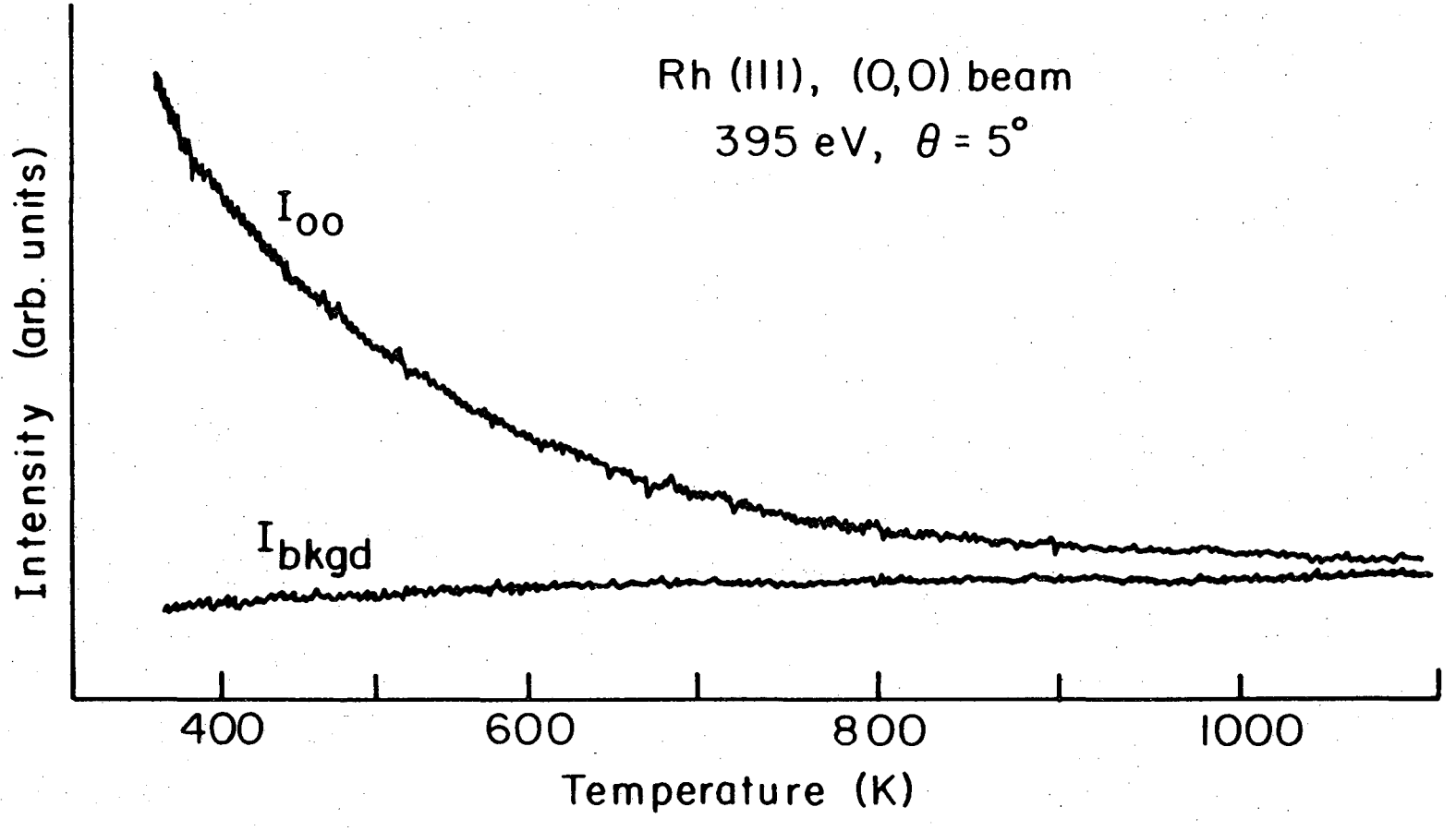

XBL796-6495

Figure III-4. Intensity vs. temperature curves for the specular $\ell = 7$ Bragg peak from Rh(111), I_{oo}, and background from Rh(111), I_{bkgd}.

Table III-4. Intensity values (arbitrary units) for the curves shown in Fig. III-4.

Temp. (K)	I_{oo}	I_{bkgd}	I_{oo}^{*}	$\ell n\ I_{oo}^{*}$
353	3.63	0.74	2.89	1.06
394	3.13	0.78	2.35	0.85
432	2.79	0.81	1.98	0.68
468	2.46	0.82	1.64	0.49
503	2.22	0.84	1.38	0.32
537	2.02	0.85	1.17	0.16
582	1.79	0.87	0.92	-0.08
625	1.61	0.88	0.73	-0.31
667	1.47	0.89	0.58	-0.54
708	1.35	0.89	0.46	-0.78
749	1.27	0.90	0.37	-0.99
800	1.19	0.90	0.29	-1.24
850	1.13	0.91	0.22	-1.51
899	1.09	0.91	0.18	-1.71
947	1.07	0.92	0.15	-1.90
1041	1.03	0.93	0.10	-2.30

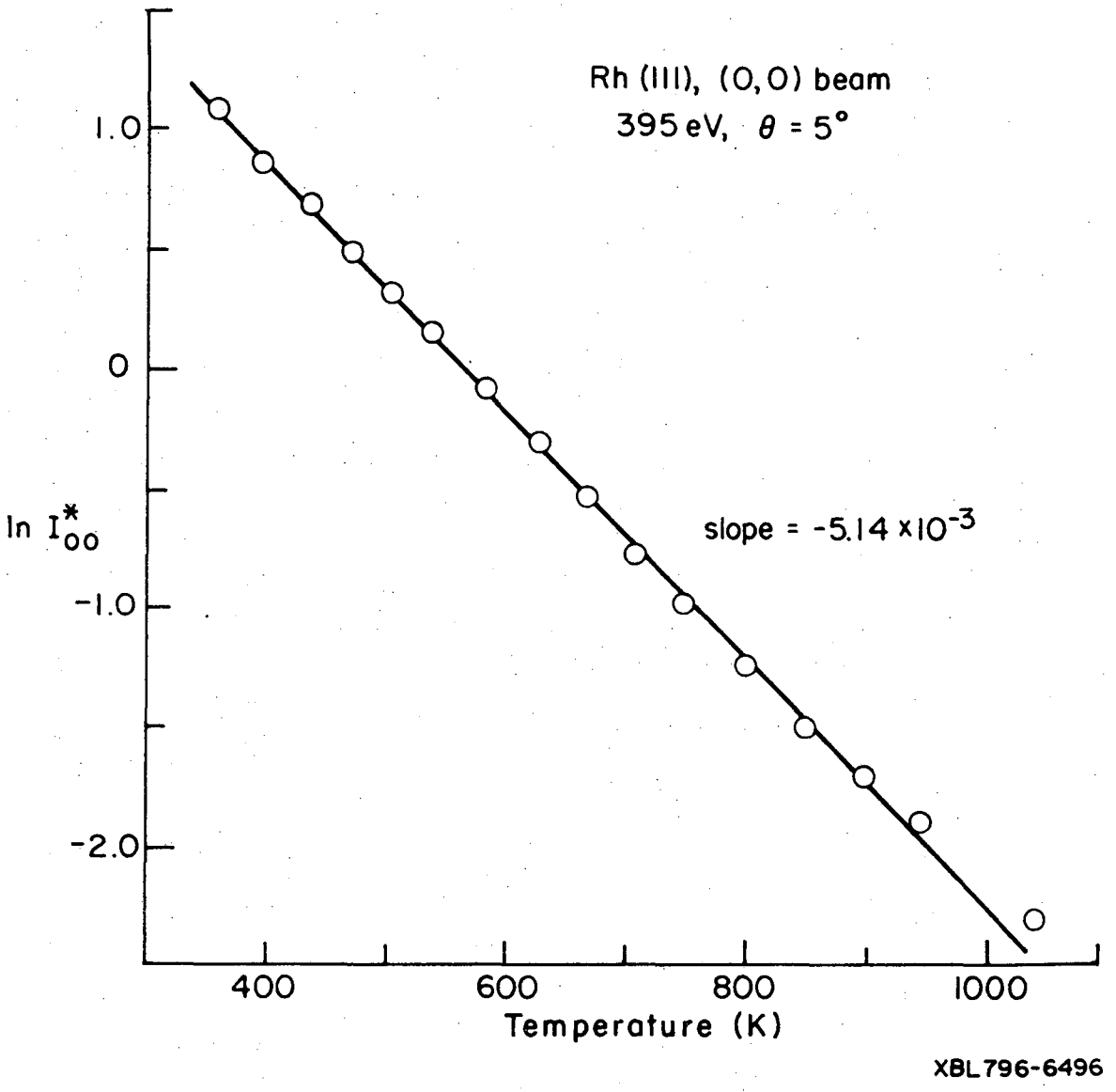

Figure III-5. A plot of $\ell n\ I_{00}^{*}$ vs temperature for the specular $\ell = 7$ Bragg peak from the Rh(111) surface.

Using this slope in Eq. (21) yields θ_D = 340 K. The values of θ_D for the other Bragg peaks were calculated in a similar manner. The results of these calculations are shown in Table III-5 and Fig. III-6. These values are the average of several experiments. The estimated errors in θ_D arose from noise in the intensity measurements and difficulty in making an accurate measurement of the beam voltage. A value of θ_D was also calculated for the 91 eV peak on Rh(100), but this value deviated significantly from the curve shown in Fig. III-6. For this reason the 77 eV peak was selected as the ℓ = 3 Bragg peak for the Rh(100) surface.

From Fig. III-6 a value of 260 K was chosen for the Debye surface temperature. This was taken from the minimum in the θ_D vs. beam voltage curve for the (111) surface. The I-V of the (111) surface is kinematical (Fig. III-3) which makes the θ_D vs. beam voltage curve similar in shape to penetration depth vs. beam voltage curve for low-energy electrons in metals. The I-V curve of the (100) surface has several multiple scattering features present (Fig. III-3), especially below 125 eV. Because of these features, the θ_D measured below 100 eV continues to decrease instead of increasing like the (111) surface. The values of θ_D at the highest beam voltage on each surface are very close to the bulk θ_D value of 350 K.[100] The value of 350 K was obtained from specific heat data at 298 K.

Chan et al.[42] have also measured values of θ_D for Rh(111). Their relationship between θ_D and electron energy disagreed with the Rh(111) results in Fig. III-6. The area of disagreement was for energies less than 100 eV, where they found θ_D to decrease (similar to the Rh(100) results) compared to the increase seen in Fig. III-6. A possible

Table III-5. Values of the Debye temperature, θ_D, for the Bragg peaks of the Rh(111) and (100) specular beams.

Rh(111)		Rh(100)	
E_{expt} (eV)	θ_D (K)	E_{expt} (eV)	θ_D (K)
27	298 ± 30	22	211 ± 25
65	293 ± 20	77	260 ± 20
112	256 ± 15	145	293 ± 15
200	282 ± 15	256	332 ± 15
284	319 ± 15	375	369 ± 15
395	351 ± 15		

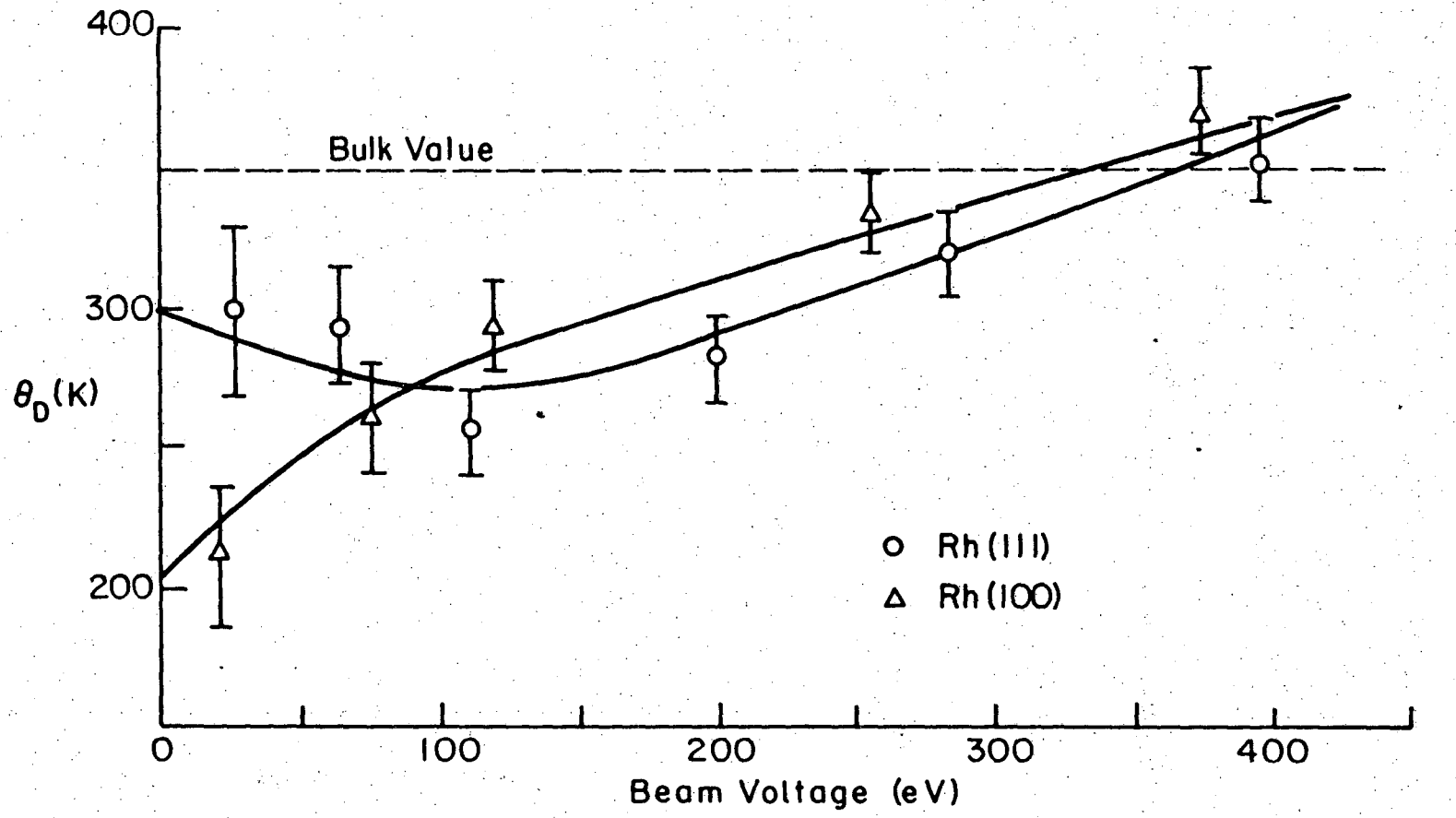

XBL 796-6497

Figure III-6. Values of θ_D for the specular Bragg peaks from the rhodium(111) and (100) surfaces.

explanation for this difference is the azimuthal angle, ϕ, dependence of the I-V profile. For kinematical scattering the intensity will not depend on ϕ, but because of the existence of multiple scattering the intensity does depend on ϕ. It is possible at the value θ used in their experiments multiple scattering was more pronounced resulting in a decreased value of θ_D. Multiple scattering calculations on Rh(100) have suggested a value of 250 K for the surface θ_D.[38]

2) The Clean Stepped Rhodium (755) and (331) Surfaces

LEED patterns and real space representations for the clean Rh(755) and (331) surfaces are shown in Fig. III-7. These patterns exhibit the (1x1) summetry characteristics of an unreconstructed clean surface. The AES spectrum from the clean rhodium surfaces is shown in Fig. III-2.

The (755) surface is at an angle of 9.5° from the (111) surface and can also be labeled as Rh(S)-[6(111)×(100)].[77] This notation is more descriptive of the surface structure since LEED shows surface is actually made up of a series of six atom wide (111) terraces separated by one atom high (100) steps. The LEED pattern can be thought of as a set of hexagonal spots due to the (111) terraces in which all spots are split by the step periodicity. The terrace width was calculated from the splitting observed in the LEED pattern. The LEED patterns observed on the (755) surface can be easily indexed as diffraction spots from structures on the (111) terraces which have been split by the step periodicity therefore the Rh(S)-[6(111)×(100)] notation will be used here.

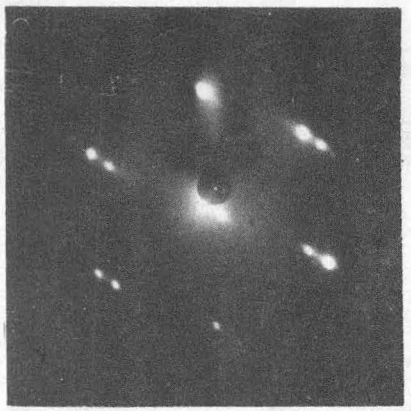

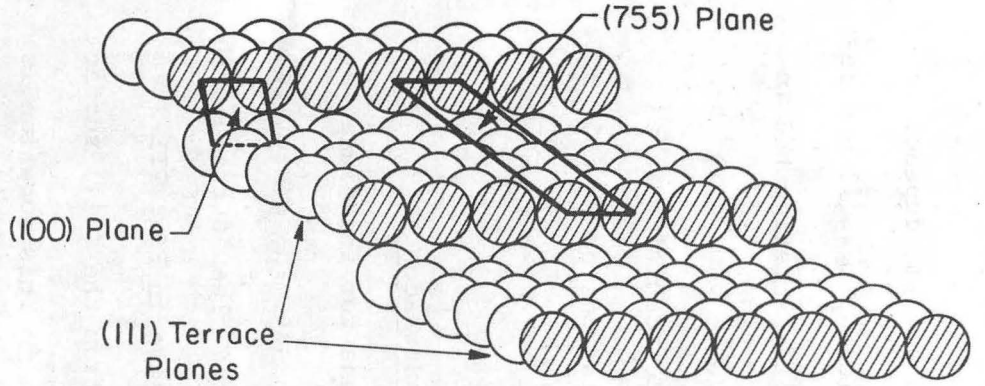

(a) Rh (755) ⟷ Rh (S) - [6 (111) x (100)]

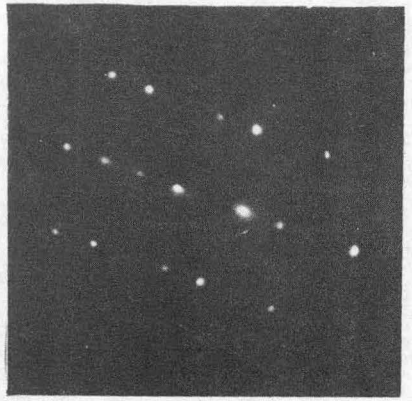

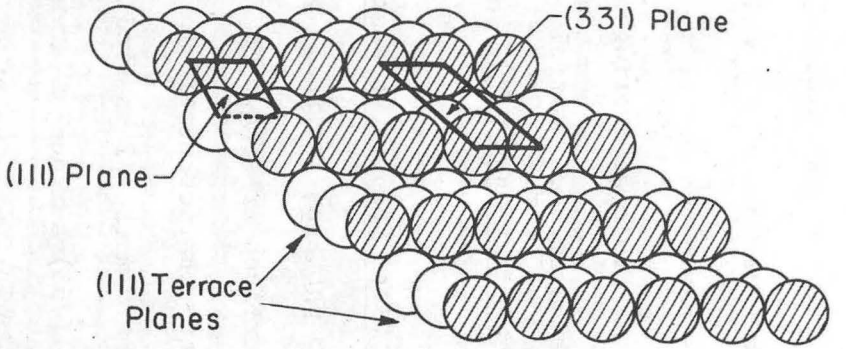

XBB 786-7517

(b) Rh (331) ⟷ Rh (S) - [3 (111) x (111)]

Figure III-7. LEED patterns at (a) 90 eV and (b) 139 eV and the real space models of the clean rhodium stepped surfaces. Cross hatched circles represent step atoms and the unit cells of the (755), (331) and step planes are shown. Both surfaces have (111) terrace planes.

From the LEED pattern in Fig. III-7b the (331) surface was determined to correspond to a Rh(S)-[3(111)×(111)] surface, but the adsorbate LEED patterns produced on this surface could be most easily indexed using the (331) unit cell vectors therefore the (331) notation will be used here. The unit cell of the (331) surface is oblique as can be seen from Fig. III-7b. The expected ratio of the two real space (331) unit cell vectors is 2.24. The value of 2.20 calculated from the LEED pattern in Fig. III-7 is in good agreement with the expected value. No intensity data was taken for either stepped surface.

B. The Chemisorption of Small Molecules on the Rhodium(111) and (100) Surfaces

The adsorption of H_2, O_2, CO, CO_2, NO, C_2H_4 and C_2H_2 gases were investigated. The LEED structures observed upon adsorption of these gases on the Rh(111) surface along with those produced by carbon are summarized in Table III-6. Also included in Table III-6 are the reported structures for these molecules adsorbed on the hexagonal faces of Pd, Ni, Ir, Pt and Ru. Similarly in Table III-7 the surface structures observed for these adsorbates on Rh(100) are compared with previously reported structures of these adsorbates on the (100) faces of Pd, Ni, Ir and Pt. A more complete tabulation of surface structures has been presented elsewhere.[97]

On the (100) face, the disordering temperatures of the ordered surface structures were in excess of 100°C, while for the (111) face most disordering temperatures were below 100°C. Table III-8 shows the estimated disordering temperatures for the various adsorbates. Because of

Table III-6. Surface structure of chemisorbed small molecules on the (111) surfaces of Rh, Pd, Ni, Ir and Pt and the (001) surface of Ru.

Gas	Rh(111) (This paper)	Pd(111)	Ni(111)	Ir(111)	Pt(111)	Ru(001)
H_2	disordered	(1×1)[101]	disordered[138] (2×2)[139]	(1×1) or disordered[102]	(1×1)[104]	
O_2	(2×1)	(2×2)[107] ($\sqrt{3}\times\sqrt{3}$) R30°[107]	(2×2)[106] ($\sqrt{3}\times\sqrt{3}$) R30°[106]	(2×2)[110] (2×1)[109]	(2×2)[143]	(2×2)[145]
CO	($\sqrt{3}\times\sqrt{3}$) R30° split (2×2) (2×2)	($\sqrt{3}\times\sqrt{3}$) R30°[107] c(4×2)[107] split (2×2)[107]	($\sqrt{3}\times\sqrt{3}$) R30°[105,106] c(4×2)[106] ($\sqrt{7}/2\sqrt{7}/2$)R19.1°[106]	($\sqrt{3}\times\sqrt{3}$) R30°[109-111] ($2\sqrt{3}\times2\sqrt{3}$) R30°[109,110] split($2\sqrt{3}\times2\sqrt{3}$) R30°[110]	($\sqrt{3}\times\sqrt{3}$) R30°[108] c(4×2)[108] "hexagonal"[108]	($\sqrt{3}\times\sqrt{3}$) R30°[25, 112] (2×2)[25] disorder[112]
CO_2	($\sqrt{3}\times\sqrt{3}$) R30° split (2×2) (2×2)		(2×2)[140] (2×$\sqrt{3}$)[140]			($\sqrt{3}\times\sqrt{3}$) R30°[25] (2×2)[25]
NO	c(4×2) (2×2)	c(4×2)[119] "star" structure[119] (2×2)[119]	c(4×2)[120] "hexagonal"[120]	(2×2)[142]		
C_2H_4	(2×2) c(4×2)		(2×2)[139]	($\sqrt{3}\times\sqrt{3}$) R30°[102]	(2×2)[144]	
C_2H_2	(2×2) c(4×2)		(2×2)[141]	($\sqrt{3}\times\sqrt{3}$) R30°[102]	(2×2)[144]	
C	(8×8) (2×2) R30° ($\sqrt{19}\times\sqrt{19}$) R23.4° ($2\sqrt{3}\times2\sqrt{3}$) R30° (12×12)		(1×1)[134] ($\sqrt{39}\times\sqrt{39}$)[140]	(9×9)[102]	graphite rings[137]	(12×12)[25]

Table III-7. Surface structures of chemisorbed small molecules of the (100) surfaces of Rh, Pd, Ni, Ir and Pt.

Gas	Rh(100)	Pd(100)	Ni(100)	Ir(100) (1×1)	Ir(100) (5×1)	Pt(100) (1×1)	Pt(100) (5×20)
H_2	(1×1) or disordered		disordered[101] c(2×2)[146]		(5×1) or disordered[151]	(1×1) or disordered[117]	(5×20) or disordered[117]
O_2	(2×2) c(2×2)		(2×2)[147] c(2×2)[147]	(2×1)[116]	(2×1)[151]	(1×1)[117]	not adsorbed[117]
CO	c(2×2) split (2×1)	c(4×2) R45°[118] compressed c(4×2) R45°[118]	c(2×2)[114] "hexagonal"[114]	c(2×2)[116]	(2×2)[116] (1×1)[152]	c(2×2)[117] (1×1)[117]	(1×1)[117] c(4×2)[153] (2×2)[153]
CO_2	c(2×2) split (2×1)			c(2×2)[116] (7×20)[116]	(2×2)[116]		
NO	c(2×2)				(1×1)[142]		(1×1)[145]
C_2H_4	c(2×2)		c(2×2)[148]	(1×1)[150]	(1×1)[150]		c(2×2)[154]
C_2H_2	c(2×2)		c(2×2)[148]	(1×1)[150]	(1×1)[150]		c(2×2)[154]
C	c(2×2) graphite rings		"quasi" c(2×2)[136] graphite rings[136] (2×2)[147] ($\sqrt{7}\times\sqrt{7}$) R19°[149]		c(2×2)[150]		graphite rings[137]

Table III-8. Approximate disordering temperatures (°C) for various structures on Rh(111) and (100).

	CO	CO_2	O_2	NO	C_2H_4	C_2H_2	C
Rh(111)	75	75	>150	50	150 (decomposes)	150 (decomposes)	800°C (dissolves)
Rh(100)	125	125	>200	150	150 (decomposes)	150 (decomposes)	800°C (dissolves)

the low disordering temperatures on the (111) surface, it was necessary to perform the adsorptions at 25°C or below to obtain rapid formation of well ordered LEED patterns.

1) Hydrogen

Hydrogen did not noticeably alter the (1×1) clean surface LEED pattern on either surface, although it was adsorbed, as indicated by the thermal desorption spectra shown in Fig. III-8. The peak maximum shifts to lower temperatures with increasing exposure which suggests second order desorption kinetics. Hydrogen was one of the more weakly adsorbed species and was readily displaced by CO, NO, O_2, C_2H_4 or C_2H_2. No evidence for $CO-H_2$ interactions were observed during co-adsorption of those gases.

Since adsorption of hydrogen caused no noticeable change in the (1×1) LEED patterns of the clean (111) and (100) rhodium surfaces and hydrogen is a weak scatterer, it was necessary to perform intensity vs voltage measurements in order to determine whether hydrogen forms a (1×1) structure as is the case on Pd(111)[101] or a disordered layer as on Ni(100).[101] The I-V curves of the specular diffraction beam from a clean and hydrogen covered Rh(111) surface are shown in Fig. III-9. Hydrogen adsorption does not result in the appearance of any new peaks in the Rh(111) I-V curve which indicate the hydrogen overlayer is disordered. The thermal desorption spectra shown in Fig. III-8 are similar those seen on Ir(111),[102] Ni(111) and (100),[103] and Pt(111).[104] The fact that hydrogen has been shown to be dissociatively adsorbed on Ni(111),[103] Ni(100)[103] and Pt(111)[104] indicates that hydrogen is

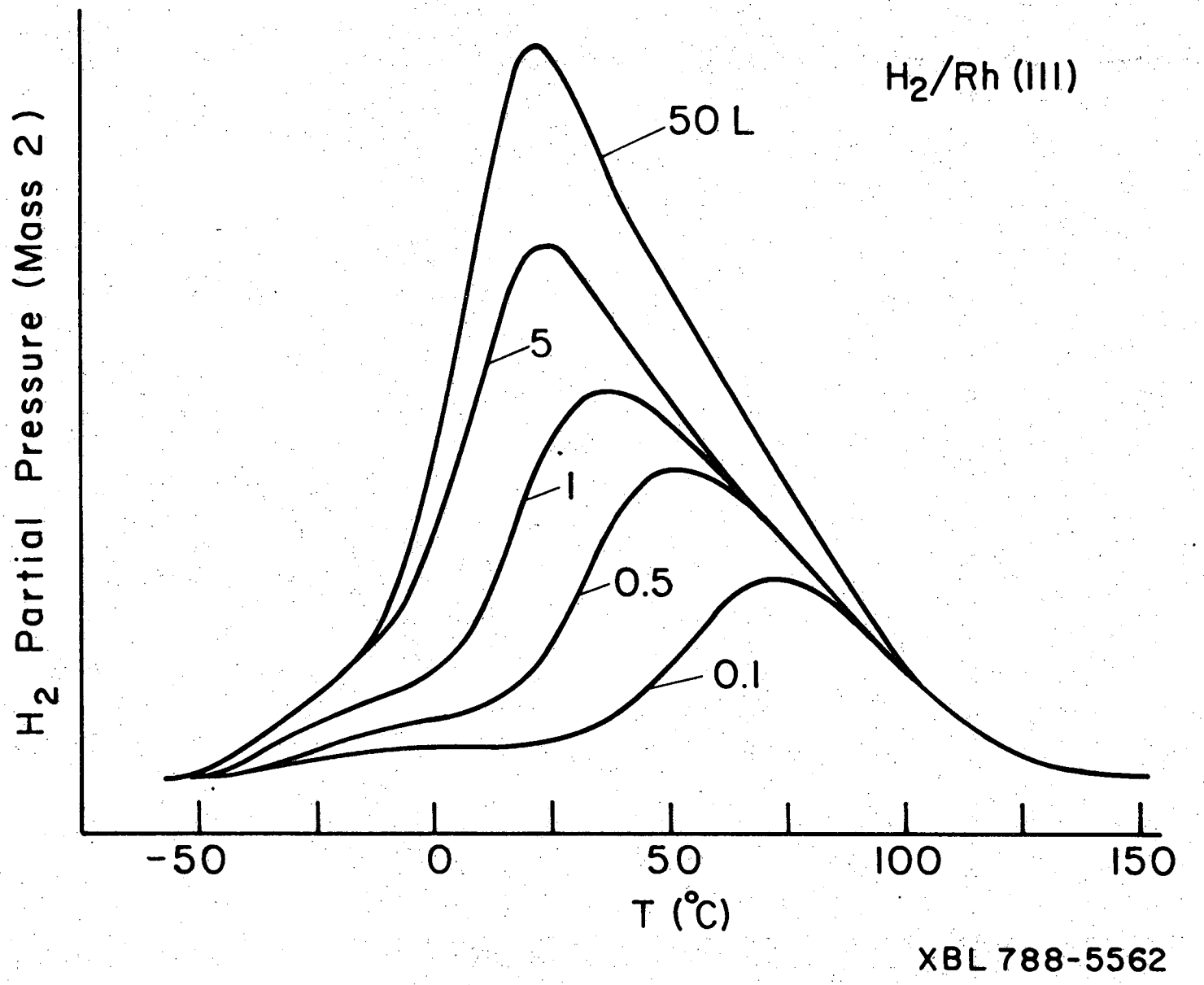

Figure III-8. Thermal desorption spectra obtained from adsorbing 0.1 to 50 L of hydrogen on Rh(111).

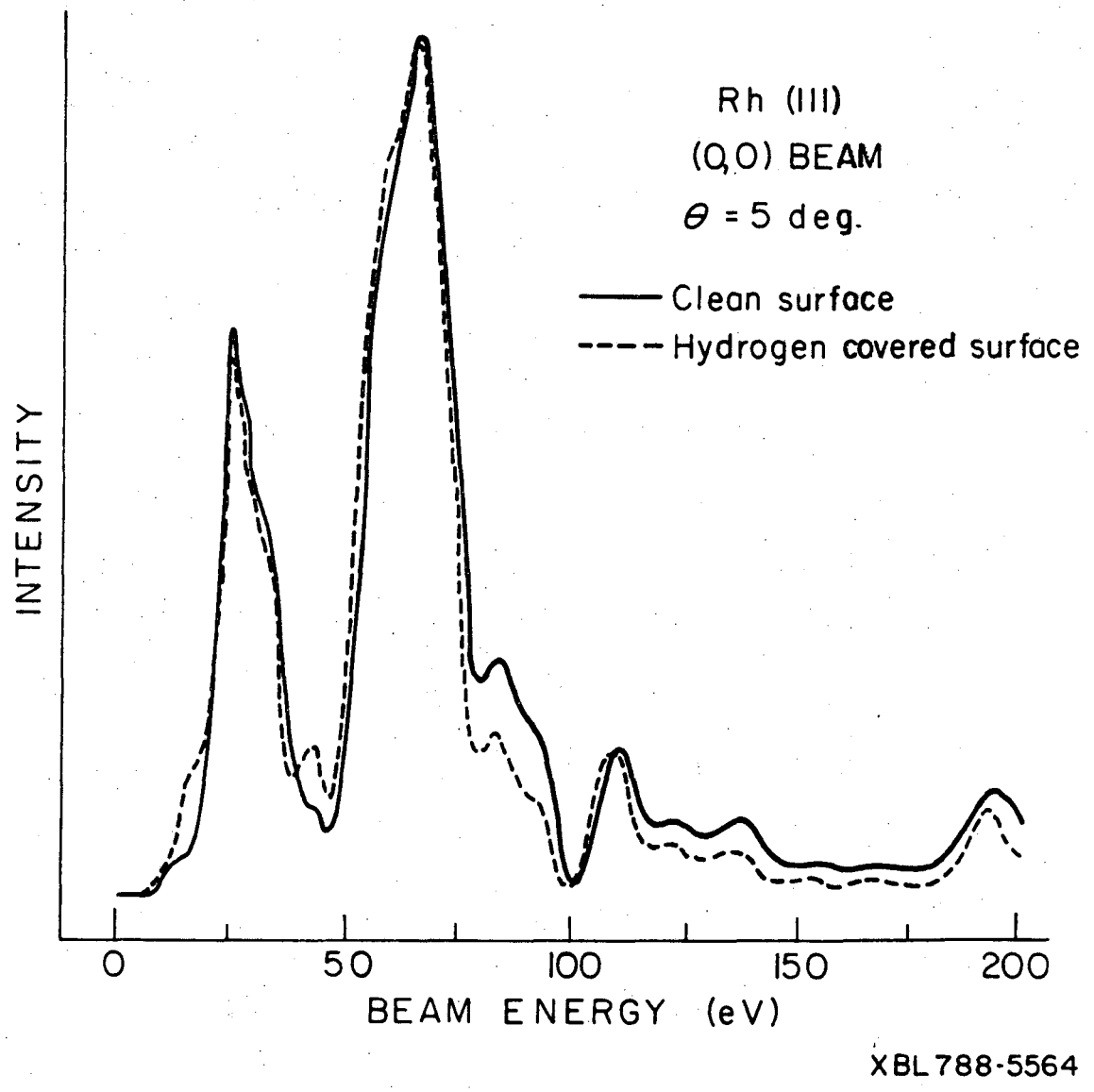

Figure III-9. Intensity curves of the specular diffraction beam from Rh(111) before (——) and after (– – –) hydrogen adsorption.

also dissociatively adsorbed on the rhodium surfaces.

2) Oxygen

In this section only the Rh(100) results will be discussed. The oxygen chemisorption results on the Rh(111) surface will be presented and discussed in III-D. Oxygen adsorbed with a high sticking probability on the (100) surface, forming (2×2) and c(2×2) structures, as shown by the LEED patterns in Fig. III-10. On the (100)surface the (2×2) structure was formed at about 1L (1L = 1×10^{-6} torr.sec) and then transformed to a c(2×2) structure upon increasing the oxygen exposure above 1L. The (2×2) structure could be regenerated from the c(2×2) by either heating the crystal to about 125°C in the presence of gaseous oxygen or by reaction of the adsorbed oxygen with H_2 or CO gas.

The oxygen structures, when heated above 50°C, were extremely reactive with gaseous H_2 or CO. All oxygen structures were removed after a few seconds of exposure to 5×10^{-7} torr of either gas. Oxygen was readily readsorbed on the surface after this reaction. The disordering temperatures for the oxygen structures may actually be significantly higher than those given in Table III-8 as the LEED patterns were susceptible to removal by ambient CO and H_2 at the temperatures listed in the table. Exposure to NO gas did not cause a removal or displacement of the oxygen structures.

Our results of oxygen adsorption on Rh(100) are not in agreement with the early work done by Tucker on Rh(100).[24] He found (2×2), (3×1) and (2×8) oxygen structures, but no c(2×2) structure. The (2×8) structure was stated to be a coincident layer of oxygen having a coverage of

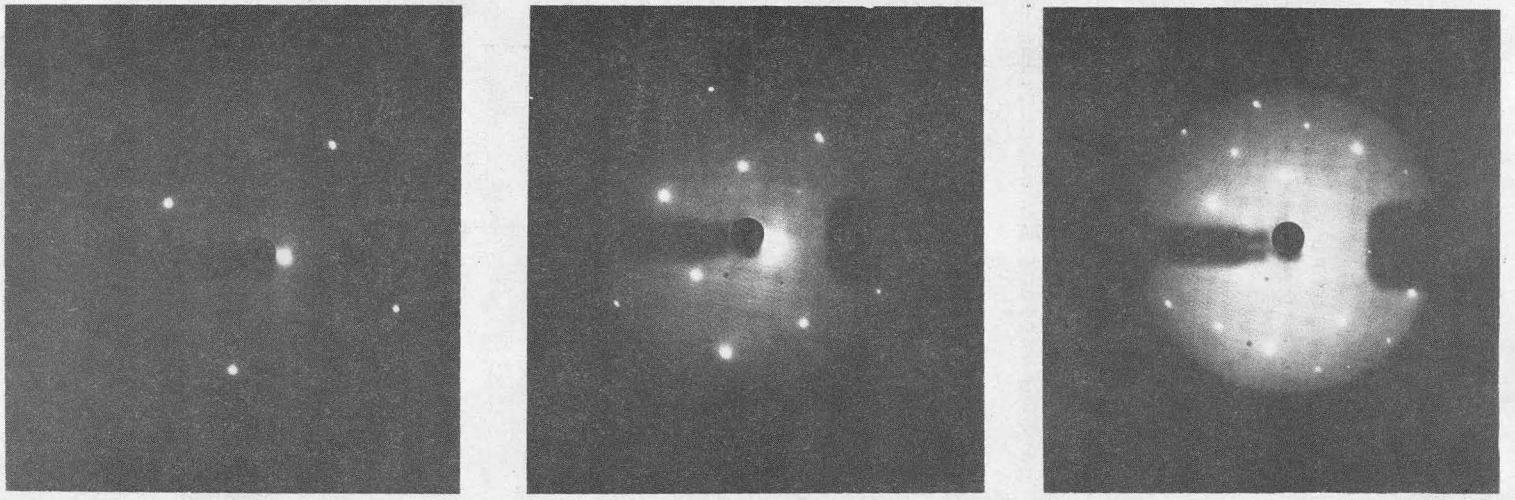

XBB 771-18

a. clean b. c(2x2) c. 2x2

Figure III-10. LEED patterns from (a) clean Rh(100) at 74 eV; (b) Rh(100) - c(2×2)-O at 85 eV; (c) Rh(100) - (2×2)-O at 98 eV.

7/8. Oxygen adsorption was examined over a wide range of pressures and temperatures and neither the (3×1) or (2×8) structures were ever seen. It is possible that his crystals were either misoriented or contaminated.

3) Carbon Monoxide and Carbon Dioxide

CO and CO_2 formed a series of surface structures on both the (111) and (100) surfaces. CO_2 appeared to dissociate to CO upon adsorption since CO and CO_2 gave identical LEED patterns and thermal desorption spectra, with CO the only gas detected during desorption. On both surfaces the gases formed an initial low coverage structure which then compressed into a hexagonally closed packed overlayer of CO. In order to observe the CO structures it was necessary to keep the crystal temperature below 25°C. The only difference between CO and CO_2 adsorption was that a factor of 5 higher pressure of CO_2 gas was needed to form the same structure. Thus we will present only the results of the CO adsorption studies.

On the (111) surface a $(\sqrt{3}\times\sqrt{3})$ R30° is formed at an exposure of about 0.5L (Fig. III-11b). Upon increasing the CO partial pressure to 1×10^{-6} torr, the LEED pattern shown in Fig. III-11c is obtained. This structure is designated as a "split" (2×2) and can be explained by double diffraction from a hexagonal overlayer of CO on the (111) surface. This is shown schematically in Fig. III-12. By a further increase of the pressure to 1×10^{-5} torr and with the crystal temperature below 25°C, the split (2×2) condensed into a (2×2) structure. To produce a (2×2) structure on Rh(111) from a hexagonal overlayer requires a diameter of about 3.2 Å for each CO molecule. The real space representations of the

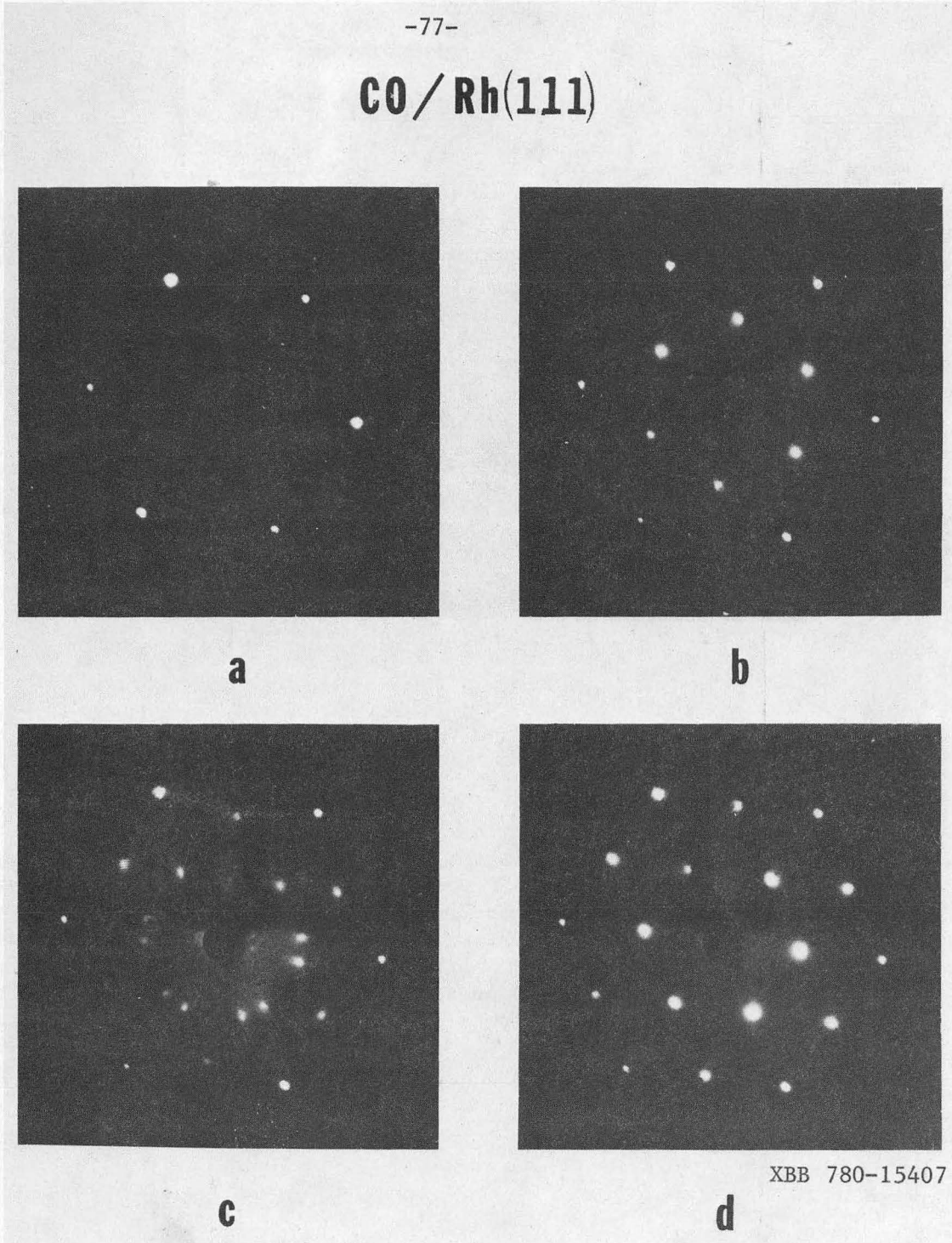

Figure III-11. LEED patterns from (a) clean Rh(111) at 88 eV; and (b) a $(\sqrt{3}\times\sqrt{3})$ R30°- CO structure at 75 eV; (c) a split (2×2)-CO structure at 65 eV and (d) a (2×2)-CO structure at 65 eV on Rh(111).

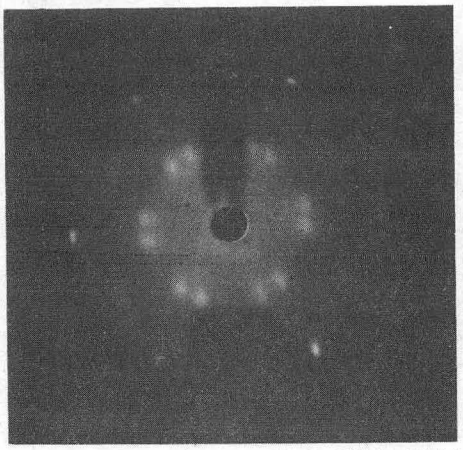

XBB 776-6148

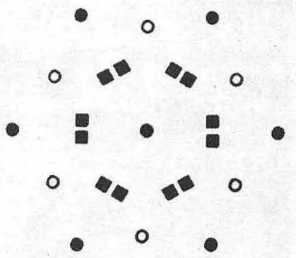

A B

Figure III-12. (A) LEED pattern of the split (2×2) structure of CO on Rh(111) at 71 eV. (B) Diagram of the LEED where ● are diffraction spots from the rhodium lattice, o are diffraction spots from the CO overlayer and ■ are the double diffraction spots from both the rhodium and CO lattices.

$(\sqrt{3}\times\sqrt{3})$ R30° and (2×2) structures are shown in Fig. III-13. The position of the CO molecules in these structures was determined by high resolution ELS studies.[35] The order-order transition between the split (2×2) and (2×2) structures was reversible. The split (2×2) could be generated from the (2×2) by either reducing the CO partial pressure to 1×10^{-8} torr or heating the crystal to 50°C. Exposing the (111) surface to 800 torr of CO by using the isolation cell[66] produced no new surface structures but demonstrated the importance of the crystal temperature. If the crystal temperature was above 50°C only a split (2×2) was observed, even after the high pressure exposure.

Adsorption of CO on the (100) surface initially forms a c(2×2) structure. At exposures above 1L the c(2×2) structure is compressed into a hexagonal overlayer of CO yielding the LEED pattern shown in Fig. III-14a. This pattern is designated as a "split" (2×1) can again be explained by double diffraction. This is diagrammed in Fig. III-14b. Some complex streaking was observed as the CO overlayer was compressing from the c(2×2) structure into the split (2×1). As in the case of the (2×2) structure on Rh(111), the split (2×1) requires the diameter of CO molecules in the hexagonal overlayer to be about 3.2 Å. The real space representations of the c(2×2) and split (2×1) structures are shown in Fig. III-15.

The thermal desorption spectra for CO on the (111) and (100) surfaces are shown in Figs. III-16 and III-17. Molecular CO was the only species detected desorbing and no evidence was found for dissociation of

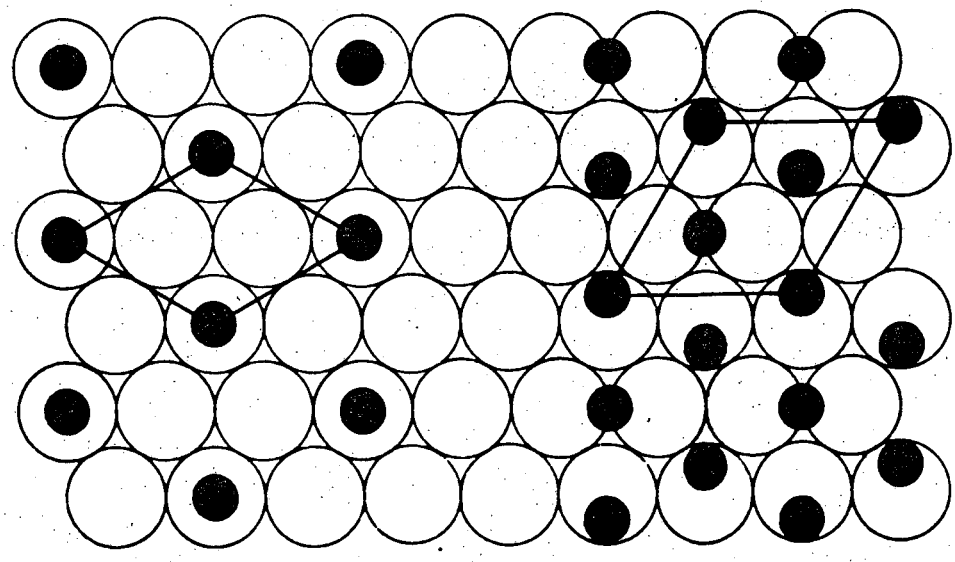

Figure III-13. Real space models for the ($\sqrt{3}\times\sqrt{3}$) R30° and (2×2) CO surface structures. Open circles are Rh atoms with a nearest neighbor distance of 2.69 Å. The CO molecules are represented by the filled circles and the ($\sqrt{3}\times\sqrt{3}$) R30° and (2×2) unit cells are shown.

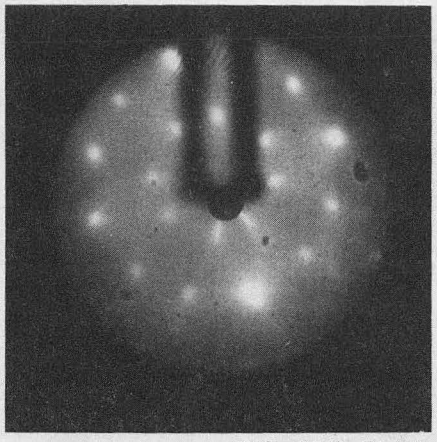

XBB 776-6149

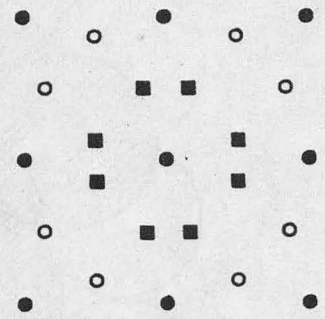

A B

Figure III-14. (A) LEED pattern of the split (2×1) CO surface structure on Rh(100) at 59 eV. (B) Diagram of the LEED pattern where ● are diffraction spots from the rhodium lattice, o are diffraction spots from CO overlayer and ■ are the double diffraction spots from both the rhodium and CO lattices. There are two domains present in this pattern.

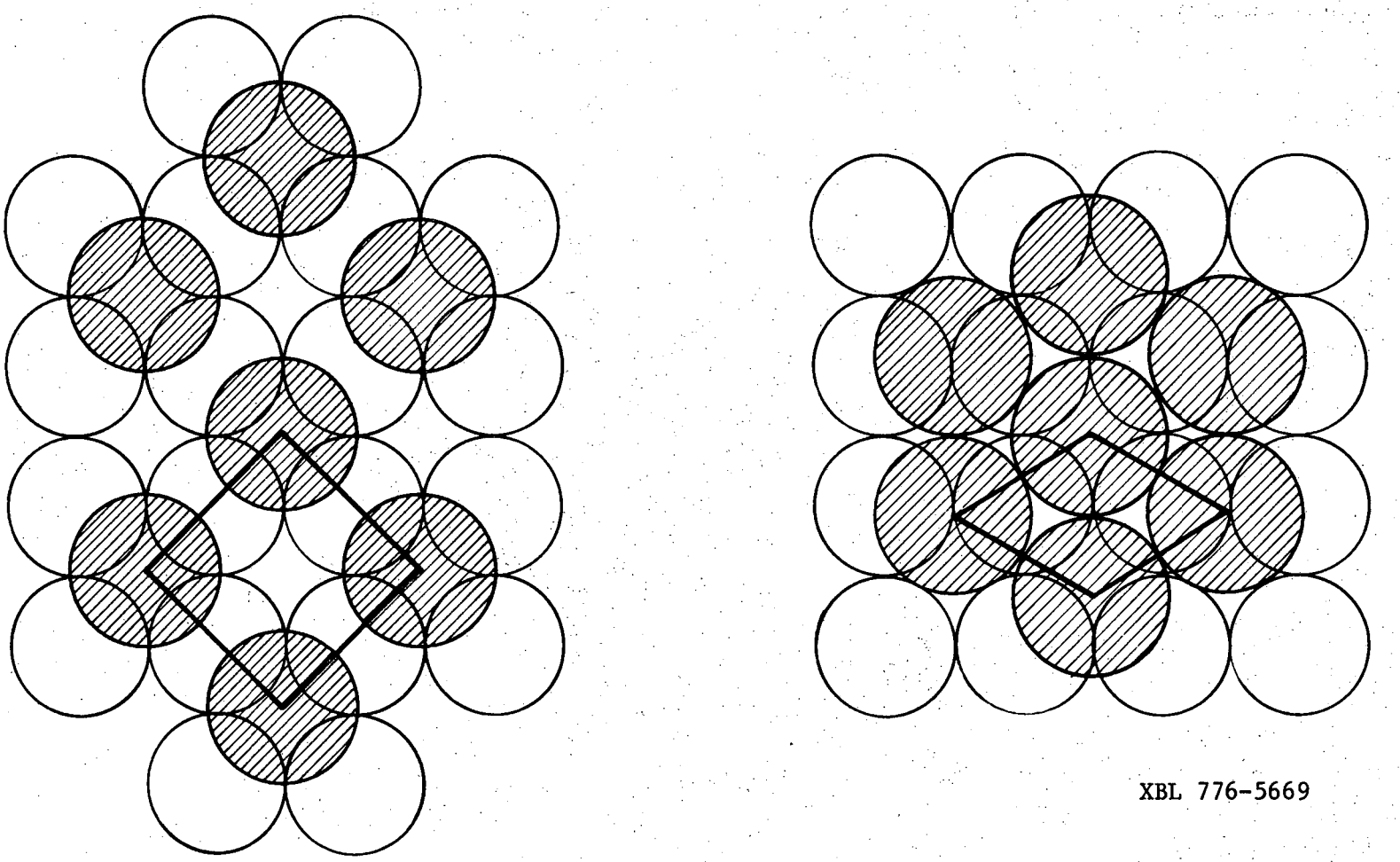

Figure III-15. Real space models for the CO surface structures on Rh(100). The diameter of the CO molecules is 3.2 Å and the rhodium nearest neighbor distance is 2.69 Å. The CO molecules have been arbitrarily placed in the 4-fold hollow and bridge sites.

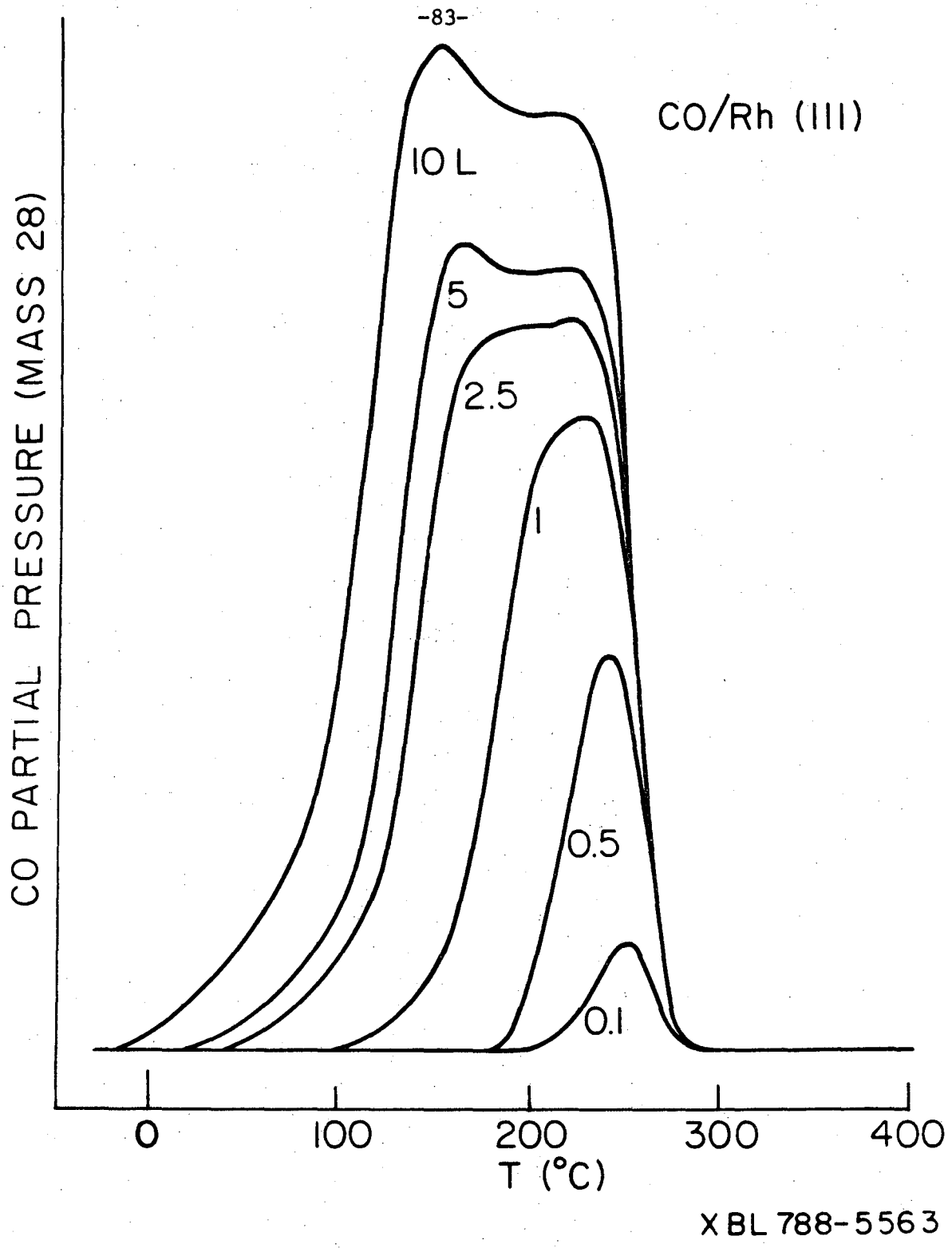

Figure III-16. CO TDS spectra from the Rh(111) surface.

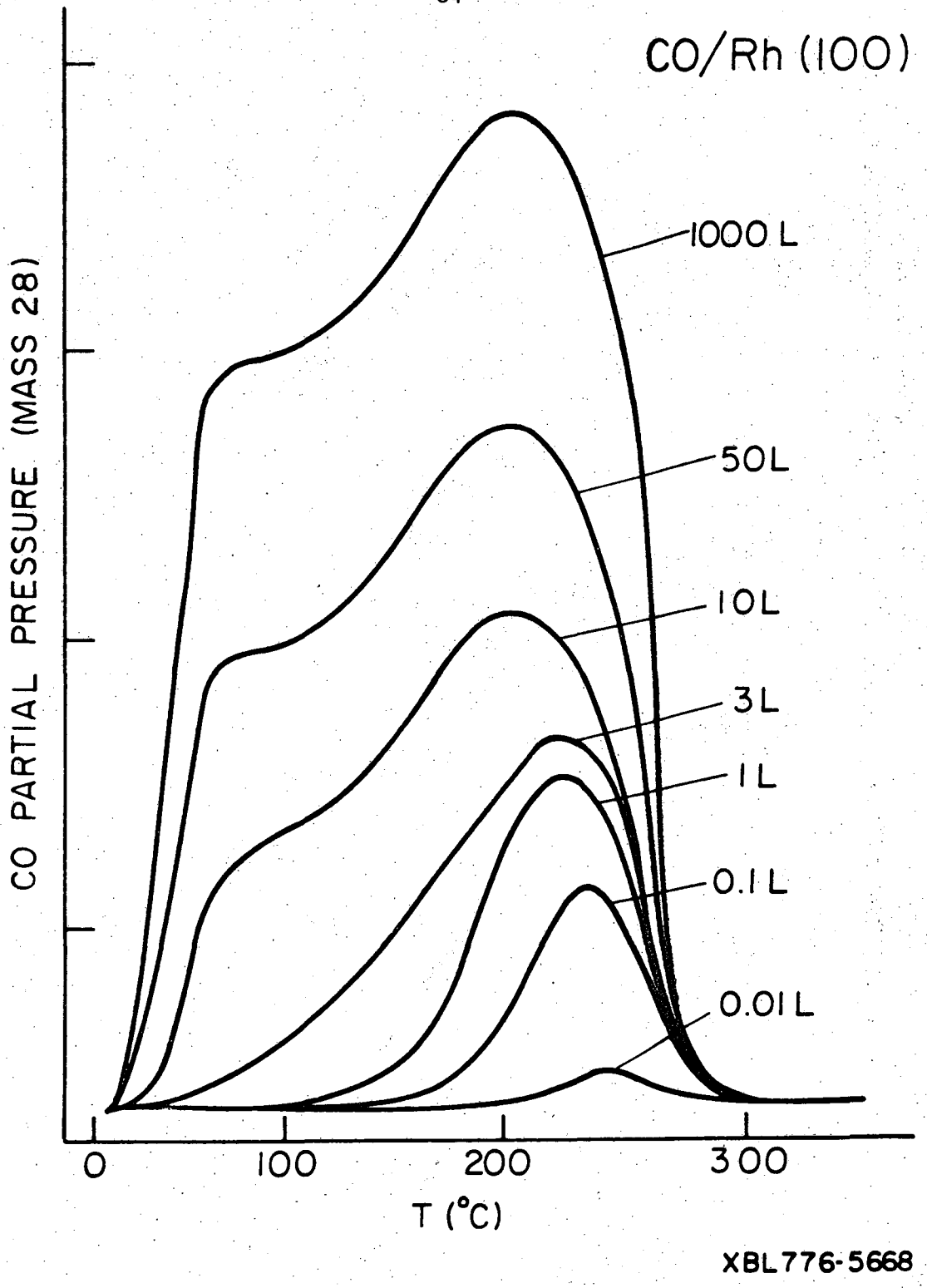

Figure III-17. CO TDS spectra from the Rh(100) surface.

CO on either surface. The peak maximum decreases from 250°C to 225°C as the CO exposure is increased. As the exposure was increased above 1L, a shoulder began developing on the left side of the original peak. By an exposure of 5L the shoulder had become a resolvable peak. The appearance of this shoulder appears at the same exposure as the onset of compression of the CO overlayer observed by LEED. As stated previously, thermal desorption spectra for CO and CO_2 were identical. No oxygen, CO_2 or extra CO desorption peaks were ever observed from CO_2 adsorption. The extra oxygen atom may penetrate the rhodium lattice upon adsorption or heating but further studies are needed to determine the fate of the oxygen atom.

Adsorbed CO was not displaced by H_2, O_2 or NO at room temperature. No evidence for changes in either the thermal desorption spectra or LEED patterns were found by exposing adsorbed CO to gaseous hydrogen.

The adsorption of CO on rhodium correlates well with previous adsorption studies of CO on other transition metal surfaces. The general pattern of CO adsorption is to initially form a low coverage surface structure which then compresses into hexagonally close packed overlayer of CO molecules as the CO exposure is increased.

CO readily adsorbed on both rhodium surfaces as long as they were scrupulously clean as determined by AES (Fig. III-2). On the clean surfaces we found no evidence for dissociation of the CO molecules and the structures formed were stable in the electron beam of the LEED gun ($\sim$1 μAmp). If more than 10% of a monolayer of carbon was present on the surface, the LEED patterns rapidly disordered when exposed to the electron beam.

The $(\sqrt{3}\times\sqrt{3})$ R30° low coverage CO structure ($\theta = 1/3$) seen on Rh(111) has also been observed as the low coverage structure for CO on Ni(111),[105,106] Pd,[107] Pt,[108] Ir(111),[109-111] and Ru(001).[25,112] The split (2×2) structure corresponds to a coverage of $\theta = 0.6$ and has also been observed for CO on Pd(111).[107] On Pd(111) the split (2×2) structure is the highest coverage observed which is in contrast to Rh(111) where the split (2×2) condenses into a (2×2) structure with a coverage of $\theta = 0.75$. Compression of the CO overlayer has been observed on Ni(111),[105,106] Pd(111),[107] Pt(111)[108] and Ir(111).[109-111] A (2×2) structure for CO on Ru(001) has been observed,[25] but a more recent study[112] states that the (2×2) is electron beam induced and that increasing the coverage above the $(\sqrt{3}\times\sqrt{3})$ R30° structure produces only disorder in the LEED pattern. In a previous study of Rh(111), Grant and Haas[25] reported a (2×2) structure of CO and a split (2×2) for CO_2 but offered no explanation of these structures. As stated earlier, no difference was found in these studies between CO and CO_2 adsorption as both gases gave identical results. The results of a recent study of CO on Rh(111) by Neumann are in agreement with the present results.[113]

On the Rh(100) surface a c(2×2) structure was the low coverage structure ($\theta = 0.5$) observed for CO adsorption. The c(2×2) structure has also been observed as the low coverage structure for CO adsorbed on Ni(100)[114] and Cu(100),[115] and on the unreconstructed (100) faces of Ir[116] and Pt[117]. On Rh(100) the c(2×2) structure compresses into a hexagonal overlayer at higher CO exposures to give a split (2×1) pattern with a coverage of $\theta = 0.83$. The c(2×2) structures on Ni(100)[114] and Cu(100)[115] were also found to compress into a hexagonal overlayer.

CO on Pd(100)[118] also has a compression structure. The present results are again in disagreement with Tucker's results for CO on Rh(100).[24] As pointed out above, the cleanliness of his sample is questionable. This is reinforced by the fact that his diffraction patterns were electron beam sensitive, while in the present studies this was only found to be the case when the adsorption was carried out on a contaminated surface. The CO structures were stable under the electron beam when adsorbed on a clean surface.

The thermal desorption spectra for CO on Rh(111) and Rh(100) are similar to spectra published for CO on Ni(111),[106] Pd(111),[107] Ir(111)[109-111] and Ru(001).[112] The spectra suggest that CO desorbs with first order kinetics but has an activation energy of desorption, E_d, which decreases with increasing coverage. This may be explained by the fact that as the CO overlayer compresses the repulsive forces between CO molecules will increase giving a decrease in E_d. The activation energies of desorption of CO on Ni, Pd, Rh, Ir and Ru are listed in Table III-9. These activation energies at CO exposures of 5L have been calculated following Redhead[90] by assuming first order desorption kinetics and a pre-exponential factor of 10^{13} sec^{-1}.

As stated above, there was substantial evidence for the dissociation of CO_2 into adsorbed CO on both rhodium surfaces. This is an important first step in the generation of hydrocarbons from CO_2-H_2 gas mixtures over metal catalysts. It has previously been shown that rhodium foils produce CH_4 from CO_2 and H_2 at a pressure of 800 torr.[11]

Table III-9. Activation energy for desorption, E_d, of CO on Ni, Pd, Ir and Ru. Calculated assuming first order desorption kinetics and a pre-exponential factor of 1×10^{13} sec^{-1}. The values of E_d are for the highest binding state at exposures of 5L (1L = 1×10^{-6} torr°sec).

Surface	E_d (kcal/mole)	Reference
Ni(111)	26	(106)
Pd(111)	30.1	(107)
Rh(111)	30	This study
Rh(100)	30	This study
Ir(111)	29.5	(102)
	32	(111)
Ru(001)	28	(112)

4) Nitric Oxide

NO adsorbed with a high sticking probability on both surfaces at 25°C, forming a c(2×2) structure on Rh(100) and c(4×2) and (2×2) structures on Rh(111). The c(4×2) structure (Fig. III-18) was formed at about 0.1L and then was converted to (2×2) structure upon increasing the exposure above 1L. During this conversion complex streaking of the LEED pattern occurred. The Rh(111)-(2×2) structure disordered at a low temperature (50°C) and was best observed at room temperature or below. TDS detected N_2 (mass 28), NO (mass 30), O_2 (mass 32) and N_2O (mass 44) desorption after exposing the Rh(111) surface to NO. The N_2, NO and N_2O desorption traces are shown in Fig. III-19. Oxygen desorption from NO adsorption was similar oxygen desorption after O_2 adsorption. At low NO exposures (< 0.5L) no NO desorption was detected, but N_2 desorption was detected. Above 0.5L NO desorption is observed. These results indicate that NO is dissociatively adsorbed below 0.5L and associatively adsorbed above 0.5L with the different desorption traces resulting from the two types of adsorption. The NO desorption peak appears to follow first order desorption kinetics and assuming a pre-exponential factor of 10^{13} sec^{-1} yields a value of 30 kcal/mole for E_d.

The c(4×2) structure is formed during the dissociative adsorption phase of NO adsorption, indicating it is comprised of an overlayer of oxygen and nitrogen atoms. The (2×2) structure is formed during the associative adsorption phase of NO adsorption indicating it is comprised of an overlayer of molecular NO. The LEED results for NO adsorption at 300 K on Rh(111) were similar to results of NO adsorption at 200 K on Pd(111).[119] As on Rh(111) adsorption of NO on Pd(111) initially

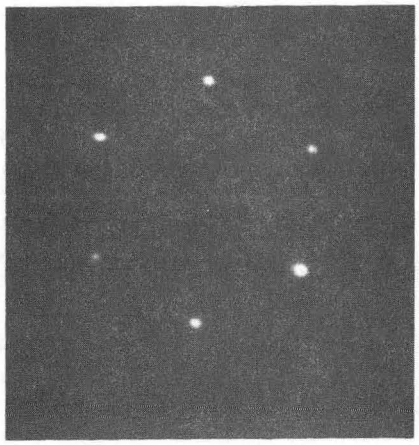

Rh (1 1 1)
76 eV

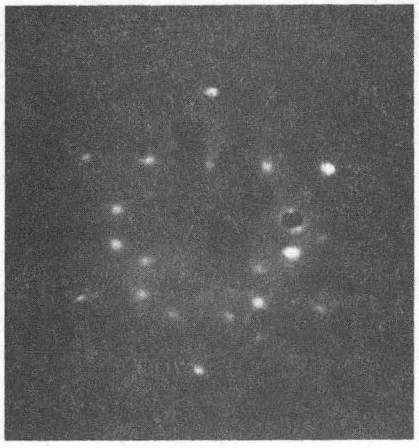

c(4x2)-NO
66 eV

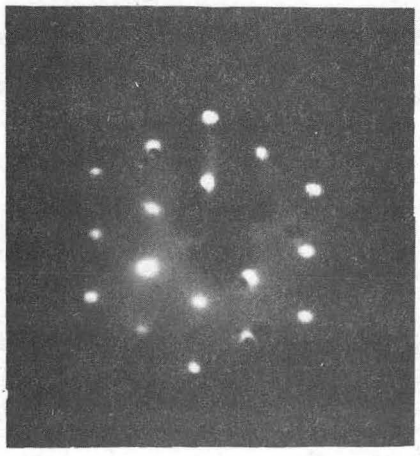

(2x2)-NO
81 eV

XBB 771-84

Figure III-18. LEED patterns formed by NO adsorption on the Rh(111) surface.

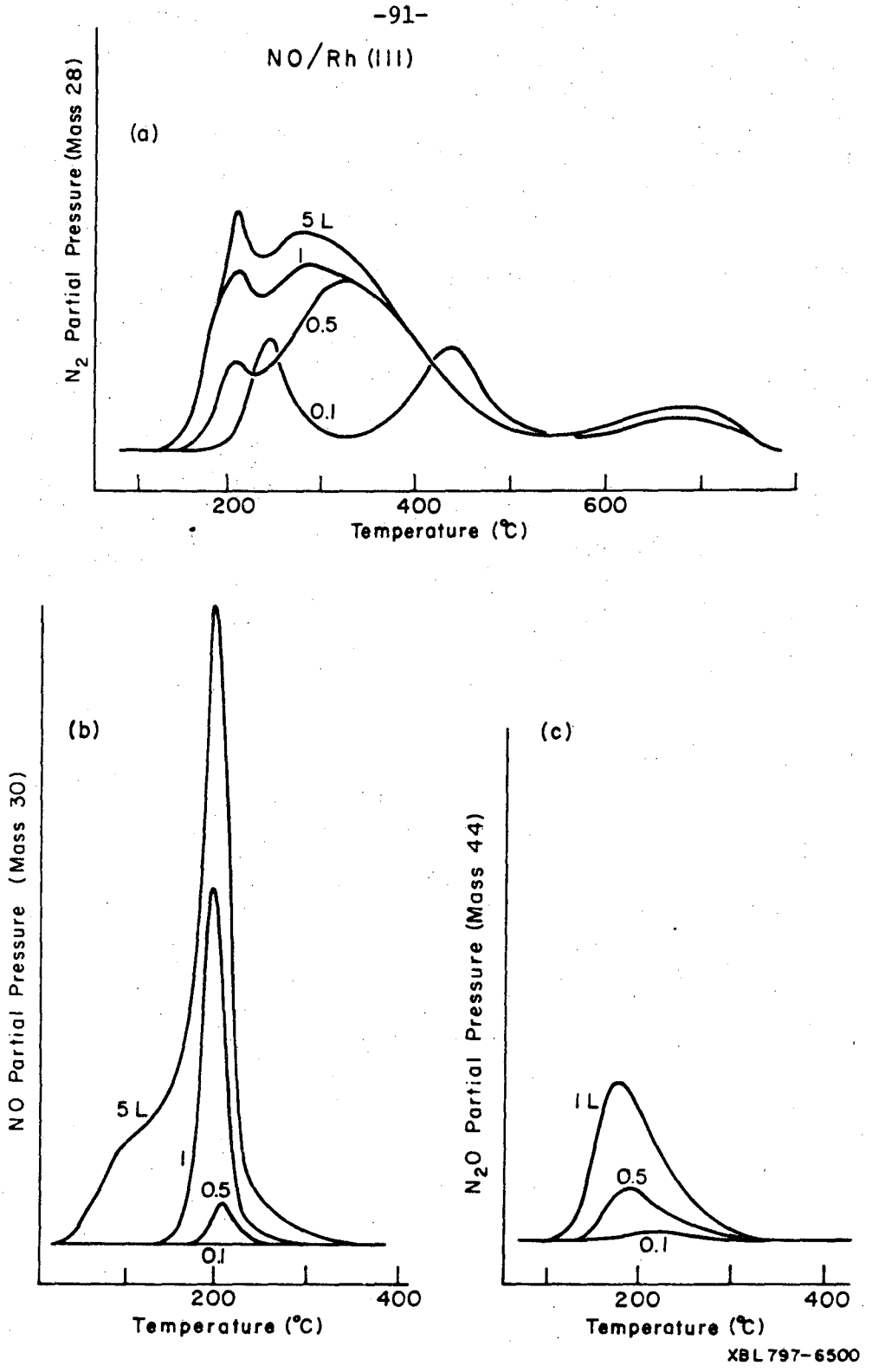

Figure III-19. TDS spectra obtained from NO adsorption on Rh(111). (a) N_2 (mass 28) desorption; (b) NO (mass 30) desorption; and (c) N_2O (mass 44) desorption.

forms a c(4×2) structure which then converts into (2×2) structure at higher NO exposures. The model proposed for Pd(111)[119] has coverages of $\theta = 0.5$ for the c(4×2) structure and $\theta = 0.75$ for the (2×2) structure with the (2×2) structure being a hexagonal overlayer of NO. An initial c(4×2) structure has also been seen for NO adsorbing on Ni(111) at 300 K, which is then converted into a hexagonal structure at higher NO coverages.[120] The formation of these structures are similar to the compression of CO overlayers on these metals. Because of the above similarities it is likely that NO also forms a hexagonal overlayer on Rh(111).

5) Ethylene and Acetylene

Exposing the clean Rh(111) surface (Fig. III-20a) below -30°C to 1.5L of either C_2H_2 or C_2H_4 results in the appearance of sharp half order diffraction spots (Fig. III-20b) from a (2×2) surface structure. The half order diffraction spots were very sensitive to exposure. They were visible by 1L but did not become sharp and intense until 1.5L and then immediately began disordering above 1.5L. Because of this exposure sensitivity a 15 sec exposure of 1×10^{-7} torr C_2H_4 or a 150 sec exposure of 1×10^{-8} C_2H_2 were used to produce optimum (2×2) structures.

The diffraction pattern from a c(4×2) surface structure (Fig. III-20c) could be generated from the (2×2) structures without additional hydrocarbon exposure. For adsorbed C_2H_4 the transformation occurred by slowly warming the crystal room temperature in vacuum. Too rapid of heating resulted in formation of a disordered c(4×2) structure (broad diffuse diffraction features and some streaking) thus the c(4×2) structure

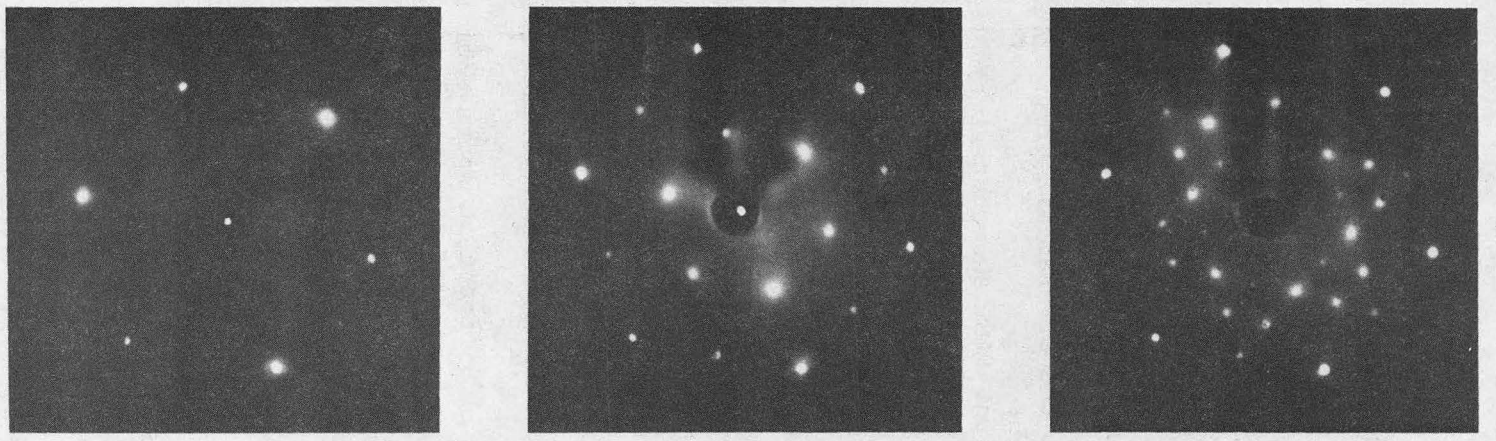

XBB 788-10161

Figure III-20. LEED patterns from surface structures produced by either C_2H_4 or C_2H_2 adsorption on Rh(111). (a) clean Rh(111) at 92.5 eV; (b) Rh(111)-(2×2) at 74 eV; (c) Rh(111)-c(4×2) at 67.5 eV.

was formed by removing the LN_2 dewars from the heating leads and allowing the crystal to warm up to room temperature, over a period of 1-2 hours. For adsorbed C_2H_2 even the slow warmup of 1-2 hours resulted in a disordered c(4×2) structure. To form a well ordered c(4×2) structure from adsorbed C_2H_2 the crystal had to be annealed for 4 minutes at 0°C in 1×10^{-8} torr of H_2 with the mass spectrometer filaments on. These filaments were close to the crystal and provided the surface with a good source of atomic hydrogen. AES showed that the carbon coverage for the (2×2) C_2H_2 and C_2H_4 structures was the same and remained constant during the transformation to the c(4×2) structures. This transformation appeared to be irreversible because once the c(4×2) structures were formed the crystal could be cooled to -63°C with no visible changes in the diffraction pattern. The c(4×2) structures could only be altered by heating the crystal above 150°C which caused the structures to irreversibly disorder. The adsorption of C_2H_4 and C_2H_2 at 25°C yielded a c(2×2) structure on the (100) surface. The c(2×2) diffraction spots from the hydrocarbon structures were diffuse, but upon heating to 200°C they become very sharp, forming a well ordered carbon c(2×2) structure. The surface carbon generated from the hydrocarbon decomposition on either surface prevented readsorption of either C_2H_4 or C_2H_2. Upon flashing the crystal to 800°C, the surface carbon diffused into the near surface layers and further reassorptions were then possible. After several doses of the hydrocarbons, the surface region appeared to become saturated with carbon and ordered structures appeared on the (111) surface. These structures are described in more detail in III-B-6.

The hydrogen desorption spectra from C_2H_4 and C_2H_2 adsorption on Rh(111) are shown in Fig. III-21. The hydrocarbons were adsorbed at -30°C and the crystal was heated at a rate of 40 deg/sec. Desorption of molecular C_2H_4 and C_2H_2 occurred at ~ 100°C but the amount of hydrocarbon desorbed was less than 1% of the hydrogen desorbed, thus the vast majority of the adsorbed hydrocarbons decomposed instead of desorbing. The hydrogen desorption spectra from C_2H_2 adsorption (Fig. III-21b) has one major peak at 175°C followed by a continuous evolution of hydrogen until 450°C. The hydrogen desorption spectra from C_2H_4 adsorption (Fig. III-21a) has 3 peaks followed by the continuous hydrogen evolution.

The hydrogen desorption spectra from the (2×2) and c(4×2) hydrocarbon structures on Rh(111) are shown in Fig. III-22. Traces a and d are from the (2×2) structures and traces b and c are from the c(4×2) structures. Desorption traces a and b are similar, but trace b has an additional desorption peak at 75°C. This peak results from the presence of chemisorbed hydrogen on the surface (see Fig. III-8) since the crystal is exposed to hydrogen during the (2×2) to c(4×2) transformation. Desorption trace c is similar to traces a and b and the area under this trace is significantly less than the area under trace d, indicating C_2H_4 is partially dehydrogenated during the (2×2) to c(4×2) transformation. These TDS and LEED results indicate the possibility of molecular rearrangement of the hydrocarbons on the Rh(111) surface.

Detailed investigations of the Pt(111) - ethylene and acetylene systems have been carried out by high resolution ELS,[121,122] LEED surface crystallography,[123-125] ultra-violet photoelectron spectroscopy (UPS)[126,127] and TDS.[127] Below room temperature the hydrocarbons are

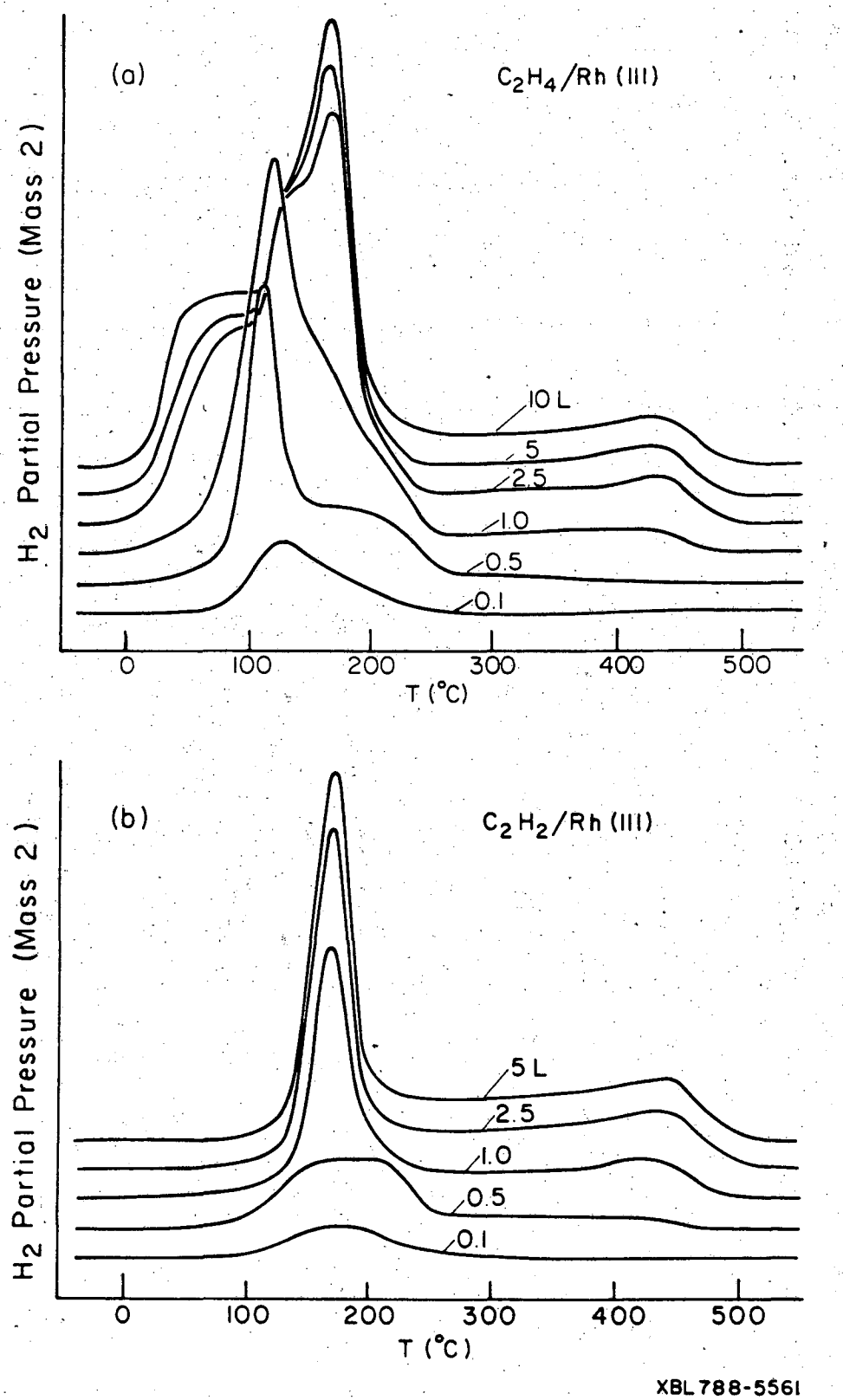

Figure III-21. Hydrogen desorption spectra obtained from the adsorption of (a) C_2H_4 and (b) C_2H_2 on Rh(111). The heating rate was 40°/sec.

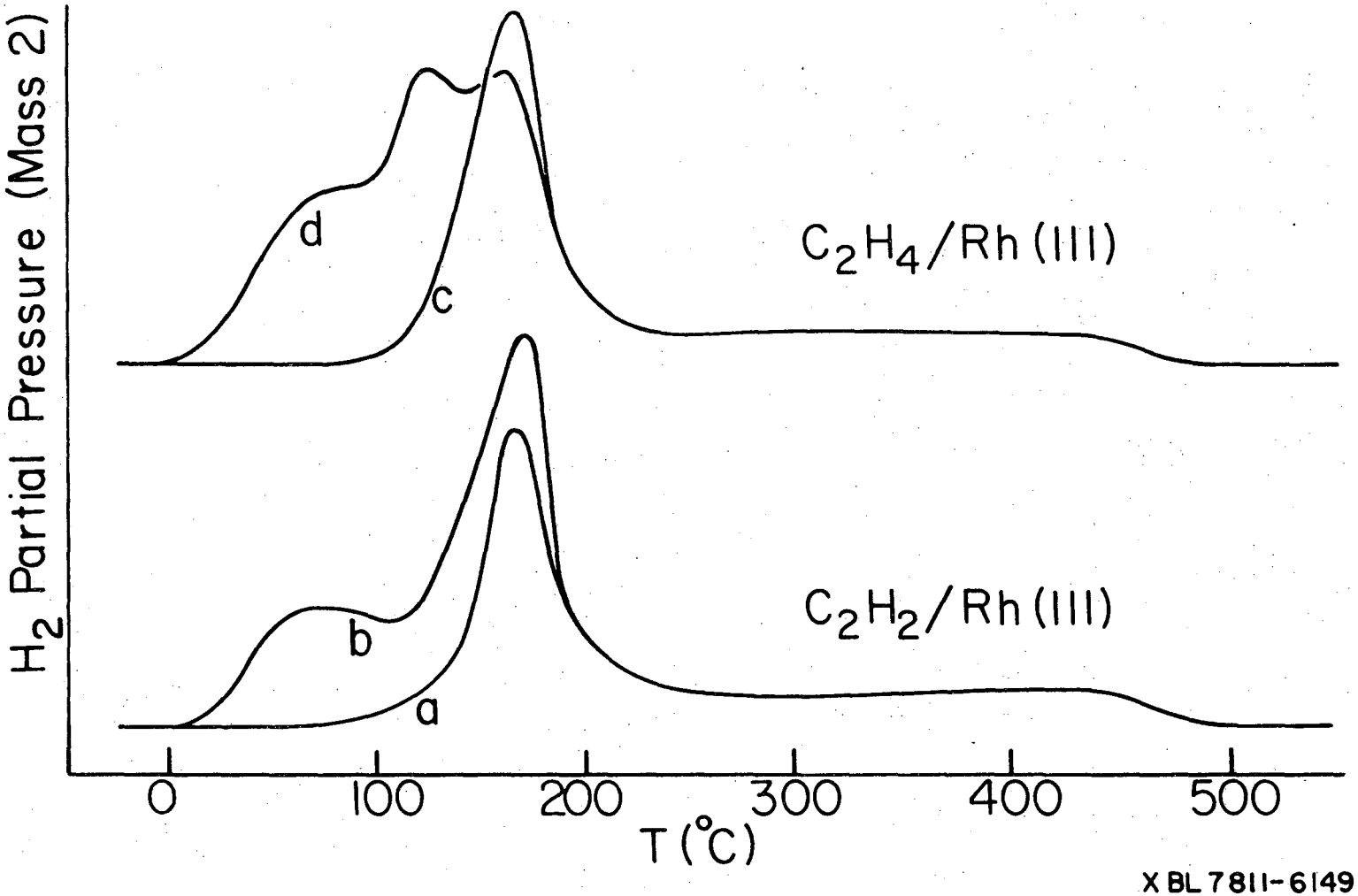

Figure III-22. Hydrogen desorption from the (a) (2×2) and (b) c(4×2) structures formed during C_2H_2 adsorption on Rh(111) and from the (c) c(4×2) and (d) (2×2) structures formed during C_2H_4 adsorption on Rh(111).

associatively adsorbed and when the crystal is heated they undergo a molecular rearrangement. Ethylidyne,[125] ethylidene[121,122] and a vinyl species[127] have been proposed as possible structures of the high temperature species. ELS[128,129] and UPS[130] investigations of the Ni(111)-ethylene and acetylene systems have also been carried out. On Ni(111) associative adsorption of these hydrocarbons occurs at low temperatures. When the crystal is heated the C-C bond of adsorbed C_2H_2 is broken before the C-H bonds producing a CH species on the surface and adsorbed C_2H_4 is dehydrogenated to C_2H_2 which then undergoes C-C bond breaking to form the CH species. In light of the Ni(111) and Pt(111) results further studies by high resolution ELS[36] and LEED surface crystallography[131] will be carried out on the Rh(111)-ethylene and acetylene systems to determine the details of the hydrocarbon rearrangements on this surface.

6) Carbon

The best method of generating carbon surface structures on rhodium was to saturate the near surface region with carbon by heating the crystals at 800°C for 10 mins in 5×10^{-7} torr of C_2H_4 or C_2H_2. When the surfaces were cooled, and the hydrocarbon pumped away, graphite rings were seen on the (100) face and a (12×12) coincidence lattice structure on the (111) face. If these surfaces were reacted with oxygen (5×10^{-7} torr, 800°C) for short periods, the graphite rings on the (100) surface disappeared and the c(2×2) structure reappeared as carbon was removed. As carbon was removed from the (111) surface, a sequence of ordered carbon structures was observed and then finally the clean (1×1) pattern.

The sequence observed was:

$$(12\times12) \leftrightarrow (2\sqrt{3}\times2\sqrt{3})R30° \leftrightarrow (\sqrt{19}\times\sqrt{19})R23.4° \leftrightarrow (2\times2)R30° \leftrightarrow (8\times8)$$
coincidence lattice
$$\leftrightarrow \text{Clean Rh(111)-(1}\times\text{1)}.$$

These patterns are shown in Fig. III-23. Each structure was stable over a range of near surface carbon concentrations, and was only ordered after flashing to 1000°C. In fact the sequence of structures was completely reversible by either subtracting carbon in the near surface layers by reaction with O_2 (5×10^{-7} torr, 800°C) or adding carbon by decomposition of C_2H_4 (5×10^{-7} torr, 800°C). Only the near surface layers were participating in the equilibrium. A gradual reduction of surface carbon coverage and change in the structures was observed after prolonged heating at 1000°C (near surface carbon diffusing into the bulk).

The (12×12) structure can be explained by postulating the existence of a basal plane of graphite on the rhodium surface. Using a carbon-carbon distance of 1.42 Å[132] and a rhodium nearest neighbor distance of 2.69 Å,[133] it can be calculated that the graphite overlayer will come in registry every 11 Rh spacings. The predicted (11×11) structure is in good agreement with the (12×12) lattice observed experimentally. The coincident (12×12) lattice would have 13 graphite unit cells over a distance of 12 rhodium atoms. A drawing of a graphite unit cell on the (111) face of rhodium is shown in Fig. III-24. A (9×9) carbon structure has been seen on Ir(111).[102] A carbon structure has also been observed on Ru(001).[25] Although it was not indexed, from

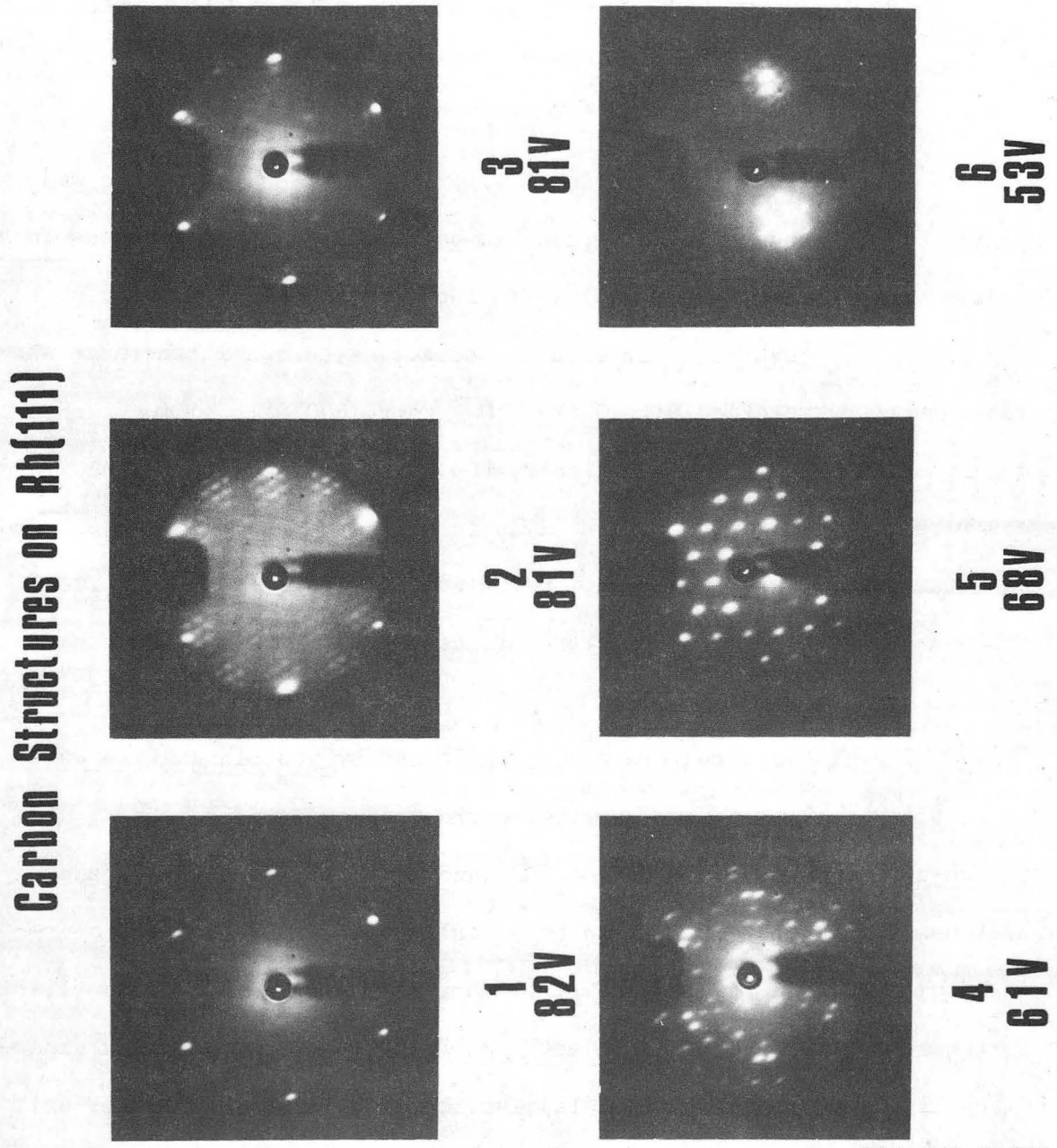

XBB 760-10650

Figure III-23. LEED patterns of the carbon surface structures observed on Rh(111). (1) Clean Rh(111)-(1×1), (2) (8×8) structure, (3) (2×2) R30° structure, (4) ($\sqrt{19}\times\sqrt{19}$) R23.4° structure, (5) ($2\sqrt{3}\times2\sqrt{3}$) R30° structure and (6) (12×12) coincidence lattice.

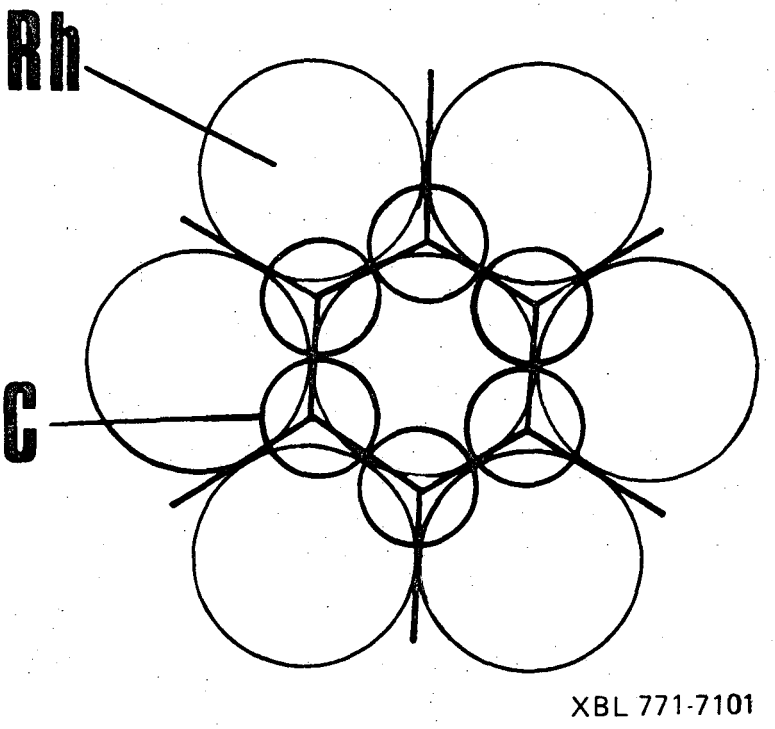

Figure III-24. Real space model for the unit cell of the graphite basal plane on Rh(111).

the LEED pattern presented in the paper, it can be estimated to be a (12×12) structure. A (1×1) structure has been observed for graphite on Ni(111).[134] Both monolayer and multilayer graphite structures were seen on Ni(111). Intensity vs voltage and line shape of the carbon Auger peak were used to show the (1×1) structure was due to a graphite overlayer and not the Ni surface. A summary is given in Table III-10 of the experimentally observed structures along with the predicted graphite coincident lattices and calculated C-C bond lengths. Table III-10 shows that the experimental results for Rh, Ru, Ir and Ni are in very good agreement with the results predicted from a basal plane of graphite on the hexagonal faces of these metals. It should be noted that Ir(111) and Ru(001) gave only one carbon structure while Rh(111) produced a series of five ordered structures indicating an interesting equilibrium between ordered surface carbon and carbon in the near surface region. The lower coverage carbon structures are not as easily explained but could be due to remnants of the original graphite overlayer. These low coverage carbon structures have not been seen on other transition metals. Their existence on the Rh(111) surface show unique and complex aspects of carbon-rhodium surface chemistry.

In contrast to the (111) face, only two carbon structures, a c(2×2) and graphite rings, were seen on (100) face of rhodium. A c(2×2) carbon structure has also been generated from C_2H_4 decomposition on Ir(100).[135] A "quasi" c(2×2) carbon structure and graphite rings have been observed on Ni(100).[136] Graphite rings have also been observed on Pt(111) and (100) surfaces.[137]

Table III-10. Predicted and experimental graphite structures.

Metal	Crystal Face	Nearest Neighbor Distance (Å)[a]	Predicted Structure[b]	Experimental Structure	Calculated C-C Bond Lenght from Experimental Structure (Å)	Reference
Rh	(111)	2.69	(11×11)	(12×12)	1.43	This study
Ru	(001)	2.65	(13×13)	(12×12)	1.41	(25)
Ir	(111)	2.71	(10×10)	(9×9)	1.41	(102)
Ni	(111)	2.49	(1×1)	(1×1)	1.44	(134)

[a] From Reference 133.

[b] Based on C-C bond length of 1.42 (132).

C. The Chemisorption of Small Molecules on the Stepped Rhodium (755) and (331) Surfaces

The surface structures which were observed in the investigations on the two Rh stepped surfaces are summarized in Table III-11. Also included in Table III-11 are the structures reported for the same adsorbates on the Rh(111) surface. In Table III-12 the surface structures observed on the Rh(S)-[6(111)×(100)] surface are compared with surface structures reported for the Pt(S)-[6(111)×(100)] and Ir(S)-[6(111)×(100)] surfaces.

1) Hydrogen

The chemisorption properties of hydrogen on the two rhodium stepped surfaces were very similar to those found for hydrogen on Rh(111). Exposing either stepped surface to hydrogen did not noticeably alter their clean (1×1) LEED patterns. Hydrogen was adsorbed as indicated by the TDS spectra shown in Fig. III-25. The spectra from both surfaces were identical so that only the results from the (331) surface are shown in Fig. III-25. The hydrogen desorption peak is slightly asymmetric, tailing on the high temperature side. The desorption temperature decreases as the exposure is increased indicating second order desorption kinetics.

The LEED and TDS results for hydrogen adsorption on the various rhodium crystal faces were similar to results reported on the Ir(S)-[6(111)×(100)] and Ir(111) surfaces.[102] The only difference was that the high temperature tailing was more pronounced on the Ir(S)-[6(111)×(100)] surface, indicating more strongly bound hydrogen

Table III-11. Surface structures of chemisorbed small molecules on the (111), [6(111)×(100)] and (331) rhodium surfaces.

Gas	Rh(111)	Rh(S)-[6(111)×(100)][a]	Rh(331)[b]
H_2	(1×1) or disordered	(1×1) or disordered	(1×1) or disordered
O_2	(2×1)	(2×1)	2(1d) $\begin{pmatrix}1 & 2\\ 2 & 0\end{pmatrix}$ $\begin{pmatrix}1 & 2\\ 7 & -1\end{pmatrix}$
CO, CO_2	$(\sqrt{3}\times\sqrt{3})$ R30° split (2×2) (2×2)	$(\sqrt{3}\times\sqrt{3})$ R30° (2×2)	$\begin{pmatrix}1 & 2\\ 3 & -1\end{pmatrix}$ $\begin{pmatrix}1 & 2\\ 2 & 0\end{pmatrix}$ "hexagonal"
NO	c(4×2) (2×2)	(2×2)	disordered
C_2H_4, C_2H_2	(2×2) c(4×2)	disordered	$\begin{pmatrix}-1 & 1\\ 3 & 0\end{pmatrix}$
C	(8×8) (2×2) R30° $(\sqrt{19}\times\sqrt{19})$ R23.4° $(2\sqrt{3}\times2\sqrt{3})$ R30° (12×12)	carbon covered Rh surface facets to (111) and (100) planes	graphite overlayer

[a] Structures indexed with respect to (111) terraces.

[b] Structures indexed with respect to (331) unit cell vectors.

Table III-12. Surface structures of chemisorbed small molecules on the [6(111)×(100)] surfaces of rhodium, iridium and platinum.

Gas	Rh(S)-[6(111)×(100)]	Ir(S)-[6(111)×(100)]	Pt(S)-[6(111)×(100)]
H_2	(1×1) or disordered	(1×1) or disordered [102]	2(1d) [77]
O_2	(2×1)	(2×1) [109]	2(1d) [77]
CO	$(\sqrt{3}\times\sqrt{3})$ R30° (2×2)	disordered [109]	disordered [77]
CO_2	$(\sqrt{3}\times\sqrt{3})$ R30° (2×2)		
NO	(2×2)		
C_2H_4	disordered	(2×2) [102]	(2×2) [163]
C_2H_2	disordered	(2×2 [102]	
C	carbon covered Rh surface facets to (111) and (100) planes	disordered [102]	$\begin{pmatrix} 3 & 2 \\ -2 & 5 \end{pmatrix}$ [163] $\begin{pmatrix} 6 & 1 \\ -1 & 7 \end{pmatrix}$ [163] $(\sqrt{19}\times\sqrt{19})$-R23.4° -[137] $(\sqrt{13}\times\sqrt{13})$-R13.9° -[137] $(\sqrt{39}\times\sqrt{39})$-R16.1° -[137]

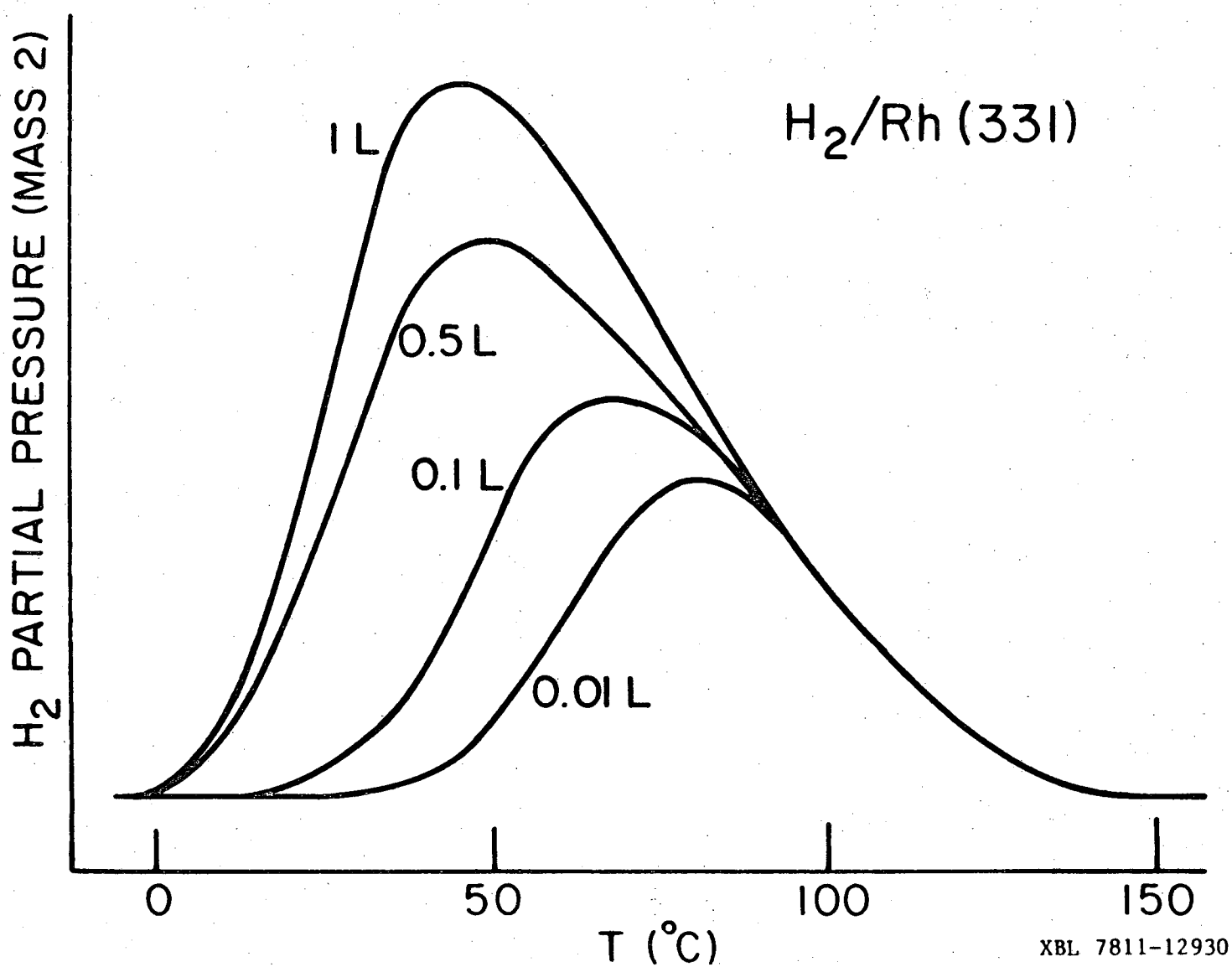

Figure III-25. TDS spectra obtained from adsorbing 0.01L to 1L of hydrogen at 0°C on Rh(331).

at the step sites. Comparison of the TDS results from the Pt(S)-[6(111)×(100)],[155] Pt(S)[6(111)×(111)][155] and Pt(S)-[3(111)×(100)][155] surfaces to the Pt(111) surface[104,155] shows the presence of an additional peak on the stepped surfaces due to more strongly bound hydrogen at the step sites. This additional peak is also detectable on a Pt(111) surface which has been roughened by ion bombardment.[104] From these observations it can be concluded that for hydrogen adsorption platinum surfaces show the most pronounced step effects, rhodium surfaces show no step effects and iridium surfaces are in between these two metals.

2) Oxygen

The oxygen chemisorption properties were markedly different on the two rhodium stepped surfaces. The only step effect detected on Rh(S)-[6(111)×(100)] was enlarged diffraction spots while on Rh(331) more pronounced step effects were seen by both LEED and TDS.

Several ordered oxygen LEED patterns were observed on the Rh stepped surfaces. Exposing the clean Rh(S)-[6(111)×(100)] surface to 1L (1L = 1×10^{-6} torr·sec) of oxygen at 25°C produced the LEED pattern in Fig. III-26b corresponding to a (2×2) surface structure on the (111) terraces. This chemisorbed oxygen structure was very reactive and disappeared in a few seconds when heated to 50°C in 5×10^{-7} torr of H_2. Upon heating the [6(111)×(100)] surface in oxygen (1×10^{-7} torr, 800°C) two new faceted surfaces were seen. First the splitting of the substrate and overlayer doublets decreased by one half as shown in Fig. III-26c. This surface converted back to the clean Rh(S)-[6(111)×(100)]

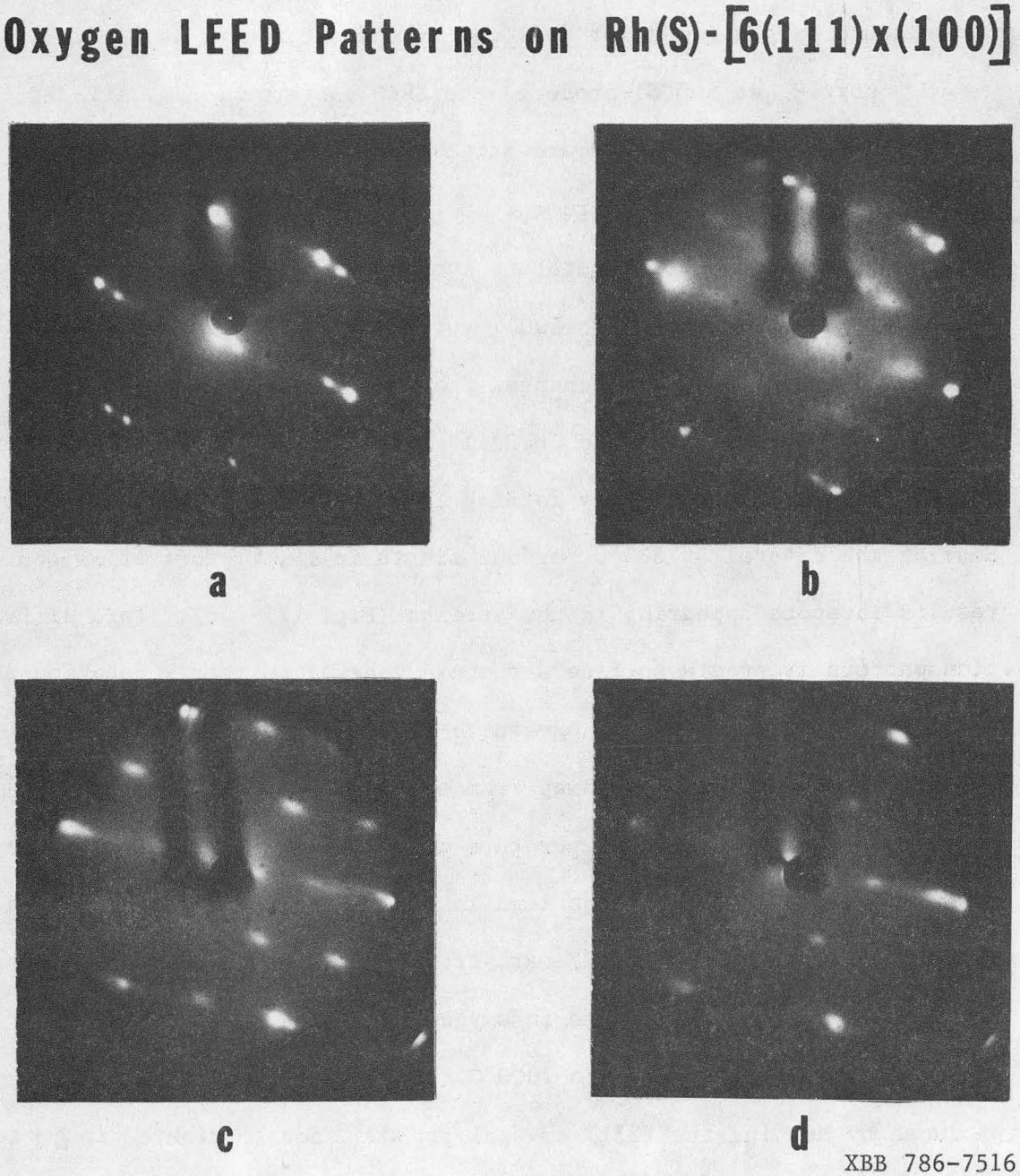

Figure III-26. LEED patterns formed from oxygen adsorption on Rh(S)-[6(111)×(100)].
(a) clean Rh(S)-[6(111)×(100)] at 90 eV; (b) (2×2) structure on Rh(S)-[6(111)×(100)] at 65 eV; (c) (2×2) structure on Rh(S)-[12(111)×2(100)] at 56 eV; (d) (2×2) structure on Rh(111) facets at 52 eV.

surface when heated for 30 seconds in vacuum at 900°C. Further high temperature oxygen treatment followed by a short anneal in H_2 (2 min., 5×10^{-7} torr H_2 at 500°C) produced the LEED pattern in Fig. III-26d where the substrate doublets are streaked and overlayer spots are not split. The oxygen species present in this structure was not easily removed and required high temperature anneals (900°C) in hydrogen to regenerate the clean [6(111)×(100)] surface. The oxygen AES signal increases as the LEED pattern changes from 26a to 26d.

Exposure of the clean Rh(331) surface to 1L of oxygen at 25°C results in half order streaks forming in the LEED pattern (Fig. III-27b). Heating the crystal at 800°C for one minute in 1×10^{-7} torr of oxygen results in spots appearing in the streaks (Fig. III-27c). This diffraction pattern is from a surface structure indexed in matrix notation as a $\begin{pmatrix} 1 & 2 \\ 2 & 0 \end{pmatrix}$. Further heating in oxygen (1×10^{-6} torr, 800°C for 5 min.) results in the spots moving away from the half order positions (Fig. III-27d). Prolonged high temperature oxygen treatment results in the fully developed diffraction pattern in Fig. III-27e. The diffraction pattern in Fig. III-27d and 27e are from a $\begin{pmatrix} 1 & 2 \\ 7 & -1 \end{pmatrix}$ surface structure. The Rh(331) surface was stable in oxygen pressures up to 1×10^{-5} torr and crystal temperatures up to 1000°C. A heavily faceted surface was produced by heating the (331) crystal at 800°C for 15 minutes in ~1 torr of oxygen. Immediately after this treatment the LEED pattern had a very high background intensity with almost no discernable spots, but flashing the crystal to 900°C in vacuum revealed the faceted surface in Fig. III-27g. Removing oxygen from the surface region by annealing the crystal

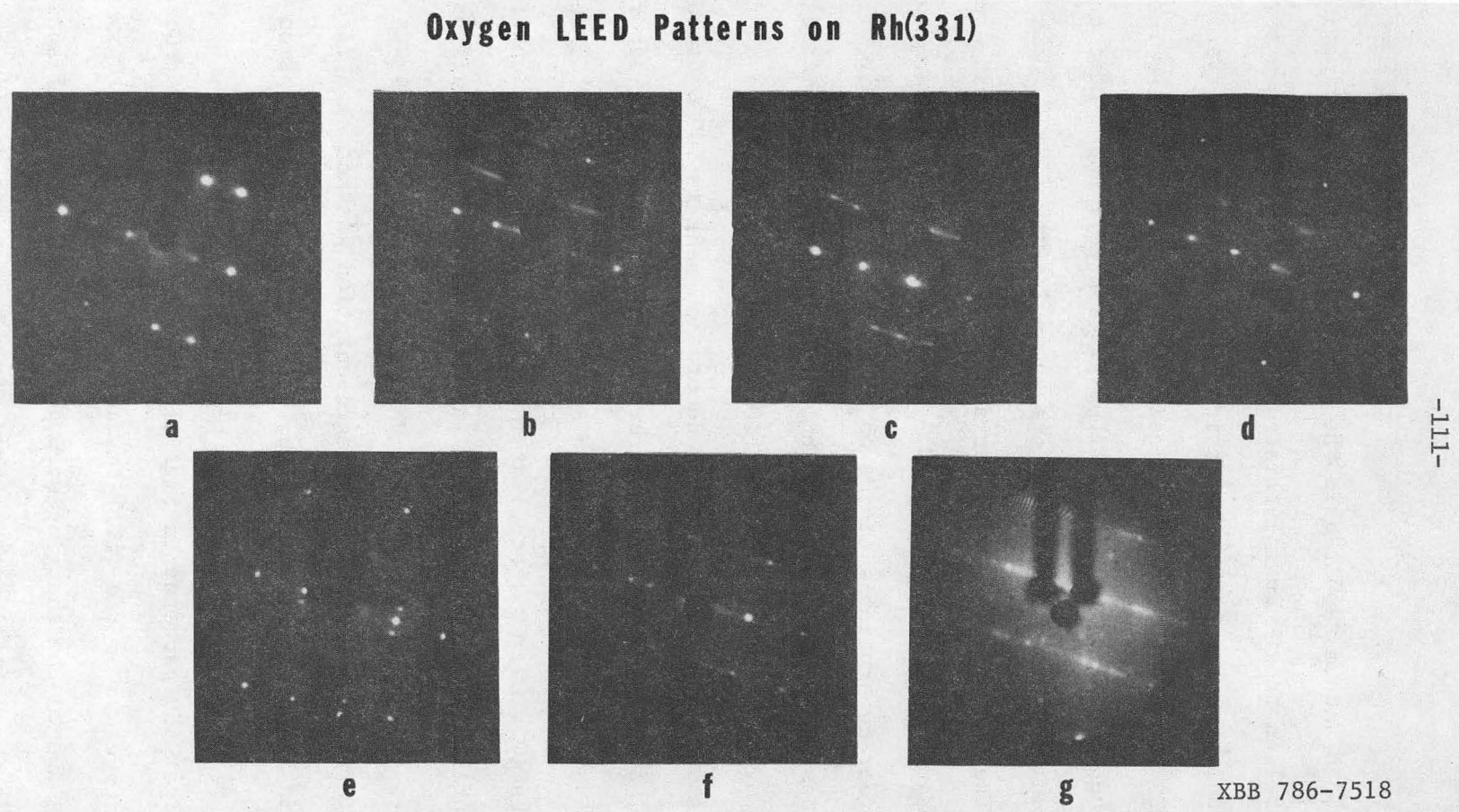

Figure III-27. LEED patterns formed from oxygen adsorption on Rh(331). (a) clean Rh(331) at 93 eV; (b) 2(1d) structure at 68.5 eV; (c) $\begin{pmatrix} 1 & 2 \\ 2 & 0 \end{pmatrix}$ structure at 46 eV; (d) $\begin{pmatrix} 1 & 2 \\ 7 & -1 \end{pmatrix}$ structure forming at 66 eV; (e) full developed $\begin{pmatrix} 1 & 2 \\ 7 & -1 \end{pmatrix}$ structure at 53 eV; (f) $\begin{pmatrix} \frac{1}{2} & 1 \\ 2 & 0 \end{pmatrix}$ structure at 43.5 eV; (g) faceted surface at 33.5 eV.

at 1000°C in vacuum resulted in the faceted surface reverting into a clean (331) surface. During this conversion a $\begin{pmatrix} \frac{1}{2} & 1 \\ -2 & 0 \end{pmatrix}$ oxygen structure corresponding to the LEED pattern in Fig. III-27f was observed. The oxygen AES signal increases upon going from the LEED pattern in Fig. III-27a to the LEED pattern in Fig. III-27g. The real space unit cells of the oxygen structures on Rh(331) are shown in Fig. III-28.

The TDS spectra for oxygen adsorbed on the two clean stepped Rh surfaces are shown in Fig. III-29. Oxygen desorption appears to follow second order desorption kinetics on both surfaces. From Fig. III-29 two differences between the stepped Rh surfaces are apparent. At exposures below 5L oxygen desorption occurs 100°C higher on the (331) surface. At exposures of 5 and 10L the oxygen desorption peak is 100°C broader on the (331) surface. The first two or three times oxygen is adsorbed at 25°C on a clean Rh surface and the crystal flashed to 1000°C, no desorption peaks (O_2, CO, CO_2, etc.) are detected by TDS. After the flashing no oxygen AES signal is detected, implying the oxygen has diffused into the bulk. Following two to three oxygen adsorptions oxygen was detected desorbing from the surface. Oxygen desorption was not seen if carbon was present in the near surface region, but instead a CO desorption peak was detected at $\sim$600°C.

The LEED patterns in Fig. III-26 are from a (2×1) structure or a (2×2) structure on the (111) terraces, with the changes in spot splitting due to the changing step periodicity of the metal substrate. Results on the Rh(111) surface have shown that three domains of a (2×1) structure is the correct structure.[29] In Fig. III-26b the surface is

OXYGEN SURFACE STRUCTURES ON Rh(331)

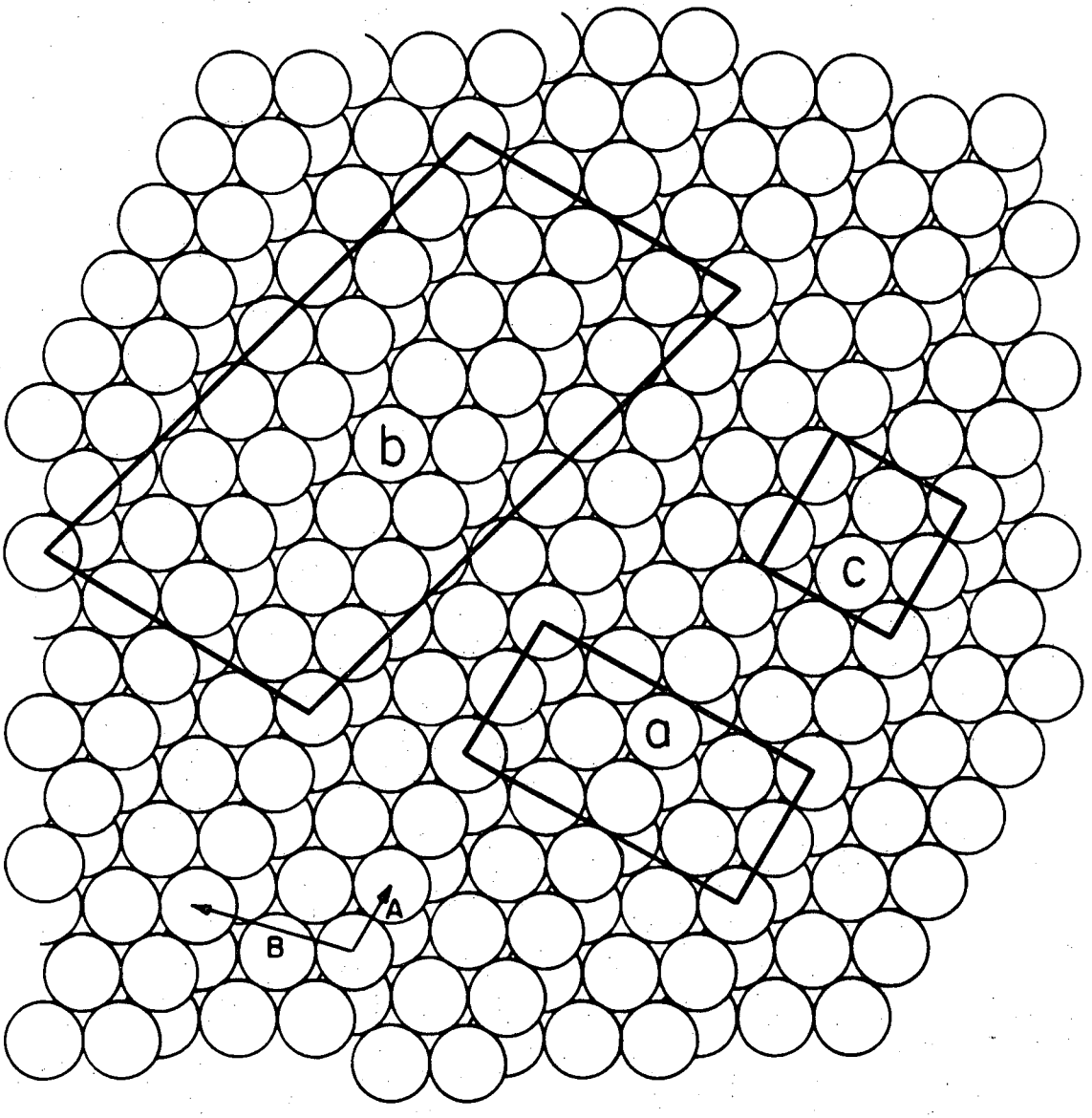

XBL 786-9266

Figure III-28. Real space unit cells of the oxygen surface structures on Rh(331). (a) $\begin{pmatrix} 1 & 2 \\ 2 & 0 \end{pmatrix}$; (b) $\begin{pmatrix} 1 & 2 \\ 7 & -1 \end{pmatrix}$; (c) $\begin{pmatrix} \frac{1}{2} & 1 \\ 2 & 0 \end{pmatrix}$. A and B are the Rh(331) unit cell vectors.

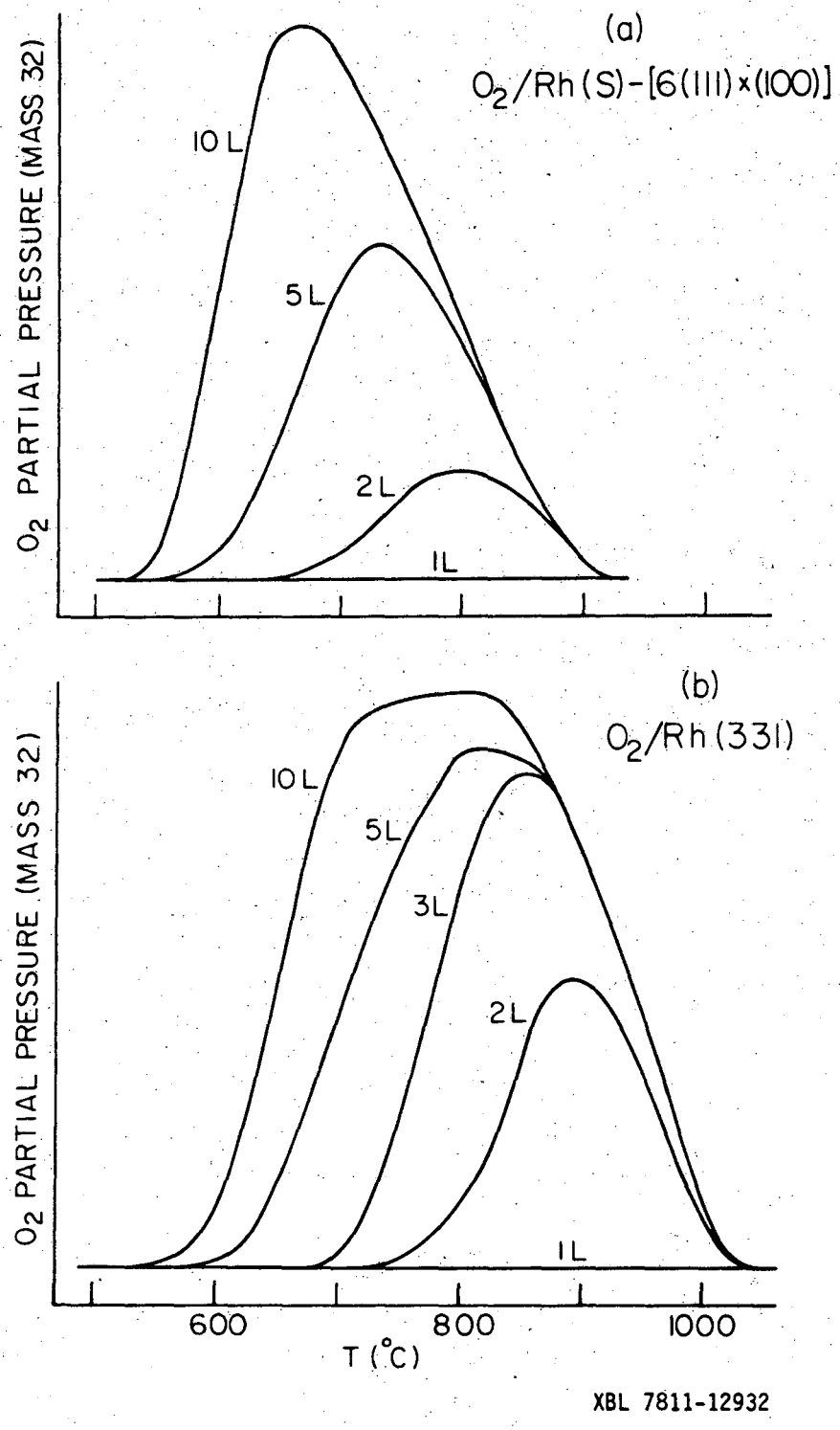

Figure III-29. TDS spectra from oxygen adsorption on (a) Rh(S)-[6(111)×(100)] and (b) Rh(331).

is still the [6(111)×(100)], but in Fig. III-26c the substrate has faceted to a [12(111)×2(100)] surface. The half order spots in Fig. III-26d are due to a (2×1) structure on large (111) facets and substrate doublets are streaked due to oxygen free areas of the crystal returning to the [6(111)×(100)] configuration. Half order LEED patterns have been observed for oxygen adsorption on Ir(S)-[6(111)×(100)],[109] Pt(S)-[9(111)×(100)][156] and Rh(111).[26] Half order streaks indicating one dimensional order have been observed for oxygen on Pt(S)-[6(111)×(100)].[77,78]

Step effects were seen with LEED for oxygen adsorption on Rh(331). The half order streaks in Fig. III-27b resulting from oxygen adsorption at room temperature correspond to a 2(1d) surface structure. The 2(1d) label denotes an ordered one dimensional array parallel to the step edge having a repeat distance of two rhodium atoms. Two dimensionally ordered surface structures appear only after the (331) surface is annealed in O_2. Correlations among the Rh(331) oxygen structures and the Rh(111)-(2×1) oxygen structure are evident from Fig. III-28. The 2(1d) and $\begin{pmatrix} 1 & 2 \\ 2 & 0 \end{pmatrix}$ structures have repeat distances of two rhodium atoms only along the step edge and the (2×1) structure has a repeat distance of two rhodium atoms in one direction. For the case of the 2(1d) structure the steps prevent ordering in one direction and for the $\begin{pmatrix} 1 & 2 \\ 2 & 0 \end{pmatrix}$ structure the step periodicity determines the repeat distance in that direction. The $\begin{pmatrix} 1 & 2 \\ 2 & 0 \end{pmatrix}$ and $\begin{pmatrix} 1 & 2 \\ 7 & 1 \end{pmatrix}$ structures both have a periodicity of two terrace widths. This periodicity is the shortest repeat distance perpendicular to the step edge on the (331) surface. The $\begin{pmatrix} \frac{1}{2} & 1 \\ 2 & 0 \end{pmatrix}$ structure seen during the removal of oxygen from the faceted surface has a repeat distance of just one

terrace width. Since the (331) surface does not possess this periodicity is reasonable to assume the step atoms have not completely reverted from the faceted surface to their (331) positions. Further removal of oxygen does result in the reappearance of oxygen structures possessing repeat distances of two terrace widths. No ordered oxygen structures were found on Ag(331), but high exposures of O_2 (~2000L) on the Ag(331) surface was found to produce a faceted Ag(110)-(2×1)-O phase.[157] Third order streaks have been seen on Pt(S)-[3(111)×(100)],[78] a surface which differs from the (331) only by the fact that it has (100) oriented steps.

The oxygen TDS spectra for the Rh(S)-[6(111)×(100)] surface are identical to the previous spectra published for the Rh(111) surface.[26] This is in contrast to the TDS results on Ir(S)-[6(111)×(100)][109] and Pt(S)-[6(111)×(100)][155] where an additional high temperature shoulder is seen on the stepped surfaces. Two binding states are present in the TDS spectra on the Rh(331) surface, however. Apparently the high density of step atoms on the (331) surface is needed to observe a step effect on rhodium surfaces. The diffusion of oxygen into the bulk which was detected during the TDS experiments has also been observed for oxygen on Rh(110).[32]

The LEED and TDS results for oxygen adsorption on the Rh(S)-[6(111)×(100)] surface are essentially identical to the results found on Rh(111), indicating that the steps of this surface do not effect oxygen chemisorption. On the Rh(331) surface an additional binding state and several new LEED patterns show that a high density of step atoms is needed before a definite step effect is detected in the oxygen chemisorption

properties. In this way rhodium surfaces differ from the platinum and iridium surfaces since step effects are already present on the Pt and Ir[6(111)×(100)] surfaces.

3) Carbon Monoxide and Carbon Dioxide

Step effects were observed in the chemisorption properties of both carbon monoxide and carbon dioxide on the rhodium stepped surfaces. Dissociated CO, which was not seen on Rh(111), was detected on both rhodium stepped surfaces. The CO and CO_2 chemisorption properties were identical indicating that CO_2 dissociates to CO upon adsorption. Since CO and CO_2 behaved similarly this section will pertain mainly to CO, but any differences between the two gases will be pointed out.

Both CO and CO_2 produced an identical sequence of LEED patterns, with the only difference being that a factor of 5 higher pressure of CO_2 was required to form the patterns. On the [6(111)×(100)] surface the first CO diffraction pattern occurs at 3L and corresponds to a $(\sqrt{3}\times\sqrt{3})$ R30° structure on the (111) terrace. Increasing the CO exposure further caused the $(\sqrt{3}\times\sqrt{3})$ R30° pattern to fade and streaks to form in the diffraction pattern. Raising the CO pressure to 1×10^{-5} torr caused these streaks to coalesce into a (2×2) structure on the (111) terraces. All diffraction spots in both CO LEED patterns are split by the step periodicity. The diffraction spots formed by the CO structures on the [6(111)×(100)] surface were not as sharp as those formed on the (111) surface.

The three LEED patterns observed for CO adsorption on the Rh(331) surface are shown in Fig. III-30. The LEED pattern in Fig. III-30a forms at a CO exposure of 3L and corresponde to a $\begin{pmatrix} 1 & 2 \\ 3 & -1 \end{pmatrix}$ surface structure.

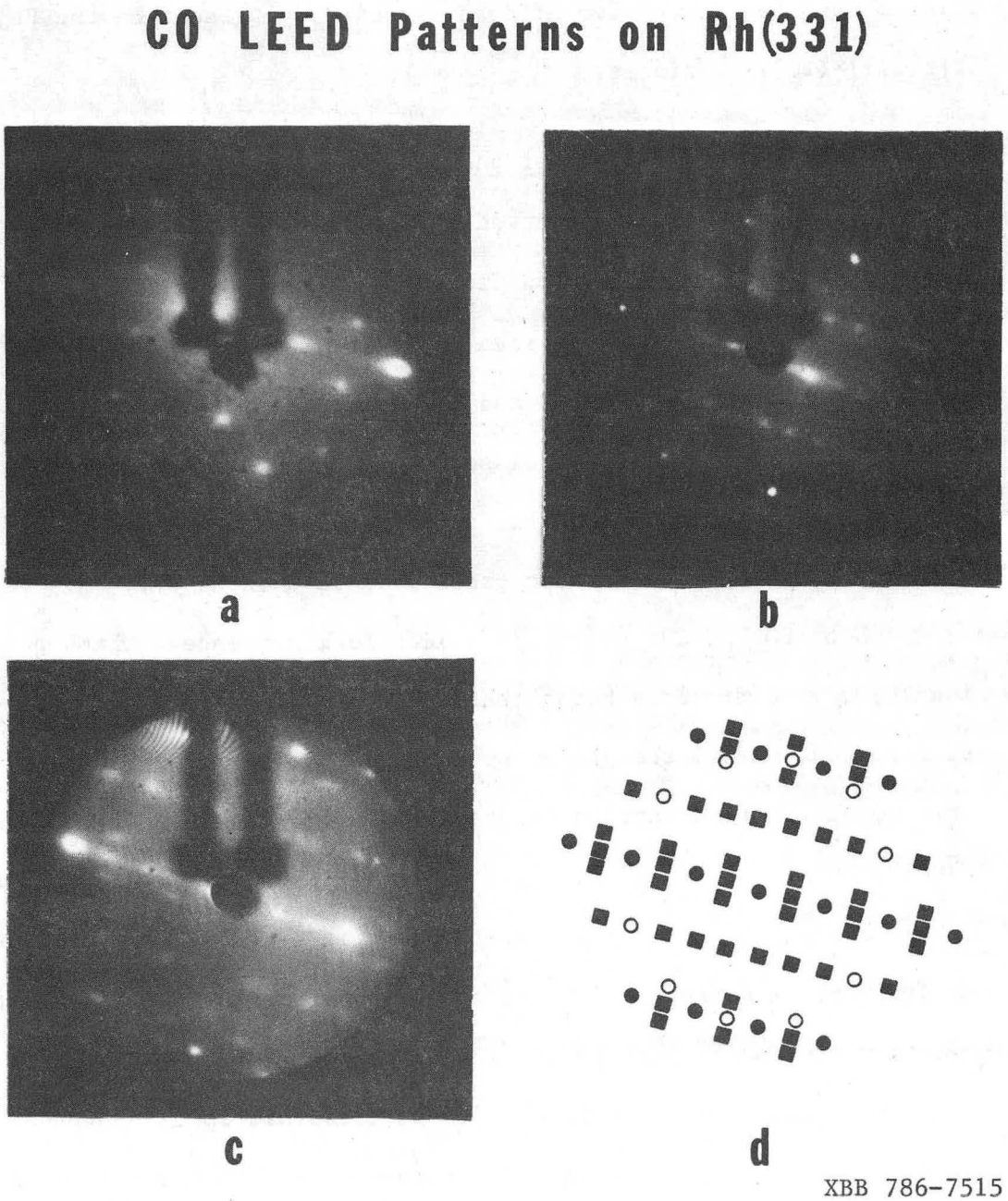

XBB 786-7515

Figure III-30. LEED patterns formed from CO adsorption on Rh(331). (a) $\begin{pmatrix} 1 & 2 \\ 3 & -1 \end{pmatrix}$ structure at 25.5 eV; (b) $\begin{pmatrix} 1 & 2 \\ 2 & 0 \end{pmatrix}$ structure at 82 eV; (c) hexagonal CO overlayer at 54 eV. (d) Schematic of LEED pattern (c) where • are diffraction spots from the rhodium lattice, o are diffraction spots from the CO overlayer and ■ are the multiple diffraction spots from both the rhodium and CO lattices.

Increasing the CO exposure to 7L causes the extra diffraction spots to move to the positions shown in Fig. III-30b. This is the LEED pattern of a $\begin{pmatrix} 1 & 2 \\ 2 & 0 \end{pmatrix}$ surface structure. Increasing the CO pressure to 1×10^{-5} torr results in the formation of the LEED pattern shown in Fig. III-30c. The real space unit cells of these CO structures are shown in Fig. III-31.

The TDS spectra for CO and CO_2 on the Rh stepped surfaces are shown in Fig. III-32. The CO TDS spectra was the same on both stepped surfaces. As can be seen from Fig. III-32, the CO_2 desorption spectra has two peaks, whereas the CO desorption spectra only has one. Using AES in conjunction with TDS showed that after adsorbing CO on the stepped surfaces at 25°C and then flashing the crystal to 400°C so that all the CO had desorbed by TDS, a carbon AES signal was present. This carbon signal was present until 800°C at which time the carbon diffused into the bulk. By pretreating either step surface in oxygen (1×10^{-6} torr O_2 at 800°C) this surface carbon desorbed from the surface between 500 and 600°C as CO, giving a TDS spectrum essentially identical to that for CO_2 on Rh(S)-[6(111)×(100)]. CO was the only gas detected desorbing during the CO and CO_2 TDS experiments. No CO_2 (mass 44) was seen, even after CO_2 adsorptions.

The $(\sqrt{3}\times\sqrt{3})$ R30° and (2×2) CO surface structures observed on Rh(S)-[6(111)×(100)] have been seen on Rh(111).[26] The (2×2) structure is due to a close pack hexagonal CO overlayer with a coverage of $\theta = 0.75$. The hexagonal CO overlayer results from compressing the $(\sqrt{3}\times\sqrt{3})$ R30° structure by increasing the CO exposure. The steps of the Rh(S)-[6(111)×(100)] surface do not interfere with the formation of the hexagonal CO overlayer but do limit the long range order as evident from the enlarged

CO SURFACE STRUCTURES ON Rh(331)

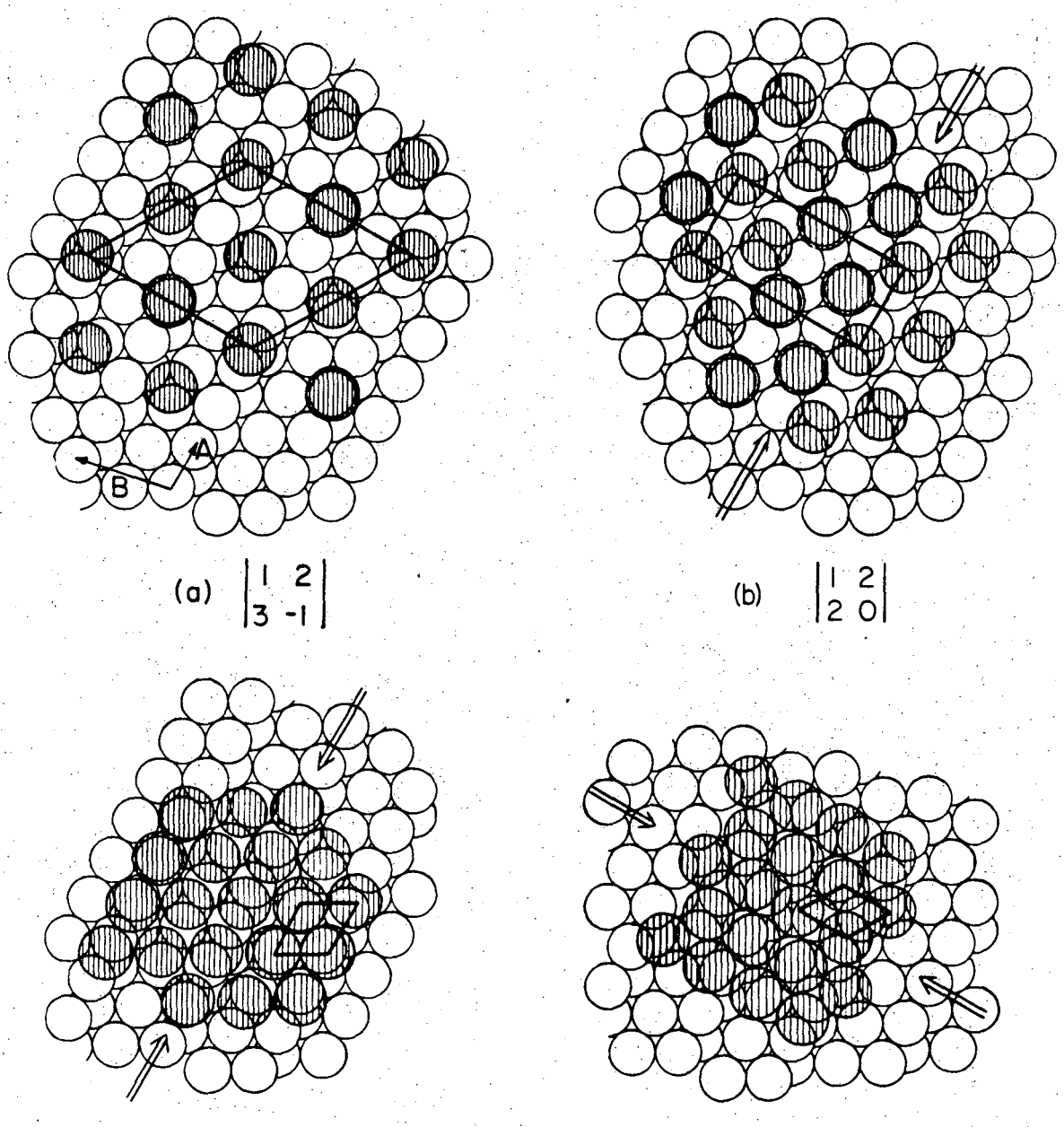

XBL 786-5201

Figure III-31. Real space models for the CO surface structures on Rh(331). The cross hatched circles represent CO molecules, the open circles are the rhodium atoms, A and B are the Rh(331) unit cell vectors and the arrows show the direction of compression. The CO molecule diameter is 3.2 Å and the rhodium nearest neighbor distance is 2.69 Å. (a) $\begin{pmatrix} 1 & 2 \\ 3 & -1 \end{pmatrix}$; (b) $\begin{pmatrix} 1 & 2 \\ 2 & 0 \end{pmatrix}$; (c) one domain of hexagonal overlayer; (d) second domain of hexagonal overlayer.

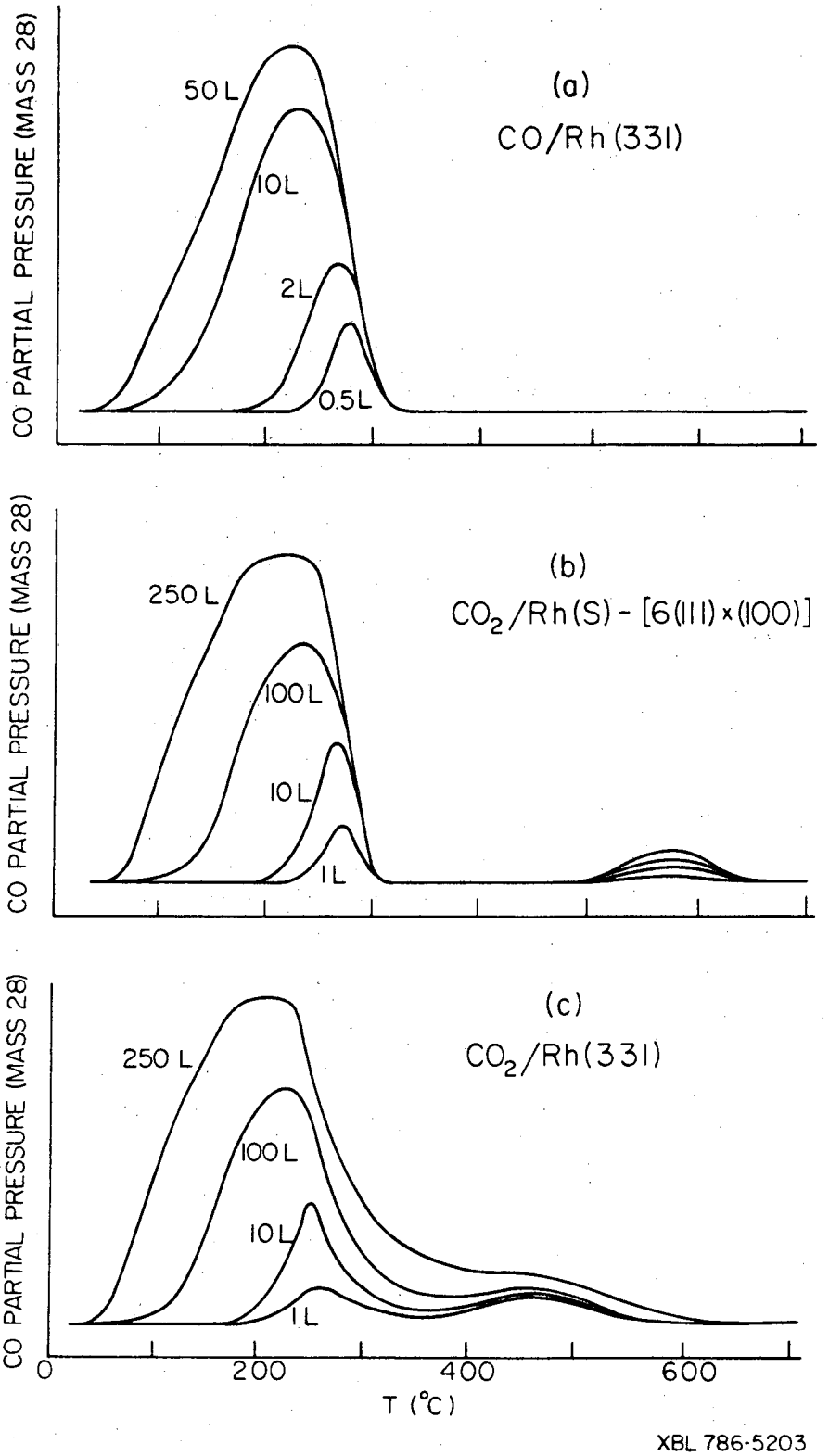

Figure III-32. TDS spectra from adsorption of (a) CO on Rh(331), (b) CO_2 on Rh(S)-[6(111)×(100)] and (c) CO_2 on Rh(331). The only species detected desorbing in all three cases was CO.

diffraction spots on the stepped surface.

The CO LEED patterns on Rh(331) can also be related to the Rh(111) surface. The highest coverage CO LEED pattern on Rh(331), Fig. III-30c, is due to a close packed hexagonal CO overlayer. This CO LEED pattern is explained by scattering from the CO overlayer, the rhodium substrate and multiple scattering from both layers as shown in the schematic in Fig. III-30d. Two domains are present in the LEED pattern and their real space structures are given in Fig. III-31c and 31d. An arrangement of CO molecules within the unit cells of the first two structures formed on Rh(331) can be proposed using the results obtained on the Rh(111) and [6(111)×(100)] surfaces. On those two Rh surfaces the first structure formed is the $(\sqrt{3}\times\sqrt{3})R30°$, a hexagonal array of CO molecules. Placing CO molecules in a hexagonal array on the (331) surface as shown in Fig. III-31a the $\begin{pmatrix}1 & 2\\ 3 & -1\end{pmatrix}$ structure is obtained. The $\begin{pmatrix}1 & 2\\ 2 & 0\end{pmatrix}$-CO structure is an intermediate in the transformation between the $\begin{pmatrix}1 & 2\\ 3 & -1\end{pmatrix}$ and hexagonal overlayer. A reasonable transformation mechanism would be compression parallel to the steps, giving the structure shown in Fig. III-31b. From this structure further compression along the steps would give one of the domains of the hexagonal overlayer (Fig. III-31c). Compression perpendicular to the steps would give the other domain (Fig. III-31d).

Rhodium seems to be one of a few metals studied whose stepped surfaces produce ordered CO LEED patterns. No ordered CO LEED patterns have been observed for Ir(S)-[6(111)×(100)][109] or the (111) vicinal surfaces of Pt.[77,78] On Pd, CO forms identical LEED patterns on both the [9(111)×(111)] and (111) surfaces,[158] with the extra diffraction spots more diffuse on the stepped surface. This is the same relationship

observed between the [6(111)×(100)] and (111) Rh surfaces. Ordered (1×1) and (1×2) CO structures formed on the Pd(210) surface have been interpreted as a close packed overlayer of CO on the Pd surface.[158] CO adsorption on Pd(311) results in streaks occurring in the LEED pattern indicating that only one dimensional order is present in the CO overlayer.[158]

The large low temperature desorption peak in the CO TDS spectra is due to molecular CO bound on the (111) terraces. The position and behavior of this peak is identical to the CO desorption peak on Rh(111).[26] The molecular CO desorbs with first order kinetics but has an activation energy of desorption, E_d, which decreases with increasing coverage. This is reasonable since as the CO overlayer compresses the repulsive forces between CO molecules will increase yielding a decrease in E_d. Following Readhead[90] and assuming first order desorption kinetics and a pre-exponential factor of 10^{13} sec^{-1} a value of 31 kcal/mole is calculated for E_d at a CO exposure of 5L. The high temperature desorption peak seen on the Rh stepped surfaces is due to dissociated CO. This peak was not detected in either the CO or CO_2 TDS spectra on Rh(111) but was reported for CO desorption from Rh foils[11] and Re.[159,160] The evidence for dissociation of CO on the Rh stepped surfaces is the presence of a carbon AES signal after all the molecular CO had desorbed and the desorption of this carbon as CO when excess surface oxygen is present. Carbon was not present on the Rh(111) surface under identical conditions indicating that C-O bond breaking occurs at the step sites. Since no major step effects were discernible by LEED for room temperature CO adsorption, it appears that CO dissociation occurs as the crystal is heated in the TDS

experiments. A possible explanation why no high temperature desorption peak is detected after CO adsorption on a clean Rh stepped surface is that oxygen would rather diffuse into the bulk than recombine with carbon and desorb as CO. In the previous section it was reproted that oxygen diffuses preferentially into the bulk.

Comparing the TDS results of Rh to Pt and Ir stepped surfaces different types of step effects are seen. On Pt(111) vicinal surfaces[78,155] there is, in addition to the desorption peak seen on Pt(111), a resolvable high temperature shoulder due to stronger binding of molecular CO at the step sites. On Ir(S)-[6(111)×(100)][109] this shoulder is not resolved, but there is a definite tailing on the high temperature side of the main desorption peak. On the Pt and Ir stepped surfaces no evidence for CO dissociation was seen. Thus, all three metals show step effects, but only rhodium stepped surfaces dissociate CO.

4) Nitric Oxide

The presence of steps has a major effect on the ordering of NO. NO adsorption produced only one ordered structure on Rh(S)-[6(111)×(100)] and no ordered structures at room temperature on Rh(331). This is in contrast to Rh(111) where two ordered structures were formed by NO adsorption.[26] Exposing the Rh(S)-[6(111)×(100)] surface to NO at 25°C initially resulted in complex streaking in the LEED pattern. Further NO exposure caused the streaking to coalesce into a LEED pattern from a (2χ2) structure on the (111) terraces. The extra diffraction spots were split by the step periodicity and are larger than those found on the (111) surface. NO adsorption on Rh(331) at 25°C was disordered producing only an

increased background intensity in the LEED pattern. Half order streaks and the LEED pattern in Fig. III-32a formed as the (331) surface was flashed to 500°C then cooled to 100°C in a NO background pressure of 1×10^{-8} torr. The half order streaks formed at 500°C then transformed into a $\begin{pmatrix} -1 & 1 \\ 3 & 0 \end{pmatrix}$ structure upon cooling to 100°C. The real space unit cell of the $\begin{pmatrix} -1 & 1 \\ 3 & 0 \end{pmatrix}$ structure is shown in Fig. III-33b. The half order streaks were also observed when a disordered layer of NO was flashed to 500°C in vacuum.

TDS studies detected gases desorbing at masses 28(N_2), 30(NO), 32(O_2) and 44(N_2O). The TDS spectra for N_2, NO and N_2O are shown in Fig. III-34. The spectra for both stepped surfaces were similar so only the [6(111)×(100)] data is shown. The N_2 spectrum has one dominant peak which occurs at 200°C. The NO spectrum exhibits a first order desorption peak at 175°C with a second peak appearing at 150°C for higher NO exposures. No NO was detected desorbing for exposures less than 1L. The 150°C desorption peak was not detected until the (2×2) structure had formed. The only difference between the TDS spectra of the two Rh stepped surfaces was that the 150°C NO desorption peak was only a very small shoulder on the (331) surface. The oxygen desorption peak from NO adsorption occurred 150°C higher than the oxygen desorption peak from oxygen adsorption. The N_2O spectrum has 2 peaks whose relative intensities change with exposure as shown in Fig. III-34c.

The (2×2) structure formed on the Rh(S)-[6(111)×(100)] surface is the same as the highest coverage structure formed on the Rh(111) surface.[26] The (2×2) structure has also been seen for NO on Pt(S)-[12(111)×(111)][16] and Pd(111).[119] On Pd(111) and Rh(111) the

$$\text{Rh(331)-}\begin{vmatrix} -1 & 1 \\ 3 & 0 \end{vmatrix}$$

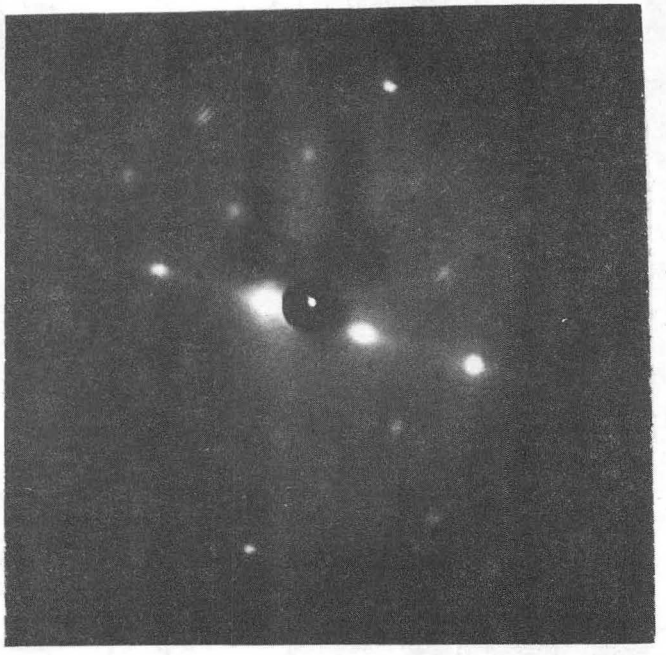

A

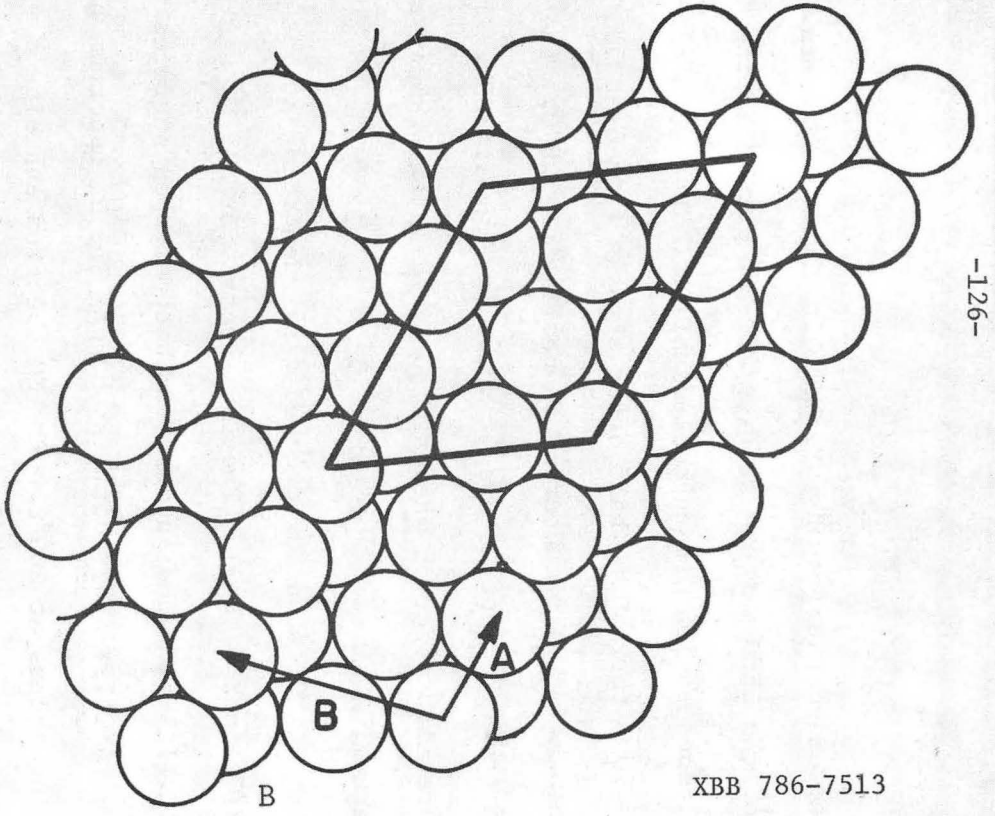

B

XBB 786-7513

Figure III-33. (a) LEED pattern of Rh(331)-$\begin{pmatrix} -1 & 1 \\ 3 & 0 \end{pmatrix}$ structure at 44 eV. (b) Real space unit cell of $\begin{pmatrix} -1 & 1 \\ 3 & 0 \end{pmatrix}$ structure. A and B are Rh(331) unit cell vectors.

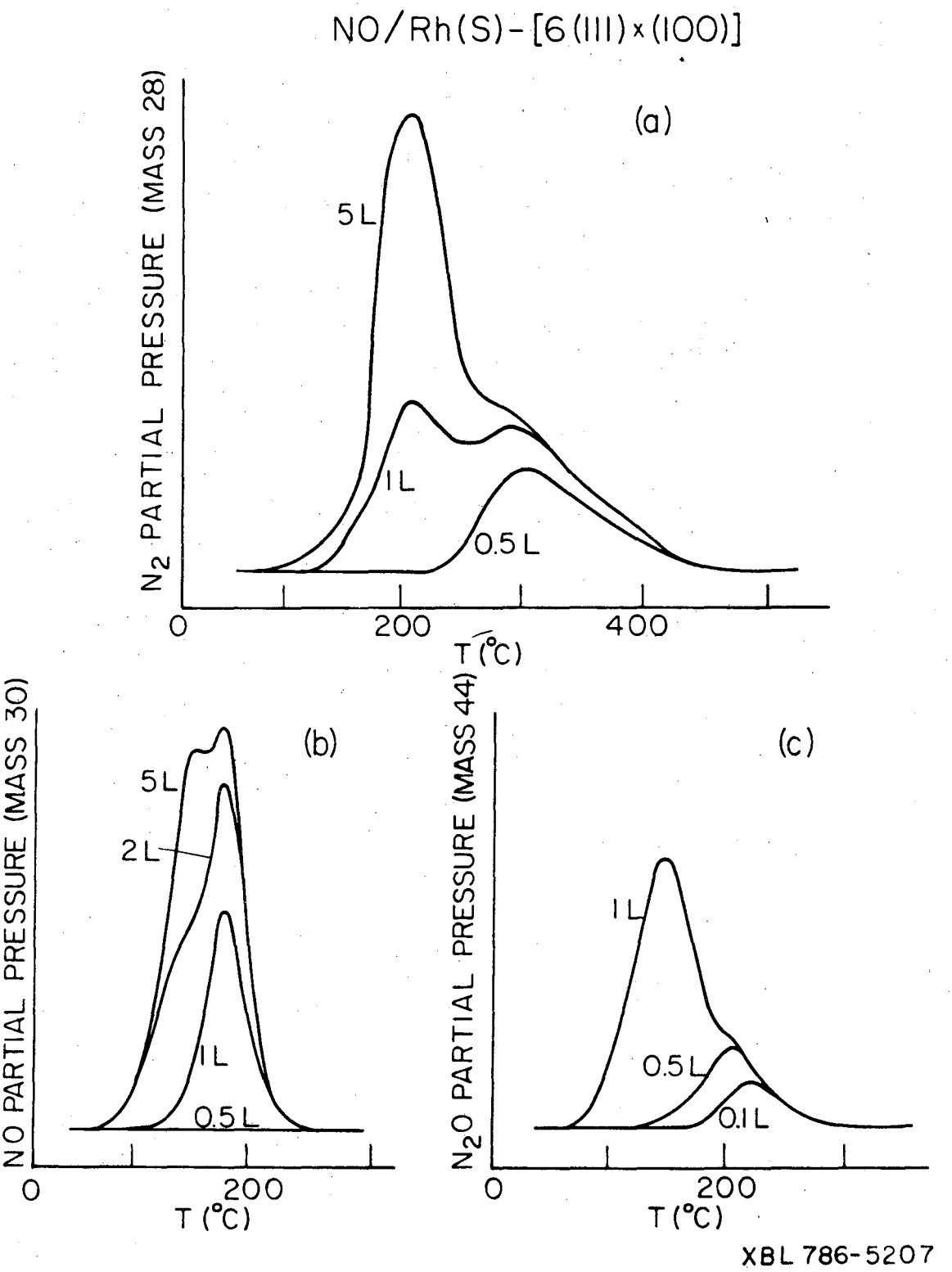

Figure III-34. TDS spectra obtained from NO adsorption on Rh(S)-[6(111)×(100)]. (a) N_2 desorption, (b) NO desorption and (c) N_2O desorption.

(2×2)-NO structure has been interpreted as a hexagonal overlayer of NO, similar to the CO case. NO also form a hexagonal overlayer on Ni(111).[120] The amount of compression and ordering in the NO overlayer is affected by the step density. On the [6(111)×(100)] surface the full (2×2) structure is still reached although the domain size is smaller than on the (111) surface. On the (331) surface complete compression and ordering could not be attained as shown by the presence of only one peak in the mass 30 TDS spectra and the existence of no ordered LEED patterns at room temperature.

The half order streaks formed from heating the NO overlayer on the (331) surface are due to adsorbed oxygen. The TDS spectra in Fig. III-34 show that all of the nitrogen containing species have been desorbed by 500°C, so only adsorbed oxygen is present when the streaks form. The same half order streaks were also seen for oxygen adsorbed on the clean (331) surface. The $\begin{pmatrix} -1 & 1 \\ 3 & 0 \end{pmatrix}$ surface structure is formed from the adsorbed oxygen interacting with gaseous NO. Since several different types of adsorbed species could be formed from the interaction of oxygen and NO further studies are needed to determine the identify of this adsorbed species.

The TDS spectra indicate that NO is dissociatively adsorbed at exposures less than 1L and associatively adsorbed above 1L. The desorption peaks correlate with the type of NO adsorption that is occurring. The high temperature N_2 and N_2O desorption peaks result from dissociative adsorption and reach their maximum height by 1L. As associative adsorption begins the NO and low temperature N_2 and N_2O desorption peaks appear.

N_2 desorption is detected for both types adsorption, the low temperature peak from the NO dissociating as the crystal is heated and the high temperature peak from the NO dissociating upon adsorption. The NO desorption peaks appear with the onset of associative adsorption and follow first order desorption kinetics. Assuming a pre-exponential factor of 10^{13} sec^{-1} yields values of 24.5 and 26 kcal/mole for the E_d's of the 150 and 175°C NO desorption peaks. The dissociative adsorption of NO at low exposures followed by associative adsorption at higher exposures has been observed on other surfaces. On Rh(110),[32] the crossover to associative adsorption is at 0.5L, while on Ni(111),[120] the crossover occurs at 6L. For NO adsorbed on Ru(1010) at 90°C the crossover is at 5L.[162] Dissociative and associative NO adsorption have been detected on Ir(111) and (100).[142] Only associative adsorption has been detected on Pt(S)-[12(111)×(111)][161] and Pd(111).[119] Thus these six metals can be separated into two groups. One group (Pt and Pd) where NO always adsorbs associatively and another group (Rh, Ru, Ir and Ni) where dissociative adsorption occurs at low NO exposures and associative adsorption at higher NO exposures.

5) Ethylene and Acetylene

The ordering of ethylene amd acetylene were markedly affected by the steps present on the two Rh surfaces. Adsorbing C_2H_4 and C_2H_2 at 25°C produced no ordered structures on the [6(111)×(100)] surface and a $\begin{pmatrix} -1 & 1 \\ 3 & 0 \end{pmatrix}$ structure on the (331) surface. On the [6(111)×(100)] surface two spots near the $(\sqrt{3}\times\sqrt{3})$ R30° position were seen, but these spots were diffuse and streaked. The diffraction spots of the $\begin{pmatrix} -1 & 1 \\ 3 & 0 \end{pmatrix}$ hydrogen

structures were larger than the spots in the $\begin{pmatrix} -1 & 1 \\ 3 & 0 \end{pmatrix}$ structure seen during NO adsorption. The hydrocarbon LEED patterns irreversibly disordered when heated above 150°C in vacuum. By 150°C the hydrocarbons had begun decomposing with H_2 the major gas detected desorbing. The TDS spectra for H_2 desorption after adsorbing C_2H_4 on the [6(111)×(100)] surface at 25°C are shown in Fig. III-35. The H_2 desorption spectra from acetylene adsorption on both stepped surfaces and ethylene on the (331) surface were the same as the spectra shown in Fig. III-35. The amount of C_2H_4 desorbed from C_2H_4 adsorption was less than 1% of the desorbed H_2. The C_2H_4 desorbed at 100°C. No C_2H_2 could be detected desorbing after C_2H_2 adsorption.

After all the hydrogen had desorbed (~550°C) AES showed that carbon was still present on the surface. By heating the crystal to 900°C this surface carbon dissolved into the bulk and further hydrocarbon adsorptions could be carried out. After several cycles of hydrocarbon adsorption and heating to 900°C the near surface region became saturated with carbon and this resulted in the appearance of new surface structures. These structures will be discussed in the next section.

C_2H_4 and C_2H_2 were the only two molecules in this study that did not form ordered structures on the [6(111)×(100)] surface. These hydrocarbons formed ordered c(4×2) surface structures on Rh(111).[26] The first two spots seen on Rh(111) when the c(4×2) structure was forming were in the same location as the diffuse spots observed from C_2H_4 adsorption on the [6(111)×(100)] surface. Thus a c(4×2) structure was beginning to form on the terraces, but apparently never fully developed

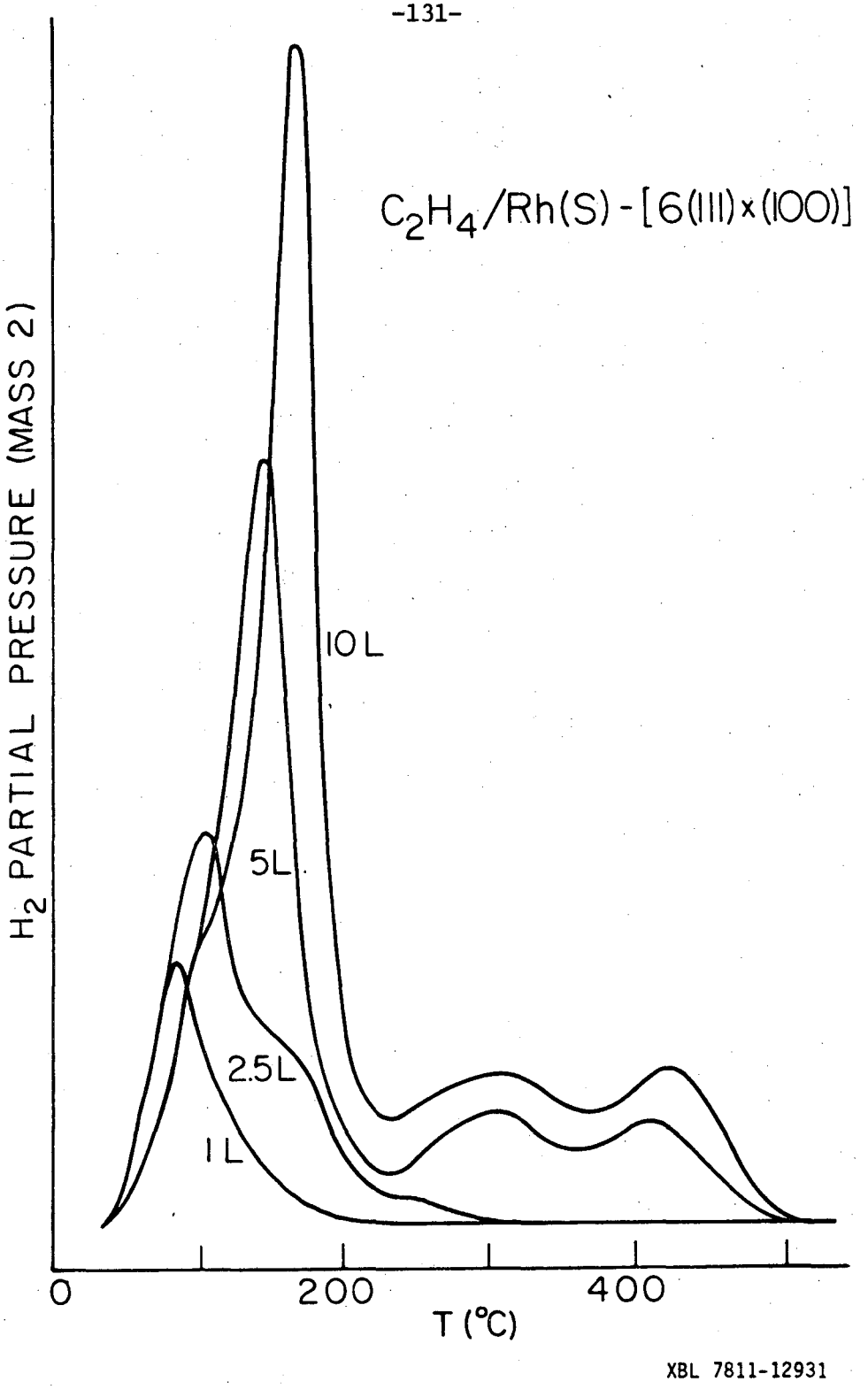

Figure III-35. (a) Hydrogen desorption from C_2H_4 adsorption on Rh(S)-[6(111)×(100)].

due to the presence of the steps. Poorly ordered (2×2) structures have been seen for C_2H_4 and C_2H_2 adsorption on Ir(S)-[6(111)×(100)].[77,163] The unit cell of Rh(331)-$\begin{pmatrix} -1 & 1 \\ 3 & 0 \end{pmatrix}$ hydrocarbon structure is 75% larger than the primitive unit cell of the c(4×2) structure, indicating the step periodicity influences the arrangement of the hydrocarbons on the (331) surface. The TDS spectra from C_2H_2 adsorption on the stepped surfaces is similar to the spectra for Rh(111)[26] and Ir(S)-[6(111)×(100)].[102] Due to the similar chemisorption properties of C_2H_4 and C_2H_2 it is likely that room temperature adsorption of these hydrocarbons yields the same adsorbed species.

6) Carbon

Carbon structures on the two stepped surfaces were obtained by heating the crystal at 800°C in a C_2H_4 pressure of 5×10^{-7} torr for 5 to 10 minutes. The behavior of the two stepped surfaces under these conditions were markedly different. The [6(111)×(100)] surface faceted into large domains of (111) and (100) orientation. The faceting is accompanied by an increased background intensity in the LEED pattern and the formation of a (12×12) coincident lattice structure on the (111) facets. This (12×12) coincident lattice has been seen for carbon on Rh(111) and is due to the formation of the graphite basal plane on the rhodium surface.[26]

The (331) surface was stable when heated in C_2H_4 and a segmented carbon ring was formed from C_2H_4 decomposition. LEED patterns of the carbon ring are shown in Fig. III-36. The segmented carbon ring indicates the existence of a partially disordered graphite overlayer on

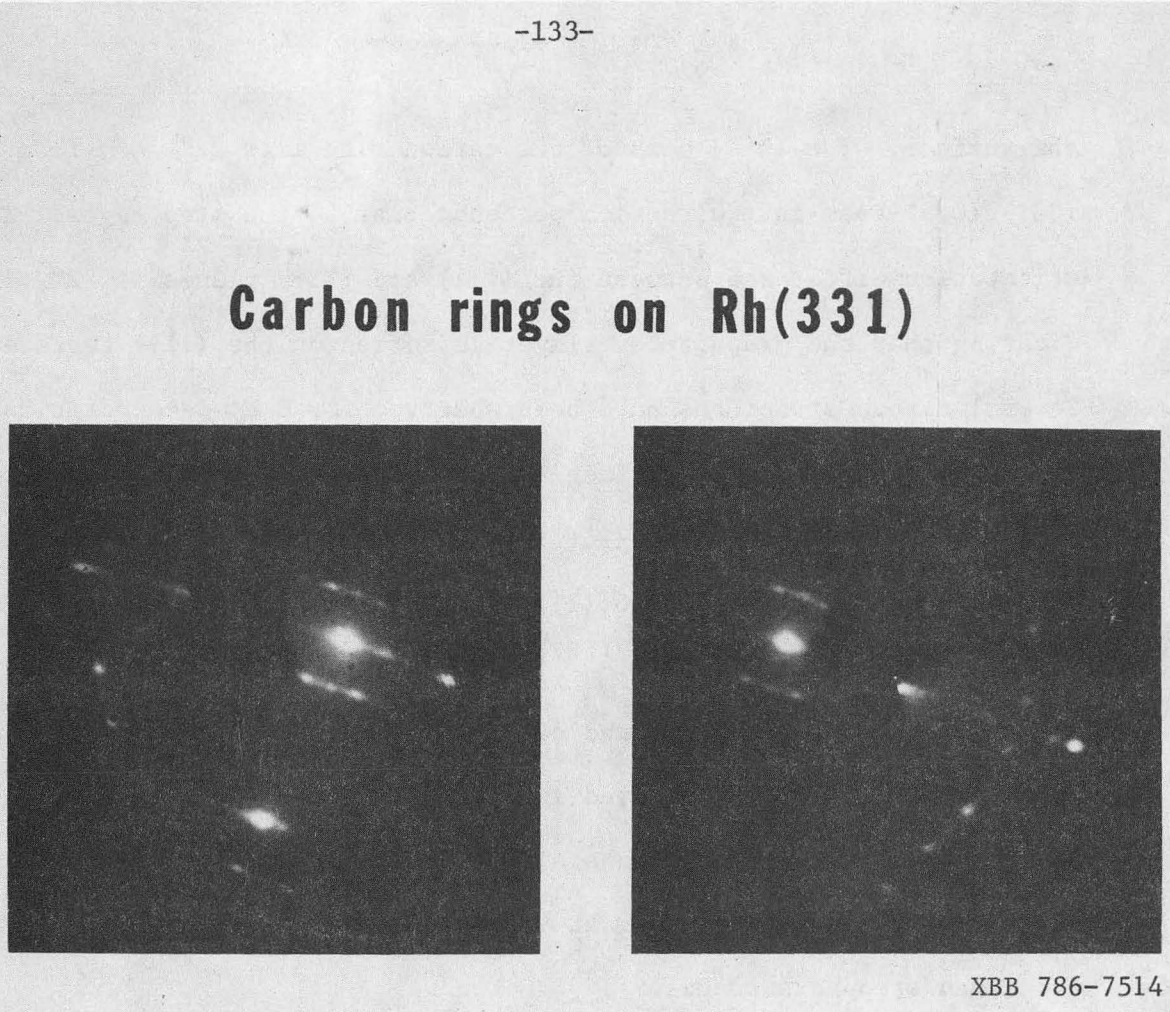

Figure III-36. LEED patterns of segmented carbon ring on Rh(331) at 47.5 eV.

the surface. The (0,0) beam of the carbon ring lies 22° away from the (331) (0,0) beam in a direction perpendicular to the step edges. The orientation difference between the (111) and (331) planes is 22°, indicating that the graphite overlayer is formed on the (111) terraces. Several carbon structures have been observed for C_2H_4 decomposition on the Pt(S)-[6(111)×(100)] surface[137,163] while no ordered carbon structures were seen on the Ir(S)-[6(111)×(100)] surface.[102] Carbon deposition also caused the Pt(S)-[6(111)×(100)] surface to facet into large domains of (111) orientation.[137]

Carbon was not detected desorbing from the surface, but as noted above carbon could be dissolved in the bulk by heating the crystal to 900°C. To remove large amounts of carbon the crystal had to be heated in oxygen (1×10^{-6} torr of O_2 at 900°C). This led to a regeneration of the clean stepped surfaces.

D. Oxidation Studies on the Rhodium(111) Surface

1) LEED Results of the Oxidation Study on Rh(111)

The adsorption of 10L(1L = 1×10^{-6} torr·sec) of oxygen at -63°C on the clean Rh(111) surface resulted in the appearance of large diffuse diffraction beams at the half order positions. These new diffraction features were slightly elongated and by rapdily cooling the clean Rh(111) surface from 250 to -63°C (~50 sec) in an oxygen pressure of 2×10^{-7} torr they became sharper and the elongation more pronounced. The diffraction pattern observed during this rapid cooling in oxygen is shown in Fig. III-37b. The diffraction pattern in Fig. III-37c with sharp half

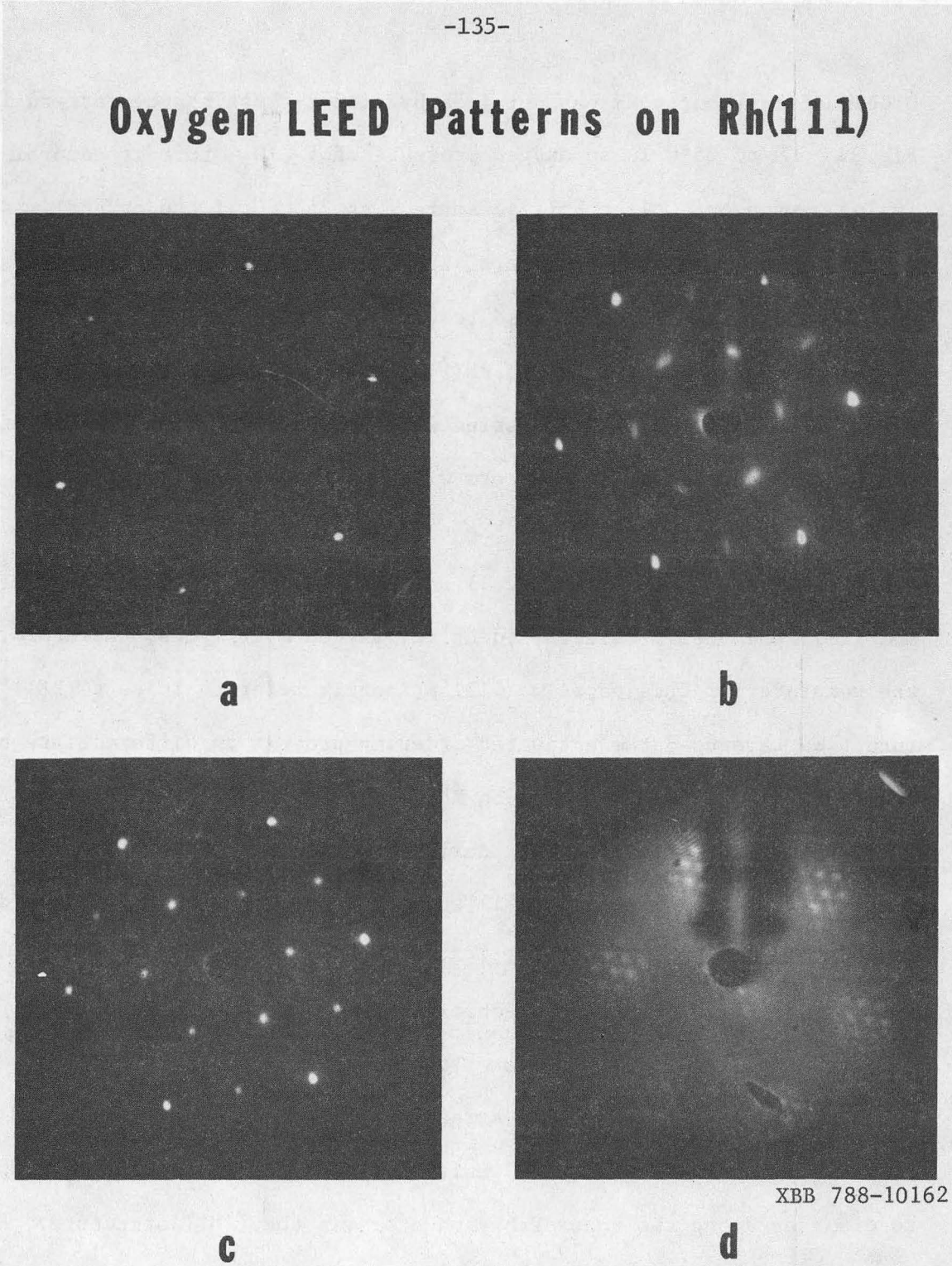

Figure III-37. Oxygen LEED patterns on Rh(111). (a) the clean Rh(111) surface at 64.5 eV; (b) slightly disordered Rh(111)-(2×1)-O at 67 eV; (c) well ordered Rh(111)-(2×1)-O at 67 eV; (d) Rh(111)-(8×8) coincidence lattice from Rh_2O_3 (0001)||Rh(111) at 73 eV.

order diffraction spots was obtained by either flashing the pattern in Fig. III-37b to 25°C in an oxygen pressure of 1×10^{-7} torr or adsorbing 10 L of oxygen on a clean Rh(111) surface at 25°C. If the crystal was cooled to -63°C after formation of the sharp half order diffraction spots, the spots remained sharp. These results indicate the ordering of the chemisorbed oxygen overlayer on Rh(111) is an activated process.

Two different surface structures, a (2×2) or three domains of a (2×1), can generate a LEED pattern with sharp half order diffraction spots (Fig. III-37c). In Fig. III-38 the unit cells of the (2×2) structure and one domain of the c(2×2) and (2×1) unit cells are shown. Both the c(2×2) and (2×1) unit cells describe identical oxygen overlayers; therefore, for the remainder of this paper we will primarily refer to it as a (2×1) structure. We have used the activated ordering process to differentiate between the (2×1) and (2×2) structures on Rh(111). By following the shape of the half order diffraction features during the ordering process, it was determined that three domains of (2×1) structure was consistent with the direction of spot elongation (Fig. III-37b). This is illustrated in Fig. III-39. Figure III-39a shows the schematic LEED pattern of Fig. III-37b and the reciprocal space unit cells of the (2×1) and c(2×2) structures. Only one direction of elongation or streaking of the diffraction features is present in the (2×1) and c(2×2) unit cells and this streaking corresponds to disorder along the rows of oxygen atoms in the (2×1) structure. As shown schematically in Fig. III-39b, the (2×2) reciprocal space unit cell only indexes a half order diffraction pattern with sharp spots. If the (2×2) reciprocal space unit cell was used to index the schematic LEED

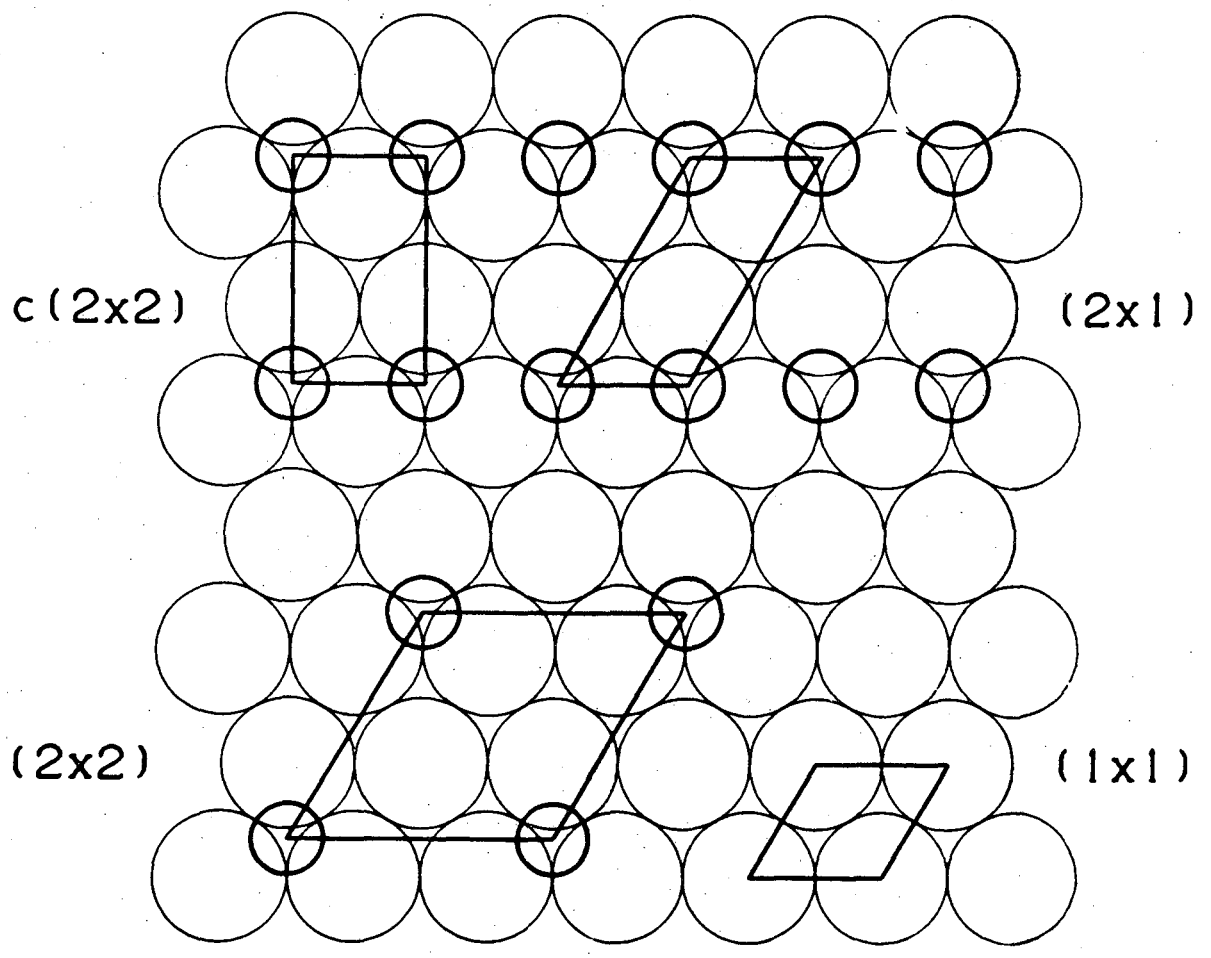

XBL 795-9676

Figure III-38. Real space unit cells for (2×2), c(2×2) and (2×1) surface structures on Rh(111). The large circles represent the rhodium atoms and the small circles represent the oxygen atoms. The (1×1) structure is the unit cell of the Rh(111) surface. The rhodium nearest neighbor distance is 2.69 Å. The oxygen atoms have arbitrarily been placed in the three-fold hollow sites and only one domain of the c(2×2) and (2×1) structures have been shown.

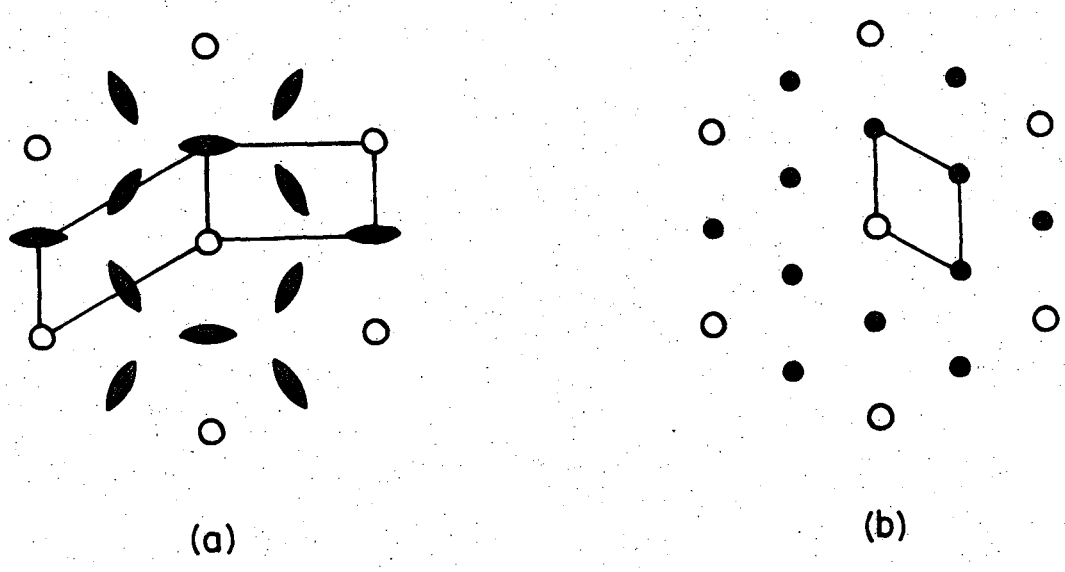

Figure III-39. (a) and (b) are schematics of the LEED patterns in Figs. III-37b and 37c where O are diffraction spots from the Rh(111) surface, ⬬ and ● are diffraction features from the oxygen overlayer. In (a) the reciprocal space unit cells of one domain of the c(2×2) and (2×1) structures are shown. In (b) the reciprocal space unit cell of a (2×2) structure is shown.

pattern in Fig. III-39a, it would contain three different directions of elongated diffraction features, corresponding to disorder in three crystallographic directions. Disordering in three directions of the (2×2) structure would tend to make the half order diffraction features round, broad and diffuse, not elongated as shown in Fig. III-39a. Therefore chemisorbed oxygen forms a (2×1)-O surface structure on Rh(111). The chemisorbed oxygen species present in the (2×1) structures was very reactive with hydrogen and the half order diffraction features shown in Fig. III-37b and 37c were rapidly removed when the rhodium surface was heated to 50°C in 1×10^{-7} torr of H_2.

Further oxidation of the rhodium surface was carried out by heating the crystal to high temperatures in the presence of oxygen. For temperatures up to 800°C and oxygen pressures up to 1×10^{-5} torr only half order diffraction spots were observed in the LEED pattern. Although this is the same diffraction pattern as was shown for chemisorbed oxygen, the reactivity with hydrogen of the oxygen species that make up this surface structure was much lower than was observed for the chemisorbed oxygen. After prolonged heating (> 30 min.) at 800°C in 1×10^{-5} torr of O_2, the half order diffraction spots could not be removed by heating the crystal to 50°C in 1×10^{-7} torr of H_2 and high temperature anneals (900°C) in hydrogen were required to regenerate the clean Rh(111) surface. This unreactive oxygen species has also been referred to as "strongly bound oxygen" or "surface oxide" in the literature and these three descriptions will be used interchangeably here.

Increasing the oxygen pressure to 1 torr and heating the crystal at 700°C for 10 minutes resulted in the appearance of a diffraction pattern from a (8×8) surface structure (Fig. III-37d). This (8×8) coincidence lattice structure can be identified as the expitaxial growth of Rh_2O_3(0001) on the Rh(111) surface. Rh_2O_3 has the corundum structure with unit cell vectors of a=5.108 Å and c=13.81 Å.[164] Four unit cells of Rh_2O_3(0001), expanded by 5%, would fit into an (8×8) structure on Rh(111). The formation of a slightly expanded hexagonal Rh_2O_3 structure at 700° in 1 torr of O_2 is reasonable since the corundum form of Rh_2O_3 expands into an orthorhombic structure with unit cell vectors of a=5.149 Å and c=14.688 Å when heated above 750°C in air.[164] The corundum structure is just a hexagonal closest packed (hcp) lattice of oxide ions with 2/3 of the octahedral holes occupied by metal ions. The basal plane of Rh_2O_3 would consist of an hcp layer of oxide ions with Rh ions arranged in the threefold hollow sites of the oxygen layer to form a $(\sqrt{3}\times\sqrt{3})R30°$ structure (see Fig. III-40).

Epitaxial Rh_2O_3 was inert and neither hydrogen nor CO adsorption could be detected on this surface at 25°C. The (8×8) structure could be removed by either heating the crystal to 500°C in vacuum or to 800°C in 1×10^{-5} torr of O_2. Rh_2O_3 decomposes in air at 1050°C;[164] thus the oxide decomposition temperature increases as the partial pressure of O_2 above the oxide is increased.

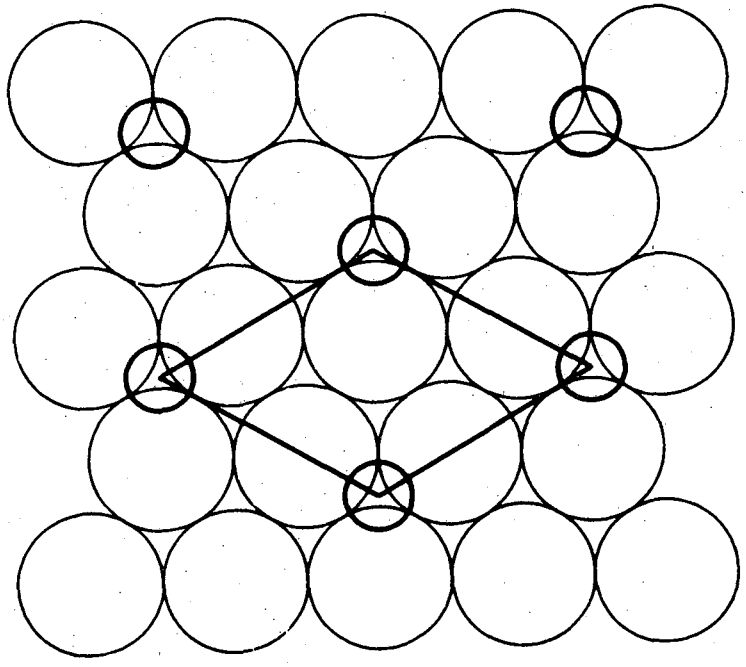

$Rh_2O_3(0001)$

XBL 795-9889

Figure III-40. The basal plane of Rh_2O_3. The large circles represent oxide ions and the small circles represent Rh ions. The oxide ions are arranged in hcp lattice with a nearest neighbor distance of 2.949 Å. The Rh ions occupy 2/3 of the octahedral holes with an in-plane nearest neighbor distance of 5.108 Å. The unit cell of $Rh_2O_3(0001)$ is shown.(164)

2) AES Results of the Oxidation Study on Rh(111)

The AES spectra for the Rh(111)-oxygen system are shown in Figs. III-41 and 42. The spectra in Fig. III-41 show the rhodium MNN and oxygen KLL transitions. In Fig. III-42 the rhodium NVV transition is shown. The low energy NVV transition involves the d band electrons and therefore is ideally suited for following the changes which occur in the d band during oxidation. The top spectra in Figs. III-41 and 42 are for the clean Rh(111) surface. Adsorbing 10 L of oxygen at 25°C on a clean Rh(111) surface results in the appearance of low intensity oxygen transitions at 496 and 518 eV (middle spectrum of Fig. III-41). The O_{518}/Rh_{302} peak-to-peak ratio in this spectrum is 0.06. No change in the 39 eV rhodium transition was detected during oxygen adsorption at 25°C. High temperature oxidation of the rhodium surface resulted in the oxygen transitions growing in intensity and shifting to lower energies. The bottom spectrum in Fig. III-41 is from a Rh(111) crystal with an epitaxial layer of $Rh_2O_3(0001)$. In this spectrum the major oxygen transition has shifted from 518 eV to 515 eV and has a O_{515}/Rh_{302} peak-to-peak ratio of 0.25. High temperature oxidation also resulted in the appearance of a transition from Rh oxide at 35 eV. This transition grew in intensity as the amount of oxygen in the near-surface region increased. The spectra in Figs. III-42a and 42b are from surfaces with O_{515}/Rh_{302} peak-to-peak ratios of 0.18 and 0.25, respectively. Due to the small energy difference between the 35 and 39 eV peaks and the modulation voltage used (2 eV, peak-to-peak) these peaks were not well resolved. The 35 eV Rh oxide transition was also broader than the 39 eV transition of the clean Rh(111) surface. These results indicate the Rh oxide d band is broader

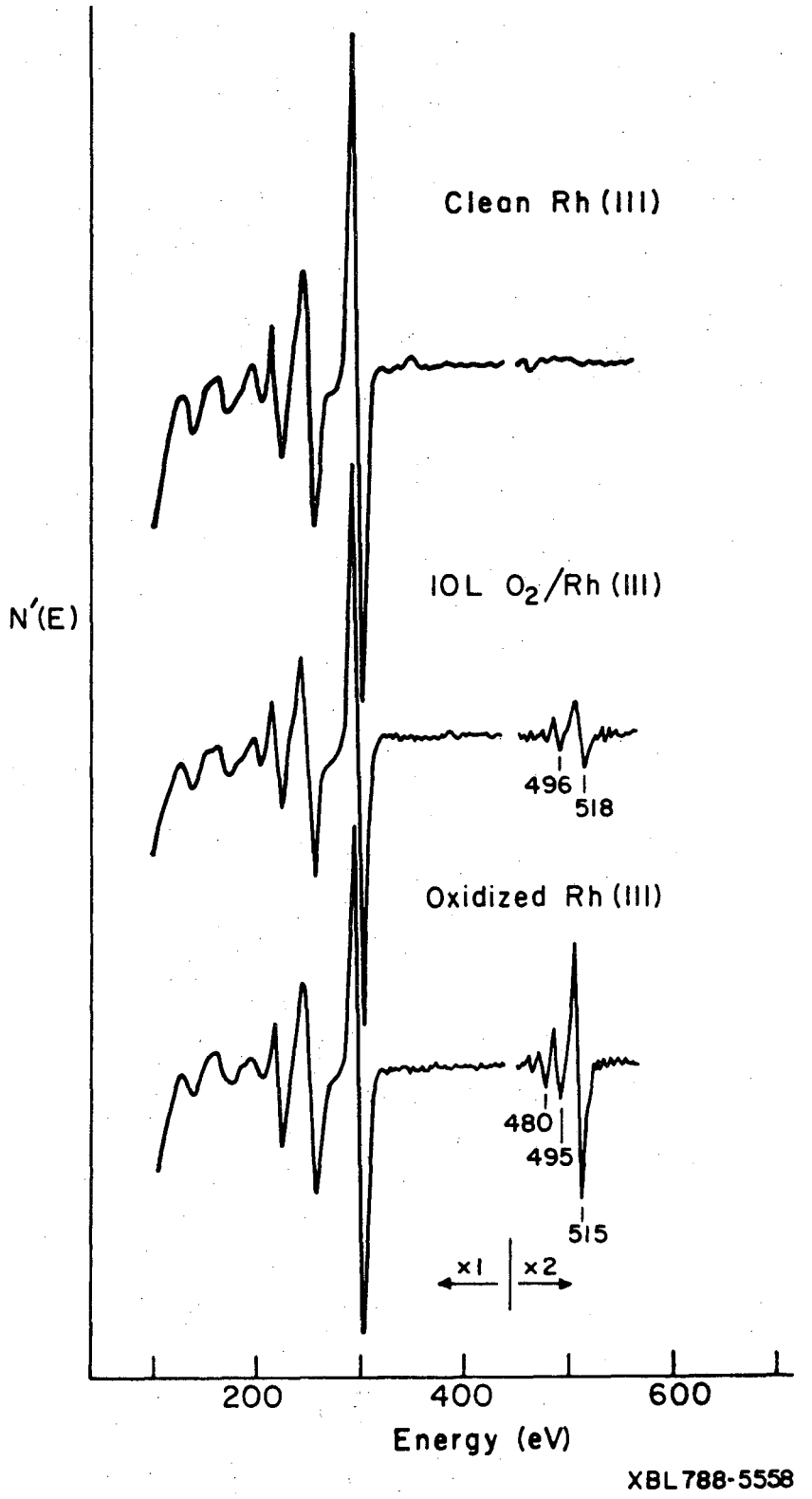

Figure III-41. AES spectra for clean (top), chemisorbed oxygen (middle), and epitaxial Rh_2O_3 (bottom) on the Rh(111) surface.

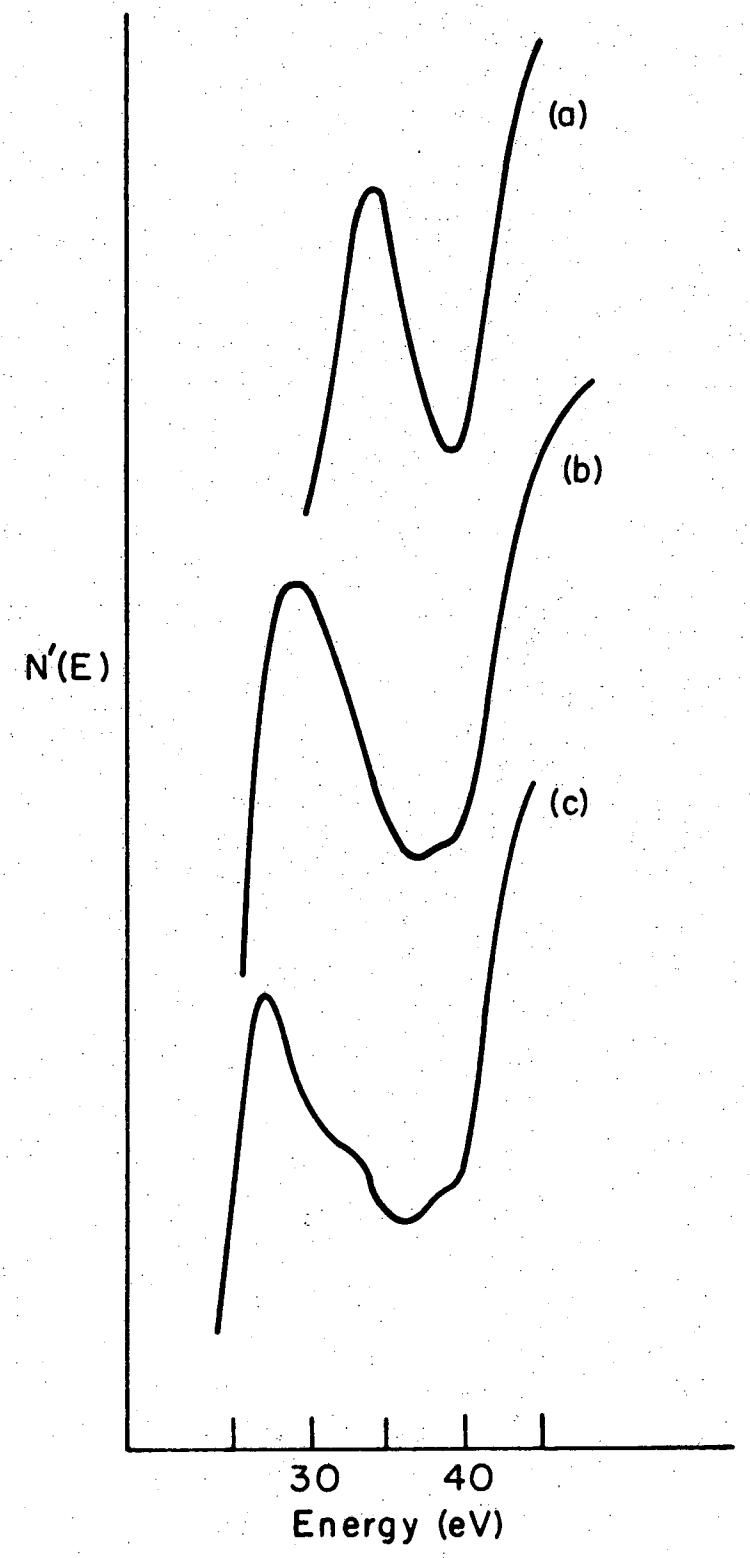

Figure III-42. Low energy AES spectra for a Rh(111) surface with O_{515}/Rh_{302} peak-to-peak ratios of (a) 0.0, (b) 0.18, and (c) 0.25.

and shifted downward in energy relative to the metallic Rh d band.

3) TDS Results of the Oxidation Study on Rh(111)

The TDS spectra for oxygen adsorbed at 300 K on a clean Rh(111) surface are shown in Fig. III-43. For low O_2 exposures no oxygen desorption (mass 32) was detected. An oxygen signal was present in the AES spectrum before but not after the desorption experiments. This adsorbed oxygen was not being removed during the desorption experiments by any near surface region impurities or residual background gases since no desorption of any oxygen containing species (CO, CO_2, H_2O, etc.) was detected. The lack of oxygen desorption can be explained by diffusion of oxygen into the near surface region. The diffusion of oxygen into the near surface region has been previously observed on rhodium.[26,27,30,32] After higher O_2 exposures oxygen desorbed from the rhodium surface and the desorption temperature decreased with increasing O_2 exposure. The TDS spectrum of chemisorbed oxygen is characteristic of a second order desorption process, indicating that two oxygen atoms recombine at a slow rate to form an oxygen molecule before desorbing. This implies that O_2 is dissociatively adsorbed since this would provide the source of oxygen atoms needed for a second order desorption process.

Hydrogen, oxygen and CO TDS experiments were attempted on the oxidized (8×8) surface structure so that a comparison with TDS results on clean rhodium surfaces could be made. It was found that neither hydrogen nor CO adsorbed in sufficient amounts to be detectible on the (8×8) structure at 25°C and the (8×8) structure began decomposing as the crystal was heated during the desorption experiments. For this reason only the

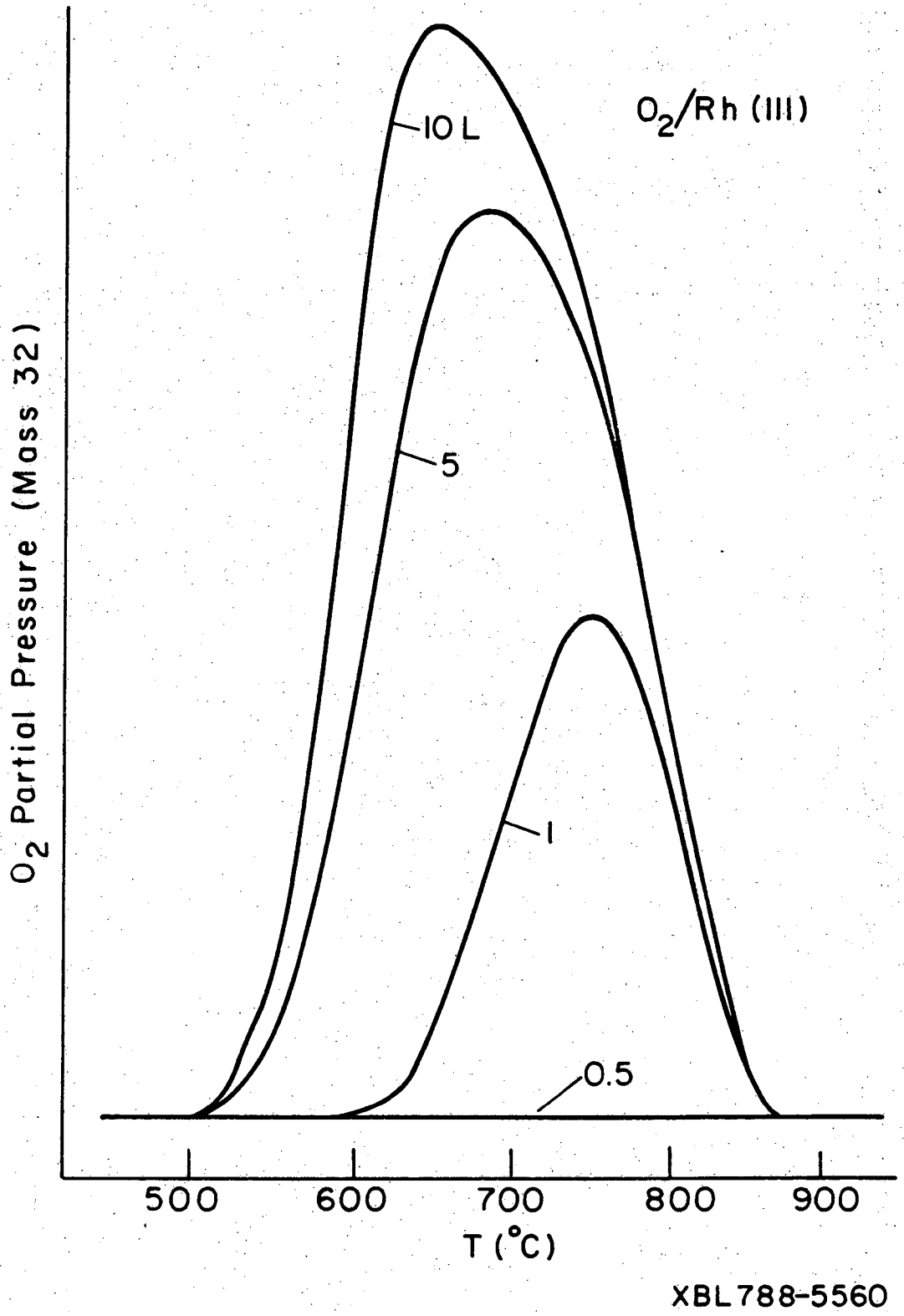

Figure III-43. TDS spectra from chemisorbed oxygen on Rh(111).

decomposition of the epitaxial oxide was investigated. Heating the oxidized surface to 500°C resulted in a large oxygen (mass 32) desorption signal as the epitaxial oxide LEED pattern reverted to a half order LEED pattern. If this pattern was then heated to 900°C a large oxygen desorption signal (more than 100 times the signal from the chemisorbed oxygen in Fig. III-43) was observed between 500 and 900°C. The initial heating to 500°C decomposed the epitaxial Rh_2O_3, but still left a large amount of oxygen in the near surface region which could be removed by heating the crystal to 900°C. Most of the oxygen removed at this temperature must be from the near surface region, since the amount of oxygen desorbed was far too large to be just due to a monolayer of adsorbed oxygen. The size of this desorption peak indicates that the rhodium lattice can dissolve large amounts of oxygen. Thus, oxidation of the Rh(111) surface not only results in the epitaxial growth of Rh_2O_3(0001) but also the dissolution of oxygen into the near surface region.

4) Discussion of the Oxidation Studies

Four different oxygen species can be identified during the oxidation of the Rh(111) surface: chemisorbed oxygen atoms, oxygen dissolved in the rhodium lattice, surface oxide and epitaxial Rh_2O_3(0001). The production of these four oxygen species is interdependent and interconversion between the different species could be accomplished by making the appropriate changes in O_2 partial pressure and crystal temperature. This section will contain a general discussion of the oxidation properties of the Rh(111) surface and a comparison of these properties to other Rh crystal faces and other transition metals.

The chemical and structural properties of the chemisorbed oxygen species on Rh(111) has been extensively discussed and compared to other Group VIII transition metals in previous investigations.[20,25,26,30] The present results are in good agreement with the previous work. Chemisorbed oxygen atoms were produced by low temperature dissociative adsorption of oxygen. Dissociative adsorption of O_2 and the resulting second order desorption kinetics indicated by our results are consistent with previous investigations on Rh(111),[26,30] Ir(111)[109,165] and Pd(111).[166] More evidence for O_2 dissociative adsorption can be obtained from high resolution electron loss spectroscopy (ELS) experiments. Oxygen adsorption of Rh(111) produces a single loss peak at 520 cm^{-1} in the ELS spectrum.[35] This peak is the metal-oxygen stretch of a chemisorbed oxygen atom and falls in the range of values seen for the metal-oxygen stretching frequencies on Cu,[167] Ni,[168] Ru[169] and W.[170]

Chemisorbed oxygen produces half order diffraction patterns on the hexagonal surfaces of Ir,[109,165] Ni,[171] Pd,[166] Rh[25,26,30] and Ru.[25,172] Several methods have been used to determine whether these half order diffraction patterns are from a (2×2) or three domains of a (2×1) surface structure. LEED surface crystallography investigations of the Ni(111)-oxygen[173] and Ir(111)-oxygen[174] systems have been undertaken. These studies were unable to differentiate between the two structures but did determine that the oxygen atoms resided in threefold hollow sites. On Ir(111)[109] the activated ordering of oxygen was used to determine that chemisorbed oxygen forms a (2×1) surface structure, just as in the present studies on Rh(111). A previous low temperature study of oxygen adsorption on Rh(111)[30] found that ordering of the oxygen overlayer was

activated, but did not identify whether the oxygen structure was a (2×1) or (2×2) structure. Determination of surface coverage has also been used to make the distinction between the (2×1) and (2×2) structures since for the (2×1) structure $\theta = 1/2$ while for the (2×2) structure θ could be 1/4, 1/2 or 3/4 (in Fig. III-38, $\theta = 1/4$ is shown). On Ni(111)[171] and Pd(111)[166] $(\sqrt{3}\times\sqrt{3})$ R30°-O structures with $\theta = 1/3$ are observed at oxygen coverages higher than those in the (2×2)-O structures, implying that a true (2×2) surface structure with $\theta = 1/4$ is formed on Ni and Pd. On Ir(111), Pt(111), Rh(111) and Ru(0001) a $(\sqrt{3}\times\sqrt{3})$ 30° structure has not been observed for chemisorbed oxygen. For Ir(111),[109,165] Pt(111)[143] and Ru(0001)[172] surface coverage measurements have shown $\theta = 1/2$ and three domains of a (2×1) structure have been suggested to be the proper structure.

Heating the crystal in the presence of oxygen results in the dissolution of oxygen into the rhodium lattice. If the oxygen pressure and crystal temperature are high enough, oxide formation will occur in addition to the dissolution of oxygen. At the highest oxygen pressures and crystal temperatures, the growth of epitaxial Rh_2O_3 is observed. Thus, while initially low temperature oxygen adsorption just produces chemisorbed oxygen once the temperature is raised, oxygen interaction with the Rh(111) surface rapidly becomes more complex. The two extreme stages of Rh(111) oxidation, the initial chemisorbed oxygen and the final epitaxial oxide, are the easiest to characterize, but the intermediate stages where the nonreactive surface oxide and dissolved oxygen are present are probably of more catalytic importance. Rh_2O_3 would only be stable under highly oxidizing conditions, while chemisorbed oxygen would rapidly

be converted to H_2O or CO_2 if any H_2 or CO were present. The nonreactive surface oxide and dissolved oxygen, however, would be much more stable under reaction conditions and could alter the catalytic properties of rhodium. For CO hydrogenation over polycrystalline Rh[11] and Rh (111)[12] catalysts oxygen pretreatment resulted in both an increase in activity and a change in selectivity. On Pt single crystal catalysts the formation of a surface oxide increased dehydrogenation and hydrogenation activities and changed the dehydrogenation-hydrogenation selectivity.[175] The oxygen AES signal from the surface oxide on Rh[12] and Pt[175] remained constant throughout the experiments indicating these surface oxides were not removed under the reaction conditions. Nonreactive oxygen species have also been formed by high temperature oxidation of the Ir(111)[165] and Pd(111)[166] surfaces.

The structure sensitivity of the platinum metal surface oxides should also be considered. On Pt surfaces preoxidation yielded a higher relative enhancement of dehydrogenation and hydrogenation activities for a kinked surface than for a stepped or flat surface.[175] Oxygen diffusion into the near surface region of Pd was found to be more pronounced on the (111) than on the (110) surface.[166] For Rh oxygen dissolution and nonreactive surface oxide formation has been observed on the (111),[26,30] (100),[22,26] (110)[23,32] and several stepped[24,27] surfaces.

The relationship of dissolved oxygen to these surface oxides is also important to consider. One possibility that the results suggest is that only after the near surface region becomes saturated with dissolved oxygen does oxygen precipitate at the surface and form the surface oxide.

This is reasonable since at the high temperatures needed to form the surface oxide oxygen is soluble in the rhodium lattice and the crystal must be heated for extended periods of time to form the nonreactive surface oxide. If this is the case, then dissolved oxygen and the surface oxide are very closely related and it will be important to consider the oxygen concentration gradient in the near surface region. Large changes in the oxygen concentration profile could occur that would not be detected by AES if the oxygen concentration in the upper two or three layers was not markedly affected. The low energy AES transitions are useful in following changes in the distribution of valence band electrons during oxidation, but use of the oxygen AES signal to follow changes in the oxygen concentrations during reactions may be misleading.

Epitaxial growth of Rh_2O_3 has not previously been reported on rhodium single crystals but studies on Rh(110)[23,32] observed the formation of several ordered surface structures when the crystal was heated in oxygen. Some of these structures were proposed to contain an adlayer of rhodium and oxygen atoms.[23] The growth of epitaxial oxides has been observed on most of the other Group VIII transition metals, however. In Table III-13 the surface orientation and approximate temperatures of formation of these epitaxially grown transition metal oxides have been summarized.

The transition metals in Table III-13 can be divided into two groups, the 3d metals (Fe, Co, Ni) which readily form epitaxial oxides at or near room temperature and the platinum metals (Rh, Pd, Ir, Pt) which are much more resistant to oxidation and only exhibit epitaxial

Table III-13. The structure and approximate temperatures of epitaxial oxide formation on the Group VIII transition metals.

Substrate	Epitaxial Oxide	Approximate Temperatures of Epitaxial Oxide Formation (°C)	Reference
Fe(001)	FeO(001)	200	178
Fe(001)	FeO(111)	200	178
CO(0001)	CoO(111)	25	176
Co(0001)	Co_3O_4(111)	325	176
Ni(111)	NiO(111)	25	177
Rh(111)	Rh_2O_3(0001)	700	this study
Pd(111)	PdO(100)	725	166
Ir(111)	Ir oxide	1025	183
Pt(111)	PtO_2(0001)	1000	87
Pt(110)	PtO(100)	800	184

oxide formation at high temperatures. This difference generates distinctly different behavior of these two groups during oxidation. For the 3d metals oxidation proceeds directly from chemisorbed oxygen to the epitaxial oxide.[175-178] On the platinum metals, there are large temperature differences between the chemisorbed oxygen and the epitaxial oxide growth stages and dissolved oxygen and nonreactive surface oxides are formed during the intermediate stages of oxidation.[165,166,175]

The AES results on oxidized Rh(111) are in good agreement with results on other oxidized transition metals. On Pt[87,88] and Ni[179] the oxygen KLL transitions shift to lower energies during oxidation by 6 and 1.7 eV, respectively, similar to the 3 eV shift we encountered for the Rh-oxygen system. The oxidation of Zn produced low energy AES transitions from Zn oxide which were broader and shifted downward in energy by 3 to 4 eV compared to the low energy AES transitions of clean Zn,[180] as is the case for oxidized Rh. For Zn[180] the broadening and shift of the low energy oxide peaks have been interpreted as an increase in the d band width and variation of extra-atomic relaxation energies. Peak broadening and shifts have also been seen on oxidized Ni,[179,181,182] resulting from differences between the d band in Ni oxide and metallic Ni. A low energy oxide peak shifted downward 3 eV in energy from the low energy metallic peak has been observed during the oxidation of Fe(001)[178] and was interpreted as resulting from positively charged Fe in an Fe oxide phase.

E. CO Hydrogenation Over Rhodium Crystals

1) Clean Polycrystalline Rh Foil and Single Crystalline Rh(111) Surfaces

The buildup of reaction products during a typical three hour CO hydrogenation experiment at 300°C, 6 atm and $3H_2$:1CO over the clean rhodium crystals is shown in Fig. III-44. CO hydrogenation over both the clean polycrystalline Rh foil and the clean single crystal Rh(111) samples yielded the same results. In determining the hydrocarbon concentration (molecules·site^{-1}) the atom density of the Rh(111)surface (1.6×10^{15} atoms·cm^{-2}) was used as the site density. This procedure should result in a conservative estimate of the hydrocarbon concentration because it assumes all of the rhodium atoms in the surface are active. Methane was the major product (90 wt %) having an initial turnover number (TN) of 0.15 molecules·site^{-1}·sec^{-1} at 300°C. Small amounts of C_2 and C_3 hydrocarbons were also formed, but no oxygenated products were detected under these conditions.

As the reaction progresses the CH_4 TN decreases and the relative amounts of C_2H_4 and C_2H_6 change, indicating catalyst poisoning and selectivity changes are occurring during the reaction. AES spectra were recorded at various stages of the reaction to determine if the surface composition was changing during the reaction. After a three hour reaction small amounts of carbon, sulfur and chlorine were detected on the surface (see Fig. III-45b). The carbon AES signal in Fig. III-45b corresponds to less than a monolayer of carbon on the surface. The carbon concentration increased to this value during the initial 30 minutes of

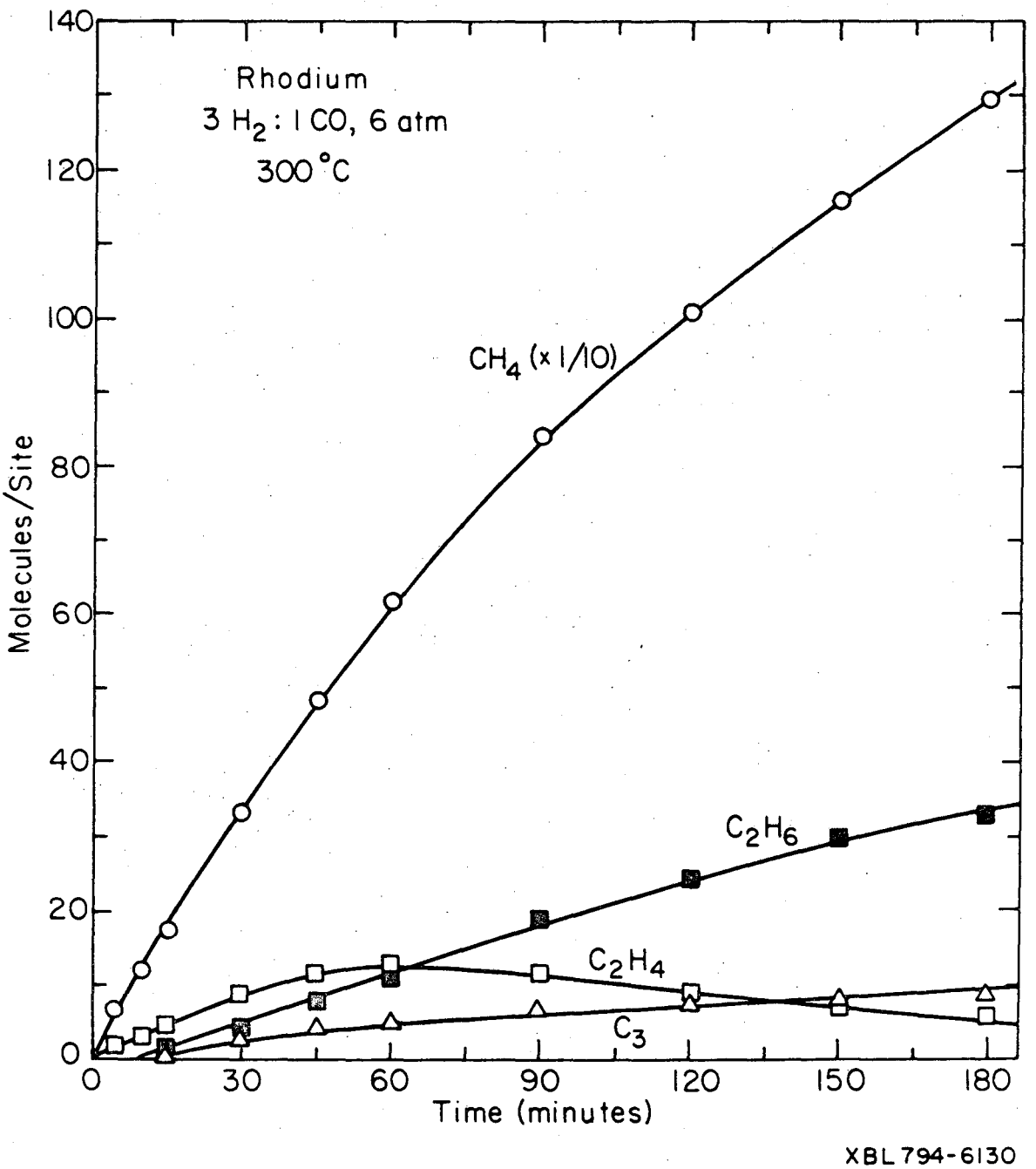

Figure III-44. Production of hydrocarbons over a clean rhodium crystal from a $3H_2$:1CO mixture at 6 atm and 300°C.

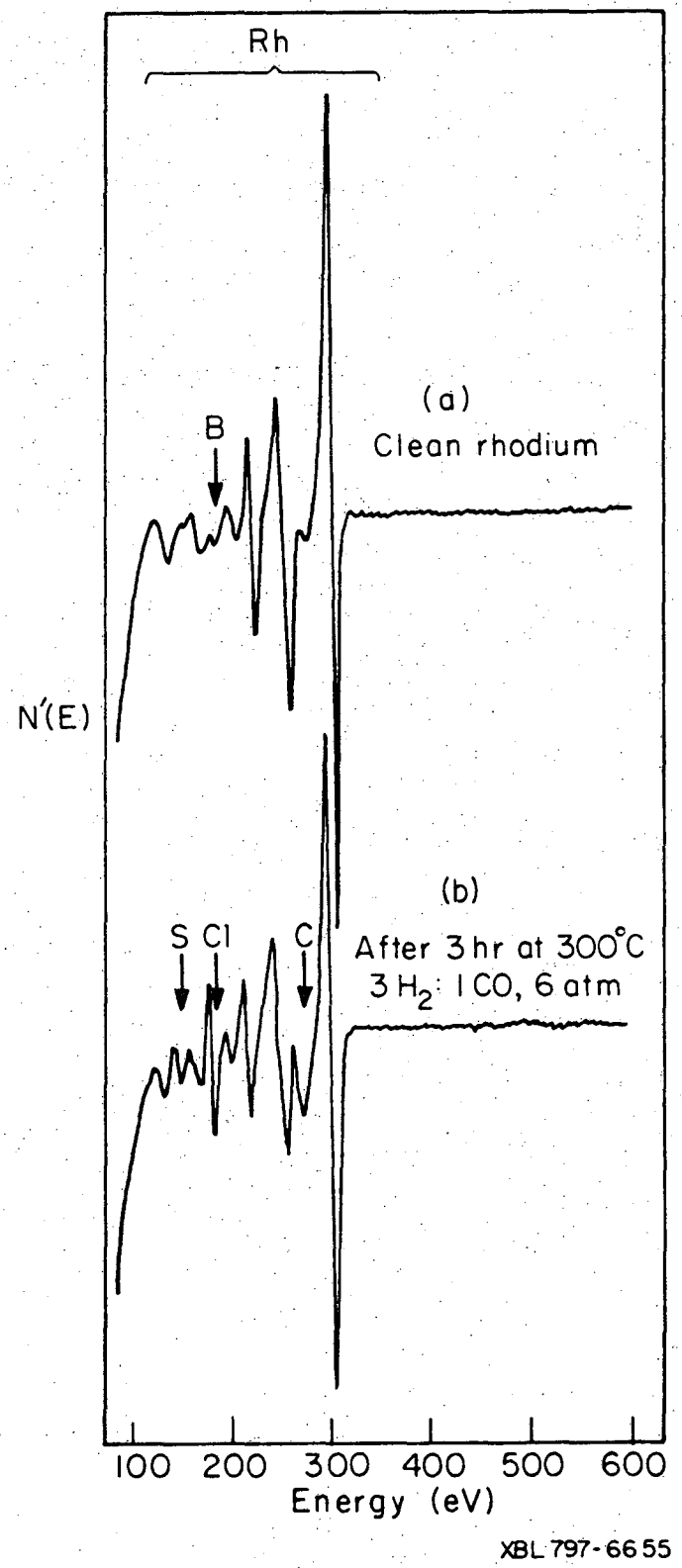

Figure III-45. AES spectra from rhodium crystals (a) before a reaction over a clean surface and (b) after a 3 hour reaction of a $3H_2$:1CO gas mixture at 300°C and 6 atm.

the reaction and then remained constant for the remainder of the reaction. Thus the carbon concentration is constant while changes in the catalyst poisoning and selectivity are occurring. The close proximity of the Rh AES peaks (256 and 302 eV) to the C AES peak (272) prevented analyzing the lineshape of the carbon peak to determine whether a change in the chemical state of carbon was occurring during the reaction, for example carbide to graphite. The Cl AES signal also reached its maximum intensity during the first 30 minutes of the reaction. Most of the increase in the S AES signal occurred during the first 30 minutes of reaction, but unlike the Cl and C intensities the S intensity increased slightly during the remainder of the reaction. Therefore the observed changes in the reaction could be due to either the buildup of sulfur on the surface or a conversion of the carbon overlayer from active form to an inactive form.

Experiments were carried out varying the H_2:CO ratio and reaction temperature. These results obtained over the clean Rh crystals at 6 atm were similar to the previously reported results for clean Rh polycrystalline foil at 1 atm.[11] No oxygenated products were detected during any of these experiments. Thus the clean surface results will not be described further.

2) Preoxidized Rh(111) Crystal

Oxygen pretreatment (800 torr, 600°C, 30 minutes) of the Rh(111) crystal had a dramatic effect on the CO hydrogenation results. All the initial hydrocarbon TN's increased by at least an order of magnitude, small amounts of C_4^+ hydrocarbons were produced and three oxygenated

hydrocarbons (methanol, ethanol and acetaldehyde) were produced. The buildup of the C_1 to C_3 hydrocarbon reaction products during a three hour CO hydrogenation experiment over a preoxidized Rh(111) surface at 300°C, $3H_2$:1CO, and 6 atm is shown in Fig. III-46. The product distributions after two hours of CO hydrogenation over pretreated Rh(111) crystals are shown in Fig. III-47.

The TN's which were calculated still using a site density of 1.6×10^{15} sites$\cdot$cm^{-2}, decreased markedly during the first 30 minutes then slowly decreased until they had reached a fairly constant value by 180 minutes. Even after 180 minutes the CH_4 TN was a factor of three to four times higher than the initial CH_4 TN from a clean Rh crystal. The fall off in the TN's can be correlated with the amount of oxygen in the near surface region. AES spectra taken at before and after the reaction are shown in Fig. III-48. During the first 30 minutes of the reaction the O_{515}/Rh_{302} peak-to-peak ratio decreases from 0.6 to 0.05 and slightly less than a monolayer of carbon is deposited on the surface. After the first 30 minutes the oxygen and carbon AES signals remain fairly constant. Thus the highest activity is attained at the highest oxygen concentrations and after the steady state concentrations of oxygen and carbon are reached the activity decreases to a constant value. Significant amounts of methanol, ethanol and acetaldehyde continue to be produced after the first 30 minutes of reaction. The constant intensity of the oxygen AES signal during this time would indicate that the oxygen in these molecules originate from the CO molecules and not the oxygen in the near surface region. The constant intensity of the oxygen AES signal

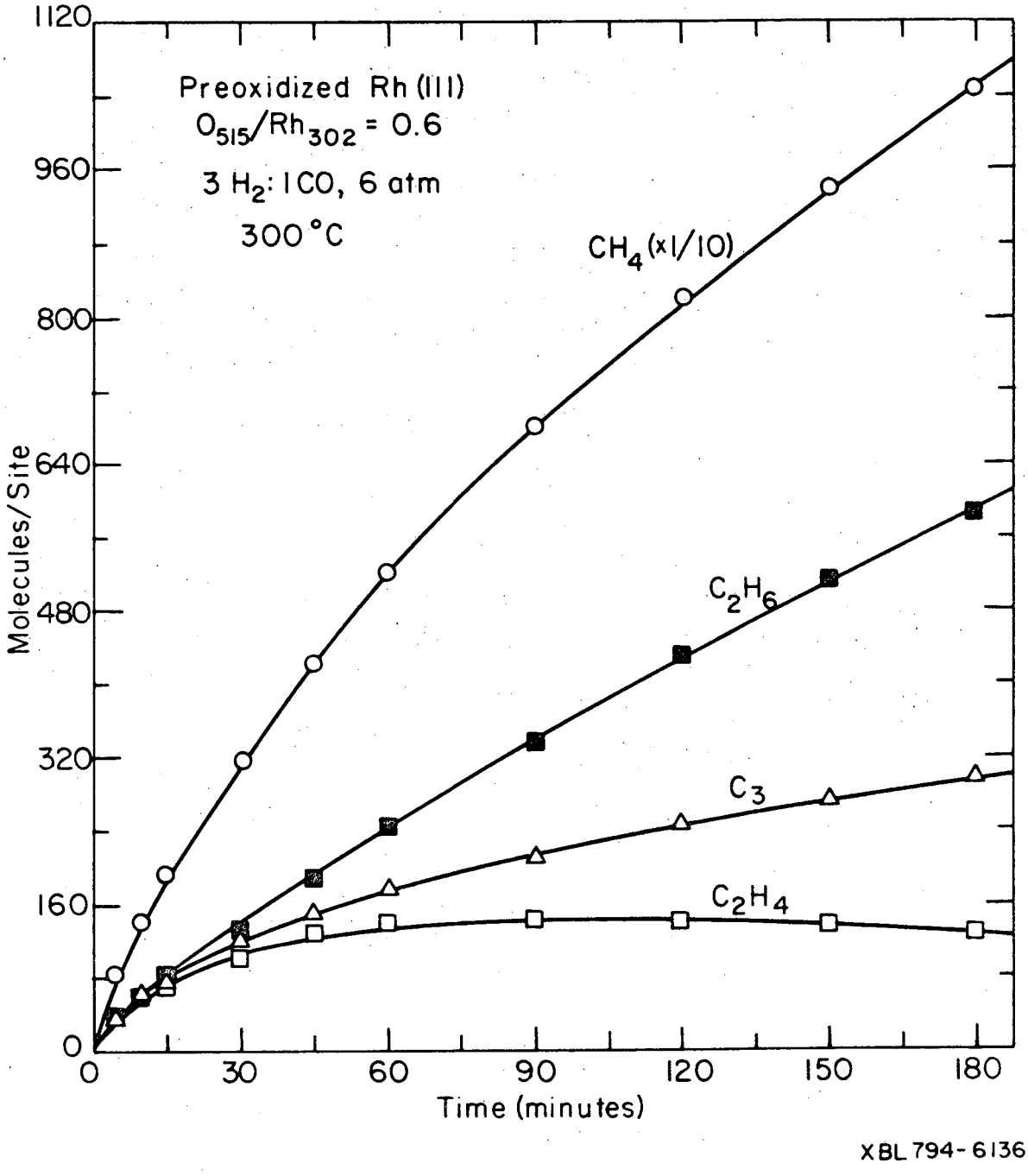

Figure III-46. Buildup of C_1 to C_3 hydrocarbons during CO hydrogenation over a preoxidized Rh(111) crystal.

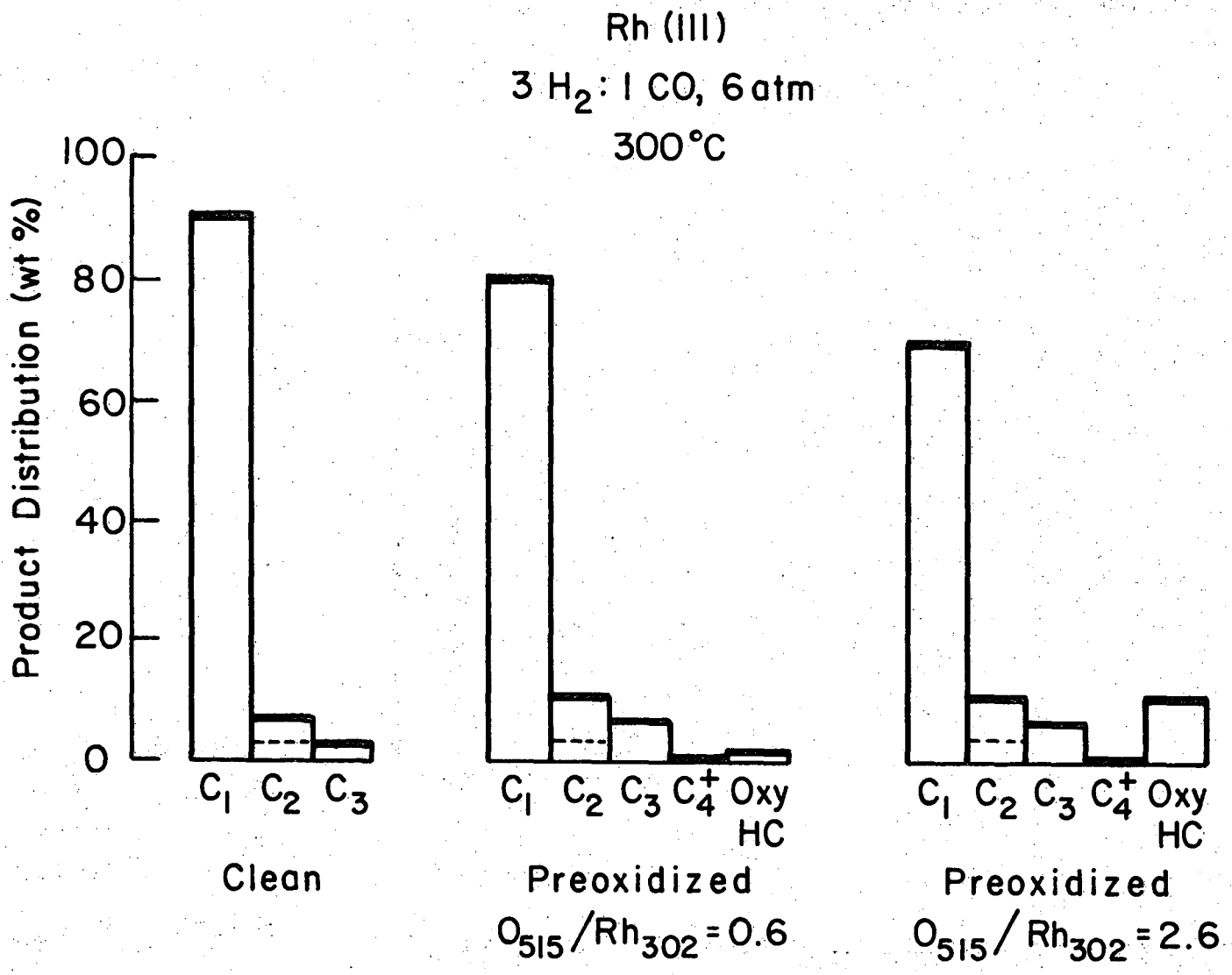

XBL 794-6137

Figure III-47. Product distribution, in weight percent, after two hours of CO hydrogenation over pretreated Rh(111) crystals. The areas above and below the dotted line in the C_2 fraction represent the amount of ethane and ethylene, respectively. Oxy HC is the sum of the CH_3OH, CH_3CH_2OH and CH_3CHO fractions.

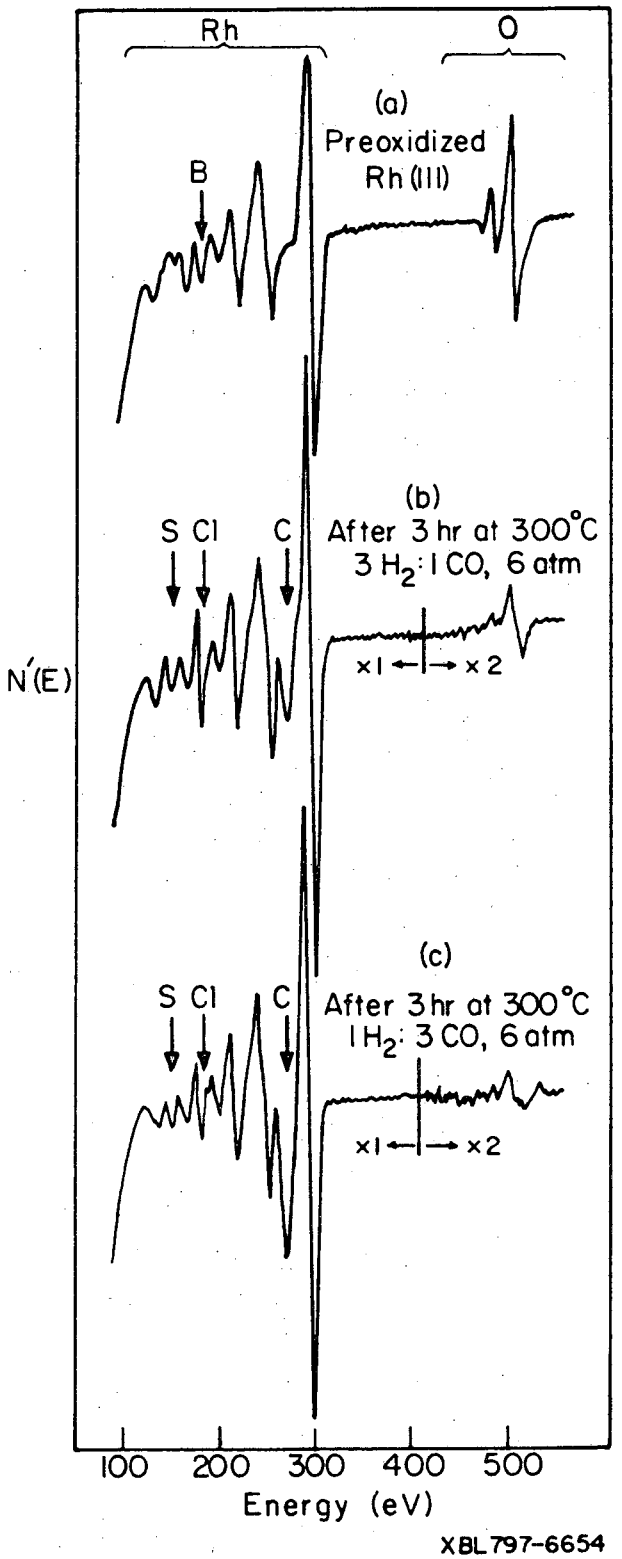

Figure III-48. AES spectra from a preoxidized Rh(111) crystal. (a) before a reaction $O_{515}/Rh_{302} = 0.6$), (b) after a 3 hour reaction of a $3H_2$:1CO gas mixture at 300° and 6 atm, and (c) after 3 hour reaction of a $1H_2$:3CO gas mixture at 300°C and 6 atm.

could be misleading because during the oxidation pretreatment a large amount of oxygen is dissolved in the rhodium lattice.[29] Therefore if oxygen was being removed from the surface during this stage of the reaction it could be replaced by oxygen diffusing from the bulk to the near surface region resulting in no detectable change in the oxygen concentration in the upper 2 or 3 rhodium layers, the region probed with AES.

The decrease in the weight percent of methane in the product distributions with increasing oxygen concentration (Fig. III-47) is not due to the decrease in the amount of methane produced. The CH_4 TN increases with increasing oxygen concentration but the increase in the TN's of the other reaction products is even greater. Increasing the oxygen concentration to $O_{515}/Rh_{302} = 0.6$ increases the initial C_2H_6 and C_3 TN's by two orders of magnitude compared to the one order of magnitude increase in the CH_4 TN. Further increase of the O_{515}/Rh_{302} ratio to 2.6 increased all the initial hydrocarbon TN's by a factor of 4 to 6 and while the production of methanol, ethanol and acetaldehyde was markedly increased.

The effect of varying the H_2:CO ratio is shown in Figs. III-49 to III-51. Decreasing the H_2:CO ratio from 3:1 to 1:3 resulted in an increase in the amount of higher molecular weight hydrocarbons and the C_2H_4 to C_2H_6 ratio in the product distribution. These increases are due to a slight falloff in the initial CH_4 TN and an order of magnitude decrease in the initial C_2H_6 TN while the initial C_2H_4 and C_3 TN's remained constant. These trends continued if the reaction temperature was decreased to 250°C for the $1H_2$:3CO mixture (see Fig. III-52). The product distribution under these reaction conditions contains less than

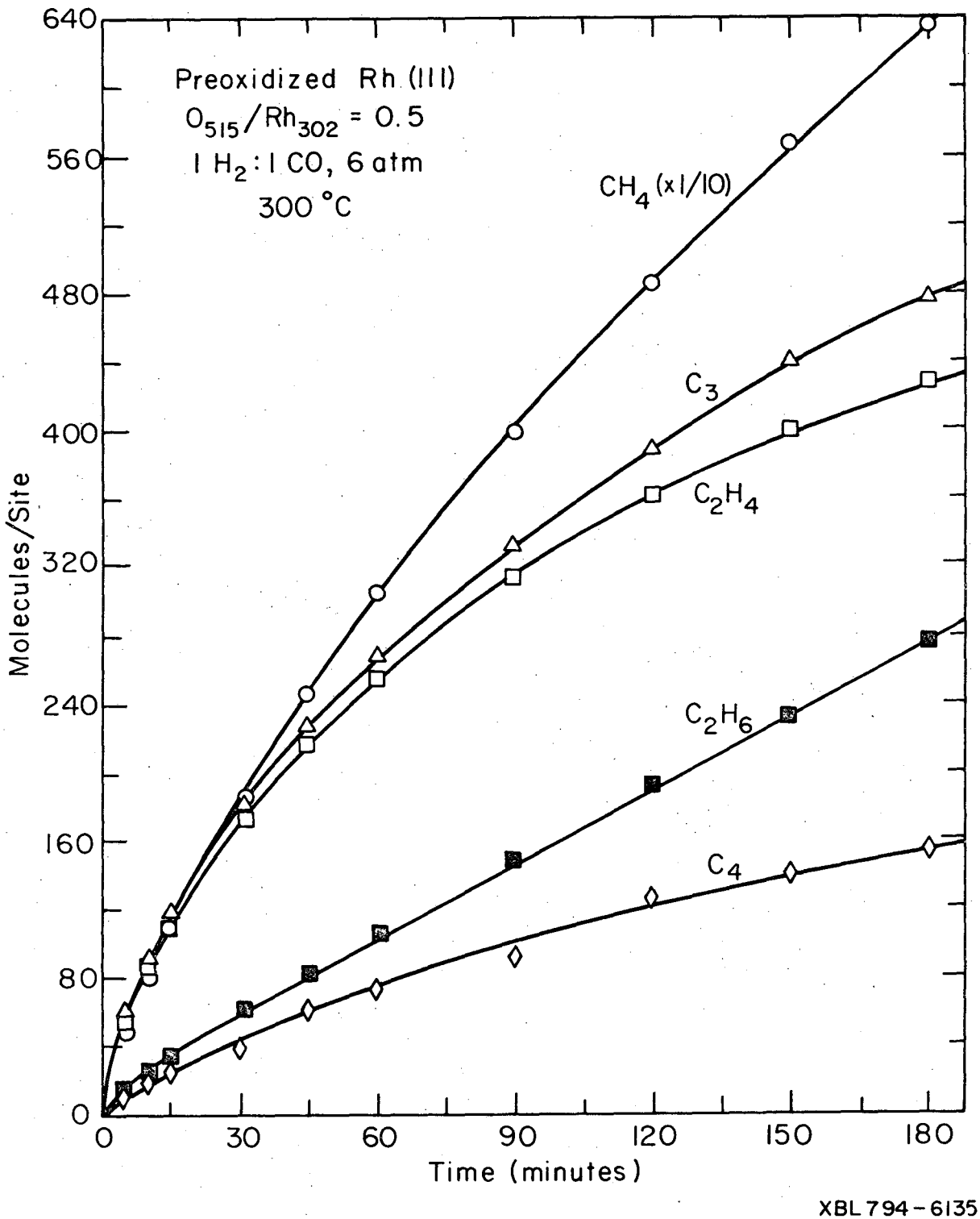

Figure III-49. Buildup of C_1 to C_4 hydrocarbon products during CO hydrogenation over a preoxidized Rh crystal.

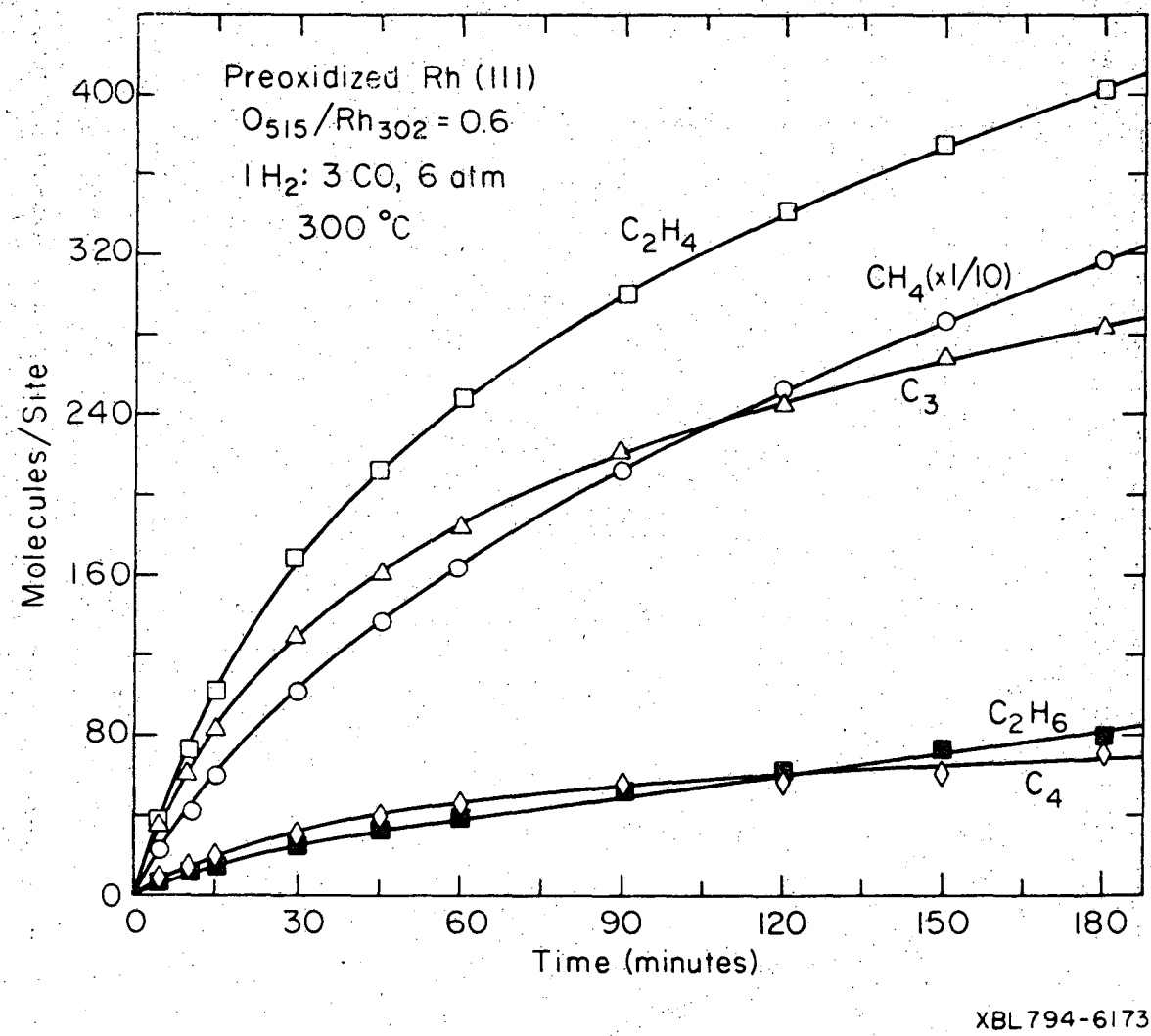

Figure III-50. Buildup of C_1 to C_4 hydrocarbon products during CO hydrogenation over a preoxidized Rh crystal.

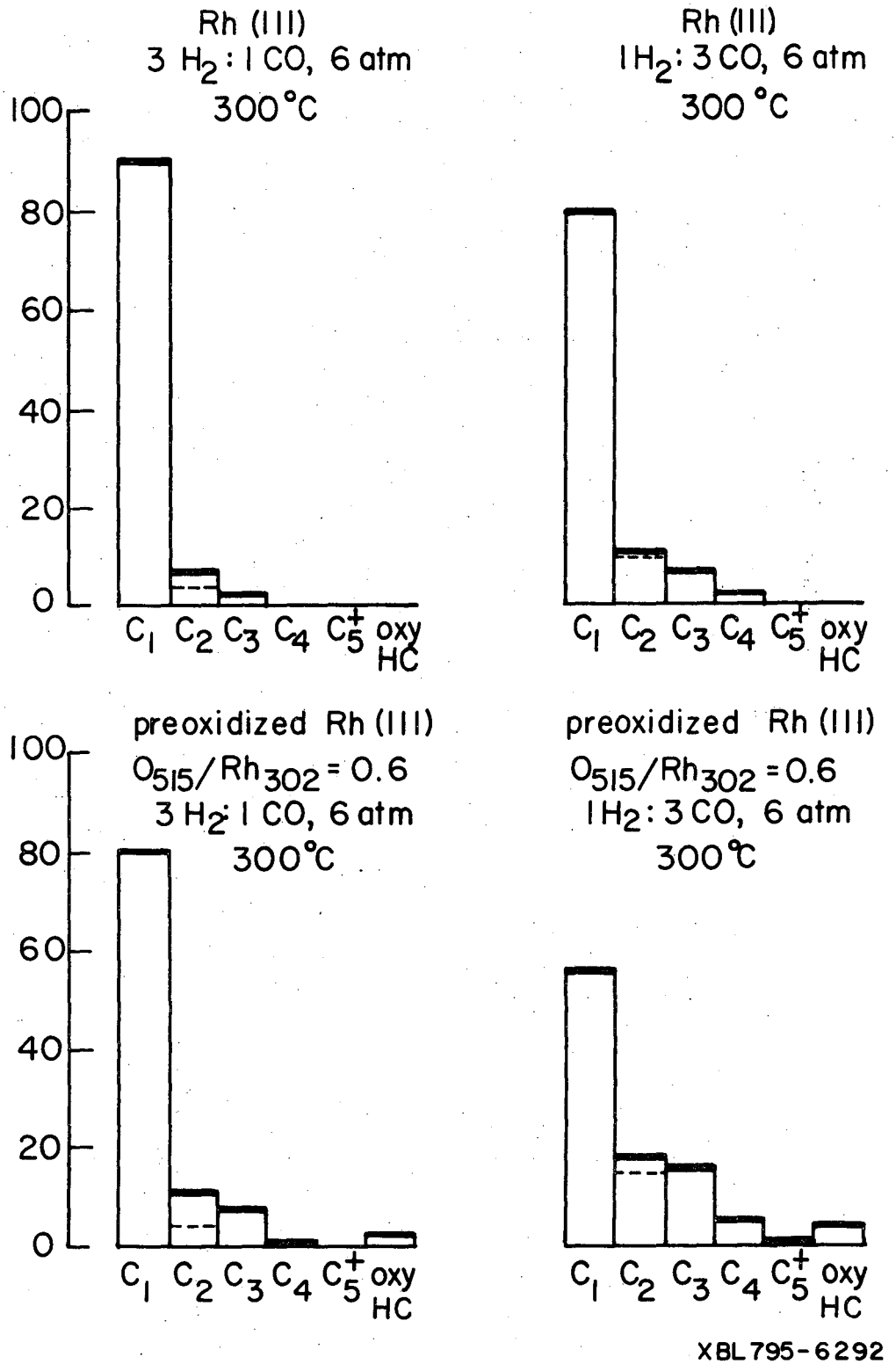

Figure III-51. Product distribution, in weight percent, after 2 hours of CO hydrocarbon over pretreated Rh(111) crystals. The areas above and below the dotted line in the C_2 fraction represent the amount of ethane and ethylene, respectively. Oxy HC is the sum of the CH_3OH, CH_3CH_2OH and CH_3CHO fractions.

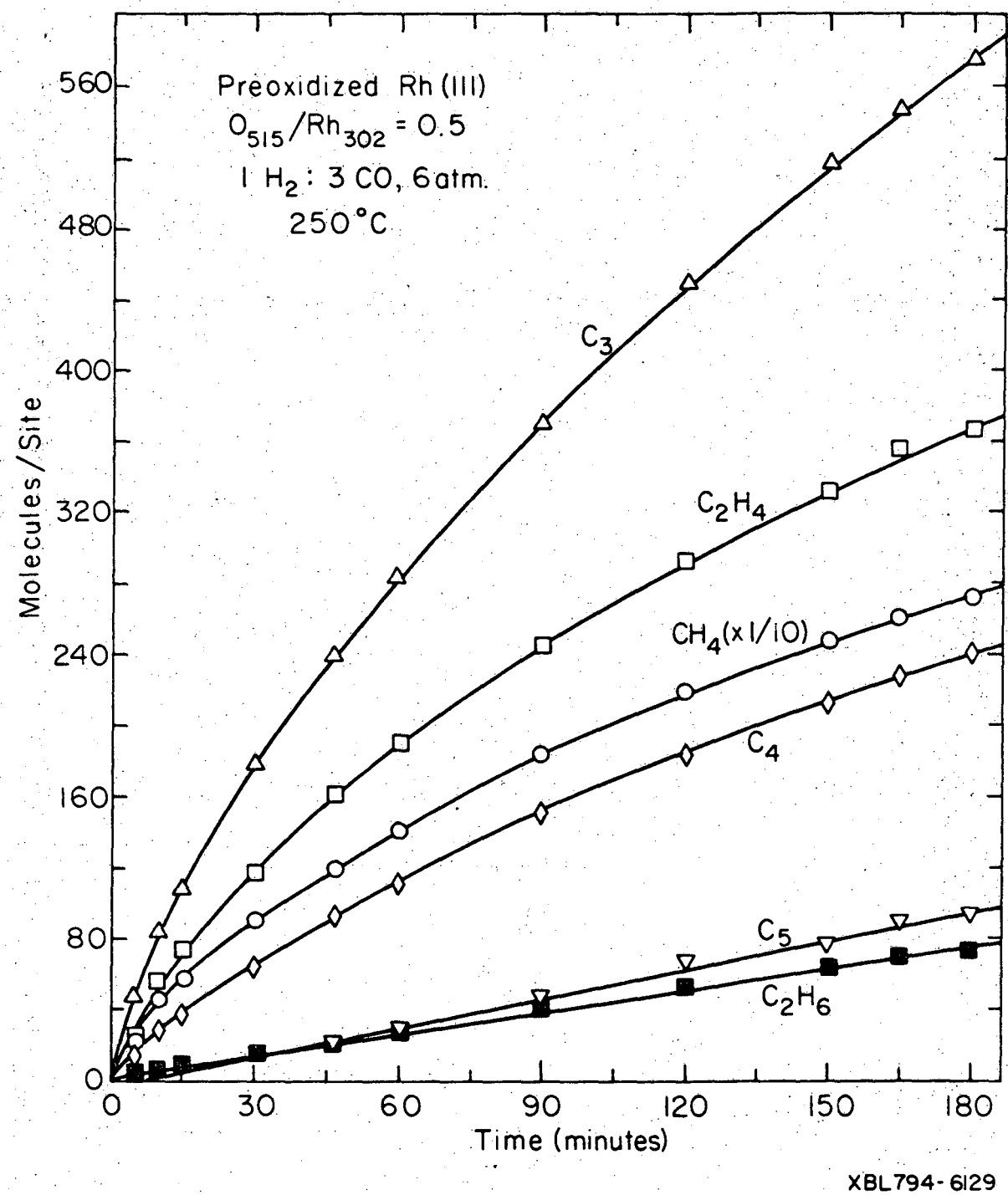

Figure III-52. Buildup of C_1 to C_5 hydrocarbons products during CO hydrogenation over a preoxidized Rh crystal.

40 wt % CH_4 and an increased amount C_5 hydrocarbons ($\sim$10 wt %). More carbon was deposited during the CO rich reactions resulting increased in an amount of curvature in the first 90 minutes of the product versus time plots in Figs. III-50 and 52. The AES results in Fig. III-48c show that two to four monolayers of carbon were deposited during the CO rich reactions. Generally a slightly larger carbon AES signal is seen after a CO rich reaction over an initially clean Rh(111) crystal than over a preoxidized Rh(111) crystal. The type of oxygenated products formed during CO hydrogenation depends on the H_2:CO ratio. Methanol, ethanol and acetaldehyde are produced from a $3H_2$:1CO mixture but only acetaldehyde is produced from a $1H_2$:3CO mixture.

3) Preoxidized Rh Foil

The results of CO hydrogenation over a preoxidized Rh polycrystalline foil were similar to those obtained over the preoxidized Rh(111) single crystal. Figures III-53 and 54 show the CO hydrogenation results over a preoxidized Rh foil at 300°C, $3H_2$:1CO and 6 atm. Preoxidation of the Rh foil resulted in increased initial TN's, formation of oxygenated products and formation of small amounts of C_4^+ hydrocarbons. During the CO hydrogenation there was a large decrease in the O_{515}/Rh_{302} ratio and an increase in the carbon signal during the first 30 minutes. By 30 minutes a steady state concentration of oxygen and carbon in the near surface region had been reached. The AES spectra from the preoxidized Rh foil under H_2 rich reaction conditions was the same as shown for the preoxidized Rh(111) crystal in Fig. 48a and 48b, except more boron segregated to the surface during oxidation of the Rh foil.

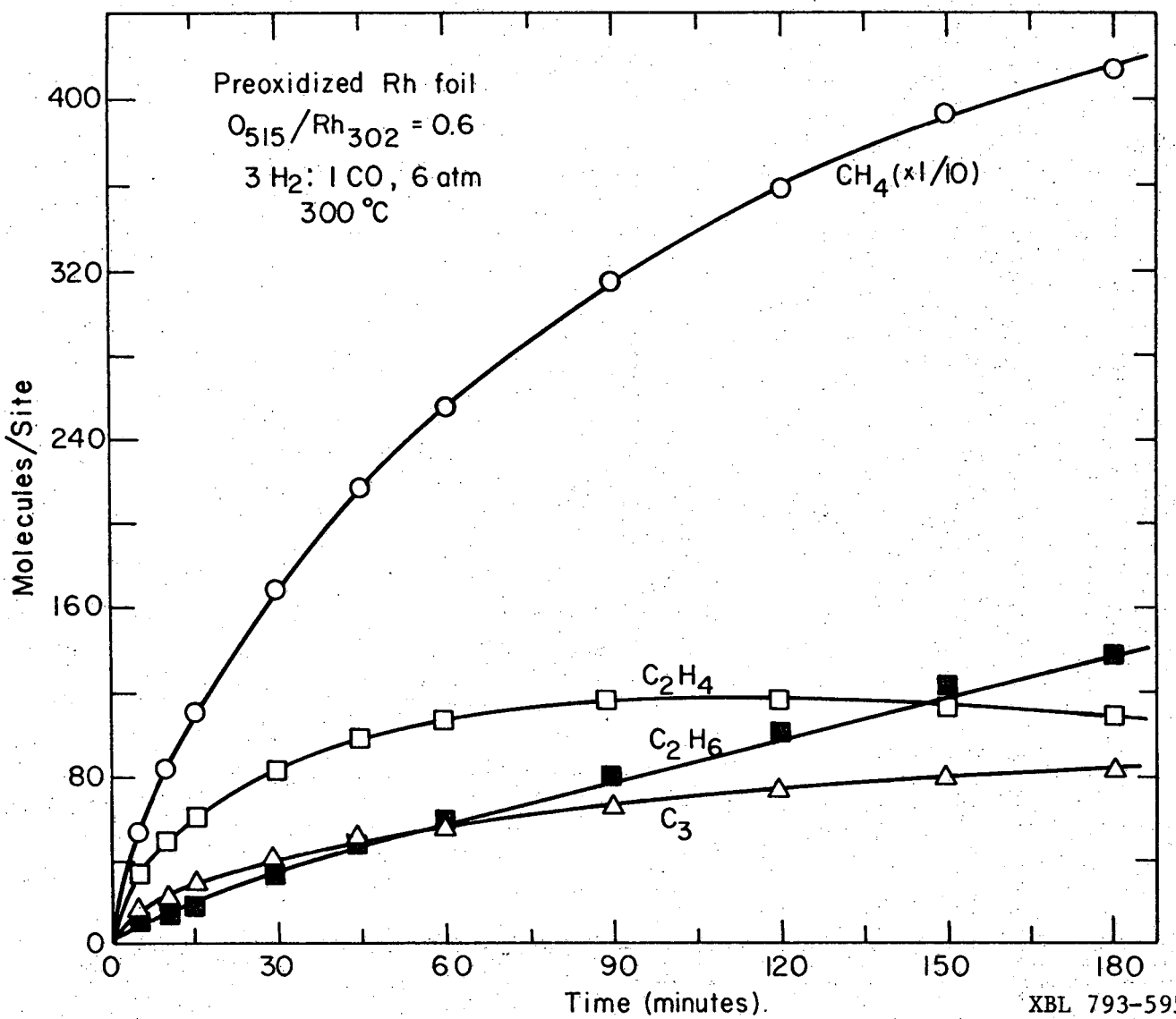

Figure III-53. Buildup of C_1 to C_3 hydrocarbon products during CO hydrogenation over a preoxidized Rh foil.

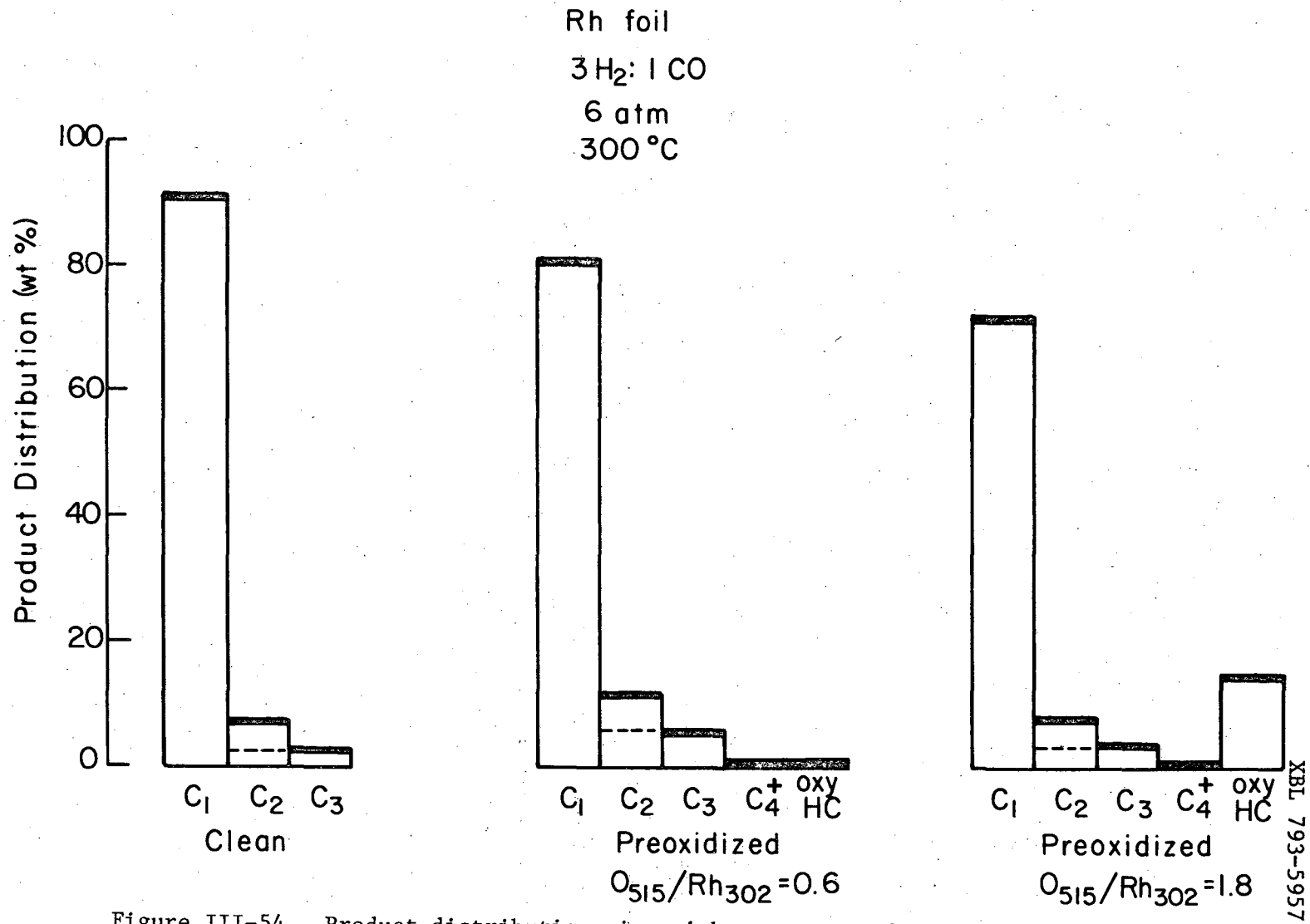

Figure III-54. Product distribution, in weight percent, after 2 hours of CO hydrogenation over pretreated Rh foil. The areas above and below the dotted line in the C_2 fraction represent the amount of ethane and ethylene, respectively. Oxy HC is the sum of the CH_3OH, CH_3CH_2OH and CH_3CHO fractions.

Preoxidation of the foil did not increase the initial TN's as much as was observed on the (111) cyrstal, especially the C_2H_6 TN which yielded a higher olefin to paraffin ratio for the C_2 fraction on the preoxidized Rh foil. Both preoxidized surfaces produced methanol, ethanol, and acetaldehyde but smaller amounts of ethanol were produced over the preoxidized foil.

The results of decreasing the H_2:CO ratio over the preoxidized Rh foil are shown in Figs. III-55 to 57. As over the preoxidized Rh(111) crystal the percent of higher weight hydrocarbons increased, the C_2H_4 to C_2H_6 ratio increased and the initial CH_4 and C_2H_6 TN's decreased. Again the only oxygenated product formed under CO rich conditions was acetaldehyde. The major difference between the CO rich reactions over the two preoxidized surfaces was the increased amount of carbon deposited on the preoxidized foil. This resulted in the large amount of curvature in the product versus time plots in Fig. III-56. By 60 minutes several monolayers of carbon had been deposited on the preoxidized foil and the TN's had decreased by almost an order of magnitude. After 60 minutes carbon continued to buildup but the TN's remained constant.

The results of varying the reaction temperature for a $3H_2$:1CO gas mixture over a preoxidized Rh foil are shown in Figs. III-58 to 60. These figures show that as the reaction temperature is decreased the C_2H_4 to C_2H_6 ratio increases and relative amount of higher weight hydrocarbons and oxygenated products increase. At 400°C CH_4 and C_2H_6 are essentially the only reaction products, while at 250°C significant amounts of C_3, C_4^+ and oxygenated hydrocarbons are produced. The activation energy of methane formation, E_a, over the preoxidized Rh foil was

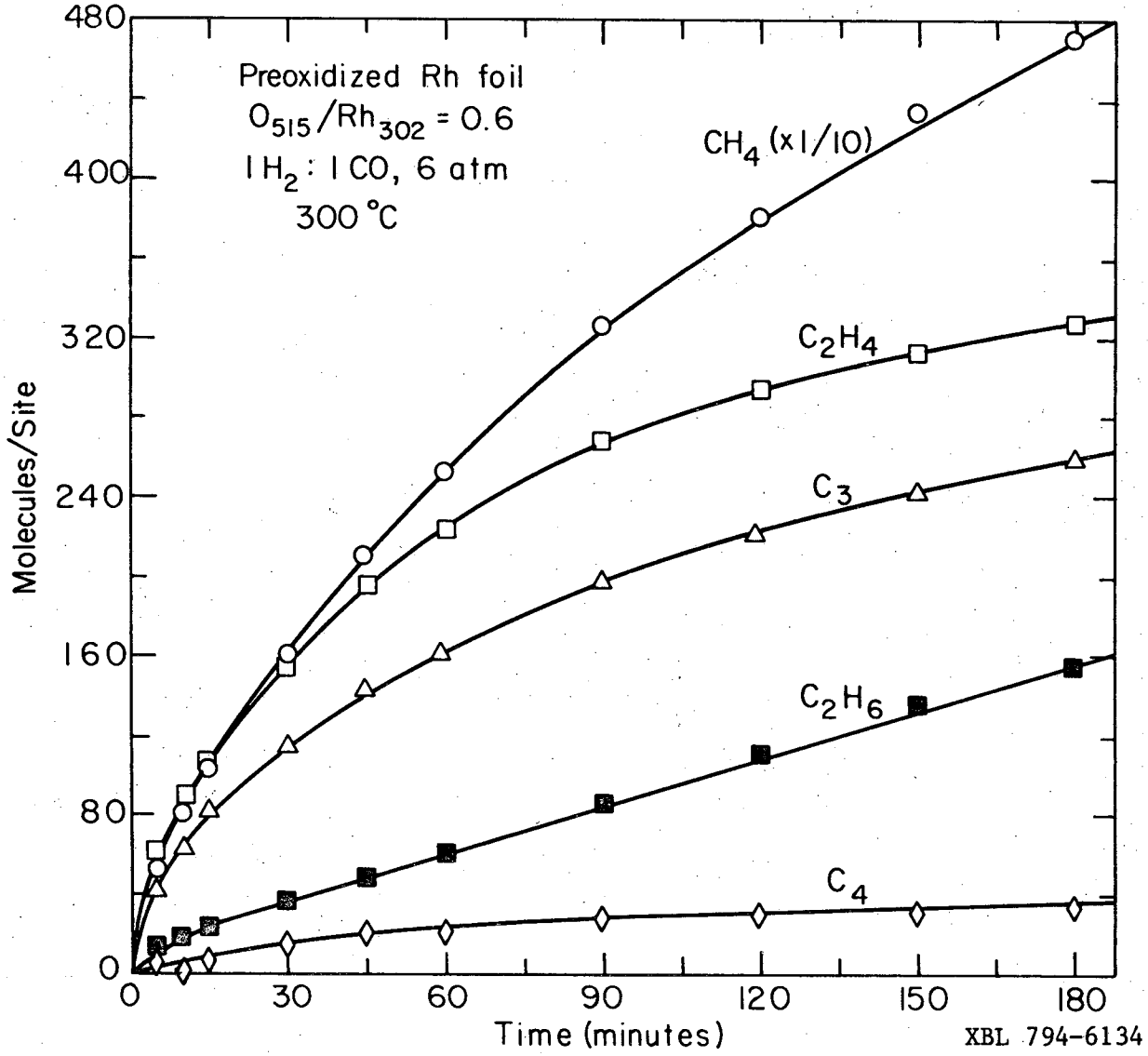

Figure III-55. Buildup of C_1 to C_4 hydrocarbon products during CO hydrogenation over a preoxidized Rh foil.

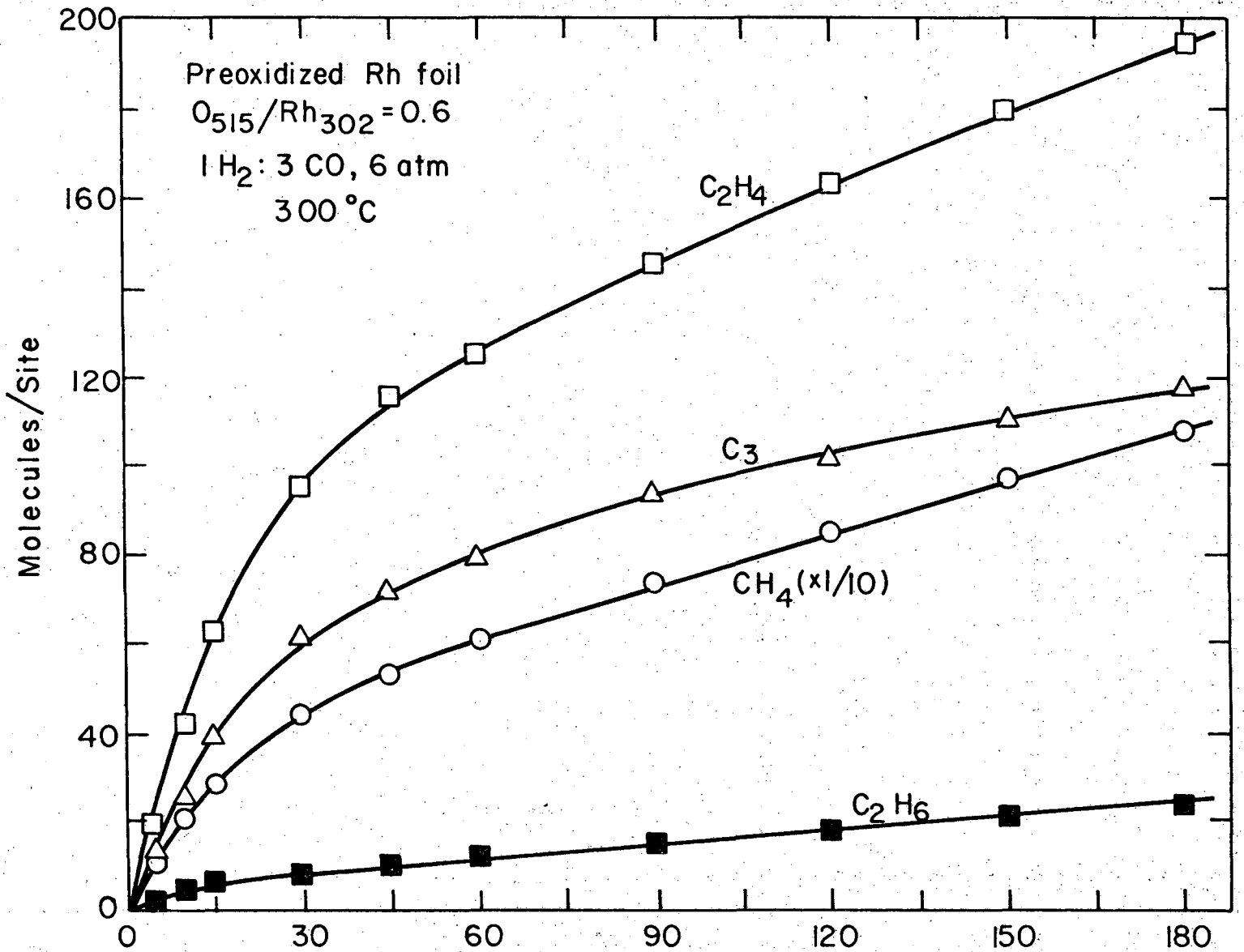

Figure III-56. Buildup of C_1 to C_3 hydrocarbon products during hydrogenation over a preoxidized Rh foil.

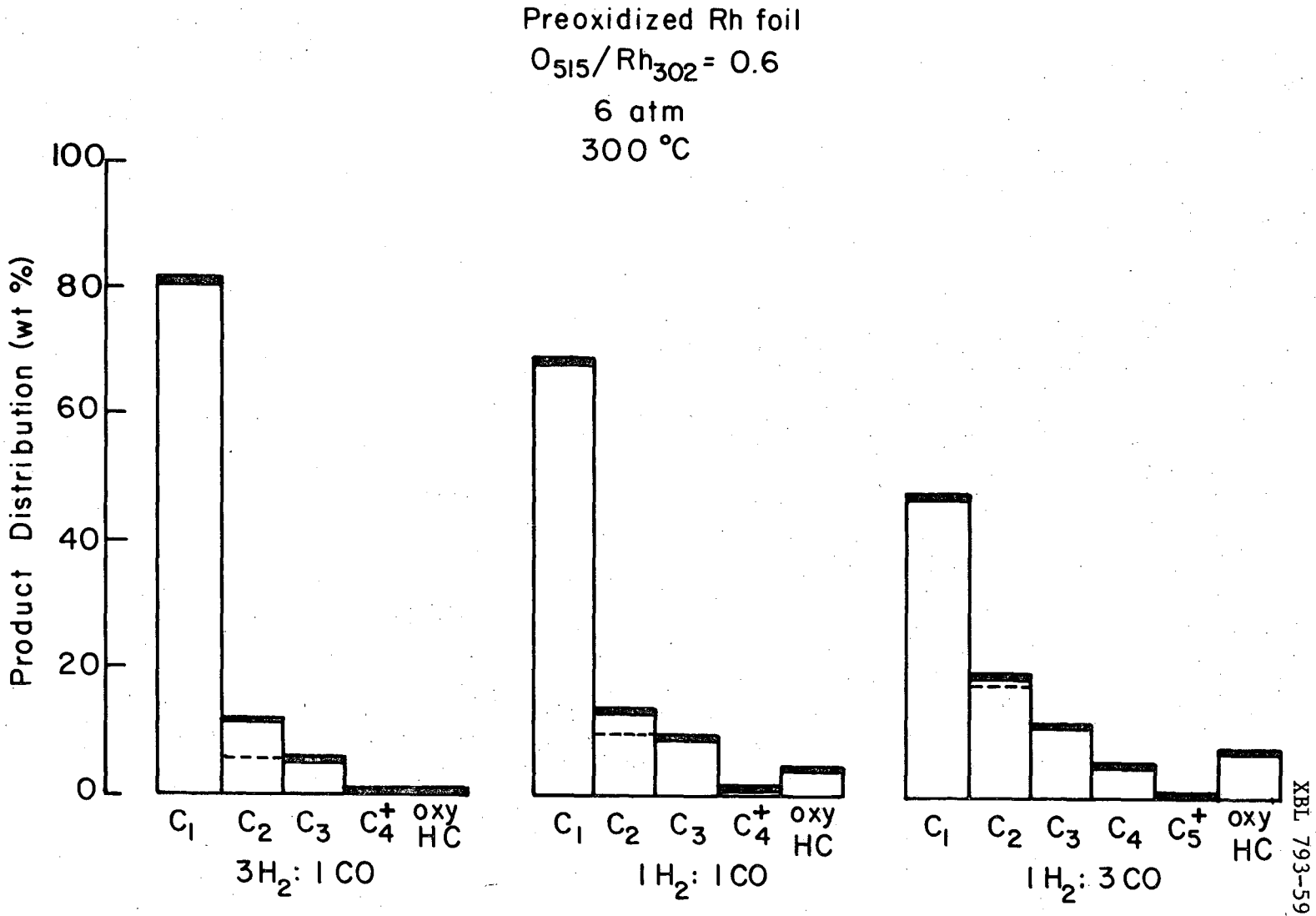

Figure III-57. Product distribution, in wieght percent, after 2 hours of CO hydrogenation over preoxidized Rh foil. The areas above and below the dotted line in the C_2 fraction represent the amount of ethane and ethylene, respectively. Oxy HC is the sum of the CH_3OH, CH_3CH_2OH and CH_3CHO fractions.

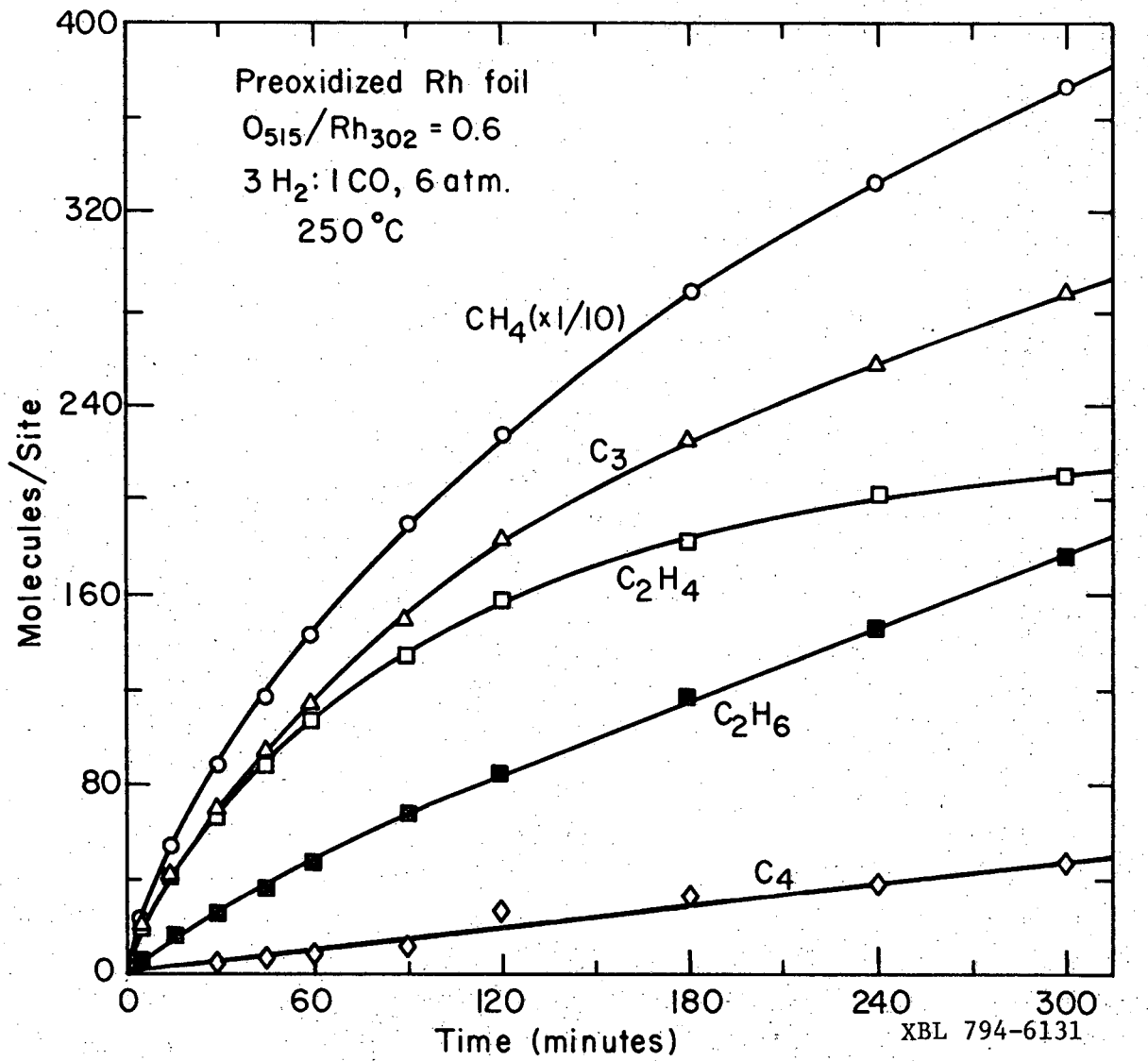

Figure III-58. Buildup of C_1 to C_4 hydrocarbon products during CO hydrogenation over a preoxidized Rh foil at 250°C.

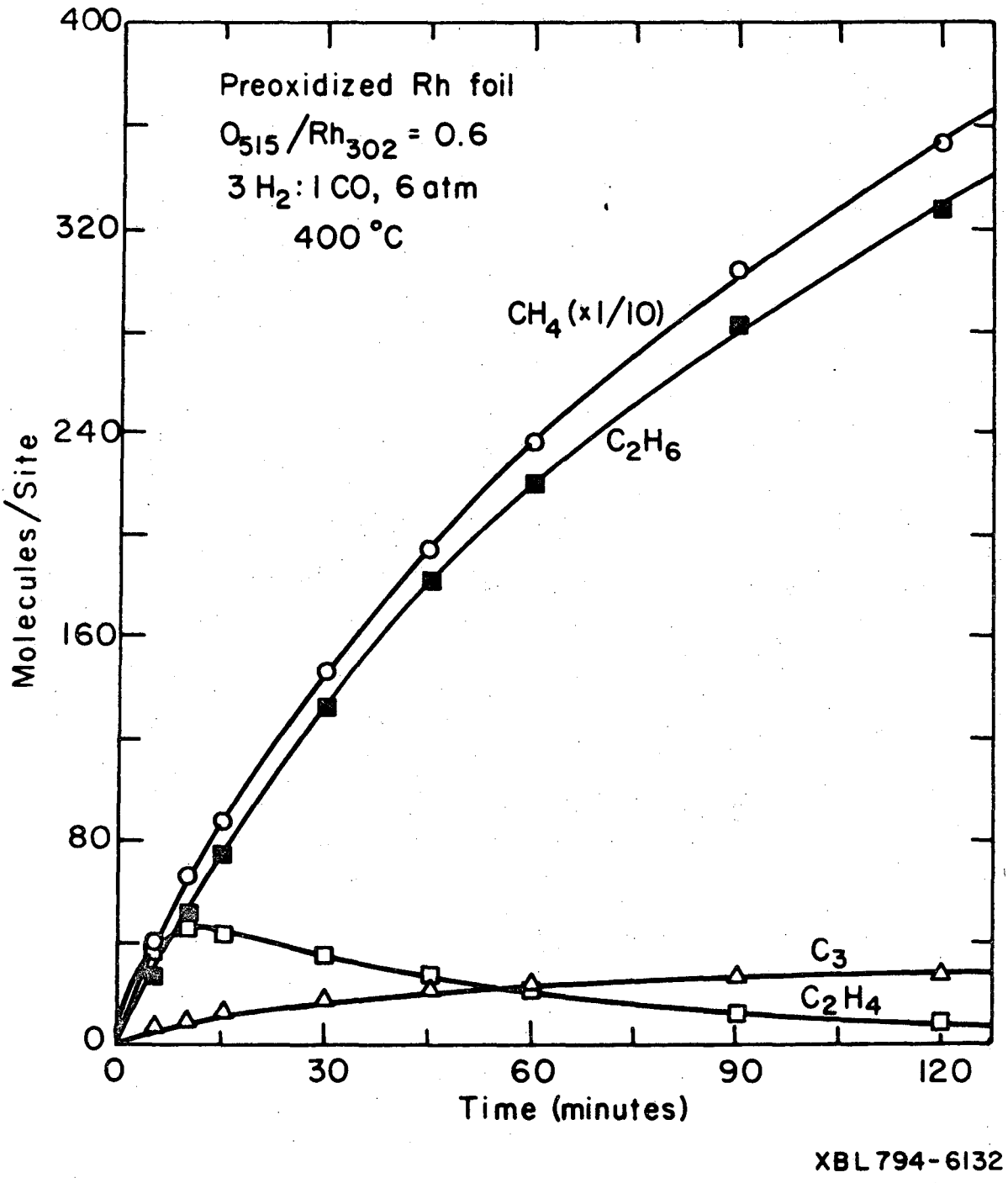

Figure III-59. Buildup of C_1 to C_3 hydrocarbon products during CO hydorgenation over a preoxidized Rh foil at 400°C.

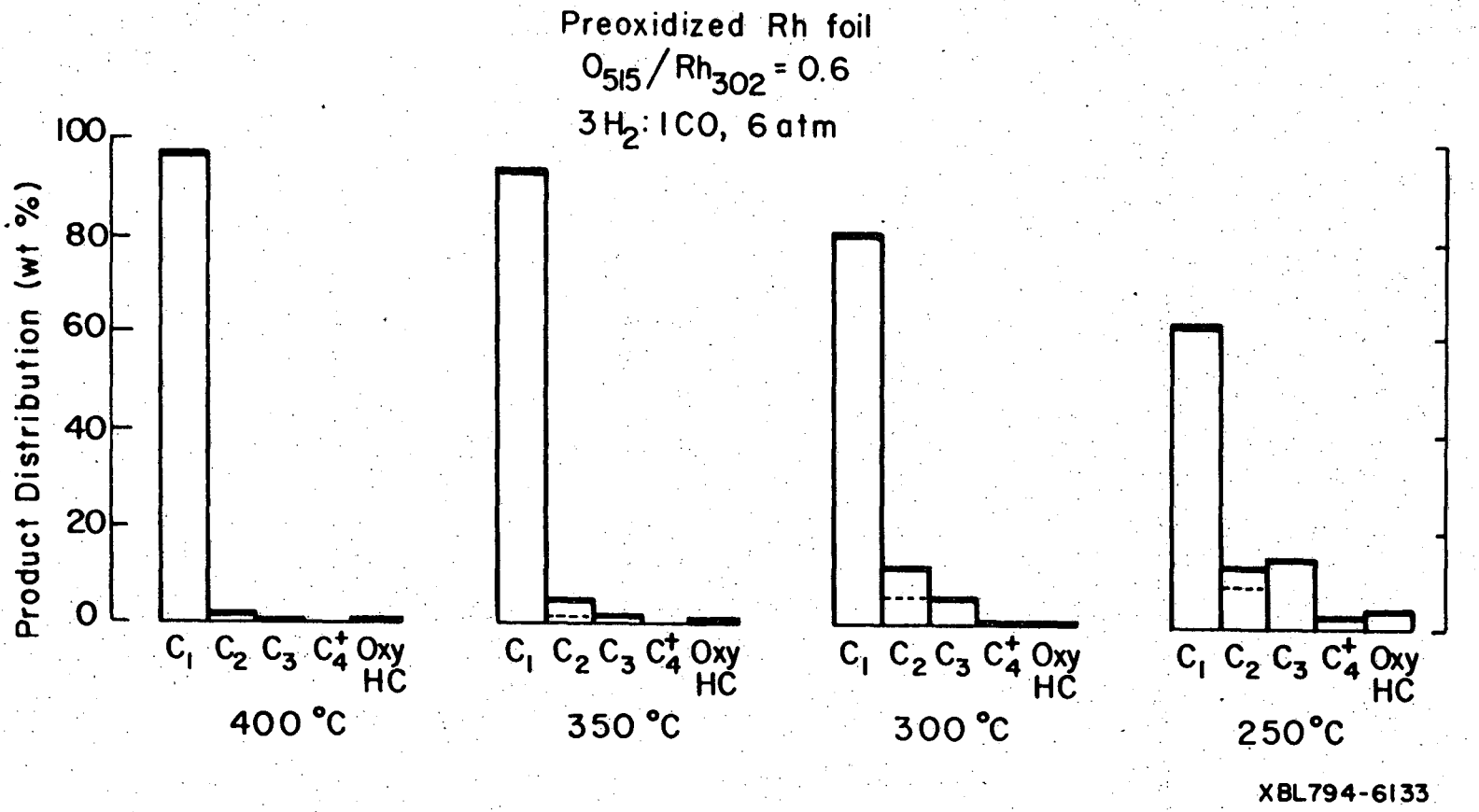

Figure III-60. Product distribution, in weight percent, after 2 hours of hydrogenation over preoxodized Rh foil. The areas above and below the dotted line in the C_2 fraction represent the amount of ethane and ethylene respectively. Oxy HC is the sum of the CH_3OH, CH_3CH_2OH and CH_3CHO fractions.

determined to be 12± 2 kcal/mole for the temperature range 250 to 400°C. This value was obtained from plotting $\ell n(CH_4TN)$ versus 1/T(Arrhenius plot) which yields a straight line with a slope of $-E_a/R$. The initial CH_4TN was used in the calculations thus E_a should be representative of a heavily oxidized Rh foil.

4) Gas Phase Additives

In the previous two sections the effects of a surface additive (oxygen pretreatment) were described. In this section the effects of adding ~ 1 mole percent of CH_3OH, CH_3CH_2OH and C_2H_4 to a $3H_2$:1CO reaction mixture at 250°C over a preoxidized Rh(111) crystal will be described. These experiments were carried out to determine the importance of readsorption of the initial reaction products in the CO hydrogenation reaction over rhodium crystals. Due to the high reactor volume to catalyst area ratio (159.5 cm^3 to 0.6 cm^2) less than 1% of the CO is converted into products. At this low conversion the concentration of reaction products is so low that the readsorption processes of these products is minor compared to the CO and H_2 adsorption processes. By adding a significant amount of a given reaction product to the initial reaction mixture high conversion conditions can be simulated and the importance of product readsorption can be determined.

The effects of the gas phase additives on the product distribution over a preoxidized Rh(111) crystal at 250°C, $3H_2$:1CO and 6 atm are shown in Fig. III-61. Unfortunately the amount of the gas phase additive completely overshadows the amount of that particular product which the Rh crystal produces. Therefore in the experiments with the CH_3OH

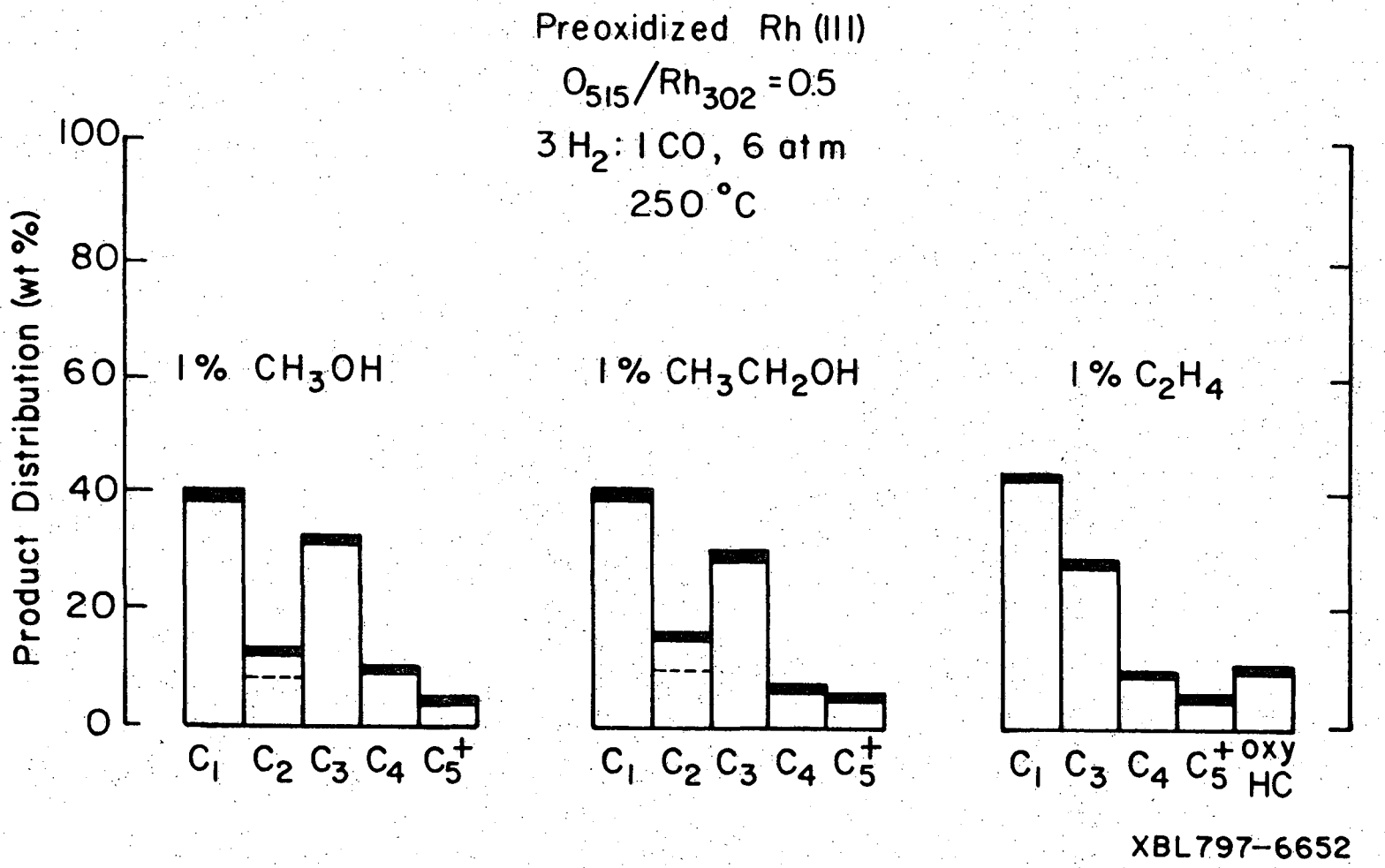

Figure III-61. Product distributions, in weight percent, after 2 hours of CO hydrogenation over a preoxidized Rh(111) crystal with 1 mole percent methanol, ethanol and ethylene added to the reaction mixture. The areas above and below the dotted line in the C_2 fraction represent the amount of ethane and ethylene, respectively. Oxy HC is the sum of the CH_3OH, CH_3CH_2OH and CH_3CHO fractions.

and CH_3CH_2OH additives the amount of oxygenated products was not measured and in the experiments with the C_2H_4 additive the amount of C_2 hydrocarbons was not measured. The absolute amount of methane produced and the initial CH_4 TN does not change significantly when ethylene, methanol or ethanol is added to the reaction mixture. The percentage of CH_4 in the product distribution does decrease noticeably however, due to the increase in amount of higher molecular weight products. The most marked increase was in the C_3 hydrocarbon fraction with smaller increases occurring in the C_4 and C_5^+ hydrocarbon fractions.

5) Discussion of CO Hydrogenation Results

In this section a general discussion of the CO hydrogenation results over polycrystalline Rh foil and single crystalline Rh(111) catalysts will be presented. A comparison of these results will be made to previous CO hydrogenation results over a variety of rhodium catalysts. Comparisons will also be made to previous results on iron foils and single crystals which were obtained under the same reaction conditions used here.

The results obtained at 6 atm over the clean Rh surfaces are in good agreement with previous CO hydrogenation studies at 1 atm over Rh foil[11] and 1% Rh supported on Al_2O_3.[10] The initial CH_4 TN's over the unsupported Rh catalysts are the same within experimental error and about a factor of 4 times greater than the CH_4 TN over 1% Rh/Al_2O_3. This is reasonable agreement considering the different methods of surface area measurement (geometrical versus hydrogen chemisorption). The major difference lies in the composition of the C_2 hydrocarbon fraction.

Over the supported Rh catalyst only ethane was produced while over the unsupported Rh catalyst both ethylene and ethane were produced. For the unsupported Rh catalysts the selectivity change from C_2H_4 to C_2H_6 which occurred during the reaction of $3H_2$:1CO at 6 atm was not present at 1 atm, but a noticeable conversion of C_2H_4 to C_2H_6 was seen for reaction temperatures above 300°C in $9H_2$:1CO gas mixtures. The hydrogenation of C_2H_4 could explain the selectivity change from C_2H_4 to C_2H_6 as the reaction progresses. It is evident that rhodium is a good hydrogenation catalyst from the gas phase additive experiments with C_2H_4 because most of the initially added C_2H_4 is rapidly converted to C_2H_6. At the higher H_2 partial pressure in 6 atm experiments the hydrogenation reaction would be enhanced relative to the 1 atm experiments and this difference could result in the differences in the C_2 hydrocarbon fractions between the two experiments. Another difference between the unsupported Rh catalysts was catalyst poisoning. At 1 atm no poisoning was detected over a 5 hour reaction while at 6 atm poisoning was observed. About the same amount of carbon was deposited in both experiments but possibly the conversion of this active carbon layer to an nonreactive carbon layer was enhanced at the higher pressures. Also the effect of the sulfur and chlorine impurities could be more pronounced at 6 atm.

Comparison of the CO hydrogenation results over clean Rh crystals to clean Fe crystals[185-187] show several differences. The Fe catalysts have about a factor of ten higher CH_4 TN, produce more higher weight hydrocarbons and poison more rapidly. The poisoning is the result of the buildup of a multilayer carbon deposit on the Fe catalyst. When the carbon multilayer has formed (after 2-3 hours of reaction) only methane

is produced. Thus under similar CO hydrogenation conditions rhodium is initially less active than iron but it runs cleaner (less carbon build-ups) and continues its FT activity for longer periods of time. During their FT activity periods both metals are covered by about a monolayer of carbon. The unsupported clean rhodium CO hydrogenation results differ from the results of experiments done between 25 and 200 atm over supported Rh on SiO_2.[13,14] At the higher pressures large amounts of C_2 oxygenated products (> 40%) were produced. One possible explanation could be that at the higher pressures the formation of the oxygenated products becomes more favorable. This pressure dependence is unlikely because methanol, ethanol and other oxygenated products have been produced by supported rhodium catalysts below 1 atm.[188-190] These studies showed amount and type of oxygenated product formed depended on the metal oxide support and how the rhodium was deposited on the support. The most active methanol catalysts were formed by decomposing various Rh carbonyl complexes on MgO, ZnO, BeO and CaO supports.[188] The most active ethanol catalysts were formed by decomposing various Rh carbonyl complexes on La_2O_3, TiO_2, ThO_2, ZrO_2 and CeO_2 supports.[189] In contrast, catalysts formed by decomposition of Rh carbonyls on SiO_2 and γ-Al_2O_3 suports or hydrogen reduction of impregnated $RhCl_3$ on La_2O_3 and ZnO supports primarily produced hydrocarbon products.[188,189] These results point out the importance of the chemical state of rhodium and its environment in determining the product distribution. Therefore the Rh foil and (111) catalysts are good models for the Rh catalysts which produce only hydrocarbons from H_2-CO mixtures but are not good models

for the Rh catalysts which produce oxygenated products from these same H_2-CO mixtures. Thus metallic rhodium or a carbon-rhodium complex is active for hydrocarbon formation but not for oxygenated product formation.

Changing the chemical environment of rhodium by oxidizing the Rh crystals produced dramatic changes in catalyst activity and selectivity. Oxidizing the Rh(111) crystal was shown to result in the epitaxial growth of Rh_2O_3 on the crystal and dissolution of large amounts of oxygen in the rhodium lattice.[29] Thus the rhodium chemical environment changes from metallic to oxide during the oxidation process. This change could explain the large increase in catalyst activity and the production of oxygenated products over preoxidized Rh catalysts. It would be important in the future to carry out x-ray photoelectron spectroscopy (XPS) experiments on these catalysts to determine a more quantitative relationship between the oxidation state of rhodium and its catalytic properties. Methanol, ethanol and acetaldehyde were produced over preoxidized Rh foil and Rh(111) crystals, but the hydrocarbon production still dominated the product distribution. Thus preoxidizing the crystals does increase the production of oxygenated hydrocarbons, but does not optimize it. The deposition of surface additives such as K, Mn or other promotors on the oxiidized surface might be useful in further increasing the amount of oxygenated products formed. They also might stabilize the Rh oxide so it will not be rapidly reduced as it was in these experiments.

The increased catalytic activity that was observed for CO hydrogenation over preoxidized Rh crystals at 6 atm is in agreement with

previous results over Rh and Fe foils. The CH_4 TN from these studies are summarized in Table III-14 along with the CH_4 TN for the H_2-CO_2 reaction over these catalysts. In the calculation of the CH_4 TN the same site density (the atom density of the particular metal) was used for both the clean and preoxidized surfaces. For the clean surfaces this value should represent a lower limit for the CH_4TN because it assumes all atoms on the surface are active. Using the same site density for the preoxidized surfaces could influence the CH_4 TN in two ways. Preoxidation could increase the surface area of the catalyst slightly causing a slight increase in CH_4 TN. Preoxidation significantly decreases the concentration of metal atoms in the surface region and if the only active sites are metal atoms then the CH_4 TN would be understated. Because of these influences and the changing surface composition from the rapid oxide decomposition under the reaction conditions only the trends which occur during preoxidation will be discussed.

From Table III-14 it can be seen that the CH_4 TN increases as the oxygen concentration is increased. The clean surfaces have the lowest methane TN's. Oxidizing the Rh foil then heating the oxidized foil to 1000°C in vacuum enhances the CH_4 TN by a factor of ~ 3. Heating an oxidized Rh foil to 1000°C would result in removal of any epitaxial oxide and leave only a small concentration of oxygen in the near surface region. The CH_4 TN from this surface is the same as the one observed in the H_2-CO_2 reaction over a clean Rh foil and slightly lower than the CH_4 TN after 2 to 3 hours of CO hydrogenation over a preoxidized Rh foil which was not heated in vacuum after oxidizing. CO_2 has been

Table III-14. Comparison of methanation TN for CO and CO_2 hydrogenation in a batch reactor at 300°C over rhodium and iron catalysts. Methane TN in molec·site^{-1}·sec^{-1}.

Catalyst	Reaction Conditions	Surface Pretreatment	Methane TN	Reference
Rh foil	$3H_2$:1CO, 0.92 atm	clean	0.13	(11)
		preoxidized[a]	0.33	(11)
Rh foil	$3H_2$:1CO_2, 0.92 atm	clean	0.33	(11)
		preoxidized[a]	1.7	(11)
Rh foil	$3H_2$:1CO, 6 atm	clean	0.15	this
		preoxidized[b]	1.7	study
Rh(111)	$3H_2$:1CO, 6 atm	clean	0.15	this
		preoxidized[b]	4.6	study
Fe foil	$3H_2$:1CO, 6 atm	clean	1.9	(185)
		preoxidized[c]	18.7	(185)
Fe foil	$3H_2$:1CO_2, 6 atm	clean	10.9	(185)

(a) 15 min. at 300°C in 700 torr O_2, then heated to 1000°C in vacuum.

(b) 30 min. at 600°C in 800 torr O_2.

(c) 20 min. at 300°C in 4 atm O_2.

shown to dissociatively adsorb on rhodium surfaces[26,27,34,35] which suggests some of the oxygen produced during CO_2 adsorption is oxidizing the Rh surface and increasing the CH_4 TN. Two to three hours of CO hydrogenation over a Rh foil with an epitaxial oxide removes the epitaxial oxide leaving oxygen only in the near surface region. This reduces the CH_4 TN to the value observed for CO hydrogenation over a oxidized Rh foil which has been heated in vacuum to remove the epitaxial oxide prior to the reaction. Further increases in the oxygen concentration by either hydrogenating CO_2 over a Rh foil with oxygen in the near surface region or hydrogenating CO over a Rh foil with an epitaxial oxide yields a further increase in the CH_4 TN. The results of CO and CO_2 hydrogenation over Fe foils[185] follow the same trends observed for the Rh foils. On Fe foils the ability of CO_2 to oxidize the metal was readily apparent since an iron oxide phase was formed during the initial stages of the H_2-CO_2 reaction over the clean Fe foil.[185] Thus the CH_4 TN increases as the oxygen concentration in the near surface region increases.

The methane E_a decreases as the oxygen concentration increases. On the clean Rh foil E_a is 24± 2 kcal/mole for the H_2-CO reaction, and 16 ± 2 kcal/moles for the H_2-CO_2 reaction.[11] On a preoxidized Rh foil E_a drops to 12 ± 2 kcal/mole for the H_2-CO reaction. The pre-exponential factor in the Anhenius expression must also be varying with the oxygen concentration because this large decrease in E_a with a constant pre-exponential factor would generate a CH_4 TN three orders of magnitude larger than was observed. Some of the difference may be accounted for by the fact that the observed TN's are lower limits to actual TN's, but

clearly some change in the pre-exponential factor must be occurring to fully account for this large difference.

There was no evidence for structure sensitivity of the H_2-CO reaction over the clean Rh foil and Rh(111) samples. This is reasonable since it is likely that an annealed polycrystalline foil would contain a large fraction of (111) facets. The results do imply, however, that surface imperfections such as grain boundaries do not play an important role in the H_2-CO reaction over clean rhodium surfaces. Similar results have been observed for polycrystalline Fe foils and Fe(111) single crystals.[187] It would be important to extend the Rh experiments to stepped and/or kinked single crystals to see if these type of surfaces would show any structure sensitivity. It was observed under UHV conditions that CO dissociation occurs on the stepped Rh surfaces but not on the Rh(111) surface.[26,27] If CO dissociation is important in the FT synthesis, as has been proposed in the carbide theory, it is possible there will be differences between the results over stepped and Rh(111) surfaces.

Oxidizing the two Rh surfaces did produce some structure sensitivity. The CH_4 and C_2H_6 TN's were larger for the preoxidized Rh(111) crystal than for the preoxidized Rh foil while the C_2H_4 TN was the same for both surfaces. This indicates the oxidized Rh(111) crystal has a higher activity for paraffin production than the oxidized Rh foil. It could not be determined whether this relationship existed in the C_3 and higher hydrocarbon fractions because the chromasorb 102 column used in the gas chromatography did not separate the paraffin and olefins in these

hydrocarbons fractions. The increase in the C_3 and C_4 TN's did correlate with the increase in the C_2H_6 TN on the two surfaces, though. Thus it is likely that the enhancement of paraffin production on the oxidized Rh(111) crystal holds for all the hydrocarbon fractions.

The variation of the product distribution with reaction temperature and H_2:CO ratio was as expected. As the reaction temperature is decreased from 400°C the free energy of formation, ΔG_f, of the higher molecular weight hydrocarbons decrease more rapidly than the lower molecular weight hydrocarbons and the olefin ΔG_f's approach the paraffin ΔG_f's.[186] Thus a larger percentage of higher weight hydrocarbons and olefins should be present in the product distribution at the lower reaction temperatures, in agreement with the experimental results. Decreasing the H_2:CO ratio will reduce the amount of hydrogen available for incorporation into the reaction products and reduce the hydrogeneration of these reactions products. Thus CO rich mixtures would produce larger percentages of olefins and aldehydes in the product distributions than the H_2 rich mixtures, again in agreement with the experimental results.

Gas phase additives (methanol, ethanol and ethylene) changed the product distributions over oxidized Rh crystals, but not as markedly as was observed for ethylene and propylene additives over oxidized Fe crystals.[187] Thus the readsorption of initial reaction products is more important on the Fe catalysts than on the Rh catalysts. The gas phase additive experiments indicate that the results obtained at low CO conversions should vary slightly but be representative of results

that would be obtained at higher CO conversion. It also should be noted that the CH_3OH, CH_3CH_2OH and C_2H_4 additives effected the product distribution in the same manner, indicating they are incorporated into the chain growth mechanism in the same manner. One possibility would be dehydration of the alcohols.

IV. CONCLUSION

The chemisorption properties of H_2, O_2, CO, CO_2, NO, C_2H_4, C_2H_2 and carbon have been investigated on the Rh(111), (100), (755) and (331) surfaces by LEED, TDS and AES. All the gases readily adsorbed on the rhodium surfaces and several ordered surface structures were observed. Chemisorbed oxygen was very reactive and was readily removed from the surface by H_2 or CO at temperatures above 50°C. Upon adsorption carbon dioxide was dissociated to CO by rhodium and its chemisorption behavior was identical to that of CO. On all the rhodium surfaces CO adsorption initially produces a low coverage structure which compresses into a close packed hexagonal CO overlayer at high coverages. Both dissociative and associative NO adsorption occurred on the rhodium surfaces, with the changeover from dissociative to associative adsorption occurring at $\sim$ 1L. The similar chemisorption properties of C_2H_4 and C_2H_2 at 25°C indicate that these adsorbed hydrocarbons undergo molecular rearrangement to produce the same surface species. Low temperature adsorption of these hydrocarbons is associative. Heating the adsorbed hydrocarbons resulted their decomposition to gaseous hydrogen and surface carbon. Several ordered carbon structures were generated on the (111) surface from saturating the near surface region with carbon from C_2H_4 decomposition. These structures were interconvertible by either addition or subtraction of surface carbon and represent an important bulk-surface carbon equilibrium.

Many of the chemisorption properties were markedly influenced by the presence of steps on the high step density (40%) Rh(331) crystal face while the effects due to steps were minimal on the low step density (17%) Rh(S)-[6(111)×(100)] surface. Thus, the influence of steps on the rhodium surface chemistry increases with step density, Rh(111)<Rh(S)-[6(111)×(100)]<Rh(331). The most important step effect was the dissociation of adsorbed CO by both rhodium stepped surfaces. The stepped surfaces also affected the adsorbate ordering. On Rh(S)-[6(111)×(100)] long range ordering was decreased while on Rh(331) several new adsorbate unit cells were observed. The stability of the two stepped surfaces in the presence of O_2 and C_2H_4 at high temperatures were very different, with the (331) surface more stable. Comparison of the rhodium results to the reported results on stepped iridium and platinum show that the chemical effects of steps during the chemisorption of small molecules increase in the order Rh<Ir<Pt. The important exception is CO, since its dissociation was only detected on the stepped rhodium surfaces. The differences detected between chemisorption on rhodium, iridium and platinum stepped surfaces is in contrast to the very similar chemisorption properties of these small molecules on the (111) and (100) crystal faces of these metals.

In the oxidation studies on the Rh(111) surface four oxygen species were identified and characterized. These four oxygen species were interdependent and interconversion between the different species could be accomplished by making appropriate changes in O_2 partial pressure and crystal temperature. Low temperature dissociative adsorption

produced very reactive chenisorbed oxygen atoms which underwent an activated ordering process to form three domains of a (2×1) surface structure. Heating the crystal in the presence of oxygen resulted in dissolution of large amounts of oxygen in the rhodium lattice. Prolonged high temperature annealing in 1×10^{-5} torr of O_2 produced a non-reactive surface oxide. High temperature annealing in 1 torr of O_2 resulted in an epitaxial growth of $Rh_2O_3(0001)$ on the Rh(111) surface.

CO hydrogenation at 300°C, $3H_2$:1CO and 6 atm over clean polycrystalline Rh foil and single crystalline Rh(111) catalysts produced primarily methane (90 wt %), at an initial methanation rate of 0.15 molec·site^{-1}·sec^{-1}. No oxygenated products were detected during CO hydrogenation over the clean Rh crystals. Preoxidation of the Rh crystals had a marked effect on the CO hydrogenation results. Initial TN's increased, a larger percentage of higher weight hydrocarbons were present in the product distribution and three oxygenated hydrocarbons (CH_3OH, CH_3CH_2OH and CH_3CHO) were produced. For the H_2 rich H_2:CO gas mixtures ~ 1 monolayer of carbon buildup on the Rh catalysts during a reaction. The primary effect of gas phase additives (1 mole % of CH_3OH, CH_3CH_2OH or C_2H_4) was to increase the percentage of C_3 hydrocarbons in the product distribution.

ACKNOWLEDGMENTS

I am especially grateful to Professor Gabor Somorjai for introducing me to surface sicence and catalysis, and providing me with a constant source of ideas, support and insight into my research. The members of the Somorjai group, past and present, have provided me with a lot of very helpful assistance by imparting the basics of surface science to me, allowing me to draw on their extensive experience and knowledge, and being an excellent source of many intriguing conversations. The help of the Chemistry Dept and MMRD staffs has made it possible to keep my vacuum system operating and has allowed my research project to be completed with a minimum amount of difficulties.

My wife Beverly deserves special thanks for the loving support, understanding and encouragement she provided during our stay in Berkeley. Her presence has made the long hours and difficulties of my graduate studies much more bearable. My daughter Jean has provided me with several very happy and proud moments during the last year. I have enjoyed the support and friendship of the Chem. Pistols, especially Professor Mahan's group, in a variety of social, athletic and academic activities at Berkeley.

I gratefully acknowledge the support of the National Science Foundation for an Energy Traineeship (1/77 to 9/78). This work was carried out with support from the Division of Materials Science, Office of Basic Energy Sciences, U.S. Department of Energy.

REFERENCES

1. G. W, Parshall, J. Molec.Catal.4 (1978) 243.
2. R. L. Pruett and J. A. Smith, U. S. Patent 3,917,661 (1975).
3. R. Fowler, H. Connor and R. A. Baehl, Chem. Tech. 6 (1976) 772.
4. F. E. Paulik, A. Hershman, W. R. Knox and J. F. Roth, U. S. Patent 3,769,329 (1973).
5. J. F. Roth, J. H. Craddock, A. Hershman and F. E. Paulik, Chem. Tech. 1 (1971) 600.
6. R. L. Pruett and W. E. Walker, U. S. Patent 3,957,857 (1976).
7. R. L. Pruett, Ann. NY Acad.Sci.295 (1977) 239.
8. J. C. Schlatter and K. C. Taylor, J. Catal.49 (1977) 42.
9. R. L. Klimisch and J. G. Larson, Eds., "The Catalytic Chemistry of Nitrogen Oxides" (Plenum Press, New York, 1975).
10. M. A. Vannice, J. Catal. 37 (1975) 449.
11. B. A. Sexton and G. A. Somorjai, J. Catal. 46 (1977) 167.
12. D. G. Castner, R. L. Blackador and G. A. Somorjai, submitted.
13. M. M. Bhasin, W. J. Bartley, P. C. Ellgen and T. P. Wilson, J. Catal. 54 (1978) 120.
14. P. C. Ellgen, W. J. Bartley, M. M. Bhasin and T. P. Wilson, 175th National ACS Meeting, Anaheim, Calif., Div. Petrol. Chem. Prepr. 23 (1978) 616.
15. J. G. Ekerdt, Ph.D. Thesis, University of California, Berkeley, (1979), LBL-9108 and references therein.
16. O. Beeck, Faraday Soc. 8 (1950) 118.

17. G. C. Bond, "Catalysis by Metals" (Academic Press, London, 1962).

18. J. R. Anderson and C. Kemball, Proc. Roy. Soc. (London) A223 (1954) 361.

19. C. Kemball, Proc. Roy. Soc. (London) A214 (1952) 413.

20. J. T. Yates, P. A. Thiel and W. H. Weinberg, Surface Sci. 82 (1979) 45.

21. T. Pignet and L. D. Schmidt, J. Catal. 40 (1975) 212.

22. C. W. Tucker, Acta Metallurgica 15 (1967) 1465.

23. C. W. Tucker, J. Appl. Phys. 37 (1966) 4147 and 38 (1967) 2696.

24. C. W. Tucker, J. Appl. Phys. 37 (1966) 3013.

25. J. T. Grant and T. W. Haas, Surface Sci. 21 (1970) 76.

26. D. G. Castner, B. A. Sexton and G. A. Somorjai, Surface Sci. 71 (1978) 519.

27. D. G. Castner and G. A. Somorjai, Surface Sci. 83 (1979) 60.

28. J. T. Yates, P. A. Thiel and W. H. Weinberg, Surface Sci., submitted.

29. D. G. Castner and G. A. Somorjai, LBL-9288.

30. P. A. Thiel, J. T. Yates and W. H. Weinberg, Surface Sci. 82 (1978) 22.

31. P. A. Thiel, E. D. Williams, J. T. Yates and W. H. Weinberg, Surface Sci. 84 (1979) 54.

32. R. A. Marbrow, Ph.D. Thesis, University of Cambridge, 1977.

33. R. A. Marbrow and R. M. Lambert, Surface Sci. 67 (1977) 489.

34. L. H. Dubois and G. A. Somorjai, LBL-8976.

35. L. H. Dubois and G. A. Somorjai, LBL-9280.

36. L. H. Dubois, D. G. Castner and G. A. Somorjai, to be published.

37. F. R. Shephard, P. R. Watson, D. C. Frost and K. A. R. Mitchell, J. Phys. C, submitted.

38. K. A. R. Mitchell, P. R. Watson, F. R. Shepherd and D. C. Frost, Surface Sci. 64 (1977) 737.

39. P. R. Watson, F. R. Shepherd, D. C. Frost and K. A. R. Mitchell, Surface Sci. 72 (1978) 562.

40. D. C. Frost, S. Hengrasmee, K. A. R. Mitchell, F. R. Shepherd and P. R. Watson, Surface Sci. 76 (1978) L585.

41. D. Castiel, L. Dobrzynski, R. F. Wallis, D. G. Castner and G. A. Somorjai, to be published.

42. C. M. Chan, P. A. Thiel, J. T. Yates and W. H. Weinberg, Surface Sci. 76 (1978) 296.

43. C. T. Campbell and J. M. White, J. Catal. 54 (1978) 289.

44. C. T. Campbell, S. K. Shi and J. M. White, Appl. Surface Sci. 2 (1979) 382.

45. C. T. Campbell and J. M. White, Appl. Surface Sci. 1 (1978) 347.

46. T. Pignet and L. D. Schmidt, J. Catal. 40 (1975) 212.

47. L. L. Hegedus, J. C. Summers, J. C. Schlatter and K. Baron, J. Catal. 56 (1979) 321.

48. J. C. Summers and K. Baron, J. Catal. 57 (1979) 380.

49. H. C. Yao, Y. F. Yu Yao and K. Otto, J. Catal. 56 (1979) 21; H. C. Yao and M. Shelef, J. Catal. 56 (1979) 12.

50. Y. Okamoto, N. Ishida, T. Imanaka and S. Teranishi, T. Catal. 58 (1979) 82.

51. P. Sabatier and J. B. Senderens, C. R. Acad. Sci., Paris, 134 (1902) 514.

52. F. Fischer and H. Tropsch, Brennst-Chem. 4 (1923) 276.

53. F. Fischer and H. Tropsch, Brennst-Chem. 7 (1926) 97.

54. S. R. Craxford and E. K. Rideal, J. Chem. Soc. (1939) 1604.

55. S. R. Craxford and E. K. Rideal, Trans. Faraday Soc. 42 (1946) 576.

56. H. Storch, N. Golumbic and R. Anderson, "The Fischer-Tropsch and Related Synthesis" (Wiley, New York, 1951).

57. R. S. Sapienza, M. J. Sansone, L. D. Spaulding and J. F. Lynch, BNL-24857, submitted to Chemtech.

58. G. Hemici-Olivé and S. Olivé, Angew Chem.Int. Ed. Engl., 15(1976)136.

59. I. Wender, Catal. Rev. Sci. Eng. 14 (1976) 97.

60. G. A. Mills and F. W. Steffgen, Catal. Rev. 8 (1973) 159.

61. Y. T. Eidus, Russ. Chem. Rev. 36 (1967) 338.

62. H. Schulz and A. Zein El Deen, Fuel Processing Tech. 1 (1977) 31 and 1 (1977) 45.

63. M. A. Vannice, Catal. Rev.-Sci. Eng. 14 (1976) 153.

64. M. A. Vannice, J. Catal. 37 (1975) 462.

65. P. Biloen, J. N. Helle and W. M. H. Sachtler, J. Catal. 58 (1979) 95.

66. D. W. Blakely, E. I. Kozak, B. A. Sexton and G. A. Somorjai, J. Vac. Sci. Technol. 13 (1976) 1091.

67. G. A. Somorjai and M. A. Van Hove, LBL-8566.

68. J. B. Pendry, "Low-Energy Electron Diffraction" (Academic Press, London, 1974).

69. J. A. Strozier, D. W. Jepsen and F. Jona, in "Surface Physics of Materials", J. M. Blakely, Ed. (Academic Press, New York 1975).

70. L. L. Kesmodel and G. A. Somorjai, Acc. Chem. Res. 9 (1976) 392.

71. M. A. Van Hove and S. Y. Tong, "Surface Crystallography by LEED: Theory, Computation and Structural Results" (Springer, Heidelberg, 1979).

72. G. A. Somorjai and L. L. Kesmodel, Trans. Am. Cryst Assoc. 13 (1977) 67.

73. L. E. Firment, Ph.D. Thesis, Univ. of Calif., Berkeley, 1977, LBL-6017.

74. P. C. Stair, Ph.D. Thesis, Univ. of Calif., Berkeley, 1977, LBL-6221.

75. C. Kittel, "Introduction to Solid State Physics" (Wiley and Sons, New York, 1976).

76. E. A. Wood, J. Appl. Phys. 35 (1964) 1306.

77. B. Lang, R. W. Joyner and G. A. Somorjai, Surface Sci. 30 (1972) 454.

78. D. W. Blakely, Ph.D. Thesis, Univ. of Calif., Berkeley, 1977, LBL-6064.

78. J. E. Houston and R. L. Park, Surface Sci. 21 (1970) 209.

80. J. E. Houston and R. L. Park, Surface Sci. 26 (1971) 269.

81. C. C. Chang, Surface Sci. 25 (1971) 53.

82. S. H. Overbury, Ph.D. Thesis, Univ. of Calif., Berkeley, 1976, LBL-5720.

83. G. A. Somorjai, "Principles of Surface Chemistry" (Prentice-Hall, Englewood Cliffs, 1972).

84. G. Ertl and J. Küppers, "Low-Energy Electrons and Surface Chemistry" (Verlag Chemie, Weinheim, 1974).

85. G. A. Somorjai and F. J. Szalkowski, "Advances in High Temperature Chemistry", L. Eyring, Ed. (Academic Press, New York, 1971).

86. R. D. Kelley, D. W. Goodman, T. E. Madey and J. T. Yates, Conference on Catalyst Deactivation and Poisoning, Lawrence Berkeley Laboratory, Calif., May 24-26, 1978; DOE Pub-238.

87. P. Légaré, G. Marie, B. Carière and J. P. Deville, Surface Sci. 68 (1977) 348.

88. T. Matsushima, D. B. Almy and J. M. White, Surface Sci. 67 (1977) 89.

89. J. P. Biberian and G. A. Somorjai, Appl. Surface Sci. 2 (1979) 352.

90. P. A. Redhead, Vacuum 12 (1962) 203.

91. G. Ehrlich, J. Appl. Phys. 32 (1961) 4.

92. G. Ehrlich, Advan. Catal. 14 (1963) 255.

93. L. D. Schmidt, Catal. Rev.-Sci. Eng. 9 (1974) 115.

94. D. A. King, Surface Sci. 47 (1975) 384.

95. C. M. Chan, R. Aris and W. H. Weinberg, Appl. Surface Sci. 1 (1978) 360.

96. C. M. Chan and W. H. Weinberg, Appl. Surface Sci. 1 (1978) 377.

97. D. G. Castner and G. A. Somorjai, Chem. Rev. 79 (1979) 233.

98. C. E. Smith, Ph.D. Thesis, Univ. of Calif., Berkeley, 1978, LBL-8044.

99. W. A. Dietz, J. Gas Chromotogr. 5 (1967) 68.

100. K. A. Gschneider, Solid State Physics 16 (1964) 370.

101. K. Christmann, G. Ertl and O. Schober, Surface Sci. 40 (1973) 61.

102. B. E. Nieuwenhuys, D. I. Hagen, G. Rovida and G. A. Somorjai, Surface Sci. 59 (1976) 155.

103. K. Christmann, O. Schober, G. Ertl and M. Neumann, J. Chem. Phys. 60 (1974) 4528.

104. K. Christmann, G. Ertl and T. Pignet, Surface Sci. 54 (1976) 365.

105. K. Christmann, O. Schober and G. Ertl, J. Chem. Phys. 60 (1974) 4719.

106. H. Conrad, G. Ertl, J. Küppers and E. E. Latta, Surface Sci. 57 (1976) 475.

107. H. Conrad, Ph.D. Thesis, Univ. of Munich, 1976.

108. G. Ertl, M. Neuman and K. M. Streit, Surface Sci. 64 (1977) 393.

109. D. I. Hagen, B. E. Nieuwenhuys, G. Rovida and G. A. Somorjai, Surface Sci. 57 (1976) 632.

110. J. Küppers and A. Plagge, J. Vac. Sci. Tech. 13, (1976) 259.

111. C. M. Comrie and W. H. Weinberg, J. Chem. Phys. 64 (1976) 250.

112. T. E. Madey and D. Menzel, Proc. 2nd Interntl. Conf. on Solid Surfs. (1974) 229.

113. M. Neumann, private communication.

114. J. C. Tracy, J. Chem. Phys. 56 (1972) 2736.

115. J. C. Tracy, J. Chem. Phys. 51 (1972) 2748.

116. J. T. Grant, Surface Sci. 18 (1969) 228.

117. C. R. Helms, H. P. Bonzel and S. Kelemen, J. Chem. Phys. 65 (9176) 1773.

118. J. C. Tracy and P. W. Palmberg, J. Chem. Phys. 51 (1969) 4852.

119. H. Conrad, G. Ertl, J. Küppers and E. E. Latta, Surface Sci. 65 (1977) 235.

120. H. Conrad, G. Ertl, J. Küppers and E. E. Latta, Surface Sci. 50 (1975) 296.

121. H. Ibach, H. Hopster and B. Sexton, Appl. Surface Sci. 1 (1977) 1.

122. H. Ibach and S. Lehwald, J. Vac. Sci. Technol. 15 (1978) 407.

123. P. C. Stair and G. A. Somorjai, Chem. Phys. Lett. 41 (1976) 391; J. Chem. Phys. 66 (1977) 2036.

124. L. L. Kesmodel, R. C. Baetzold and G. A. Somorjai, Surface Sci. 66 (1977) 299.

125. L. L. Kesmodel, L. H. Dubois and G. A. Somorjai, Chem. Phys. Lett. 56 (1978) 267; J. Chem. Phys. 70 (1979) 2180.

126. J. E. Demuth, Chem. Phys. Lett. 45 (1977) 12; IBM J. Res. Develop. 22 (1978) 265.

127. J. E. Demith, Surface Sci. 80 (1979) 367.

128. S. Lehwald and H. Ibach, to be published.

129. J. E. Demuth and H. Ibach, Surface Sci. 78 (1978) L238.

130. J. E. Demuth, Surface Sci. 76 (1978) L603; Surface Sci. 69 (1977) 365.

131. M. A. Van Hove, R. J. Koestner and G. A. Somorjai, to be published.

132. J. Suzanne, J. P. Coulomb and M. Bienfait, Surface Sci. 40 (1973) 414.

133. C. Kittel, "Introduction to Solid State Physics" (Wiley & Sons, Inc., New York, 1976), p. 32.

134. J. C. Shelton, H. R. Patil and J. M. Blakely, Surface Sci. 43 (1974) 493.

135. G. Brodén and T. N. Rhodin, Surface Sci. 61, (1976) 143.

136. L. C. Isett and J. M. Blakely, Surface Sci. 47 (1975) 645 and 58 (1976) 397.

137. B. Lang, Surface Sci. 53 (1975) 317.

138. L. H. Germer, E. J. Schneiber and C. D. Hartman, Phil. Mag. 5 (1960) 222.

139 J. C. Bertolini and G. Dalmai-Imelik, Coll. Intern. CNRS, Paris, 7-11 July 1969.

140. T. Edmonds and R. C. Pitkethly, Surface Sci. 15,(1969) 137.

141. J. E. Demuth, Surface Sci. 69 (1977) 365.

142. J. Kanski and T. N. Rhodin, Surface Sci. 65 (1977) 63.

143. H. P. Bonzel and R. Ku, Surface Sci. 40 (1973) 85.

144. P. C. Stair and G. A. Somorjai, J. Chem. Phys. 66 (1977) 2036.

145. H. P. Bonzel and G. Pirug, Surface Sci. 62 (1977) 45.

146. S. Andersson, Proc. 3rd Internat. Vac. Congr. and 7th Internat. Conf. on Solid Surf. (1977) 1019.

147. J. E. Demuth and T. N. Rhodin, Surface Sci. 45 (1975) 249.

148. G. Casalone, M. G. Cattania, M. Simonetta and M. Tescari, Surface Sci. 62 (1977) 321.

149 G. Dalmai-Imelik and J. C. Bertolini, C. R. Acad. Sci. 270 (1970) 1079.

150. G. Brodén, T. N. Rhodin and W. Capehart, Surface Sci. 61 (1976) 143.

151. T, N. Rhodin and G. Brodén, Surface Sci. 60 (1976) 466.

152. G. Brodén and T. N. Rhodin, S. S. Comm. 18 (1976) 105.

153. G. Kneringer and F. P. Netzer, Surface Sci. 49 (1975) 125.

154. A. E. Morgan and G. A. Somorjai, J. Chem. Phys. 51 (1969)3309.

155. D. M. Collins and W. E. Spicer, Surface Sci. 69 (1977) 85.

156. K. Schwaha and E. Bechtold, Surface Sci. 65 (1977) 277.

157. R. A. Marbrow and R. M. Lambert, Surface Sci. 71 (1978) 107.

158. H. Conrad, G. Ertl, J. Koch and E. E. Latta, Surface Sci. 43 (1974) 462.

159. M. Housley, R. Ducros, G. Piquard and A. Cassuto, Surface Sci. 68 (1977) 277.

160. M. Alnot, J. J. Ehrhardt, J. Fusy and A. Cassuto, Surface Sci. 46 (1974) 81.

161. J. Gland, Surface Sci. 71 (1978) 327.

162. R. Ku, N. A. Gjostein and H. P. Bonzel, Surface Sci. 64 (1977) 465.

163. K. Boron, D. W. Blakely and G. A. Somorjai, Surface Sci. 41 (1974) 54.

164. A. Wold, R. J. Arnott and W. J. Croft, Inorganic Chemistry 2 (1963) 972.

165. V. P. Ivanov, G. K. Boreskov, V. I. Savchenko, W. F. Egelhoff and W. H. Weinberg, Surface Sci. 61 (1976) 207.

166. H. Conrad, G. Ertl, J. Küppers and E. E. Latta, Surface Sci. 65 (1977) 245.

167. B. A. Sexton, to be published.

168. S. Andersson, Solid State Comm. 20 (1976) 229.

169. G. E. Thomas and W. H. Weinberg, J. Chem. Phys. 70 (1979) 954.

170. H. Froitzheim, H. Ibach and S. Lehwald, Phys. Rev. B14 (1976) 1362.

171. H. Conrad, G. Ertl, J. Küppers and E. E. Latta, Surface Sci. 57 (1976) 475.

172. T. E. Madey, H. A. Engelhardt and D. Menzel, Surface Sci. 48 (1975) 304.

173. P. M. Marcus, J. E. Demuth and D. W. Jepsen, Surface Sci. 53 (1975) 501.

174. C. M. Chen and W. H. Weinberg, to be published.

175. C. E. Smith, J. P. Biberian and G. A. Somorjai, J. Catal. 57 (1979) 426.

176. M. E. Bridge and R. M. Lambert, Surface Sci. 82 (1979) 413.

177. H. Conrad, G. Ertl, J. Küppers and E. E. Latta, Solid State Comm. 17 (1975) 497.

178. G. W. Simmons and D. J. Dwyer, Surface Sci. 48 (1975) 373.

179. C. Benndorf, B. Egert, G. Keller, H. Seidel and F. Thieme, Surface Sci. 80 (1979) 287.

180. S. Ferrer, A. M. Baró and J. M. Rojo, Surface Sci. 64 (1977) 668.

181. P. H. Holloway and J. B. Hudson, J. Vac. Sci. Technol. 12 (1975) 647.

182. A. M. Horgan and I. Dalins, Surface Sci. 36 (1973) 526.

183. H. Conrad, J. Küppers, F. Nitschké and A. Plagge, Surface Sci. 69 (1977) 668.

184. R. Ducros and R. P. Merrill, Surface Sci. 55 (1976) 227.

185. D. J. Dwyer and G. A. Somorjai, J. Catal. 52 (1978) 291.

186. D. Dwyer, K. Yoshida and G. A. Somorjai, 175th National ACS Meeting, Anaheim, Calif. Div. Petrol. Chem. Prepr. 23 (1978) 521.

187. D. J. Dwyer and G. A. Somorjai, J. Catal. 56 (1979) 249.

188. M. Ichikawa, Bull. Chem. Society Japan, 51 (1978) 2268.

189. M. Ichikawa, Bull. Chem. Society Japan, 51 (1978) 2273.

190. M. Ichikawa, J. Catal. 56 (1979) 127.

TECHNICAL INFORMATION DEPARTMENT
LAWRENCE BERKELEY LABORATORY
UNIVERSITY OF CALIFORNIA
BERKELEY, CALIFORNIA 94720